# Ultrafast Quantum Optics with Spectral Resolution



a dissertation presented by Michał Lipka

IN FULFILLMENT OF THE REQUIREMENTS

FOR THE DEGREE OF

DOCTOR OF PHILOSOPHY

IN THE SUBJECT OF

PHYSICAL SCIENCES

THESIS ADVISOR: DR HAB. MICHAŁ PARNIAK-NIEDOJADŁO

Centre of New Technologies, University of Warsaw Faculty of Physics, University of Warsaw Warsaw, Poland May 2024

#### Ultrafast Quantum Optics with Spectral Resolution

#### **ABSTRACT**

Optical photons are exceptional, reliable carriers of information and yet also excellent, extremely sensitive probes of matter. The spectro-temporal degree of freedom (DoF) of a photon plays an important role in these properties. In the context of emerging quantum technologies and partially that of fundamental phenomena, this thesis explores the spectral DoF of single-photon and single-photon level broadband light.

The thesis is based on a series of publications concerned with a relatively wide range of problems in quantum and ultrafast optics. Photon-starved light in a temporal mode of an ultrashort pulse (spectrally broadband) is the "common denominator" of these works. So is a unique measurement device developed and applied for the studies – a very fast single-photon-sensitive camera. Its creation and characterization enabled or greatly simplified many of the presented experiments. As a fairly universal scientific tool, it still holds great potential for further applications.

The predominantly experimental work presented herein encompasses 5 studies. In the first one, we characterize hybrid entanglement between the transverse and spectral DoF for pairs of photons generated in a non-collinear type-I spontaneous parametric down-conversion process. The second study explores the two-photon interference with spectrally-resolved single-photon detection, as a method to dispersively probe lightmatter interactions. In the third experiment, we turn from single photons to weak coherent states (single-photon level) and demonstrate a variation of the electro-optic shearing interferometry, albeit based on the second-order intensity correlation measurement and particularly suitable for ultrashort pulses in the near-infrared. The fourth study demonstrates an electro-optic single-photon-level-compatible ultrafast implementation of a coherent time-frequency transformation - Fractional Fourier Transform which is of interest itself as a generalization of the ordinary Fourier Transform and also constitutes an indispensable building block of the next experiment. In the final part, we turn to the frequency-domain quantum metrology and demonstrate a spectral super-resolution method motivated by the recent rapid developments in quantuminspired far-field super-resolution imaging techniques. The presented method can be regarded as a frequency-domain implementation of the ideas of image-inversion interferometry. Compared with a spectral intensity measurement, it reduces the resources required to estimate a separation between two spectral features.

#### Ultraszybka Optyka Kwantowa z Rozdzielczością Spektralną

#### STRESZCZENIE

Fotony w domenie optycznej stanowią wyjątkowe i niezawodne nośniki informacji, ale również doskonałe i niezwykle czułe sondy materii. Czasowo-spektralny stopień swobody (StSw) fotonu odgrywa w tych własnościach istotną rolę. W kontekście rozwijających się technologii kwantowych oraz po części w kontekście zjawisk fundamentalnych niniejsza praca stanowi eksplorację spektralnego StSw szerokopasmowego światła pojedyczno-fotonowego, oraz o natężeniu zbliżonym do pojedynczego fotonu.

Niniejsza praca jest oparta na serii publikacji omawiających stosunkowo szeroki zakres problemów optyki kwantowej i ultraszybkiej. Ultrasłabe światło o modzie czasowym ultrakrótkiego impulsu (spektralnie szerokopasmowe) jest "wspólnym mianownikiem" tych prac. Jak również jest nim unikalne narzędzie pomiarowe w nich użyte i dla nich stworzone – bardzo szybka kamera czuła na pojedyncze fotony. Jej opracowanie i charakteryzacja umożliwiły lub znacznie uprościły wiele z przedstawionych eksperymentów. Jako dosyć uniwersalne narzędzie badawcze, kamera ciągle ma duży potencjał do dalszych zastosowań.

Prezentowane tutaj, w znacznej części doświadczalne, badania obejmują 5 prac. W pierwszej z nich charakteryzujemy hybrydowe splątanie pomiędzy poprzecznym i spektralnym StSw pary fotonów wygenerowanych w niekolinearnym procesie parametrycznego podziału częstości typu I. Druga praca stanowi eksplorację interferencji dwufotonowej z rozdzieloną-spektralnie detekcją pojedynczych fotonów, jako metody dyspersyjnego próbkowania oddziaływań światło-materia. W trzecim eksperymencie przechodzimy od pojedynczych fotonów do słabych stanów koherentnych (natężenie zbliżone do pojedynczego fotonu) i przedstawiamy wariant elektrooptycznej interferometrii ścinania, jednakże opartej o pomiar korelacji natężeniowej drugiego rzędu i szczególnie dostosowanej do ultrakrótkich impulsów w bliskiej podczerwieni. Czwarta praca ukazuje kompatybilną z natężeniem zbliżonym do pojedynczego fotonu, elektrooptyczną, ultraszybką implementację koherentnej czasowo-spektralnej transformacji – Cząstkowej Transformaty Fouriera (CTF), która jest interesująca sama w sobie jako generalizacja zwykłej Transformaty Fouriera, oraz stanowi nieodzowny element składowy kolejnego eksperymentu. W ostatniej części przechodzimy do metrologi kwantowej w dziedzinie częstości i demonstrujemy metodę nadrozdzielczości spektralnej umotywowaną intensywnym w ostatnim czasie rozwojem kwantowo-inspirowanych metod daleko-polowego obrazowania nadrozdzielczego. Prezentowaną metodę można uznać za implementację idei interferometrii inwersji obrazu. W porównaniu z pomiarem spektralnego natężenia redukuje ona ilość wymaganych zasobów do estymacji separacji pomiędzy dwoma obiektami spektralnymi.

[This page intentionally left blank]

## List of publications & patents

#### PUBLICATIONS AND PREPRINTS DIRECTLY RELATED TO THIS THESIS

- 1. **M. Lipka** and M. Parniak, "Super-resolution of ultrafast pulses via spectral inversion", arXiv preprint arXiv:2403.12746 (2024)
- 2. **M. Lipka** and M. Parniak, "Ultrafast electro-optic time-frequency fractional Fourier imaging at the single-photon level", Opt. Express **32**, 9573–9588 (2024)
- 3. S. Kurzyna, M. Jastrzębski, N. Fabre, W. Wasilewski, **M. Lipka**, and M. Parniak, "Variable electro-optic shearing interferometry for ultrafast single-photon-level pulse characterization", Opt. Express **30**, 39826–39839 (2022)
- 4. **M. Lipka** and M. Parniak, "Single-Photon Hologram of a Zero-Area Pulse", Phys. Rev. Lett. **127**, 163601 (2021)
- 5. **M. Lipka** and M. Parniak, "Fast imaging of multimode transverse-spectral correlations for twin photons", Opt. Lett. **46**, 3009–3012 (2021)

#### OTHER PUBLICATIONS

- 6. **M. Lipka**, A. Sierant, C. Troullinou, and M. W. Mitchell, "Multiparameter quantum sensing and magnetic communication with a hybrid dc and rf optically pumped magnetometer", Phys. Rev. Appl. **21**, 034054 (2024)
- 7. W. Krokosz, M. Mazelanik, M. Lipka, M. Jarzyna, W. Wasilewski, K. Banaszek, and M. Parniak, "Beating the spectroscopic Rayleigh limit via post-processed heterodyne detection", Opt. Lett. 49, 1001–1004 (2024)
- 8. F. Albarelli, M. Mazelanik, **M. Lipka**, A. Streltsov, M. Parniak, and R. Demkowicz-Dobrzański, "Quantum Asymmetry and Noisy Multimode Interferometry", Phys. Rev. Lett. **128**, 240504 (2022)
- 9. **M. Lipka**, M. Mazelanik, A. Leszczyński, W. Wasilewski, and M. Parniak, "Massively-multiplexed generation of Bell-type entanglement using a quantum memory", Commun. Phys. **4**, 46 (2021)

- 10. M. Lipka, M. Mazelanik, and M. Parniak, "Entanglement distribution with wavevector-multiplexed quantum memory", New J. Phys. 23, 053012 (2021)
- 11. M. Mazelanik, A. Leszczyński, **M. Lipka**, W. Wasilewski, and M. Parniak, "Real-time ghost imaging of Bell-nonlocal entanglement between a photon and a quantum memory", Quantum 5, 493 (2021)
- 12. **M. Lipka**, M. Jarzyna, and K. Banaszek, "Quantum Fingerprinting Over AWGN Channels With Power-Limited Optical Signals", IEEE J. Sel. Areas Commun. **38**, 496–505 (2020)
- 13. M. Mazelanik, A. Leszczyński, **M. Lipka**, M. Parniak, and W. Wasilewski, "Temporal imaging for ultra-narrowband few-photon states of light", Optica 7, 203–208 (2020)
- M. Lipka, A. Leszczyński, M. Mazelanik, M. Parniak, and W. Wasilewski, "Spatial spin-wave modulator for quantum-memory-assisted adaptive measurements", Phys. Rev. Applied 11, 034049 (2019)
- M. Mazelanik, A. Leszczyński, M. Lipka, W. Wasilewski, and M. Parniak, "Superradiant parametric conversion of spin waves", Phys. Rev. A 100, 053850 (2019)
- M. Mazelanik, M. Parniak, A. Leszczyński, M. Lipka, and W. Wasilewski, "Coherent spin-wave processor of stored optical pulses", npj Quantum Inf. 5, 22 (2019)
- M. Parniak, M. Mazelanik, A. Leszczyński, M. Lipka, M. Dąbrowski, and W. Wasilewski, "Quantum optics of spin waves through ac Stark modulation", Phys. Rev. Lett. 122, 063604 (2019)
- 18. M. Dąbrowski, M. Mazelanik, M. Parniak, A. Leszczyński, **M. Lipka**, and W. Wasilewski, "Certification of high-dimensional entanglement and Einstein-Podolsky-Rosen steering with cold atomic quantum memory", Phys. Rev. A **98**, 042126 (2018)
- 19. M. Jachura, M. Jarzyna, M. Lipka, W. Wasilewski, and K. Banaszek, "Visibility-based hypothesis testing using higher-order optical interference", Phys. Rev. Lett. 120, 110502 (2018)
- A. Leszczyński, M. Mazelanik, M. Lipka, M. Parniak, M. Dąbrowski, and W. Wasilewski, "Spatially resolved control of fictitious magnetic fields in a cold atomic ensemble", Opt. Lett. 43, 1147–1150 (2018)

- 21. M. Lipka, M. Parniak, and W. Wasilewski, "Microchannel plate cross-talk mitigation for spatial autocorrelation measurements", Appl. Phys. Lett. 112 (2018)
- 22. M. Jachura, M. Lipka, M. Jarzyna, and K. Banaszek, "Quantum fingerprinting using two-photon interference", Opt. Express 25, 27475–27487 (2017)
- 23. M. Lipka, M. Parniak, and W. Wasilewski, "Optical frequency locked loop for long-term stabilization of broad-line DFB laser frequency difference", Appl. Phys. B 123, 1–7 (2017)
- 24. M. Parniak, M. Dabrowski, M. Mazelanik, A. Leszczyński, M. Lipka, and W. Wasilewski, "Wavevector multiplexed atomic quantum memory via spatially-resolved single-photon detection", Nat. Commun. 8, 2140 (2017)

#### **PATENTS**

- Pat.235172 "Method of calibrating image amplifier to reduce crosstalk signals at input to microchannel system and image amplifier calibration kit"
   Inventors: W. Wasilewski, M. Lipka, M. Mazelanik, M. Parniak.

   Polish patent granted on 19.02.2020. system and image amplifier calibration kit
- 2. Pat.241214 "A system for generating polarisation-entangled photon pairs for repeating a quantum signal over a distance and a method for generating polarisation-entangled photon pairs in a multi-mode quantum memory for repeating a quantum signal over a distance"
  Inventors: W. Wasilewski, M. Lipka, M. Mazelanik, A. Leszczyński, A. Ostasiuk, K. Zdanowski, M. Parniak.
  Polish patent granted on 01.06.2022. International PCT patent pending WO2021245529.
- P.441074 "System and method for characterising weak femtosecond pulses at a single photon level using second-order interferometry in a time-frequency modulator system"
   Inventors: W. Wasilewski, M. Lipka, M. Parniak, M. Jastrzębski, S. Kurzyna. Unpublished Polish patent pending. International PCT patent pending.

[This page intentionally left blank]

# Contents

O	Introduction 1							
	0.1	Quantum optics	2					
	0.2	Single photons	4					
		0.2.1 Photon as the creation operator	4					
		0.2.2 Wave packets	5					
		0.2.3 Localization of photons	8					
		0.2.4 Coherent states	8					
I	Custom single-photon camera 11							
	1.1	Motivation: wavevector-multiplexed quantum memory as a photon gun	12					
	1.2		14					
	1.3	Image intensifier	16					
		1.3.1 Custom gating module	19					
	1.4		22					
			22					
			23					
		Background subtractation	23					
		· · · · · · · · · · · · · · · · · · ·	25					
			25					
			25					
			27					
			27					
		•	28					
	1.5		28					
			28					
			29					
	1.6		 29					
2	Hyr	BRID CORRELATIONS OF PHOTON PAIRS	31					
4	2.1		31					
	2.2	Introduction						

	2.3	Theory
		2.3.1 Two-photon amplitude
		2.3.2 Photon number covariance model
		2.3.3 Experimental covariance and accidental coincidences
		2.3.4 Non-classical correlations and the mode size
		2.3.5 Reference-free efficiency estimation
		2.3.6 Beta barium borate
	2.4	Numerical calculations
		2.4.1 Process intensity
		2.4.2 Walk-off angle
		2.4.3 Number of modes
	2.5	Experiment
	2.6	Results
	2.7	Conclusion
3	Ou	ANTUM SPECTROSCOPY 51
	3.1	Foreword
	3.2	Introduction
		3.2.1 Two-photon interference
		3.2.2 Simplified experiment
	3.3	Theory
		3.3.1 Zero-area pulses
		3.3.2 Spectrally-resolved two-photon interference
		3.3.3 Resonant bandwidth-mismatched light-matter interaction 61
	3.4	Experiment
		3.4.1 Setup
		3.4.2 Measurement
	3.5	Results
	3.6	Methods and discussion
		3.6.1 Rb optical depth calculation
		3.6.2 Visibility
		3.6.3 Fidelity
		3.6.4 Join spectral intensity, uncorrelated and correlated photons 75
		3.6.5 Phase reconstruction without prior knowledge
		3.6.6 Two or more photons per pixel
		3.6.7 Comparison with homodyne tomography 80
		Homodyne detection
		Two-photon interference without spectral resolution 83
		Comparison on the grounds of estimation theory 84
	3.7	Conclusion

4	Variable shearing interferometry 85			
	4.1	Foreword	. 89	
	4.2	Introduction	92	
	4.3	Theory	93	
		4.3.1 Idea of VarSI	93	
		4.3.2 Classical case – analyzing fringe visibility	. 94	
		4.3.3 Single-photon-level pulses	. 96	
		4.3.4 Exemplary simulated spectrograms	96	
		4.3.5 Relation to Chronocyclic Wigner Function	. 97	
		4.3.6 The reconstruction of the pulse complex electric field	. 98	
	4.4	Experimental setup	99	
		4.4.1 EOM and RF setup	101	
		4.4.2 Spectral shear calibration	102	
	4.5	Results	104	
	4.6	Methods		
		4.6.1 Derivation of the $g^{(2)}$ function	107	
		4.6.2 Derivation of the gradient function and numerical errors	. 110	
	<b>4.</b> 7	Conclusions	111	
5	Ult	rafast Fractional Fourier Transform	115	
	5.1	Foreword	115	
	5.2	Introduction		
	5.3	Fractional Fourier Transform		
		5.3.1 Two pulses		
	5.4	Experiment		
	5.5	Methods		
		5.5.1 Simulation	128	
		5.5.2 Fidelity		
		5.5.3 Second stretcher	129	
		5.5.4 Grating stretcher design	130	
		5.5.5 Strecher GDD calibration	132	
		5.5.6 RF line and EO modulation	135	
		5.5.7 Pulse preparation and FRT bandwidth	137	
		5.5.8 Spectrometers	140	
	5.6	Conclusion	141	
6	Supi	ER-RESOLUTION OF ULTRAFAST PULSES VIA SPECTRAL INVERSION	143	
	6.1	Foreword	143	
	6.2	Introduction		
	6.3	Theory		
		6.3.1 Spectral versus spatial domains	149	

		6.3.2	Spectral inversion interferometry	150						
		6.3.3	Super-resolution parameter	152						
	6.4	Experi	ment							
		6.4.1	Setup							
		6.4.2	Results	154						
		6.4.3	SUSI simulation	157						
		6.4.4	Direct imaging	159						
		6.4.5	Setup details and calibration	160						
			Pulse preparation	160						
			Interferometer stabilization	161						
			Fourier transformer calibration	163						
			Single-photon histograms	164						
	6.5	Modes	sorting	165						
	6.6	Conclu	asion	166						
7	Con	CLUSIO	N	167						
Appendix A Custom camera mechanical design										
Appendix B Schematics of the image intensifier gating driver										
REFERENCES										

## Acknowledgments

I would like to express my deepest gratitude to my supervisor dr hab. Michał Parniak for his guidance and mentorship, and his deep knowledge and great intuition in physics which made seemingly insurmountable obstacles dwindle in moments. I am also grateful to dr hab. Wojciech Wasilewski, prof. UW and prof. dr hab. Konrad Banaszek for their mentorship and generous support.

I have had the great pleasure of working alongside my colleagues from the Quantum Optical Devices Laboratory and Quantum Memories Laboratory. I would like to thank dr Mateusz Mazelanik for his vast expertise and the generous advice he has lent me so often. I am grateful to Marcin Jastrzębski and Stanisław Kurzyna for pushing our experiments into new prominent directions and for a very pleasant and fruitful collaboration. I would also like to thank prof. dr Nicolas Fabre for his novel proposals and deep theoretical insight. I am grateful to dr Marcin Jarzyna, dr Michał Jachura, dr hab. Rafał Demkowicz-Dobrzański, prof. UW, and dr Jan Kołodyński for their support on the theoretical grounds, which greatly aided our research. My deep gratitude goes to our engineer mgr inż. Tomasz Kowalczyk who regularly supported me with his proficiency and expertise in electronics and precise mechanics. I would like to express my gratitude to dr hab. Wojciech Wasilewski, prof. UW and mgr inż. Karol Kosiński for the design and construction of the first prototype of our fast camera. I am grateful to dr inż. Cezary Samojłowicz for the support and expertise in preparing our patent applications. I would also like to thank mgr Sebastian Borówka, Wiktor Krokosz, and Uliana Pylypenko for their support and the amiable atmosphere in our office.

In 2022 I had a terrific opportunity to spend 3 months at ICFO, Spain in the Atomic Quantum Optics group of prof. dr Morgan Mitchell, working also with dr Aleksandra Sierant and dr Charikleia Troullinou. I am deeply grateful for the wonderful time, fascinating research, mentorship, and companionship I received. It was a brief, yet truly remarkable experience.

I am grateful to the physics community and administration in the Centre Of New Technologies, at the Faculty of Physics, and in the Doctoral School of Exact and Natural Sciences for great management, creating many professional development opportunities, conducting excellent lectures and courses, and providing excellent working conditions.

I would like to acknowledge the optics and photonics student chapter "Koło Naukowe Optyki i Fotoniki Uniwersytetu Warszawskiego" (KNOF) for creating numerous networking and self-development opportunities and their continuous effort in bringing together students in the field.

My gratitude goes to the unsung heroes – the anonymous reviewers of our papers and grant proposals whose comments most often in the end improved the quality and clarity of the results.

Last but not least, I would not go far without the never-ceasing support of my fiancée Kasia, my friends, and my family. Thank you!

#### **FUNDING**

- Fundacja na rzecz Nauki Polskiej (MAB/2018/4 "Quantum Optical Technologies");
- European Regional Development Fund;
- Narodowe Centrum Nauki (2021/41/N/ST2/02926);
- Ministerstwo Edukacji i Nauki (DI2018 010848).

The "Quantum Optical Technologies" project is carried out within the International Research Agendas programme of the Foundation for Polish Science co-financed by the European Union under the European Regional Development Fund. This research was funded in whole or in part by National Science Centre, Poland 2021/41/N/ST2/02926. The author was supported by the Foundation for Polish Science (FNP) via the START scholarship. This scientific work has been funded in whole or in part by Polish science budget funds for years 2019 to 2023 as a research project within the "Diamentowy Grant" programme of the Ministry of Education and Science (DI2018 010848).

# Introduction

Quantum optics studies the behavior and properties of individual quanta of light – photons. It is a branch of physics with a long tradition and at the same time undergoing rapid development. Photons are not only very special to all of quantum physics, being one of the motivations for the quantum theory itself [1], but they also exhibit unrivaled properties e.g. for quantum communication and sensing. The ability to precisely engineer and transform quantum states of light, their intrinsic robustness to the environment, well-understood and controlled light-matter interactions, vast Hilbert space with numerous degrees of freedom

that can be harnessed with photonic systems, or the plethora of fundamental quantum phenomena that are most easily observed in the photonic domain, make photons truly remarkable, versatile and worthwhile.

This thesis comprises results of the experimental work in quantum optics with broad-band light and different forms of spectrally resolved detection, carried out in the Quantum Optical Devices Laboratory since the year 2020. Quantum optics is a vast area of study and in this spirit, we have studied a vast range of phenomena with different applications and fundamental questions in mind. We will follow a chronological path through the 5 main research articles that this thesis is based on.

Broadband light in our context refers to the use of light with a temporal structure of a pulse from  $100\,\mathrm{fs}$  to  $10\,\mathrm{ps}$  in duration and with spectral bandwidths between  $10\,\mathrm{nm}$  and  $0.2\,\mathrm{nm}$  (ca.  $100\,\mathrm{GHz}$  at  $800\,\mathrm{nm}$ ). Three of our studies were enabled by the development of a custom fast single-photon camera, which started around 2019 in the Quantum Memories Laboratory. The device served us mostly as a fast single-photon spectrometer in the near-infrared regime ( $800\,\mathrm{nm}$ ). The remaining two experiments employ indirect methods of spectral resolution. Nevertheless, the characterization of dim classical or quantum broadband light in the spectral degree of freedom remains a central theme of this work.

#### O.I QUANTUM OPTICS

At the beginning of the 20th century, Planck postulated quantized emission and absorption of light ("quantum of action") to explain the spectrum of black-body radiation [2]. In 1905 Einstein associated the quantum of action with the electromagnetic (EM) field and introduced photons [1]. The concept was further developed by Dirac [3] and Fermi [4], creating the field of quantum electrodynamics which depicts the photon as a bosonic

particle that mediates electromagnetic interactions.

Despite these early theoretical concepts, the first experimental works that can be considered the cradle of quantum optics had to wait another half a decade for the key technological developments – creation of an ammonia MASER in the 1950s by Townes, Gordon, and Zeiger [5] and a He-Ne laser by Maiman in the early 1960s [6]. The operation of these instruments is based on the stimulated emission of photons from matter with quantized energy levels. As such, they are inherently quantum devices which led to the development of a new field called quantum electronics. Nevertheless, quantum effects that could be experimentally observed with the aid of a laser were scarce and mainly limited to the photon statistics and phase diffusion studies [7].

The existence of the photon was only experimentally confirmed in 1977 by Kimble *et al.* observing the anti-bunching phenomenon [8]. Previous experiments could have been interpreted with semi-classical theory assuming classical fields and quantized atoms. The statistical light effects which cannot be described with classical theory, are still one of the main interests in quantum optics.

Quantum optics provides an important toolbox in investigating fundamental phenomena of quantum mechanics such as complementarity or hidden variables and on the other hand, constitutes a basis for powerful measurement techniques with sensitivities reaching well beyond the standard quantum limits [9]. Quantum states of light are employed in secure communication e.g. the quantum key distribution [10], quantum networks which are the basis of entanglement-based protocols [11], and quantum metrology whose importance is well demonstrated by the gravitational waves detectors [12].

#### 0.2 SINGLE PHOTONS

#### 0.2.1 PHOTON AS THE CREATION OPERATOR

Quantization of the electromagnetic field is well described in numerous classic books on quantum optics including refs. [7, 13–15] and as such will not be repeated here. Instead, we briefly discuss the results and how a single photon can be understood in their terms.

Operators of the quantized electric and magnetic field obey equivalents of the Maxwell wave equations. Here we shall limit the discussion to the electric field. In free space, the operator of a quantized electric field takes the following decomposition in the plane-wave basis [15]

$$\hat{E}(\vec{r},t) = \sum_{\vec{k},j} \vec{\epsilon}_{\vec{k},j} \mathcal{E}_{\vec{k}} \hat{a}_{\vec{k},j} \exp\left\{-i\omega_k t + i\vec{k} \cdot \vec{r}\right\} + \text{H.c.}, \tag{1}$$

where H.c. stands for the Hermitian conjugate,  $\vec{k}$  is the wavevector,  $\vec{\epsilon}_{\vec{k},j}$  denotes the unit polarization vector,  $\mathcal{E}_{\vec{k}}$  is the amplitude of the  $\vec{k}$  mode, j indexes one of the two possible polarizations,  $\omega_k$  is the angular frequency corresponding to the wavevector  $k = \left| \vec{k} \right|$ , spatial coordinates are denoted by  $\vec{r}$ , while time is denoted by t. The operators  $\hat{a}_{\vec{k},j}$  ( $\hat{a}_{\vec{k},j}^{\dagger}$ ) are the annihilation (creation) operators of a quantum harmonic oscillator obeying the commutation relations

$$\left[\hat{a}_{\vec{k},j}, \hat{a}_{\vec{k}',j'}\right] = 0, \tag{2}$$

$$\left[\hat{a}_{\vec{k},j},\hat{a}_{\vec{k}',j'}^{\dagger}\right] = \delta_{\vec{k}\vec{k}'}\delta_{jj'}.\tag{3}$$

In this context, these operators correspond to the annihilation (creation) of a photon in a given mode and with a given polarization. The Hamiltonian of the quantized EM field is

given by

$$\hat{H} = \sum_{\vec{k},j} \hbar \omega_k (\frac{1}{2} + \hat{n}_{\vec{k},j}) = \sum_{\vec{k}} \hat{H}_{\vec{k},j}, \tag{4}$$

where  $\hat{n}_{\vec{k},j}=\hat{a}^{\dagger}_{\vec{k},j}\hat{a}_{\vec{k},j}$  is the operator of the number of photons in j polarization and mode  $\vec{k}$ . Similarly, the operator of the total number of photons is given by

$$\hat{n} = \sum_{\vec{k},j} \hat{n}_{\vec{k},j} \tag{5}$$

For clarity, let us focus on a single polarization mode and drop the j index. The photon number, or energy, eigenstates called Fock states  $\left|n_{\vec{k}_1},n_{\vec{k}_2},\ldots\right\rangle$  correspond to a well-defined number of photons in each mode. The most general pure state will be given as a linear superposition of such eigenstates. Technically, a single photon in mode  $\vec{k}_l$  is just such an eigenstate describing a single excitation in mode  $\vec{k}_l$ 

$$|1\rangle_{\vec{k}_l} \equiv \left| n_{\vec{k}_1} = 0, n_{\vec{k}_2} = 0, \dots, n_{\vec{k}_{l-1}} = 0, n_{\vec{k}_l} = 1, \dots, n_{\vec{k}_{l+1}} = 0, \dots \right\rangle.$$
 (6)

It can be also written as the action of a creation operator on the vacuum state (i.e. a state with no photons)

$$|1\rangle_{\vec{k}_l} = \hat{a}_{\vec{k}_l}^{\dagger} |\text{vac}\rangle.$$
 (7)

#### O.2.2 WAVE PACKETS

While monochromatic plane waves are a convenient idealization, they carry an implicit assumption of being unbound in space and time. All experimentally attainable states will be in the form of wave packets in space and time, although a monochromatic plane wave can be an excellent approximation in certain cases.

Here we shall assume paraxial propagation which is justified by a well-defined optical axis and the low numerical apertures of the experimental setups we will discuss. Let us decompose the wavevector of any mode

$$\vec{k}_l = \vec{k}_0 + \Delta \vec{k}_l, \tag{8}$$

where we shall associate the  $\vec{k}_0$  propagation direction with the z axis. We will limit ourselves to a finite subspace of modes obeying

$$\left|\Delta \vec{k}_l\right| \ll \left|\vec{k}_0\right|. \tag{9}$$

Modes within this subspace obey paraxial propagation i.e. the angle between  $\vec{k}_l$  and  $\vec{k}_0$  remains small. Furthermore, the condition ensures that the frequency of the modes  $\omega_{k_l}$  is close to  $\omega_{k_0}$ . Henceforth, we will consider only the modes within the subspace.

Under our assumption, we can define the annihilation operator in space. Changing to a continuous basis we have

$$\hat{a}(\vec{r}) = \int \frac{\mathrm{d}^3 \vec{k}}{(2\pi)^3} \hat{a}(\vec{k}) \exp\left\{i\vec{k} \cdot \vec{r}\right\}. \tag{10}$$

This way, we can introduce a single photon in a spatial wave packet described by a mode function  $\phi(\vec{r})$ 

$$|1\rangle_{\phi} = \int d^{3}\vec{r} \,\phi(\vec{r})\hat{a}^{\dagger}(\vec{r}) |\text{vac}\rangle$$
 (11)

obeying normalization

$$\int d^3 \vec{r} \left| \phi(\vec{r}) \right|^2 = 1 \tag{12}$$

In the coarse-grained approximation [16],  $\phi(\vec{r})$  can be treated as a spatial wave-function of

a photon which allows its modulus squared  $|\phi(\vec{r})|^2$  to be interpreted as the probability of finding the photon in a small region around  $\vec{r}$ .

While Eq. (11) defines a single photon as a single excitation of a spatial mode with finite energy, we can do the same for the spectro-temporal domain. For instance, in a spatially one-dimensional case, we can reparametrize our equations in terms of the frequency  $\omega$  and write

$$|1\rangle_f = \int d\omega f(\omega) \hat{a}^{\dagger}(\omega) |vac\rangle,$$
 (13)

where the mode function  $f(\omega)$  is normalized

$$\int d\omega |f(\omega)|^2 = 1.$$
 (14)

In fact, by isolating a single transverse dimension in the paraxial approximation there is a strict correspondence between spatial and spectro-temporal domains called space-time duality [17].

Ultimately, we could also consider a general wave packet described in space and time with the most general space-time correlations. However, in our discussion, we will be dealing with photons corresponding to either well-defined frequency  $\omega$ , transverse spatial component  $\vec{r}_{\perp}$  or to a joint decomposition of the space-time mode function  $u(\vec{r},t)$  into transverse wavevectors  $\vec{k}_{\perp}$  and frequencies  $\omega$ 

$$|1\rangle_{u} = \iint \frac{\mathrm{d}^{2}\vec{k}_{\perp}}{(2\pi)^{2}} \,\mathrm{d}\omega \,\tilde{u}(\vec{k}_{\perp},\omega)\hat{a}^{\dagger}(\vec{k}_{\perp},\omega) \,|\mathrm{vac}\rangle \,, \tag{15}$$

where

$$\iint \frac{\mathrm{d}^2 \vec{k}_{\perp}}{(2\pi)^2} \,\mathrm{d}\omega \left| \tilde{u}(\vec{k}_{\perp}, \omega) \right|^2 = 1. \tag{16}$$

Of course, in the experiment, a well-defined frequency, wavevector, or position always needs to be understood as a small range around the given central value.

Finally, while we will refer to counting photons with a given frequency  $\omega$  or wavelength  $\lambda$ , it should be understood as a process involving a conversion between the spectral and spatial degree of freedom i.e. creating a strong correlation between the two, and a subsequent spatially resolved measurement.

#### 0.2.3 LOCALIZATION OF PHOTONS

We note that from the theory perspective, the localization of photons is a complex issue broadly debated in the field. Ref. [18] provides a comprehensive review of this problem. In brief terms, the issue arises due to the incompatibility between a photon state with sharply localized electric and magnetic fields and the Maxwell equations. Accurate theoretical descriptions of the single photon wavefunction and the solution to the localization problem can be found in refs. [19–22].

Let us note that the localization problem does not arise in the interpretation of our experiments since the spatial pixel size of the single-photon detectors is always much larger than the wavelength of photons and we limit ourselves to paraxial spatial modes.

#### 0.2.4 COHERENT STATES

Let us consider a single mode and denote the associated annihilation operator by  $\hat{a}$ . Coherent state  $|\alpha\rangle$  is defined as an eigenstate of the annihilation operator

$$\hat{a} |\alpha\rangle = \alpha |\alpha\rangle. \tag{17}$$

This defining property can be used to find the decomposition of a coherent state in the Fock basis

$$|\alpha\rangle = e^{-\frac{|\alpha|^2}{2}} \sum_{n=0}^{\infty} \frac{\alpha^n}{\sqrt{n!}} |n\rangle.$$
 (18)

The photon statistic  $|\langle n|\alpha\rangle|^2$  of a coherent state follows the Poisson distribution. Coherent states have a number of unique properties such as the lowest classically attainable photon number variance for a given average photon number. Photons in a coherent state can be regarded as uncorrelated [23]. Coherent states are also the basis for one of the phase-space representations of a quantum state, the Glauber–Sudarshan  $P(\alpha)$  function [24].

Experimentally, coherent states well describe the light emitted by a laser operating well above the threshold. In our discussion, we will sometimes refer to single-photon level light. In such cases, it should be understood as a coherent state with the average photon number  $\langle n \rangle = |\alpha|^2$  relatively close to 1 (as compared to e.g.  $\approx 1 \times 10^9$  photons per second in a "weak" near-infrared laser beam with a 1 nW of average power).

[This page intentionally left blank]

1

# Custom single-photon camera

Technological advancements are often the catalyst of fundamental studies. In general terms, the invention of a laser can be regarded as such and also as much more than that [25, 26]. Another example is the technology of superconducting single-photon detectors which reach unprecedentedly high detection efficiency enabling the loop-hole-free Bell tests [27, 28]. Conclusions of which are of a fundamental and philosophical nature.

In this spirit, we shall begin by describing our development of a custom measurement apparatus – a very fast single-photon-sensitive camera. The development began around

year 2019 in the Quantum Memories Laboratory, led by Wojciech Wasilewski. The initial motivation was an idea to implement quasi-probabilistic single-photon generation in the quantum memory described in very general terms below and in detail elsewhere [29–38].

#### I.I MOTIVATION: WAVEVECTOR-MULTIPLEXED QUANTUM MEMORY AS A PHOTON GUN

The memory is implemented in a 1 cm long cloud of Rb87 atoms held in a magneto-optical trap, with a temperature of ca.  $50~\mu K$ . Its operation is based on an off-resonant Raman scattering process where a spatially large write beam with a wavevector  $\vec{K}_W$  generates a pair of excitations – a single photon (Stokes) scattered at  $\vec{k}_S$  and a spin-wave. A spin-wave refers to a collective excitation of all atoms with a spatial phase dependence described with a wavevector  $\vec{K}$ . After a controlled delay on the order of tens of  $\mu s$ , a read beam with a wavevector  $\vec{K}_R$  induces the reverse process in which the spin-wave is destroyed and a single photon (Anti-Stokes) is generated at  $\vec{k}_{AS}$ . The wavevectors of the Stokes and Anti-Stokes correspond to different wavevector (angular) modes of the memory. The process is governed by the conservation of energy and momentum. Importantly for our discussion, altering the read beam wavevector direction  $\vec{K}_R$  (i.e. the angle of the beam relative to the cloud axis) changes the wavevector mode (emission angle) of the Anti-Stokes photon. [39] Of course, this is subject to the phase matching limitations [31]. Energy levels of Rb87 used for the memory cycle, as well as the schematic of the reconfiguration idea have been depicted in Fig. 1.1.

With this picture in mind, we can imagine that one observes the wavevector of the Stokes photon  $\vec{k}_{\rm S}$  (i.e. measures transverse position in the far field of the atomic cloud), and then uses this information to adjust the read beam wavevector  $\vec{K}_R$  so that the Anti-Stokes photon is emitted in a selected, always the same mode. The mode can be then for instance cou-

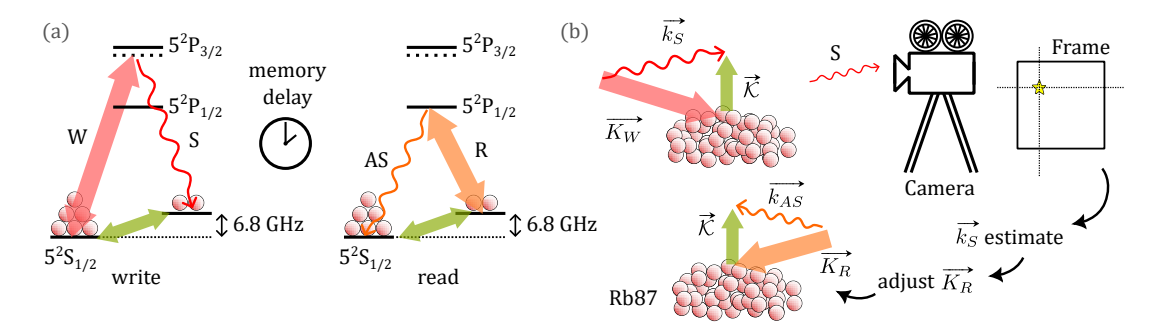


**Figure 1.1:** (a) Rb87 energy levels employed for the wavevector-multiplexed quantum memory. (b) Idea of the real-time reconfiguration of the read process.

pled to a fiber. In general, in each pair of memory modes (Stokes, Anti-Stokes), the memory cycle generates a two-mode squeezed state. It can only be well approximated by single photons (of high purity) if we keep the excitation probability low. Consequently, in each memory cycle, in most of the modes, nothing happens. Nevertheless with around 1000 mode pairs [32, 37] (and possible extension to a few thousand [40]), it is quasi-deterministic that at least in one pair the photons will be generated [29, 33]. Hence, if we can build a device that detects the Stokes photon wavevector and provides the information within the memory lifetime, we can quasi-deterministically generate single Anti-Stokes photons into a single mode. Such a device can be a single-photon sensitive camera, placed in the far-field of the atomic cloud, with a fast feedback system. The main technological challenge is the very short time required for all the processing, ideally on the order of a few  $\mu$ s.

The experiments with this memory usually employed the Andor Zyla 5.5 scientific CMOS (sCMOS) camera coupled to a 2-stage image intensifier. The setup is well analyzed and described in ref. [41]. While such off-the-shelf cameras offer terrific noise performance (not necessarily needed with an image intensifier and for quantum optics), it is at the cost of lower acquisition speeds. Furthermore, the camera frames have to be sent to the PC for processing to discriminate bright points corresponding to actual photons hitting the pho-

tocathode of the image intensifier. This process takes time on the order of ms.

To conclude, the idea of a quasi-deterministic photon source and the sub-par performance of the off-the-shelf scientific cameras motivated us to pursue the difficult task of bringing to life a custom detector. Our construction allowed almost a 10-fold increase in the frame acquisition rate and the freedom of fast processing implemented in the field programmable gate array (FPGA) without the prior need to send the frames to the PC. While ultimately we have not applied the camera as initially intended, the fast acquisition rates were indispensable in quantum optical experiments described in this thesis.

It is also worth noting that quasi-deterministic photon generation has been proposed and demonstrated in other systems [42–45]. With numerous quantum technologies based on single-photon states [46–53], it is a practically and fundamentally important direction of research. In particular, on-demand generation of N-photon Fock states would greatly benefit quantum metrology [9, 54–57].

#### I.2 CAMERA OVERVIEW

There are two main advantages of a custom construction over the off-the-shelf sCMOS cameras. The first is the freedom to choose a CMOS camera sensor. The second is the flexibility of custom image processing implemented in the camera. Let us begin with the former.

Single-photon cameras are used throughout many fields of science and technology including biology [58], medicine [59] or material science [60]. In particular, in quantum technologies, such detectors are employed from quantum information processing [61], computing [62] and communication [63, 64] to super-resolution imaging [65, 66] and localization [67] or characterization of non-classical states of light [68, 69].

In most applications beyond quantum optics, the camera is not coupled to an image intensifier as no true single-photon sensitivity is required. Instead, other figures of merit are optimized for, such as the signal-to-noise ratio, resolution, or contrast. The case of coupling the camera with an image intensifier is quite special, and the application of quantum-optical experiments, which usually deal with a very low number of photons per camera frame, is even more specialized.

The image intensifier (II) (further described in more detail) for each successfully detected photon produces a relatively bright (on the order of  $10^7$  photons for a 2-stage II) flash on an output phosphor screen. The screen is usually imaged with a bright relay lens on the CMOS sensor. The sensor has to be sensitive enough to register the flash; however, the requirement is nowhere near the single-photon sensitivity. As long as the sensor noise is most of the time below the typical flash brightness, its further reduction brings little benefit. This is in stark contrast to the task of dim-light imaging with the sCMOS camera alone. Furthermore, there is a relation between the measurement noise and the acquisition rate – slower readout reduced the noise. Hence, for our applications, a choice of a faster, more noisy CMOS sensor can be beneficial compared to a low-noise, universal but slower, off-the-shelf sCMOS camera.

Implementation of a custom image processing pipeline, while in principle possible in a commercial camera, is much more straightforward with a custom construction. Certain elements of the processing pipeline are common with off-the-shelf construction e.g. calibration and mitigation of inhomogeneity within the set of analog-digital converters (ADC) used in the CMOS chip, background subtraction, or hot pixel detection. The most worthwhile addition is the photon discrimination algorithm. In the tradition stemming from earlier works in the Quantum Memories Laboratory [41], we call the algorithm "photon-finder". The basic idea is that each  $w \times w$  pixel patch, where  $w = 3, 5, 7, \ldots$  is fixed for

a given architecture, is analyzed within the  $W \times H$  camera frame. The central pixel of the patch is checked to fulfill 2 conditions:

- 1. its value v is within a preset range  $T \leq v \leq T_{max}$ ,
- 2. it has the highest value within the patch.

The threshold T is set empirically to be above the typical sensor noise (avoiding false-positive detections), and yet as low as possible (maximizing efficiency). The idea of the photofinder is depicted in Fig. 1.2.

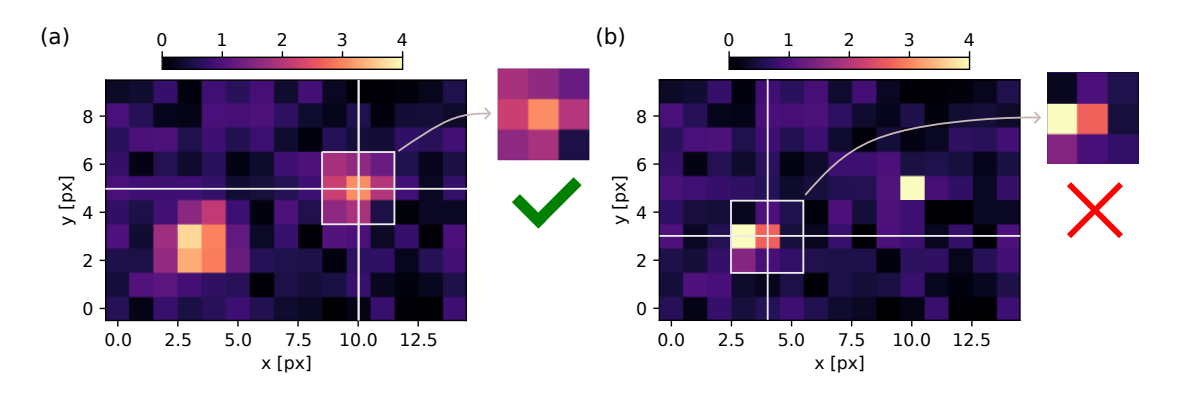


Figure 1.2: The idea of photonfinder thresholding visualized with exemplary simulated frame fragments. The typical width of a phosphor flash image is (a) above (b) below 1 px. The white crosshair in the image marks the currently processed pixel. If the value of the processed pixel is in the preset range  $T \leq v \leq T_{max}$ , it is further checked for having the maximum value in the neighbor area (here  $3 \times 3$  px). (a) The processed pixel is a local maximum and a photon count is concluded. (b) The processed pixel despite having a value in the desired range is not a local maximum (but a part of the flash centered at its left neighbor). Hence, no photon count is registered. The frame is processed pixel by pixel. In the case of large flashes (a) a model of the flash shape can be fitted to retrieve the photon position with sub-px resolution.

#### I.3 IMAGE INTENSIFIER

The operation principles of an II are depicted in Fig. 1.3, while the photograph of our unit together with the enclosure and accompanying electronics is included in Fig. 1.4. An image

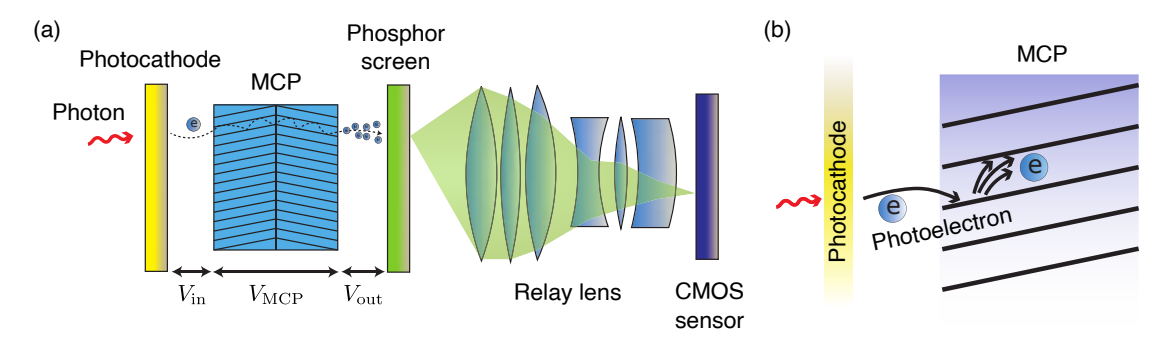
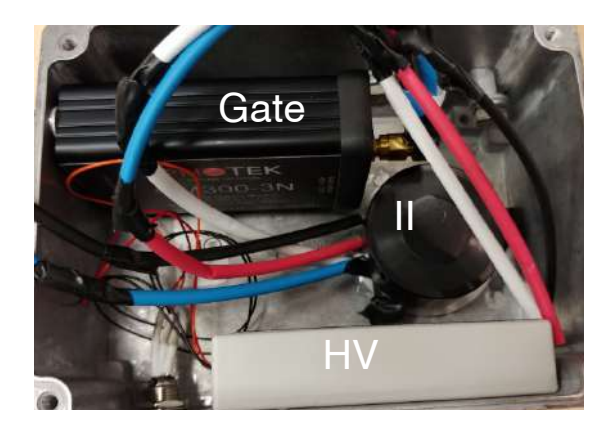


Figure 1.3: (a) Schematic depiction of an intensified camera. The image intensifier is comprised of a photocathode, a multichannel plate (MCP, here two-stage), and a phosphor screen. A photon striking the photocathode [see (b) for magnified version] releases a photoelectron which is accelerated (II gate open) or repelled (II gate closed) by a high voltage potential  $V_{\rm in}$ . MCP is composed of hexagonal microchannels of a few  $\mu m$  diameter. The walls of a microchannel are coated with a secondary emissive material. Once the electron enters a microchannel it collides with a wall and starts an avalanche process. Further accelerating potentials  $V_{\rm MCP}$  and  $V_{\rm out}$  are applied. A cloud of photoelectrons hits the phosphor screen producing a relatively bright (on the order of  $1\times10^7$  photons) flash.

intensifier consists of 3 elements enclosed in a high vacuum: a photocathode, a microchannel plate (MCP), and a phosphor screen (in some constructions instead there is a wire grid). We use an image intensifier by Hamamatsu, model V7090D-71.

The photocathode emits a photoelectron upon excitation by an impinging photon. The process is probabilistic and its probability is the main limiting factor of the quantum efficiency (QE) of image-intensified cameras. It is generally difficult to make a photocathode in the near-infrared spectral regime which would have a high QE. For wavelengths around  $800~\rm nm$  the best QE is between 20% and 30% (e.g. Hamamatsu declares slightly above 20%, while Photonis over 30%). On a limited sample of a few image intensifiers, we observed a few percent unit-to-unit variation of the QE. The photocathode aging is also the main factor limiting the lifetime of intensified cameras, and a strong reason to avoid exposing the II to stray light even if the II is not power supplied [70]. The active area of our photocathode is  $13.5~\rm mm \times 10~\rm mm$ 



**Figure 1.4:** Photograph of the image intensifier (II) together with the Photek GM10-50B gating module (Gate) and a Photek FP630 high-voltage power supply (HV), placed inside the shielding aluminum housing.

The MCP consists of a honeycomb-like structure of microchannels, each a few  $\mu m$  in diameter. The MCP is made of a highly resistive material, most often glass. Traditional (since the 1960s) manufacturing technique employs stacking in parallel and fusing together fibers with lead glass cladding and a glass inner core. Such prepared wafers are cut at a small angle to the fiber axis and the glass core is removed with etching. The obtained array of capillaries is heated in a hydrogen-rich atmosphere. In this process, the surface becomes highly resistive and emissive. Alternative methods have also been developed including e.g. atomic layer deposition [71].

A high voltage potential  $V_{\rm in}$  is applied between the photocathode and the MCP. In a closed state  $V_{\rm in} = +50\,\rm V$ , while in the active (open) state  $V_{\rm in} = -200\,\rm V$ . The voltage (which we also call gating voltage) can be changed in nanoseconds. Usually, the II is kept in the closed state and during a short gating period switched to the active state. If very fast switching is required, some designs may include a metallic thin-film electrode between the input window of the II and the photocathode, which reduces the capacitance of the photocathode. In the open state the negative voltage accelerates the photoelectron towards the MCP. Since the microchannels are slightly angled with respect to the input surface,

the photoelectron hits the wall of a microchannel soon after entering the MCP. Each microchannel acts like a photomultiplier while preserving the spatial information on the detected photon. A high voltage across the MCP  $V_{\rm MCP}=1800\,{\rm V}$  facilitates the avalanche multiplication process. In a 2-stage II (Chevron configuration) two MCPs are fused together with opposite angles of the microchannels.

Finally, the cloud of electrons exiting the MCP is accelerated in  $V_{\rm out}=6000\,{\rm V}$  and strikes the output phosphor screen. We employ a P46 phosphor with a fast  $100\,{\rm ns}$ -scale decay time (a common alternative is P43 with a higher brightness but slow  $1\,{\rm ms}$ -scale decay). The output flash contains around  $1\times 10^7$  photons per input photon. The flashes are imaged with a bright relay lens (magnification of M=0.44) onto the CMOS sensor.

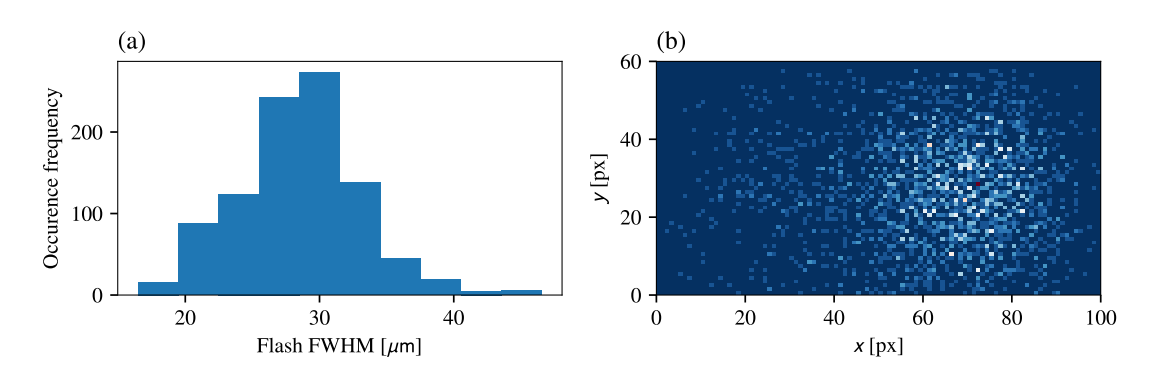


**Figure 1.5:** (a) Histogram of phosphor flash widths (full width at half maximum). (b) Spatial histogram of the flash centers.

An exemplary statistic of phosphor flashes (spatial histogram and flash width histogram) due to illumination with a weak coherent state (attenuated laser light) has been depicted in Fig. 1.5.

#### I.3.I CUSTOM GATING MODULE

The role of the image intensifier gating module is to quickly change between  $-200 \, \mathrm{V}$  and  $50 \, \mathrm{V}$  potential between the II photocathode and the microchannel plate. With the positive

voltage, the photoelectrons are repulsed and the II is inactive. Such a load for the driver is almost purely capacitive. Typically the capacitance is between 30 pF and 100 pF [72].

If short gating times are required (10s or 100s of ns), the required voltage slope becomes substantial – on the order of a  $1 \times 10^{11} \, \mathrm{V \, s^{-1}}$ . At the same time, because the separation between the photocathode and MCP is on the order of  $100 \, \mu \mathrm{m}$  it is paramount to avoid overshoot which could result in an electrical breakdown.

For the first camera tests and the experiment described in ch. 2, we used a Photek GM10-50B gating module. It is well suited to our image intensifier for up to  $1 \times 10^4$  frame per second. However, with higher frame rates, we observed a gradual drop in the apparent quantum efficiency of the camera. Around  $1 \times 10^5$  frames per second almost all signal (photon counts) disappeared.

A careful study of the experiment and the GM10-50B construction led us to conclude that the DC-DC converter responsible for the  $-200\,\mathrm{V}$  was unable to recover the necessary charge if the time between frames (hence between gating switches) was kept too low. Unfortunately, the module was damaged in the investigation process and we were unable to fix it quickly. Instead, we designed and built a custom gating module based on modern GaN transistors (Texas Instruments LMG3410). For illustration, its schematics and PCB layouts have been attached in appendix B. Ultimately, the  $-200\,\mathrm{V}$  was supplied to the driver from an external high-voltage power supply and not from a DC-DC converter indicated in the schematics.

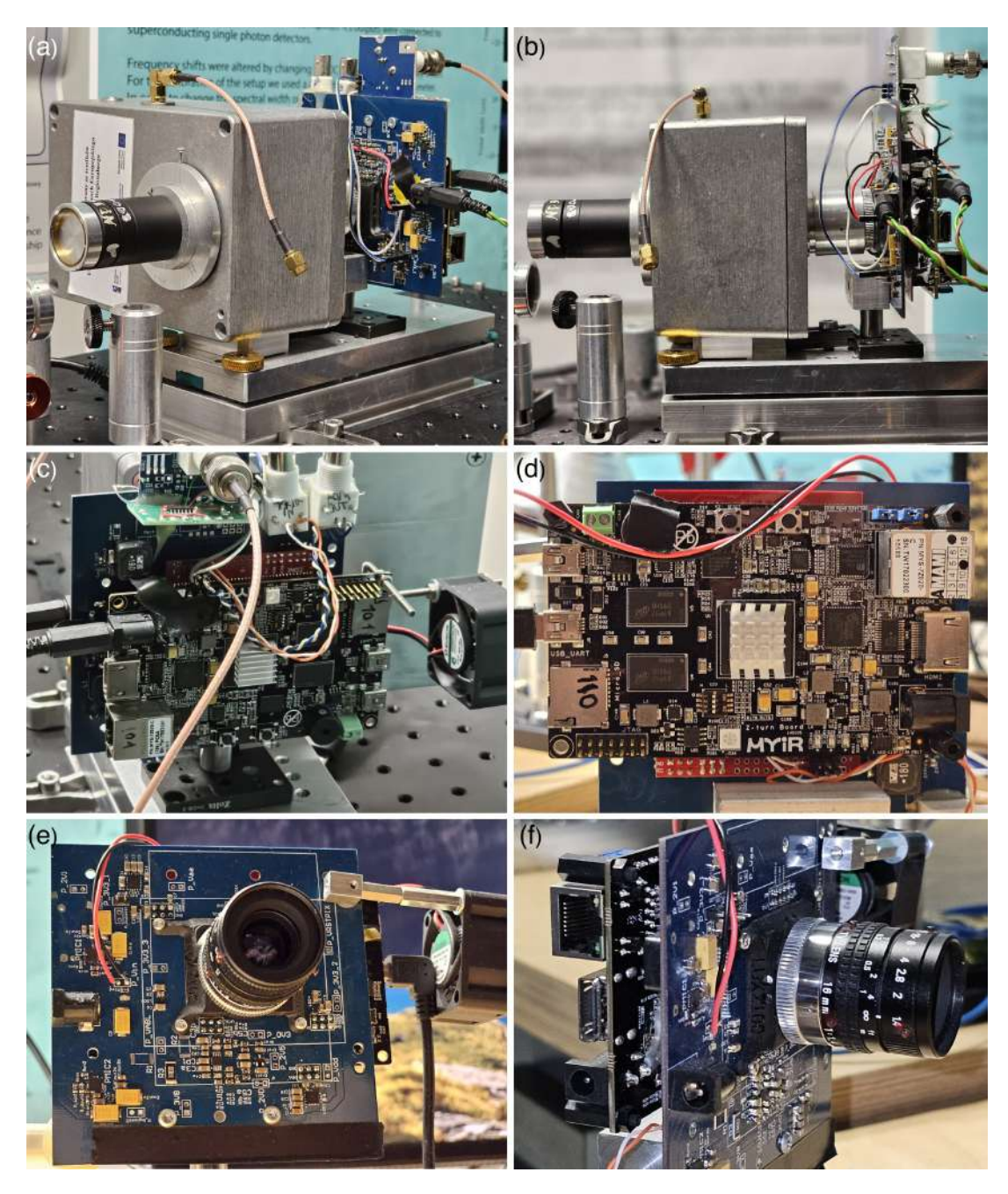


**Figure 1.6:** Photographs of the custom single-photon-sensitive camera. (a)-(b) Camera with an image intensifier housed in the left-most aluminum enclosure. The sensor and FPGA boards are visible on the right. The cylindrical connector between the II box and the PCBs houses the relay lens. The SMA cable in the top part of the II box is used to connect the custom gating module (not shown). (c)-(d) View on the sensor and FPGA PCBs. (e)-(f) A different camera unit with an objective attached instead of the image intensifier.

#### I.4 CUSTOM CAMERA IMPLEMENTATION

#### I.4.I HARDWARE

The main component of the camera is its monochrome sensor Luxima Lux2100 produced in the Complementary Metal-Oxide-Semiconductor (CMOS) technology. The 4/3" sensor offers high frame rates ( $1.25 \times 10^5$  frames per second for a  $1920 \times 8$  frame size, up to  $7 \times 10^5$  for a single line of 1920 pixels), relatively (for a fast sensor) low read noise (42 e-), and high brightness ( $7.5 \, \mathrm{V \, lx^{-1} \, s^{-1}}$ ). It outputs the data through 32 Low-Voltage Differential Signaling (LVDS) channels, each port capable of reaching 900 Mbps. The optically active area is  $1952 \times 1096$  pixels with a  $10 \, \mu \mathrm{m}$  pixel pitch.

To interface the camera sensor we use a Field Programmable Gate Array (FPGA) Xilinx Zynq-7020 (XC7Z020) in the form of a low-cost development board MYIR Z-turn. The FPGA integrated circuit additionally contains a Dual-core ARM Cortex-A9 processor which facilitates high-level operations (e.g. ordered from the PC) on the memory shared with the FPGA. The Z-turn board provides all necessary interfaces with convenient ports, as well as an integrated circuit for 1000 Mbps Ethernet and a 1 GB DDR3 SDRAM module which are crucial for the Data transmission and camera frame storage.

The camera sensor is soldered on a PCB, with another PCB stacked on top, and the Z-turn stacked to the bottom. The top PCB contains voltage regulators and filters to produce all power supplies for the sensor from a single 5V DC external power source. Boards are stacked with aligned goldpin connectors and kept mechanically rigid with sleeved bolts.

For the coupling of optical elements (objectives, relays lens to image intensifier), a C-mount connector is attached to the top PCB at a carefully chosen distance from the camera sensor.

Photographs of the camera are included in Fig. 1.6.

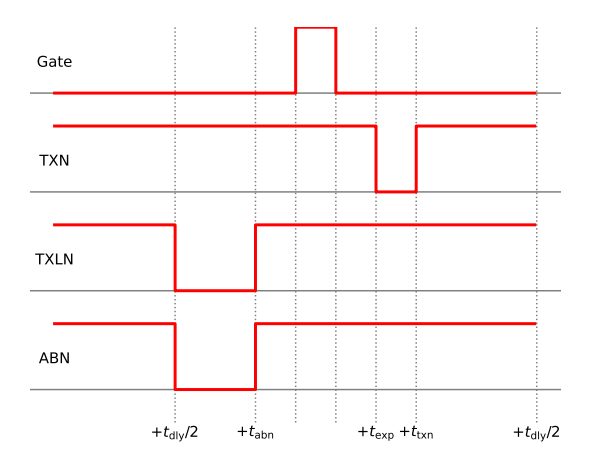


**Figure 1.7:** Sequence of a single camera frame. Active Low Global Photodiode Transfer Clearing (TXLN) and Active Low Global Photodiode Reset (ABN) pulses clear the CMOS charge and begin the exposure period of a new frame. During the Gate signal high level, the image intensifier is opened. Active Low Global Photodiode Transfer (TXN) signal induces the charge readout and concludes the frame exposure.

#### I.4.2 GATEWARE

We will refer to the part of processing implemented in the FPGA fabric (programmable logic) as "gateware" in an analogy to software running on the PC and firmware running on the ARM core inside the Zynq chip.

Two-way communication with the sensor (via serial peripheral interface), frame sequence signals, and the fast data transfer (of frames) from the sensor (via LVDS lines) are implemented in the gateware. Data from the LVDS lines is deserialized, buffered, and assembled into frames. The general sequence of a single frame has been depicted in Fig. 1.7. In each clock cycle a single LVDS line transmits pixel value from a single column in the current row. The row is changed when all columns are read.

# BACKGROUND SUBTRACTATION

To achieve a flat background in the camera frame, two methods are employed.

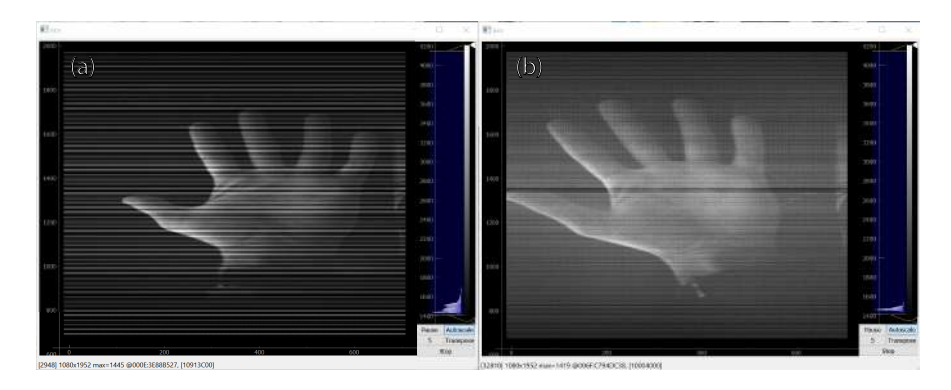


**Figure 1.8:** Exemplary camera frames with an objective attached instead of the image intensifier. (a) Without the ADC gain equalization (b) With the ADC gain equalized.

The first comprises the gain calibration of 16 ADC converters within the camera sensor. The converters work on lines of pixels in parallel. To obtain the same value of a pixel in ADC units (ADU) for an equal charge, the ADCs have to be cross-calibrated. During the procedure, the II is turned off (gated) and its input is covered. An algorithm at a high level of software control gathers camera frames and calculates the variance between the rows of pixels. Commands with a gain correction are sent based on the variance multiplied by a small constant to ensure smooth convergence. The algorithm repeats the procedure until a variance threshold is met, or the maximal number of repetitions occurs. The effect of this equalization is exemplified in Fig. 1.8.

The second method is built within the gateware and constitutes a small fragment in the block random access memory (BRAM) holding a recorded background (dark image). The stored pattern is computed on the software control level as an average of typically 100 gathered frames and sent via a command. The bit depth is reduced to 10 least-significant bits due to the BRAM size limitations. The recorded background is subtracted from the received camera frame before further processing (in particular before the localization and thresholding of photons).

## I.4.3 FIRMWARE

The (baremetal) C/C++ firmware runs on one of the ARM cores in the Zynq chip. Its main role is ensuring communication with the PC and data transfer. Networking is managed with the LWiP library. The firmware implements a server to which clients (PC software) can connect. In addition to the ethernet-based communication, a USART interface (serial port) provides basic commands and diagnostic information. The firmware can directly access regions of memory shared with the gateware, facilitating the configuration of its elements (such as the threshold of the photonfinder) and diagnostics.

## I.4.4 SOFTWARE

#### BACKEND

With very high frame rates the data reception, real-time preview, and storage pose technical challenges on the PC software side. It is true even for just the data containing detected photon positions within each frame. As already mentioned, the transmission is done over the ethernet with the UDP protocol. High throughput is a definite advantage of the UDP over TCP; however, it comes at a cost of reduced reliability. The data in these protocols is generally transmitted in small packets and further assembled at the receiver. The order of the send packets is in general not preserved and in the UDP protocol, the transmitter does not receive any feedback with regards to the packet reception.

In practice, the data for a given camera frame may turn out to be incomplete (corrupt) or arrive after the more recent frame has been received. Let us focus on the reception of the photon position data, as it is most relevant in the regime of very high frame rates. From the perspective of the gateware, the data about each photon detected in a frame is in the form of a single record (bit structure) stored in BRAM and containing a  $5 \times 5$  frame re-

gion around the photon, its coordinates in the frame, 4 youngest bits of the frame number, and a 2 bit counter for the BRAM cycle (incremented upon reaching the final address and starting the storage from the first address). The coordinates are stored as 11 bits for each dimension. Each frame pixel is 12 bits. Hence, the whole structure is 328 bits which is 41 bytes. Storing the frame regions (pixel values) around the detected photon is not only a good idea for debugging the algorithms but also provides useful information on the distribution of flash widths and amplitudes. Such distributions can be interrogated for instance to check whether the camera sensor is optimally placed in the focus of the relay lens (high amplitudes, low widths).

Let us assume on average 5 photons per frame and  $10^5$  frames per second. It amounts to ca.  $19.5\,\mathrm{MB\,s^{-1}}$  or ca.  $156\,\mathrm{Mbit\,s^{-1}}$  which is still significantly below the typical Ethernet connections of  $1\,\mathrm{Gbit}$ . The main challenge is to ensure that all photons are classified into the correct frames. Since the photon data structures appear at the receiver in an unordered fashion, each frame has to be kept "open" for further photons for a long enough time. However, it has to be concluded and "closed" at some point. This is solved with a circular buffer that remembers 2 generations of frames. Each generation refers to a full range of 4 transmitted bits of the frame number (so 16 frames per generation). Photons are classified to the current generation according to their frame number. The last seen frame number is remembered. If the incoming photon has a frame number more than 8 frames up or down from the last frame number, the last generation is closed, the current generation becomes the last, and a new generation is opened to be the current. This heuristic approach works very well in practice once implemented in a fast multiprocess application written in C++. The circular buffer is a separate process independent of the real-time analysis, saving and passing the data to the frontend.

All real-time analysis (e.g. histograms of photon positions, photon and frame rate statis-

tics etc.) is done in the backend utilizing the Boost library. Data storage is also implemented in the backend. Each module is a separate process and all processes are arranged in a series. The data is passed from process to process by queues including special queue values used to pass commands (e.g. termination).

## FRONTEND

To facilitate convenient control of the camera, live preview, and the data-saving process a frontend application has been written in Python with a Qt framework. The frontend communicates with the backend C++ application via a Cython interface. Frontend provides a live preview of the spatial photon histograms, the number of frames per second, and the average number of photons per frame. Controls allow basic configuration of the live histograms, as well as initiation and control of the data saving.

# Photon data analysis

The data is stored in the form of 3 files with "pxy", "pnn" and "pimg" extensions. The "pxy" file contains (x,y) in-frame coordinates of subsequent photons. The "pnn" file contains a number of photons detected in subsequent frames. Finally, the optional "pimg" file contains  $5 \times 5$  pixel fragments of the frame around each photon. This custom data format is further converted to our in-house standard used with other intensified scientific CMOS cameras (experiments with the quantum memory). After conversion, the photon data can be conveniently processed in Python with our "photonpacket" library. For details see ref. [29].

More sophisticated camera controls and calibrations are done directly via Python scripts.

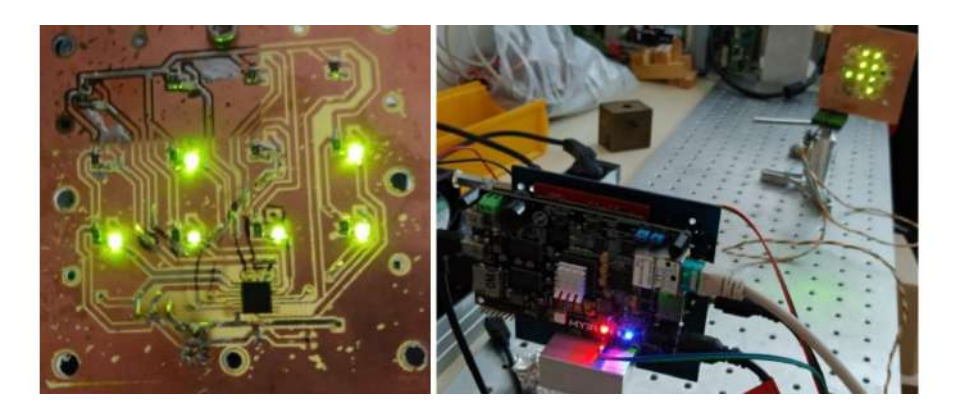


**Figure 1.9:** Photographs of (a) the PCB with a grid of LEDs for the photonfinder testing, (b) the testing setup.

# I.4.5 MECHANICAL CONSTRUCTION

The image intensifier with a high-voltage supply is kept in an aluminum housing. A relay lens is placed between the image intensifier's phosphor screen and the camera sensor. The whole camera is mounted on a rigid, stable aluminum base. The base is comprised of two parts connected with a kinematic mount which allows for easy detachment of the camera (e.g. for maintenance) and repeatable replacement. The mechanical project in its original form (untranslated) is attached for illustration in appendix A.

## 1.5 Testing

## 1.5.1 FLASHING LEDS

One of the simplest tests of the camera and the photonfinder was to observe a pattern of flashing LEDs. Instead of the image intensifier, the camera has an objective mounted. The LED flashes are similar in size to the phosphor flashes of the II. The 9 LEDs are placed on a custom PCB in a rectangular grid pattern. The PCB contains an LED driver and a binary counter incremented with a single digital pulse. The incrementing pulses are sent from

the camera in the frame sequence. This way, subsequent frames should contain different, predictable patterns. In the main test, we compared the output of the gateware photon-finder (number and position of photons) with simultaneously gathered raw frames (post-processed on PC with a software photonfinder). A photograph of the test setup is depicted in Fig. 1.9.

## 1.5.2 PSEUDOTHERMAL LIGHT

Another simple test of the camera was to repeat the measurements of the second-order photon number autocorrelation function for pseudo-thermal light (c.f. ref. [73]). Such a state of light has the same statistics as thermal light but with orders of magnitude longer coherence time. It can be obtained with a rotating ground glass diffuser illuminated with a continuous-wave laser light. It is experimentally the simplest way to observe non-trivial autocorrelation. Since we had comparable data from previous measurements with an off-the-shelf sCMOS camera and the expected result can be calculated analytically, repeating the measurement was a good test for our camera.

The setup is depicted in Fig. 1.10, while the resulting autocorrelation is presented in Fig. 1.11. Definitions and the details of the calculation and correction procedures can be found in ref. [73]. As a camera test, it is important that the result well-match the model prediction.

## I.6 CONCLUSION

In this chapter, we have briefly discussed a custom scientific tool that we developed for further experiments, a fast single-photon-sensitive camera. An overview of the camera construction, image intensifier working principles, hardware implementation, and software

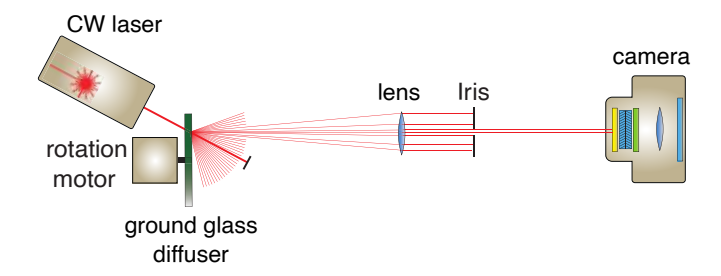


**Figure 1.10:** Simplified experimental setup for the measurement of the second-order intensity autocorrelation function. Pseudo-thermal light is obtained by illuminating a rotating ground glass diffuser with a continuous-wave (CW) laser. The ground glass diffuser is far-field imaged onto the single-photon camera sensor.

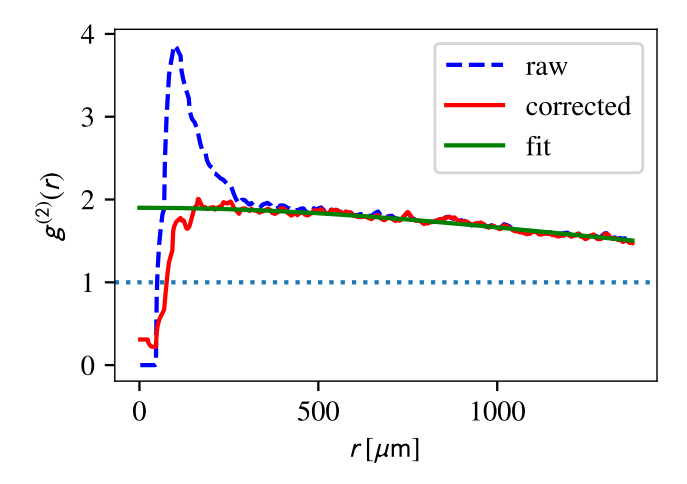


**Figure 1.11:** Results of the second-order intensity autocorrelation function measurement including the calculation from raw data (raw), the result after applying a correction for image intensifier crosstalk (c.f. ref. [73]), and a fitted analytical model.

design has been presented. Finally, we briefly described some of the tests used to check the correct camera operation.

The ability to detect single photons with excellent spatial resolution and high frame rates will prove very useful for the experiments discussed in the next chapters.

2

# Hybrid correlations of photon pairs

## 2.I FOREWORD

The first experiment with the camera was meant to be both a good test of its capabilities and still of high interest from the scientific perspective. We decided to measure hybrid spectral-angular 4-dimensional correlations between pairs of photons generated in a non-collinear spontaneous parametric process (SPDC) pumped with a spectrally-broad light. Since the correlation function is 4-dimensional and its high-fidelity reconstruction requires

a large number of collected photons, the high acquisition speed of the camera proves extremely valuable and makes a direct measurement feasible.

From the fundamental point of view, this chapter is concerned with the characterization of hyperentangled states of two photons. Non-classical photonic states are of significant importance for quantum-enhanced communication and quantum metrology. They can be easily created, and interact with the environment very weakly enabling long-distance communication. Furthermore, very efficient detection techniques have been developed in a vast range of wavelengths [74].

The chapter is based on ref. [75].

#### 2.2 Introduction

Protocols of quantum optical communication and computation can be often enhanced by using photonic states exhibiting nonclassical correlations across different degrees of freedom (DoF) [76–78]. Such states are referred to as hyperentangled states. Fundamentally, the use of several DoFs greatly expands the Hilbert state and the informational capacity of the state. Generation of pairs of photons correlated in spectro-temporal, spatial, and orbital angular momentum (OAM) DoFs has been demonstrated experimentally, including hyperentanglement generation across 4 DoFs in SPDC sources [79]. Exemplary protocols, in particular, able to benefit from the hyperentangled states are quantum teleportation [80], superdense coding [81], and complete analysis of Bell-states [82].

Nonetheless, experimental characterization of multidimensional states remains challenging. Single-pixel detectors such as superconducting nanowires offer excellent timing resolution [83], as well as spectral resolution when combined with dispersive elements such as chirped fiber gratings [84] or detector-integrated diffraction gratings [85]. Such setups pro-

vide a way to implement high-dimensional quantum communication [86], temporal super-resolved imaging [87] or observe quantum interference in time or frequency space [88, 89] - a promising approach for quantum fingerprinting [90, 91]. Single-photon-resolving cameras on the other hand naturally offer spatial or angular resolution, which can be exploited in super-resolution imaging [65, 92–95], interferometry [96], characterization [97, 98] or, similarly as in the previous case, observation of quantum interference effects such as in the Hong-Ou-Mandel–type experiments [99]. Recently however, the capability of cameras has been expanded by invoking a well-known mode conversion technique, in which Sun *et al.* simply observed spectral correlation with the help of a diffraction grating [100]. It is thus a promising approach to use a camera to observe many DoFs simultaneously.

One of the experimentally feasible examples involves the spectral DoF combined with the transverse-wavevector (or equivalently the angle of emission). In particular, we will consider a pair of hyperentangled photons. For simplicity, and without loss of generalization, we can limit the transverse-wavevector to a single spatial dimension. This way we are left with a 4 dimensional space of the two-photon state. For each photon, a single dimension corresponds to its spectral DoF and a single dimension to its transverse wavevector. Experimental generation of such states can be achieved in a straightforward way with a weakly-pumped SPDC process in a bulk crystal, set in a non-collinear configuration, and with a broadband pump. Of course, proper filtering in the spectral and spatial domains is required, as further discussed.

While simple to generate, two-photon correlations in such states are difficult to characterize. Since ideally we are dealing with a two-photon state, the object of interest is the second-order intensity correlation function, which quantifies the degree of correlation between observing one photon (s - signal) from the pair at certain spectral-wavevector coordinates  $(k_x^{(s)}, \lambda_s)$  and observing the second photon (i - idler) at some other spectral-

wavevector coordinates  $(k_x^{(i)}, \lambda_i)$ . In the experiment, what we can measure is the number of coincidences between the two photons in this 4-dimensional space  $(k_x^{(s)}, \lambda_s, k_x^{(i)}, \lambda_i)$ . As such the measurement poses the following two problems:

- 1. a conversion between wavevector and spectral DoF is required,
- 2. we need to observe a large number of photon counts to have a high resolution and accuracy in a 4-dimensional space.

The use of fast detectors certainly helps with the latter. For the former, a simple diffraction grating can provide a spectral to spatial DoF conversion, as demonstrated in a wide context by Sun *et al.* [100]. We also note that the conversion between the transverse wavevector (or angle) to a transverse position is a standard procedure of far-field imaging [101]. Since we assume that by the experiment design the two photons can be spatially separated, after the DoF conversions, we are left with two 2-dimensional spatial regions. Each region corresponds to a single photon of the pair. Each spatial dimension within the region corresponds to either the spectral or wavevector DoF. A single-photon camera is a natural choice for the characterization of coincidences between two spatial regions. A simplified experimental setup is depicted in Fig. 2.1.

Hitherto similar measurements employed time-of-flight spectrometers for the spectral resolution and involved a scan of the wavevector space with bucket detectors [102]. Such an approach is most suitable for the telecom wavelengths, where time-of-flight spectrometers are easier to implement compared to the near-infrared. Furthermore, this method requires compressed sensing techniques.

Beyond direct correlation measurements, more sophisticated high-dimensional entanglement detection techniques [103] could be adapted for the use with a single-photon camera. Furthermore, the measurement of correlations itself proves useful in the optimal utilization

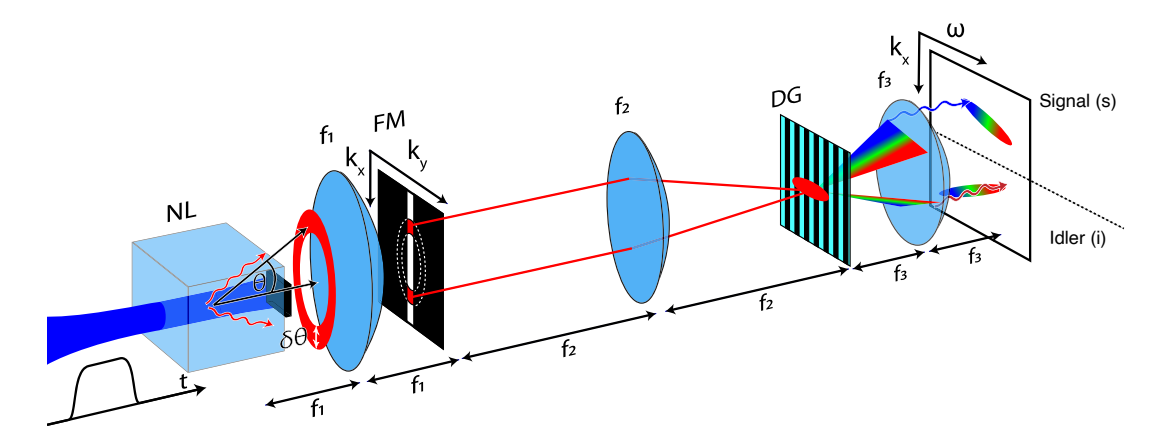


Figure 2.1: The idea of the measurement of 4-dimensional spectral-angular correlations between a pair of photons. A pair of signal (s) and idler (i) photons is generated in the SPDC process in a non-linear crystal (NL). The phase-matching in the crystal is set for the non-collinear generation of photon pairs. The emission cone is far-field imaged onto a slit (FM) which selects only a small range of transverse wavevectors  $k_y$  in the y axis. The crystal is imaged onto a diffraction grating (DG) which acts as a converter between the spectral and angular degrees of freedom in the x axis. Finally, the grating is far-field imaged onto a single-photon sensitive camera. Two distinct regions in the camera frame correspond to the signal and idler, respectively. Within each region, the position corresponds to the transverse wavevector  $k_x$  and optical frequency  $\omega$ . Coincident photo counts between the regions are registered with a spatial resolution, allowing for the reconstruction of the 4-dimensional correlations.

of entangled states e.g. for quantum key distribution whose rate can be improved by non-local dispersion compensation [104]. Another example is the measurement of higher-order correlations which finds its uses in super-resolution imaging [93, 94].

# 2.3 Theory

# 2.3.I TWO-PHOTON AMPLITUDE

We shall begin the theoretical description with the SPDC process. With a broadband, focused pump beam and a short nonlinear crystal emission from the SPDC will be highly multimode in the spectral and transverse wavevectors DoFs. Nevertheless, let us focus on a single pair of signal and idler modes. In the SPDC process a two-mode squeezed state

 $|\psi\rangle = \sum_{j=0} \chi^{j/2} |j\rangle_s |j\rangle_i$ , is generated. However, to the first order in  $\sqrt{\chi}$ , the resulting state can be approximated as a photon pair  $|1\rangle_s |1\rangle_i$ . We would like to find an expression for the joint two-photon wavefunction in transverse wavevector and spectral coordinate

$$\Psi(\mathbf{k}_{s,\perp},\lambda_s;\mathbf{k}_{i,\perp},\lambda_i) = \langle \mathbf{k}_{s,\perp},\lambda_s | 1 \rangle_s \langle \mathbf{k}_{i,\perp},\lambda_i | 1 \rangle_i.$$
(2.1)

Let us begin with the positive frequency part of the pump classical electric field as given by

$$E_p^{(+)}(\boldsymbol{r},t) = \mathcal{E}_p \int d^2 \boldsymbol{k}_{p,\perp} d\omega_p A_p(\boldsymbol{k}_{p,\perp},\omega_p) \exp[i(\boldsymbol{k}_p \cdot \boldsymbol{r} - \omega_p t)], \qquad (2.2)$$

where  $\mathcal{E}_p$  is the pump pulse amplitude,  $\mathbf{k}_{p,\perp}$  denotes the transverse wavevector and  $A_p$  describes the normalized slowly varying envelope of the pulse. We will consider only the two-photon part of the full two-mode squeezed state generated during the SPDC process [105]. The two-photon wavefunction is given by

$$|\Psi\rangle = \int d^{2}\boldsymbol{k}_{s,\perp} d^{2}\boldsymbol{k}_{i,\perp} d\omega_{s} d\omega_{i} \Psi(\boldsymbol{k}_{s,\perp}, \omega_{s}; \boldsymbol{k}_{i,\perp}, \omega_{i}) \times \hat{a}^{\dagger}(\boldsymbol{k}_{s,\perp}, \omega_{s}) \hat{a}^{\dagger}(\boldsymbol{k}_{i,\perp}, \omega_{i}) |\text{vac}\rangle,$$
(2.3)

where the i and s correspond to signal and idler photons, respectively. Let us assume a crystal with length L and that the pump beam propagates along the z axis. The two-photon amplitude  $\Psi(\mathbf{k}_{s,\perp},\omega_s;\mathbf{k}_{i,\perp},\omega_i)$  is given by

$$\Psi(\mathbf{k}_{s,\perp},\omega_s;\mathbf{k}_{i,\perp},\omega_i) = \mathcal{N} \int_{-L/2}^{L/2} dz \left\{ A_p(\mathbf{k}_{s,\perp} + \mathbf{k}_{i,\perp},\omega_s + \omega_i) \exp[i\Delta k_z(\mathbf{k}_{s,\perp},\omega_s;\mathbf{k}_{i,\perp},\omega_i)z] \right\},$$
(2.4)

where the wavevector mismatch  $\Delta k_z(\mathbf{k}_{s,\perp},\omega_s;\mathbf{k}_{i,\perp},\omega_i)$  described the phase matching of the process and is determined by the z components of the constituent wavevectors

$$\Delta k_z(\mathbf{k}_{s,\perp},\omega_s;\mathbf{k}_{i,\perp},\omega_i) = k_{p,z}(\mathbf{k}_{s,\perp} + \mathbf{k}_{i,\perp},\omega_s + \omega_i) - k_{s,z}(\mathbf{k}_{s,\perp},\omega_s) - k_{i,z}(\mathbf{k}_{i,\perp},\omega_i).$$
(2.5)

Throughout our analysis, we are assuming the paraxial approximation. In particular, it means that  $|\mathbf{k}_{\perp}| \ll |\mathbf{k}|$  and also that the crystal's index of refraction does not undergo substantial change in the range of considered wavevectors. Hence, we shall assume that the transverse wavevectors are equal within and outside the crystal. One may observe that at the boundary or air and crystal the emission angle increases by a factor equal to the crystal's index of refraction. However, the total wavevector also increases by the same factor. Therefore, in the small-angle approximation, it necessitates that the transverse component remains unchanged.

Let us integrate Eq. (2.5) along the z direction to get

$$\Psi(\boldsymbol{k}_{s,\perp},\omega_s;\boldsymbol{k}_{i,\perp},\omega_i) = \mathcal{N}A_p(\boldsymbol{k}_{s,\perp} + \boldsymbol{k}_{i,\perp},\omega_s + \omega_i)\operatorname{sinc}\left[\frac{L\Delta k_z(\boldsymbol{k}_{s,\perp},\omega_s;\boldsymbol{k}_{i,\perp},\omega_i)}{2}\right]. \tag{2.6}$$

In the experiment, we shall only transmit a small range of  $k_y$  around  $k_y=0$  and block other  $k_y$  components. For this reason henceforth we will use a simplified notation  $\mathbf{k}_{\alpha,\perp}\to k_x^{(\alpha)};\ \alpha\in\{s,i\}.$ 

# 2.3.2 PHOTON NUMBER COVARIANCE MODEL

Let us observe that  $|\Psi(k_x^{(s)},\omega_s;\ k_x^{(i)},\omega_i)|^2$  is directly proportional to the probability of generating a signal photon at the transverse wavevector  $k_x^{(s)}$  and with a wavelength of  $\lambda_s=2\pi c/\omega_s$  and at the same time an idler photon with  $k_x^{(i)}$  and  $\lambda_i=2\pi c/\omega_i$ . If the two-

photon term vanishes  $|\Psi(k_x^{(s)},\omega_s;\ k_x^{(i)},\omega_i)|^2=0$  for some  $(k_x^{(s)},\omega_s,k_x^{(i)},\omega_i)$ , then the probability of registering a pair of photons at  $(k_x^{(s)},\omega_s,k_x^{(i)},\omega_i)$  will be given by the product of marginal probabilities of registering a signal at  $(k_x^{(s)},\omega_s)$  and an idler at  $(k_x^{(i)},\omega_i)$ . Therefore,  $|\Psi(k_x^{(s)},\omega_s;\ k_x^{(i)},\omega_i)|^2$  will be directly proportional to the covariance of the photon number between idler and signal modes  $\operatorname{Cov}(k_x^{(s)},\lambda_s;\ k_x^{(i)},\lambda_i)$ .

For visualization and comparison with the experiment, we will divide the coordinates into wavelength  $\{\lambda_j\}$  and wavevector subregions  $\{k_x^{(j)}\}$  where  $j\in\{s,i\}$ , and sum the coincidences within a signal-idler pair of either wavelength or wavevector regions. This way we will obtain 2D dimensional maps. To directly compare our calculations with experimental results, let us also sum the modulus squared amplitudes in these regions

$$\left|\Psi_{\{\lambda_s\},\{\lambda_i\}}(k_x^{(s)},k_s^{(i)})\right|^2 = \sum_{\lambda_s \in \{\lambda_s\},\lambda_i \in \{\lambda_i\}} \left|\Psi\left(k_x^{(s)},\frac{2\pi c}{\lambda_s};\ k_x^{(i)},\frac{2\pi c}{\lambda_i}\right)\right|^2,\tag{2.7}$$

$$\left|\Psi_{\{k_x^{(s)}\},\{k_x^{(i)}\}}(\lambda_s,\lambda_i)\right|^2 = \sum_{k_x^{(s)}\in\{k_x^{(s)}\},k_x^{(i)}\in\{k_x^{(i)}\}} \left|\Psi\left(k_x^{(s)},\frac{2\pi c}{\lambda_s};\ k_x^{(i)},\frac{2\pi c}{\lambda_i}\right)\right|^2. \tag{2.8}$$

#### 2.3.3 EXPERIMENTAL COVARIANCE AND ACCIDENTAL COINCIDENCES

In the experiment, we will convert the x component of the transverse wavevector  $k_x$  to a spatial position in the camera frame, while selecting only photons with  $k_y \approx 0$ . The spatial dimension which would otherwise correspond to  $k_y$  is used for mapping the spectral DoF. Finally, the single-photon camera registers the number of photons in each pixel  $n(k_x^{(\xi)}, \lambda_\xi) \in \{0, 1\}; \ \xi \in \{s, i\}$ . The average number of photons across many camera frames  $\langle n(k_x^{(\xi)}, \lambda_\xi) \rangle$  corresponds to an estimate of the probability of observing a photon at a given coordinate. Hence, the experimental photon number covariance which is given by

$$Cov(k_x^{(s)}, \lambda_s; k_x^{(i)}, \lambda_i) = \langle n(k_x^{(s)}, \lambda_s) n(k_x^{(i)}, \lambda_i) \rangle - \langle n(k_x^{(s)}, \lambda_s) \rangle \langle n(k_x^{(i)}, \lambda_i) \rangle$$
 (2.9)

corresponds to the estimate of the probability of detecting a non-accidental coincidence. Each camera frame corresponds in time to 96 pump laser repetitions due to a relatively long gating time of the image intensifier. This way 96 temporal modes are coalesced in a single camera frame, leading to accidental coincidences between photons originating from separate temporal modes. Let us note that the second term in Eq. (2.9) roughly corresponds to the accidental coincidences. Again, for visualization, we sum the covariance over the wavelength  $\{\lambda_s\}$ ,  $\{\lambda_i\}$  or wavevector  $\{k_x^{(s)}\}$ ,  $\{k_x^{(i)}\}$  subregions yielding:

$$Cov_{\{\lambda_s\},\{\lambda_i\}}(k_x^{(s)}, k_x^{(i)}) = \sum_{\lambda_s \in \{\lambda_s\}, \lambda_i \in \{\lambda_i\}} Cov(k_x^{(s)}, \lambda_s; k_x^{(i)}, \lambda_i),$$
(2.10)

$$Cov_{\{k_x^{(s)}\},\{k_x^{(i)}\}}(\lambda_s,\lambda_i) = \sum_{k_x^{(s)}\in\{k_x^{(s)}\},k_x^{(i)}\in\{k_x^{(i)}\}} Cov(k_x^{(s)},\lambda_s; k_x^{(i)},\lambda_i).$$
(2.11)

## 2.3.4 Non-classical correlations and the mode size

Let us start with the second-order intensity (photon number) correlation function for a pair of signal and idler modes [106]. It will be useful in estimating the mode size of the SPDC emission, and quantifying its non-classical character. The correlation function is given by

$$g^{(2)}(k_x^{(s)}, \lambda_s; \ k_x^{(i)}, \lambda_i) = \frac{\langle n(k_x^{(s)}, \lambda_s) n(k_x^{(i)}, \lambda_i) \rangle}{\langle n(k_x^{(s)}, \lambda_s) \rangle \langle n(k_x^{(i)}, \lambda_i) \rangle}, \tag{2.12}$$

where the term  $\langle n(k_x^{(s)},\lambda_s)n(k_x^{(i)},\lambda_i)\rangle$  corresponds to an average over camera frames of coincidences between the idler at  $(k_x^{(s)},\lambda_s)$  and the signal at  $(k_x^{(i)},\lambda_i)$ , and where similarly  $\langle n(k_x^{(j)},\lambda_j)\rangle\ j\in\langle s,i\rangle$  correspond to the average number of single photon counts. To tackle this 4-dimensional object we will sum the coincidences and singles over the uncorrelated directions. It is convenient to first transform these quantities to  $\pm$  coordinates with

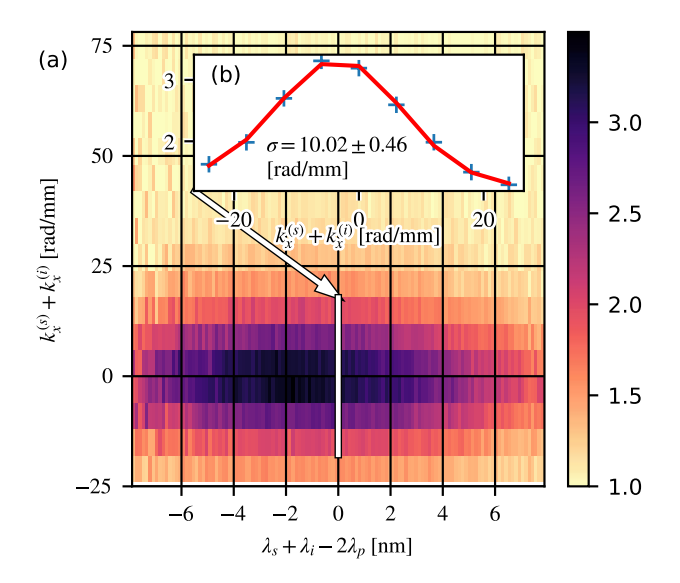


Figure 2.2: (a) Second order intensity correlation function between signal and idler modes, in reduced coordinates  $g^{(2)}(k_x^{(s)}+k_x^{(i)},\lambda_i+\lambda_s)$ . (b) A selected cross section with  $\lambda_i+\lambda_s=2\lambda_p$ . Experimental data (blue points) is presented alongside a Gaussian fit (red line) with the best-fit width of  $\sigma=10.02\pm0.46$  [rad/mm].

$$k_{\pm}=k_{x}^{(s)}\pm k_{i}^{(i)}$$
 ,  $\lambda_{\pm}=\lambda_{s}\pm\lambda_{i}$  . This way we get

$$g^{(2)}(k_{+},\lambda_{+}) = \sum_{k_{-},\lambda_{-}} \langle n(k_{x}^{(s)},\lambda_{s}) n(k_{x}^{(i)},\lambda_{i}) \rangle (k_{+},k_{-}; \lambda_{+},\lambda_{-}) /$$

$$\left\{ \sum_{k_{-},\lambda_{-}} \langle n(k_{x}^{(s)},\lambda_{s}) \rangle (k_{+},k_{-}; \lambda_{+},\lambda_{-}) \times \langle n(k_{x}^{(i)},\lambda_{i}) \rangle (k_{+},k_{-}; \lambda_{+},\lambda_{-}) \right\}. \tag{2.13}$$

The width of the 2-dimensional correlation function  $g^{(2)}(k_+, \lambda_+)$  is a good indicator of the mode size. Let us look at a cross-section  $g^{(2)}(k_+, \lambda_+) = 2\lambda_p$ . Assuming a Gaussian shape with width  $\sigma$  the mode size of the SPDC emission in the transverse wavevector DoF is given by

$$\sigma_{k\text{-mode}} = \frac{\sigma}{\sqrt{2}},\tag{2.14}$$

with the  $\sqrt{2}$  factor originating from the Jacobian of the  $(k_x^{(s)}, k_x^{(i)}) \to (k_x^{(s)} + k_x^{(i)}, k_x^{(s)} - k_x^{(i)})$  transformation. In analogous way the  $k_x^{(s)} = -k_x^{(i)}$  cross-section gives the spectral mode width.

Let us trace over the idler mode. The remaining mode of the signal photon has a thermal photon count distribution. The second-order intensity autocorrelation for this mode is given by  $g_{\text{idler,auto}}^{(2)} = g_{\text{signal,auto}}^{(2)} = g_{\text{therm,auto}}^{(2)} \leq 2$ . Therefore, using the Cauchy-Schwarz inequality we find that the upper classical bound on the second-order intensity cross-correlation function reads

$$g_{\text{classical}}^{(2)} \le \sqrt{g_{\text{signal,auto}}^{(2)} g_{\text{idler,auto}}^{(2)}} = 2.$$
 (2.15)

The 2-dimensional second-order intensity correlation function in  $\pm$  coordinates, calculated from the experimental data, has been depicted in Fig. 2.2. The cross-section for the degenerate wavelength has a width of  $\sigma=10.02(46)~\mathrm{rad\,mm^{-1}}$ . Using Eq. (2.14) this corresponds to the mode size of  $\sigma_{k\text{-mode}}=7.09(33)~\mathrm{rad\,mm^{-1}}$ . The complementary cross-section gives the spectral mode size of  $\sigma_{\lambda\text{-mode}}=4.20(6)~\mathrm{nm}$ . Note the maximum of the  $g^{(2)}$  function above the classical limit of 2.

# 2.3.5 Reference-free efficiency estimation

Following the reference-free method originally described by Klyshko *et al.* [107] (see also ref. [108]), we estimate the total efficiency of our setup. The method is based on an observation that for SPDC emission the rate of single counts and the rate of coincidences scale differently with the setup efficiency  $\eta$ . Let us assume a noiseless scenario with a single spatial mode and R temporal modes per camera frame (corresponding to the number of laser pulses per image intensifier gating time). The average number of signal or idler photons per frame is  $\langle n_j \rangle = R\eta \chi$ ,  $j \in \{i, s\}$  while the average number of coincidences

 $\langle n_i n_s \rangle = R \eta^2 \chi + \langle n_i \rangle \langle n_s \rangle$ . This way,

$$\eta = \frac{\langle n_i n_s \rangle - \langle n_i \rangle \langle n_s \rangle}{\sqrt{\langle n_i \rangle \langle n_s \rangle}} = \frac{g^{(2)} - 1}{\sqrt{\langle n_i \rangle \langle n_s \rangle}},\tag{2.16}$$

where  $g^{(2)}=\max_{\lambda_+,k_+}[g^{(2)}(\lambda_+,k_+)].$  In the experiment, we get  $\eta\approx 4\%$ 

## 2.3.6 Beta barium borate

Beta barium borate ( $\beta$ —BaB<sub>2</sub>O<sub>4</sub>) crystal abbreviated as BBO is a nonlinear uniaxial crystal first described in 1984 by Chen *et al.* [109]. BBO has very desirable properties such as a high damage threshold and a broad transmission (198 nm-2600 nm) and phase-matching ranges. Furthermore, it is chemically stable and nonhydroscopic, its polished surfaces may be easily cleaned and have the antireflection coatings applied and large, high-quality crystals of BBO can be easily obtained [110]. Therefore, BBO finds a very versatile range of applications in nonlinear optics including second (SHG) and higher harmonic generation or sum frequency generation.

The Sellmeier's equations (refractive index dispersion relations) for BBO are given for 20 °C by

$$n_o^2 = 2.7405 + \frac{0.0184}{\lambda^2 - 0.0179} - 0.0155\lambda^2$$
 (2.17)

$$n_e^2 = 2.3730 + \frac{0.0128}{\lambda^2 - 0.0156} - 0.0044\lambda^2,$$
 (2.18)

where o(e) refers to ordinary (extraordinary) polarization of the interacting light,  $n_j, j \in \{o, e\}$  is the corresponding index of refraction, and wavelength  $\lambda$  is given in  $\mu$ m [111].

## 2.4 Numerical calculations

## 2.4.I PROCESS INTENSITY

Using Eq. (2.6) we can directly evaluate the process intensity  $\left|\Psi(k_x^{(s)},\omega_s;k_x^{(i)},\omega_i)\right|^2$  for selected frequencies (or wavelengths  $\lambda_j=2\pi c/\omega_j,\ j\in s,i$ ) and transverse wavevectors of the signal and idler photons. Let us consider the type I SPDC process in a BBO crystal with a thickness of L=0.5 mm. The cutting angle i.e. the angle between our z-axis and the crystal axis is taken as  $\theta_0=29.2^\circ$ . The z-axis is perpendicular to the cutting plane of the crystal. We will use Sellmeier's equations as given by Eq. (2.17) an Eq. (2.18) to obtain an expression for the refractive index for a single ray of interacting light propagating at an azimuthal angle  $\theta$  and a polar angle  $\varphi$  relative to the z axis. While for the ordinary (o) polarization, the refractive index is independent of  $(\theta,\varphi)$ , for the extraordinary (e) we can obtain this relation as a positive solution of the following quadratic equation

$$\eta(\theta,\varphi) := [\sin(\theta)\sin(\theta_0)\sin(\varphi) + \cos(\theta)\cos(\theta_0)]^2, \tag{2.19}$$

$$\frac{1}{n_e(\lambda,\theta,\varphi)^2} = \frac{\eta(\theta,\varphi)}{n_o(\lambda)^2} + \frac{1 - \eta(\theta,\varphi)}{n_e^{(0)}(\lambda)^2}.$$
 (2.20)

For the shape of the slowly varying envelope of the pumping pulse, let us assume a Fourier-limited Gaussian in the spectral and spatial DoF, without correlations between the two DoFs. Denoting the temporal full width at half maximum (FWHM) of the pulse as  $\delta t$  and the beam waist as  $w_0$  the pump amplitude is given by

$$A_p(k_x, \omega) = \mathcal{A} \exp \left[ -\frac{1}{4} k_x^2 w_0^2 - \frac{\delta t^2 (\omega - \omega_p)^2}{16 \log(2)} \right].$$
 (2.21)

Henceforth, for numerical calculations, we will drop A (i.e. assume a unit value). We will

also assume the pumping beam propagates along the z-axis with a linear, extraordinary polarization. For a small spectral range (10 nm in the experiment), we can assume the total wavevector does not change significantly with the azimuthal angle  $\theta$  i.e.  $k(\lambda, \theta, \varphi) \approx k(\lambda, 0, \varphi)$ . Hence we can relate  $\theta$  and the transverse wavevector component  $k_x$  by

$$\theta(\lambda, k_x) = \arcsin\left[\frac{k_x}{k(\lambda, \theta = 0, \varphi)}\right],$$
 (2.22)

where  $k(\lambda, \theta, \varphi) = 2\pi n_e(\lambda, \theta, \varphi)/\lambda$ .

## 2.4.2 WALK-OFF ANGLE

Let us also briefly consider the walk-off effect in the crystal i.e. the non-collinearity of the wavevector and the Poynting vector for the extraordinary polarization. The walk-off angle i.e. the angle between these vectors is given by

$$\rho(\theta_0, \lambda, \theta, \varphi) = -\frac{1}{n_e(\theta_0, \lambda, \theta, \varphi)} \frac{\partial n_e(\theta_0, \lambda, \theta, \varphi)}{\partial \theta_0}, \tag{2.23}$$

where we now treated  $n_e$  also as a function of  $\theta_0$ . For a pumping beam with  $\lambda=400$  nm,  $\theta=0, \varphi=90^\circ$  and for  $\theta_0=29.2^\circ$ , the angle is  $\rho\approx-100$  mrad. In our case, since  $L\rho\ll w_0$  the walk-off can be neglected.

# 2.4.3 Number of modes

Let us consider the theoretical two-photon wavefunction as given by Eq. (2.6). To estimate the number of modes we first numerically compute the wavefunction in a range of experimentally observed transverse wavevectors and wavelengths, with a Gaussian pump pulse amplitude and experimental parameters. For the details of the simulation see section 2.4.

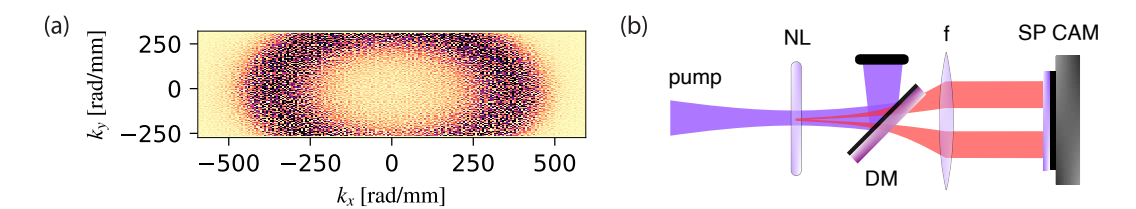


Figure 2.3: (a) Histogram of photo counts in the transverse-wavevector space, of emission from a non-collinear type I SPDC in a BBO crystal. Note the annular distribution. Photons have been registered across  $2\times 10^5$  camera frames. (b) Simplified experimental setup. NL - nonlinear crystal, pump - pumping beam, DM - dichroic mirror, f - far-field imaging lens, SP CAM - single-photon camera.

Then the obtained numerical wavefunction is reshaped into a two-dimensional matrix so that the first (second) dimension contains the spectral and transverse wavevector DoFs of the signal (idler) combined. We then perform the singular value decomposition of this matrix which yields the Schmidt coefficients  $\{\lambda_j\}$ . Following ref. [112] the Schmidt number is given by

$$M = (\sum_{j=0}^{\infty} \lambda_j^2)^{-1} \approx 4.7,$$
(2.24)

and roughly corresponds to the accessible number of entangled modes.

## 2.5 EXPERIMENT

The experimental setup starts with ca. 100 fs pulses from a Ti:Sapphire laser (Spectra Physics Mai Tai) with an  $f_{\rm rep}=80$  MHz repetition rate, a central wavelength of 800 nm and an average power of ca. 3 W. The beam is focused in a Beta Barium Borate (BBO) crystal with a thickness of 0.5 mm, cut for the second harmonic generation (SHG). The red SHG pump is filtered out with a stack of two dichroic mirrors set for multiple reflections of the blue SHG signal and with a bandpass filter with a central wavelength of 400 nm and an FWHM of 10 nm. The SHG signal has an average power of 70 mW and a beam waist of  $w_0=70$   $\mu$ m. For the generation of photon pairs we use a type I SPDC process in a

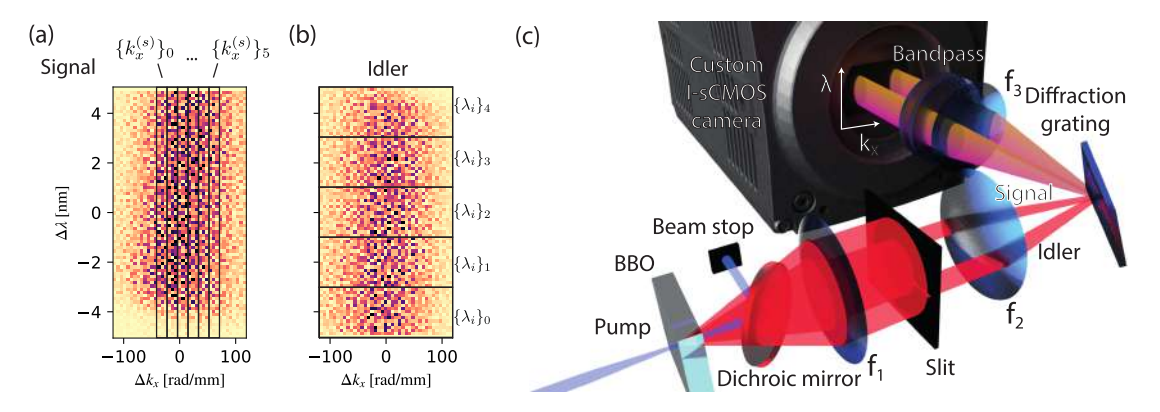


Figure 2.4: (a),(b) Histograms of photo counts in the space of the x component of the transverse wavevector and the wavelength for (a) signal photon, (b) idler photon. Signal and idler regions are spatially separated within a camera frame. Photons have been collected across  $2\times 10^5$  camera frames. Division boundaries of the transverse wavevector  $\{k_x^{(s)}\}$ ,  $\{k_x^{(i)}\}$  and wavelength  $\{\lambda_s\}$ ,  $\{\lambda_i\}$  subregions have been depicted. Signal and idler regions are both divided equally which is omitted for clarity. (c) Simplified experimental setup. SPDC emission is far-field imaged onto a rectangular slit which selects a small range of  $k_y\approx 0$ . Note that  $k_x>0$  ( $k_x<0$ ) corresponds to the signal (idler) photons and the annular distribution of the emission ensures signal-idler separation. The nonlinear crystal (BBO) is far-field imaged onto a diffraction grating which converts the spectral DoF  $\lambda$  into y-axis transverse wavevectors  $k_y(\lambda)$ . Finally, the grating is far-field imaged onto a single-photon camera, performing the conversion between the transverse wave vector and the position in a camera frame.

second BBO crystal of 2 mm thickness, in the non-collinear configuration, as depicted in Fig. 2.3. The blue beam is focused in the second BBO crystal. The Gaussian beam width parameter of the blue beam is ca.  $w_0=70~\mu \text{m}$ . Afterward, the blue beam is filtered out with two dichroic mirrors. The SPDC emission is spectrally filtered (central wavelength 800~nm, FWHM 10~nm) and far-field imaged with a lens (focal length  $f_1=60~\text{mm}$ ) onto a rectangular slit with adjustable width. The slit selects a range of transverse wavevectors  $[-\Delta k_y/2, \Delta k_y/2]$  around  $k_y=0$ . With another lens ( $f_2=300~\text{mm}$ ) the BBO crystal is imaged onto a ruled diffraction grating ( $N_{\text{lines}}=1200~\text{lines/mm}$ , the limiting resolution of  $\delta\lambda=2\lambda_p/N_{\text{lines}}=0.66~\text{nm}$ ). The grating is mounted vertically at a small horizontal angle and in a Littrow configuration for high efficiency. The grating acts by adding a transverse

wavevector in the y-axis with the magnitude dependent on the wavelength, hence mapping the spectral DoF onto the transverse wavevector DoF. Finally, a third lens ( $f_3=100\,$  mm) is placed after the grating to far-field image the first diffraction order from the grating onto our custom single-photon camera. The total effective focal length of the setup (BBO to camera) is  $f_{\rm eff}=30\,$  mm. We note that the grating resolution limit is similar to that originating from the finite slit width  $\Delta k_y$ .

The camera registers  $10^4$  frames per second, each with  $10 \times 1952$  px. The image intensifier gating is set to  $T_{\rm gate} = 1.2$  µs. We observe on average  $\bar{n}_{\rm tot} = 0.12$  photons per camera frame. Since the gating time encompasses  $T_{\rm gate}f_{\rm rep} = 96$  laser pulses a useful figure of merit is the number of observed photons per pulse  $\bar{n}_{\rm pulse} = 1.25 \times 10^{-3}$  which after accounting for the overall efficiency of the setup (ca. 4%) corresponds to the probability of generating an SPDC photon pair per laser pulse of  $\chi \approx 1.5\% \ll 1$ .

Due to the SPDC emission and setup geometry separate regions in the camera frame correspond to the signal and idler photons. Each region is  $40 \times 70\,$  px and corresponds to  $416\,$  rad/mm $\times 5.1\,$  nm where the conversion is  $5.95\,$  rad/(mm $\times$ px) and  $0.127\,$  nm/px. The BBO is cut for type I SPDC, however, by delicate alteration of the angle between the crystal axis and the pump beam  $\theta$ , the diameter and width of the annular-shaped SPDC emission can be adjusted. From numerical modeling (see section 2.4) we estimate  $\theta \approx 31.950(25)^{\circ}$ . For comparison the corresponding cutting angle is specified at  $29.2^{\circ}$ .

# 2.6 RESULTS

For the main measurement, we collected  $1 \times 10^9$  camera frames. During the data analysis stage, the signal and idler frame regions are further divided into transverse wavevector and spectral bins. The division boundaries are overlaid on an exemplary histogram of photo-

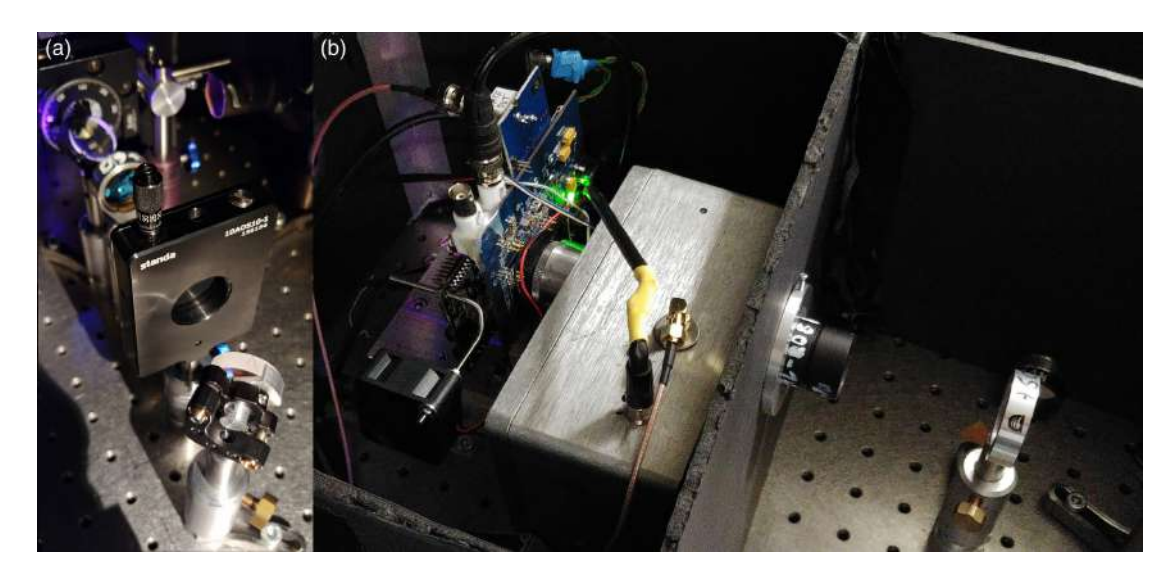


**Figure 2.5:** Photographs of experimental setup fragments. (a) BBO crystal used for SPDC together with pump filtering part, a regulated slit and a mirror routing the photon pairs to further parts of the setup. (b) The custom fast single-photon camera placed within the setup.

counts, in Fig. 2.4 (a),(b). The covariance is calculated according to Eq. (2.9 and summed over the bins to get 2-dimensional maps, as given by Eqs. (2.10), (2.11). The summed covariances together with numerical predictions are depicted in Fig. 2.6. Note that for the maps in spectral coordinates only the selected pairs of wavevector regions are depicted. In other regions, the covariance vanishes.

Generally, a good agreement with the theory is observed, although, for the maps in the spectral coordinates, a small systematic error can be observed. This is probably due to an erroneous calibration of the absolute spectral coordinates within the camera frame. For the numerical prediction, we fitted a model with only a single free parameter – the angle between the pump propagation and the crystal axis  $\theta$ . The best-fit parameter was close to the nominal crystal cutting angle  $\theta_0$ .

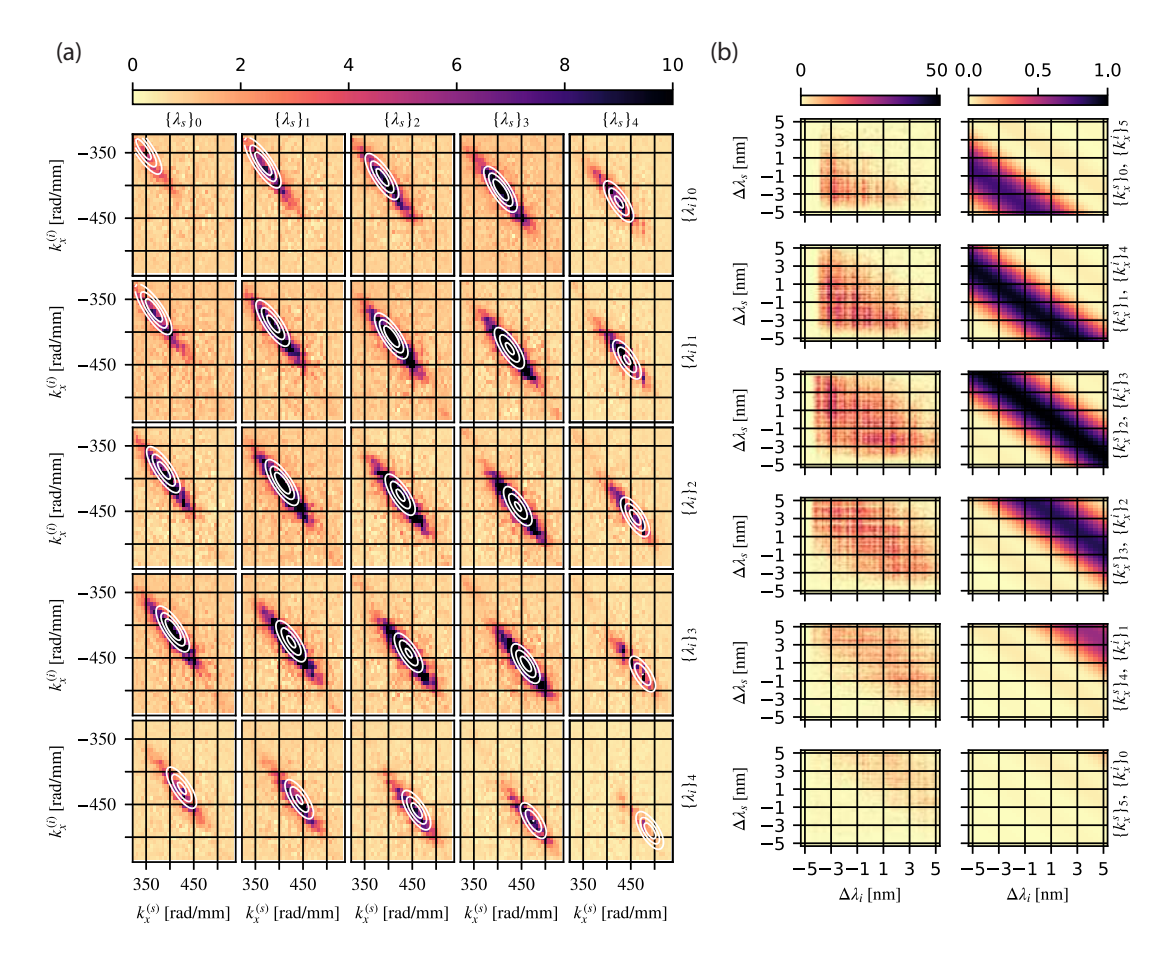


Figure 2.6: Covariance between the idler and signal photons (a) in the transverse wavevectors space, summed over different spectral ranges for each photon  $\{\lambda_s\},\{\lambda_i\}$  (b) in the spectral DoF, summed over different transverse wavevector ranges for each photon  $\{k_x^{(s)}\},\{k_x^{(i)}\}$ . (a) Color map or (b) left column depicts the experimental data. (a) White contours or (b) right column presents the numerical calculation of the corresponding SPDC process intensity  $|\Psi_{\{\lambda_s\},\{\lambda_i\}}(k_x^{(s)},k_x^{(i)})|^2$  summed over the relevant spectral or transverse wavevector ranges and normalized to a unit maximum.

# 2.7 Conclusion

In this chapter, we have described an experimental characterization of hybrid transverse-spectral correlations in two-photon states generated in an SPDC process. The measurement makes good use of the high acquisition speed of our camera to quickly gather  $1\times10^9$  frames and hence a high photocount statistic. With a simple and well-understood theory,

the experiment can be also regarded as a test of the camera's capabilities for the characterization of non-classical light.

We note that selecting only a single component of the transverse wavevector  $k_x$  with  $k_y \approx 0$  limits the in-principle 6-dimensional space to a 4-dimensional slice. This limitation may be relevant for biaxial crystals, where the correlation function would be less symmetric.

Our proof-of-principle demonstration of a fast single-photon camera as a detector of hybrid two-photon correlations opens many possibilities for further development including extensions to different DoFs such as orbital angular momentum.

3

# Quantum Spectroscopy

# 3.I FOREWORD

Photons as the single quanta of light are naturally of central interest in the field of quantum optics. Technically, the term single photon refers to a single excitation of some mode of the electromagnetic field. If the photon is in a pure quantum state, we can describe its mode

structure with a wavefunction e.g. in the spectral degree of freedom (DoF)

$$|1\rangle = \int d\omega \, \psi(\omega) \hat{a}^{\dagger}(\omega) |\text{vac}\rangle,$$
 (3.1)

where  $|1\rangle$  is a Fock state of a single photon  $|{\rm vac}\rangle$  represents a vacuum state and  $\hat{a}^{\dagger}(\omega)$  creates a photon with frequency  $\omega$ . Characterization of a single photon wavefunction  $\psi(\omega)$  can be of fundamental interest but also can prove useful for quantum-enhanced metrology. One can imagine that a photon with an *a priori* known mode structure interacts dispersively (i.e. is not absorbed or scattered) with a sample. The photon's wavefunction post-interaction contains information about the sample and the interaction itself. Remarkably, it is a minimally invasive optical method to probe the sample – one cannot use less than a single probe photon at a time.

We were inspired by the earlier work of our colleagues [113] which was concerned with the characterization of a single photon wavefunction in the spatial degree of freedom using a sptially resolved two-photon interference. Michał Parniak conceived the idea of using similar methods in the spectral DoF. While similar in essence, characterization in the spectral DoF poses significantly different challenges yet also promises new interesting applications e.g. in the context of spectroscopy or characterization of fast phenomena.

This chapter is based on ref. [114].

# 3.2 Introduction

A single photon can among others have two interesting properties.

First, it can be an excitation of a very complex mode of the electromagnetic field e.g. with added qualitative properties such as the orbital angular momentum (OAM). It is worth noting that in the spatial domain, numerous applications and fundamental studies rely on

the mode structuring including uncertainty relations [115] and improved sensitivity [116] for OAM or remote object identification [117]. However, with the predominantly single-mode optical fiber architectures, the spectro-temporal modes also attract broad attention in the context of e.g. entanglement generation on-chip [118], bandwidth matching [119] or quantum networks [120].

Second, a single-photon state is inherently non-classical and subject to unintuitive phenomena. An example of this is the two-photon interference also known as the Hong-Ou-Mandel (HOM) effect [121] demonstrating the quantized and bosonic nature of a photon. However, these two properties are relatively rarely explored or utilized together.

Here we will demonstrate how a quantum phenomenon of spectrally-resolved two-photon interference characterizes a single-photon in a complex spectro-temporal mode. Furthermore, the mode structure will be a hallmark of an earlier light-matter interaction in a rarely seen regime. A spectrally-wide (THz bandwidth) photon resonantly interacts with a spectrally narrow (GHz bandwidth) atomic line in hot <sup>87</sup>Rb vapor. This bandwidth-mismatched interaction is almost exclusively dispersive, the photon is very rarely absorbed. Hence, the method that we here describe is both a mean of non-invasive, dispersive spectroscopy and a fundamental characterization of a single photon's spectral wavefunction.

## 3.2.I Two-photon interference

Let us consider the phenomenon of two-photon interference in a simple scenario, depicted schematically in Fig. 3.1. If two identical photons enter separate ports of a balanced 50/50 beamsplitter (BS), they always leave through the same port together. In other words, no coincidences at the output ports can be observed. The effect can be understood as a destructive interference of the two-photon amplitudes corresponding to both photons being transmitted or both being reflected.

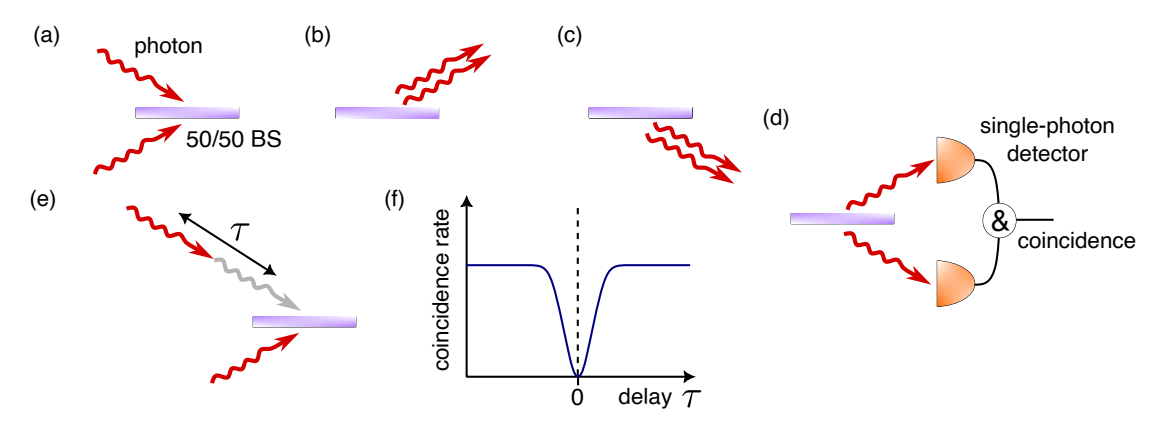


**Figure 3.1:** (a) Two identical photons simultaneously enter respective ports of balanced 50/50 beamsplitter (BS). (b),(c) Due to the Hong-Ou-Mandel effect the photons always leave together through a single output port. (d) Placing a pair of single-photon detectors at the output ports allows observing the number of coincidences i.e. events where photons appear at different output ports within a preset time window. (e) A simple way to make the mode functions of the photons different is by delaying one of the photons by  $\tau$ . (f) The rate of observed coincidences grows with  $|\tau|$  and reaches a plateau as the overlap between the mode functions of the photons approaches 0. This qualitative behavior is often referred to as the "Hong-Ou-Mandel dip" in reference to the original experiment [121].

If the photons cease to be identical i.e. their mode functions do not perfectly overlap, coincidences start to appear. The number of coincidences is a good estimator of the mode functions overlap. This property was originally explored in the seminal paper of Hong, Ou, and Mandel, where the authors delayed one of the two identical photons and were able to precisely estimate the delay from the number of observed coincidences [121].

Beyond this very important yet relatively simple scheme, a single-photon detection with a resolution in a selected DoF can be added. Chrapkiewicz *et al.* explored this possibility with a single-photon sensitive camera to estimate the overlap between spatial modes of two photons and retrieve the differences between the wavefronts of their modes.

In general, two-photon interference with or without added resolution of single-photon detection finds broad applications including super-resolution imaging [65], quantum fingerprinting [46, 122, 123] and characterization of single-photon sources [102, 124–126].

In particular, the HOM effect has been demonstrated previously with spectral resolution using a time-of-flight spectrometer [127, 128]. The two-photon interference goes beyond the photonic realm with demonstrations in other systems including atoms [129, 130], spinwaves [131, 132] or phonons [133].

## 3.2.2 SIMPLIFIED EXPERIMENT

Let us consider a simplified version of our experiment. We begin with two single photons identical in all aspects except being spatially separated. The spectro-temporal mode of each photon is an ultrafast pulse with a spectral width on the order of THz. One of the photons (reference) remains unaltered while the other (probe) resonantly interacts with a medium of hot  $^{87}{\rm Rb}$  vapor. As already mentioned, the interaction is bandwidth-mismatched. Hence it is mostly dispersive and the photon acquires a wavelength-dependent phase  $\exp[i\varphi(\lambda)]$ . The photons meet again at the respective inputs of a balanced 50/50 beamsplitter. We observe the beamsplitter outputs with a spectrally-resolving single-photon detector e.g. a diffraction grating mapping frequencies to angles and a single-photon camera in the far-field of the grating. Remarkably, the 2-dimensional pattern of spectrally-resolved coincidences is a unique (and even redundant) representation of  $\varphi(\lambda)$ . A simplified experimental setup alongside a simulated coincidence map has been depicted in Fig. 3.2.

## 3.3 Theory

## 3.3.I ZERO-AREA PULSES

A resonant (or near resonant) interaction of a short pulse with a slowly relaxing medium such as an atomic vapor has been vastly studied in the classical regime in the context of

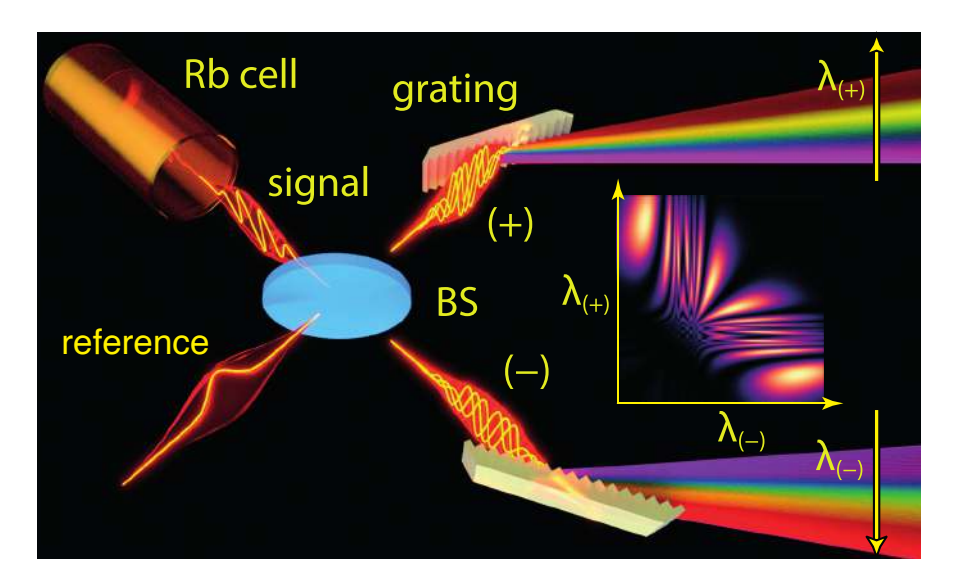


Figure 3.2: Spectral characterization of a single photon using spectrally-resolved two-photon interference. A pair of identical broadband (ca.  $10\,\mathrm{nm}$ ) single photons will serve as a reference and probe. The probe resonantly interacts with  $^{87}\mathrm{Rb}$  vapor. Via the bandwidth-mismatched interaction, its spectro-temporal mode becomes a zero-area pulse. The reference and signal photons are interfered on a balanced beamsplitter (BS) which outputs are observed with a spectrally-resolving single-photon detector. A 2-dimensional pattern of detected coincidences marks the dissimilarities in the spectral phase of the signal and the reference photon, acquired in the former light-matter interaction. (inset) Exemplary simulated pattern of coincidences.

so-called zero-area (ZA) or  $0\pi$  pulses [134–136]. Let us consider a short pulse with a real slowly varying envelope  $\mathcal{E}(z,t)$  inside a medium with an absorptive resonance near the light frequency – effectively a two-level medium. McCall and Hahn identified the pulse area  $\theta$  and predicted its evolution along the propagation axis z. Denoting the dipole matrix element of the transition by d, we define

$$\theta(z) := \int dt \, \frac{2d}{\hbar} \mathcal{E}(z, t) \tag{3.2}$$

and the McCall and Hahn's Area Theorem states

$$\partial_z \theta(z) = -\frac{\alpha}{2} \sin \theta(z),$$
 (3.3)

where  $\alpha$  is the linear optical attenuation coefficient. The notable implications of this theorem are that pulses with an initial area equal to an integer multiple of  $\pi$  have their area unchanged during propagation. All other areas approach one of these special values. In particular, in the case of a broadband pulse and a narrow absorption line (or equivalently an ultrashort pulse and and a slowly relaxing medium), the pulse area will exponentially decay to 0. The temporal envelope of such a ZA pulse consists of a series of alternating lobes with  $\pm$  signs.

Single-photon zero-area pulses have been studied experimentally by Costanzo *et al.* [137]. The authors characterized single-photon zero-area pulses in the temporal domain using homodyne detection. The local oscillator (LO) mode shape was optimized to match the temporal mode of the interrogated ZA pulse. While homodyning is a robust tomographic method [138], it is inherently affected by the shot noise of the local oscillator which can hinder its performance in certain scenarios. We shall further compare homodyning and two-photon interference in a simplified setup without spectro-temporal resolution (see section 3.6.7).

# 3.3.2 Spectrally-resolved two-photon interference

Let us consider photon pairs generated in the SPDC process in a nonlinear crystal. The setting is as already described in section 2.3.1 except now we will couple the signal and idler modes into a pair of single-mode fibers. The coupling can be considered spatial filtering as only the selected transverse components matching the fiber mode (after coupling optics transformation) will be transmitted. In general, such a filtering alters the spectral structure of the SPDC emission. For details concerning fiber coupling in our case of type I SPDC in a BBO crystal see ref. [139]. We will proceed by assuming a fairly general two-photon wavefunction  $\Psi_{\omega}(\omega_s, \omega_i)$  only requiring that the two-photon wavefunction is symmetric

with respect to the exchange of the arguments

$$\Psi_{\omega}(\omega_s, \omega_i) = \Psi_{\omega}(\omega_i, \omega_s). \tag{3.4}$$

This condition is necessary for high visibility of two-photon interference [127, 140, 141]. It also implies that the central frequencies of each photon are equal

$$\iint d\omega_i d\omega_s |\Psi_{\omega}(\omega_s, \omega_i)|^2 \omega_s = \iint d\omega_i d\omega_s |\Psi_{\omega}(\omega_s, \omega_i)|^2 \omega_i.$$
 (3.5)

We will approximate the two-mode squeezed state produced in the SPDC as

$$|\psi\rangle \approx \left(1 + \sqrt{\chi} \iint d\omega_i d\omega_s \, \Psi_{\omega}(\omega_s, \omega_i) a_s^{\dagger}(\omega_s) a_i^{\dagger}(\omega_i)\right) |\text{vac}\rangle,$$
 (3.6)

which is valid in the regime of low excitation probability  $\chi \ll 1$  [105], and where  $a_s^{\dagger}(\omega_s), a_i^{\dagger}(\omega_i)$  are the creation operators for signal and idler photons with frequencies  $\omega_s$  and  $\omega_i$ , respectively.

Omitting for the moment the details of the light-matter interaction the signal photon partakes, we will only assume that the interaction is dispersive i.e. can written as

$$\Psi_{\omega}(\omega_s, \omega_i) \to \Psi_{\omega}(\omega_s, \omega_i) \times \exp\left[i\varphi_{s,\omega}(\omega)\right] \equiv \tilde{\Psi}_{\omega}(\omega_s, \omega_i),$$
 (3.7)

where  $\tilde{\Psi}_{\omega}(\omega_s, \omega_i)$  is the two-photon wavefunction after the interaction and  $\varphi_{s,\omega}(\omega_s)$  corresponds to the acquired spectral phase of the signal photon.

The ideal transformation of a balanced beamsplitter on the creation operators reads

$$a_{\pm}^{\dagger} = \frac{1}{\sqrt{2}} (a_s^{\dagger} \pm a_i^{\dagger}), \tag{3.8}$$

where  $a_\pm^\dagger$  corresponds to the modes of the  $\pm$  BS output ports. Accordingly, under this transformation, the two-photon component of our state develops 4 terms. Since in the experiment our measurement projects the state onto a subspace containing at least one photon in each  $\pm$  mode, we shall only consider the 2 coincident terms i.e. containing  $a_+^\dagger a_-^\dagger$ . The other 2 terms correspond to both photons being in a single  $\pm$  mode i.e. contain  $a_+^\dagger a_+^\dagger$  or  $a_-^\dagger a_-^\dagger$ .

The probability of observing a coincidence between photons at  $\omega_+$  and  $\omega_-$  is given by

$$P_{\omega}(\omega_{+},\omega_{-}) = \frac{1}{4} \left| \tilde{\Psi}_{\omega}(\omega_{+},\omega_{-}) - \tilde{\Psi}_{\omega}(\omega_{-},\omega_{+}) \right|^{2}. \tag{3.9}$$

Inspecting Eq. (3.9) we can immediately see why the the condition of Eq. (3.4) is necessary for destructive interference between identical photons.

A notable property of HOM interference is its robustness to the global (i.e. here frequency-independent) phase fluctuations. Indeed any phase  $\varphi_{\rm global}$  between signal and idler just multiplies  $\Psi_{\omega}(\omega_i,\omega_s)$  by  $\exp(i\varphi_{\rm global})$  and hence does not affect  $P_{\omega}(\omega_+,\omega_-)$ . This property has been employed in among others near-term quantum repeater architectures [40, 142, 143] or proposed quantum communication protocols [46, 91, 144]. In our case, without the loss of generality, we will assume that the global phase is chosen such that  $\Psi_{\omega}(\omega_s,\omega_i)$  is real. This way we can write

$$P_{\omega}(\omega_{+},\omega_{-}) = \frac{1}{2} |\Psi_{\omega}(\omega_{+},\omega_{-})|^{2} \times \left[1 - \cos(\varphi_{\omega,s}(\omega_{+}) - \varphi_{\omega,s}(\omega_{-}))\right], \tag{3.10}$$

where the first term on the right is just the joint spectral intensity (JSI) of the two-photon state, and the second term describes a spectrally-resolved two-photon interferogram. Let us look at the 2-dimensional argument of this second term. For a fixed  $\omega_{-}$  ( $\omega_{+}$ ) its 1-dimensional

slice along  $\omega_+$  ( $\omega_-$ ) is a standard (alike e.g. probing a phase of a Mach-Zehnder interferometer) interference pattern with a phase offset given by  $\varphi_{s,\omega}(\omega_-)$  [ $\varphi_{s,\omega}(\omega_+)$ ]. Hence, up to this phase offset and the JSI weighting (a priori known) each row or column of a 2D interferogram carries the same information about the interrogated 1-dimensional phase  $\varphi_{s,\omega}(\omega)$ . As such the interferogram is a redundant representation, hence robust to noise and experimental imperfections. In section 3.6.5 we will briefly discuss how standard Fourier-domain methods can be adapted to the reconstruction of  $\varphi_{s,\omega}(\omega)$  from the interferogram.

We should also consider an important experimental limitation – non-ideal interference visibility  $\mathcal{V}$ . One way to include it into our theoretical description would be to consider a statistical mixture of two scenarios. One as we have done already and the other with each photon entering the beamsplitter separately i.e. not interfering at all. Formally we would consider a density matrix of the initial state and modify the beamsplitter transformation. Another way is by considering that the local visibility  $\mathcal{V}(\omega_+, \omega_-)$  can be defined by considering a constant phase offset  $\Delta \varphi$  such that

$$\cos(\varphi_{\omega,s}(\omega_{+}) - \varphi_{\omega,s}(\omega_{-})) \to \cos(\varphi_{\omega,s}(\omega_{+}) - \varphi_{\omega,s}(\omega_{-}) + \Delta\varphi)$$
 (3.11)

then

$$\mathcal{V}(\omega_{+}, \omega_{-}) = \frac{\max_{\Delta\varphi} P_{\omega}(\omega_{+}, \omega_{-}) - \min_{\Delta\varphi} P_{\omega}(\omega_{+}, \omega_{-})}{\max_{\Delta\varphi} P_{\omega}(\omega_{+}, \omega_{-}) + \min_{\Delta\varphi} P_{\omega}(\omega_{+}, \omega_{-})}.$$
(3.12)

With this definition, we must have

$$P_{\omega}(\omega_+, \omega_-) = \frac{1}{2} |\Psi_{\omega}(\omega_+, \omega_-)|^2 \times \left[ 1 - \mathcal{V}(\omega_+, \omega_-) \cos(\varphi_{\omega,s}(\omega_+) - \varphi_{\omega,s}(\omega_-)) \right].$$
 (3.13)

Let us note that the phase offset  $\Delta \varphi$  is just a notational convenience for expressing a range

of values the cosine can take if no assumptions are made about  $\varphi_{s,\omega}(\omega_s)$ .

Lastly, since in the experiment we will use broadband photons (ca. 10 nm spectral width), it is sometimes more convenient to work in wavelengths and not frequencies. We shall further make such conversions implicitly.

# 3.3.3 RESONANT BANDWIDTH-MISMATCHED LIGHT-MATTER INTERACTION

Considering the light-matter interaction in our experiment we shall employ a simple model of two-level atoms and a single Lorentzian resonance line – a good approximation for a bandwidth-mismatched interaction in hot  $^{87}{\rm Rb}$  vapor, previously employed in a similar context in ref. [145]. The signal photon propagates through the distance L of the atomic medium. In the classical picture, during the interaction, each spectral component of the electric field is modified

$$E(\omega) \to E(\omega) \exp\left[\frac{-\text{OD}(T)}{1 - i(\omega - \omega_0)\tau(T)}\right],$$
 (3.14)

where for the vapor temperature T, OD(T) is the optical depth and  $\tau(T)$  denotes the Doppler-broadened excited state lifetime. For OD and  $\tau$  calculation details see section 3.6.1. For employed  $^{87}\text{Rb}$  temperatures  $\tau(T)$  will be in the range of 215~ps to 240~ps.

Let us consider the absorptive and dispersive parts of the interaction

$$\operatorname{Re}\left[\frac{-\operatorname{OD}(T)}{1 - i(\omega - \omega_0)\tau}\right] = -\operatorname{OD}(T) \times \frac{1}{1 + \tau(T)^2(\omega - \omega_0)^2},\tag{3.15}$$

$$\operatorname{Im}\left[\frac{-\operatorname{OD}(T)}{1 - i(\omega - \omega_0)\tau}\right] = -\operatorname{OD}(T) \times \frac{\tau(T)(\omega - \omega_0)}{1 + \tau(T)^2(\omega - \omega_0)^2} \equiv \varphi_{s,\omega}(\omega). \tag{3.16}$$

Since there is a large mismatch between the spectral bandwidth of the photon and the transition width, for the majority of the spectral components of the electric field we have ( $\omega$  –

 $\omega_0)\tau(T)\gg 1$ . At the same time Eq. (3.15) shows that as long as  $(\omega-\omega_0)^2\tau(T)^2\gg {\rm OD}$  we can neglect the absorption. With the experimental bandwidth of ca. 5 THz (10 nm) for the photon and  $1/\tau(T)\approx 500\,$  MHz even with very high optical depths this conditions will be fulfilled (the left-hand side reads  $10^8$ ). We can convert the phase  $\varphi_{s,\omega}(\omega_s)$  to wavelengths  $\varphi_s(\lambda)$  by substituting  $(\omega-\omega_0)=-2\pi c(\lambda-\lambda_0)/\lambda_0^2$ , with c denoting the speed of light, hence

$$\varphi_s(\lambda) = \text{OD} \times \frac{x(\lambda)}{1 + x(\lambda)^2},$$
(3.17)

where  $x(\lambda) = 2\pi\tau c(\lambda - \lambda_0)/\lambda_0^2$  with  $\lambda_0 = 795$  nm corresponding to the wavelength of the D1 <sup>87</sup>Rb line. Finally, since we are describing a twin-photon state, instead of modifying the spectral components of the electric field, we shall impose the spectral phase of Eq. (3.17) onto the two-photon wavefunction (see Eq. (3.7)).

#### 3.4 EXPERIMENT

## 3.4.I SETUP

For the generation of twin-photon states of light, we used a similar setup to the one described in Chapter 2. A notable exception is that now signal and idler (reference) photons are coupled to single-mode polarization-maintaining fibers (Thorlabs P3-780PM) i.e. a pair of transverse modes is selected from the emission cone.

For coupling, we employed custom-made adjustable collimators based on an aspheric lens with a numerical aperture of 0.5 and a focal length of 8 mm. The mode width (beam waist) was initially selected  $\sqrt{2}$  wider than the pump waist. Fine-tuning of the coupled mode was done by observing in real-time single and coincident photon counts for signal and idler.

For photon counting during calibration, we used avalanche photodiodes (Excelitas



**Figure 3.3:** Photographs. (a) FPGA development board National Instruments myRIO-1900 with a custom input/output board attached, used for timetagging signals from single-photon avalanche photodiodes. (b) LabView program interface for live preview of the photon count statistic. (c) Fragment of the experimental setup showing a mounted BBO crystal for SPDC, blue pump filtering, and fiber coupling of the SPDC emission.

SPCM-AQ4C) together with a custom time-tagger implemented in a high-level FPGA device (National Instruments MyRIO, LabView software) with an added input/output board with proper terminations. Photographs of the FPGA and the SPDC setup together with a screenshot from the LabView program are included in Fig. 3.3.

We fine-tuned the photon source by maximizing the efficiency  $\eta$  estimated with a reference-free method (see section 2.3.5) and given by Eq. (2.16). The pump power was adjusted to keep the excitation probability low  $\chi$  while keeping a reasonable number of single counts – around  $5 \times 10^4$  cps signal and idler each. The excitation probability level was monitored indirectly by observing and keeping high the second-order intensity correlation  $g^{(2)}$  between signal and idler, calculated with *per pulse* quantities (and after subtraction of accidental coincidences – see sec. 2.3.3). The experimental setup is depicted in Fig. 3.4. Ti:Sapphire laser produces 100 fs pulses with a central wavelength of 795 nm at a repeti-

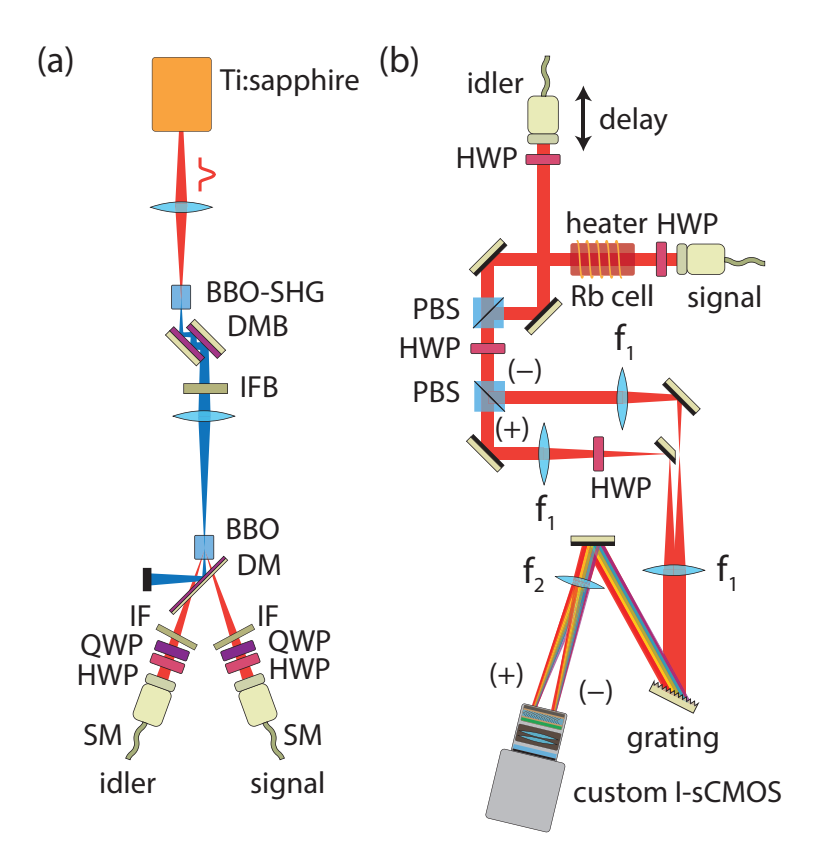


Figure 3.4: (a) State preparation. Ultrashort pulses from a Ti:Sapphire laser are frequency-doubled and used to pump a type-I SPDC (BBO). Pairs of photons from the SPDC are spectrally filtered (IF) and coupled to single-mode fibers (SM). (b) Main setup. Signal and idler (reference) photons are interfered on an equivalent of a 50/50 balanced beamsplitter implemented using the polarization DoF. Before interfering the signal photon probes a glass cell with hot  $^{87}{\rm Rb}$  vapor. Output ports of the interferometer ( $\pm$ ) undergo spectrally-resolved single-photon counting with a diffraction grating-based spectrometer employing our custom camera as the detector. BBO-SHG – BBO crystal for second harmonic generation (SHG). DM (DMB) – dichroic mirro optimized for high reflectance around  $800\,{\rm nm}$  ( $400\,{\rm nm}$ ) wavelength. IF (IFB) – interference filter with a central wavelength around  $800\,{\rm nm}$  ( $400\,{\rm nm}$ ). HWP (QWP) – half-wave (quarter-wave) plate. PBS – polarizing beamsplitter.  $f_1,\,f_2$  – lens.

tion rate of  $f_{\rm rep}=80\,{\rm MHz}$  and with an average power of ca.  $3\,{\rm W}$ . The pulses undergo second harmonic generation in a BBO crystal (0.5 mm length) producing around  $100\,{\rm mW}$  of power at a wavelength of  $397.5\,{\rm nm}$ . The red pump is filtered with a multiple-reflection stack of dichroic mirrors and an interference filter (central wavelength of  $400\,{\rm nm}$ , FWHM

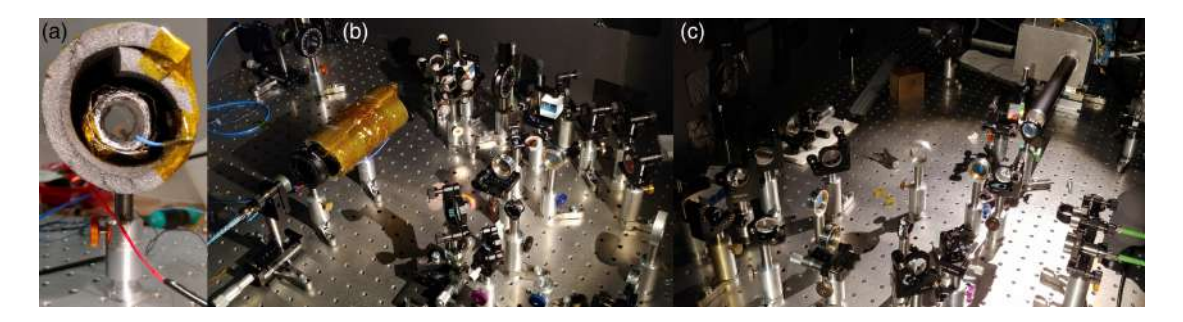


Figure 3.5: Photographs of the experimental setup fragments. (a) Insulated (aluminum foil and polyethylene foam)  $^{87}{\rm Rb}$  vapor cell with a flexible resistive-foil heater wrapped around the cell. (b) Two-photon interferometer [upper part of Fig. 3.4 (b)] (c) Single-photon spectrally-resolved detection [lower part of Fig. 3.4 (b)]

of  $10\,\mathrm{nm}$ ). The blue beam is focused ( $70\,\mu\mathrm{m}$  beam waist radius) in a second BBO crystal ( $2\,\mathrm{mm}$  length) pumping type-I non-collinear SPDC. Produced pairs of photons are spectrally filtered with a slightly tilted interference filter (central wavelength of  $797.6\,\mathrm{nm}$  as measured and of  $800\,\mathrm{nm}$  nominal, FWHM of  $10\,\mathrm{nm}$ ). Signal and idler photons are coupled to single-mode fibers and enter the main part of the setup – the two-photon interferometer. In the main part, the signal and idler (reference) undergo the two-photon interference. Before interfering the signal photon interacts with a hot  $^{87}\mathrm{Rb}$  vapor. Let us begin with the interferometer and detection and then come back to the interaction.

Since a balanced 50/50 (or close to) beamsplitter is rare and the splitting ratio is heavily wavelength-dependent, we use the polarization degree of freedom as an auxiliary and implement the 50/50 BS with polarization optics. Single and idler polarizations are already linear – they are aligned to be so in the first part of the setup (and matched with the slow axis of the single-mode polarization-maintaining fiber). The polarizations are rotated with half-wave plates (HWP) to match the horizontal (H, signal) and vertical (V, idler) polarization of a polarizing beamsplitter (PBS). This way, spatial modes of signal and idler are overlapped on the PBS and leave through a single port. A subsequent HWP rotates the po-

larization by  $45^{\circ}$  to produce  $\pm$  superpositions of signal and idler in the H, V polarization basis. Finally, a second PBS separates H and V polarizations (and hence the + and the superposition) spatially. The first PBS is far-field imaged onto a mirror (- port) or a Dshaped mirror (+) port with two lenses (one each  $\pm$  port) of  $f_1=150\,\mathrm{mm}$  focal length. The mirrors are far-field imaged  $(f_1)$  onto a diffraction grating (1200 lines/mm, 750 nm blaze). Additional HWPs before the diffraction grating set the polarizations perpendicular to the grating grooves for maximal diffraction efficiency. The grating is mounted close to the Littrow configuration. Finally, the first diffraction order is far-field imaged onto our single-photon camera with a lens of  $f_2 = 300 \,\mathrm{mm}$  focal length. Mirrors placed between  $f_1$ lenses allow to spatially separate the regions corresponding to  $\pm$  ports in the camera sensor plane. The separation is done on the same axis as the spectral dispersion (this reduces the height of the required camera frame and hence increases the acquisition speed – c.f. ch. 1). The  $\pm$  spatial modes correspond to  $140 \times 5$  px in the camera frame. The longer dimension is along the spectral dispersion  $\lambda_{\pm}$ , the shorter is integrated over during the data analysis. Acquisition speed is set to  $8.2 \times 10^4$  frames per second. The image intensifier gating time is  $t_g \,=\, 11~\mu\mathrm{s}$  which corresponds to  $R \,=\, f_\mathrm{rep} t_g \,=\, 880$  laser pulses per frame. In each frame, we observe on average  $\bar{n} \approx 0.2$  photons.

Before entering the two-photon interferometer, the signal photon passes through a cylindrical glass cell ( $1 \in \text{in diameter}$ , 5 cm long) along its longitudinal axis. The cell is filled with  $^{87}\text{Rb}$  vapor, wrapped in a flexible foil resistive heater, aluminum foil, and polyethylene foam for insulation. A thermocouple is mounted close to the glass surface to monitor the cell temperature. The current through the heater is adjusted for a desired steady-state temperature with little variation observed. No active thermostatic control was found to be required. However, it is worth noting that the experimental setup was enclosed in a cardboard container, the whole optical table was surrounded by heavy curtains, and the

conditions in the laboratory room (temperature, humidity, etc.) remained fairly constant throughout the measurement periods. The cell temperatures were between 86 °C and 188 °C corresponding to optical depths between ca. 20 and ca.  $4.6 \times 10^3$ , respectively (c.f. sec. 3.6.1). Photographs of the parts of the two-photon interferometer are depicted in Fig. 3.5.

The interaction of the signal photon and the  $^{87}$ Rb vapor can be described by imposing a spectral phase  $\varphi_s(\lambda)$ , given by Eq. (3.17) onto the two-photon wavefunction (see Eq. (3.7)). A purely dispersive interaction is in general an approximation. However, let us note that our measurement projects the *post interaction* state onto a subspace of at least one photon in the + port of the interferometer and at least one photon in the - port. Hence, by design, only these pairs of photons for which neither signal nor reference photon is absorbed contribute to the signal - the measurement post-selects purely dispersively interacting signal photons. This is true as long as the SPDC is weakly pumped and there is no significant contribution of the multi-photon terms.

#### 3.4.2 MEASUREMENT

We will consider the coincidence maps collected by observing the  $\pm$  port of the two-photon interferometer with spectral resolution. Each frame has two regions corresponding to each port and within a region subsequent pixels correspond to different spectral components.

We shall denote by  $n(\lambda_{\pm})$  the number of registered photons at a given wavelength of the  $\pm$  port (where we implicitly mean a small range of wavelengths around the nominal value, limited by the spectrometer resolution). Since the camera is not photon-number-resolving (in each pixel) and each region is integrated along the smaller (not spectrally dispersed) dimension (of 5 px), we have  $0 \le n(\lambda_{\pm}) \le 5$  in each frame. All averages  $\langle . \rangle$  are henceforth over the collection of observed frames.

An unprocessed (raw) coincidence map

$$\mathcal{R}(\lambda_{+}, \lambda_{-}) = \langle n(\lambda_{+})n(\lambda_{-})\rangle \tag{3.18}$$

is a histogram of events where within a single frame a photon is observed at  $\lambda_+$  and another at  $\lambda_-$ . Since each camera frame corresponds in time to ca. 880 laser pulses, the contributing photons may not originate from the same temporal mode. Such events are accidental coincidences and they substantially reduce the signal-to-noise ratio of the raw map. Luckily, the average of the accidental coincidences distribution can be calculated and subtracted.

Let us consider a noiseless, ideal-visibility scenario. The photon number covariance reads

$$\langle n(\lambda_{+})n(\lambda_{-})\rangle - \langle n(\lambda_{+})\rangle\langle n(\lambda_{-})\rangle =$$

$$RP_{\lambda}(\lambda_{+}, \lambda_{-})\chi\eta^{2} + R(R-1)\chi^{2}\eta^{2} - R^{2}\chi^{2}\eta^{2} \approx RP_{\lambda}(\lambda_{+}, \lambda_{-})\chi\eta^{2}, \quad (3.19)$$

where  $P_{\lambda}$  is given by Eq. 3.10 after  $\omega \to \lambda$  conversion, the term  $RP_{\rm c}(\lambda_+,\lambda_-)\chi\eta^2$  corresponds to coincidences from the same temporal mode, while the term  $R(R-1)\chi^2\eta^2$  for large R is roughly equal to the experimentally estimated average of the accidental coincidences distribution

$$\mathcal{A}(\lambda_{+}, \lambda_{-}) := \langle n(\lambda_{+}) \rangle \langle n(\lambda_{-}) \rangle = R^{2} \chi^{2} \eta^{2}, \tag{3.20}$$

where the last equality holds in this idealized scenario.

Hence, from the raw coincidence map, we subtract the estimate of the accidental coincidences to get the (processed) coincidence map

$$C(\lambda_+, \lambda_-) = R(\lambda_+, \lambda_-) - A(\lambda_+, \lambda_-). \tag{3.21}$$

# 3.5 RESULTS

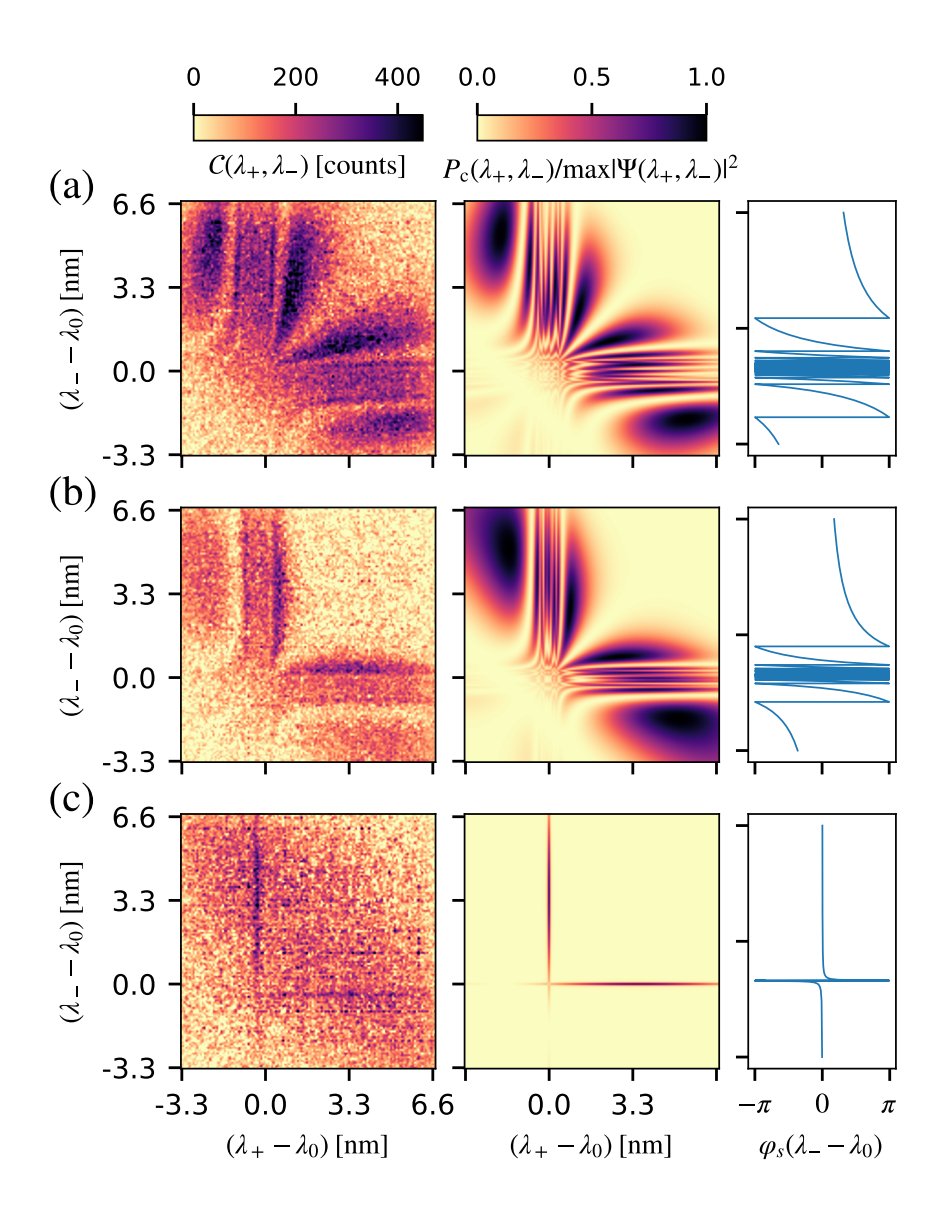


Figure 3.6: Coincidence maps for spectrally-resolved two-photon interference with signal photon interacting with hot  $^{87}\mathrm{Rb}$  vapor at a range of temperatures (a)  $T_1=188\,$  °C, (b)  $T_2=174\,$  °C, (c)  $T_3=86\,$  °C. Experimental results (photon number covariance) are depicted in the left-most column. The central column represents the result of a fitted theoretical model (normalized join spectral intensity) with the visibility  $\mathcal V$  set to  $100\,\%$  for presentation. The right-most column presents the 1-dimensional spectral phase  $\varphi_s(\lambda-\lambda_0)$  modulo  $2\pi$ , corresponding to the fitted model. Coordinates are relative to the D1 line wavelength  $\lambda_0=795\,\mathrm{nm}$  in  $^{87}\mathrm{Rb}$ .

Experimental results have been depicted in Fig. 3.6. Coincidence maps were measured for 3 distinct temperatures of the  $^{87}$ Rb cell  $T_1=188\,^{\circ}$ C,  $T_2=174\,^{\circ}$ C, and  $T_3=86\,^{\circ}$ C. A theoretical model, given by Eq. (3.13), has been fitted to the data. The fidelity  $0 \leq \mathcal{F} \leq 1$  [146] between the experimental and fitted results was found to be 94%, 86%, 89% for  $T_1$ ,  $T_2$  and  $T_3$ , respectively. For the details of fidelity calculations see sec. 3.6.3. The optical depths corresponding to the best model fit were  $\mathrm{OD}(T_1)=4.6\times 10^3$ ,  $\mathrm{OD}(T_2)=2.6\times 10^3$  and  $\mathrm{OD}(T_3)\approx 20$  and are in a good agreement with independent calculation (c.f. sec. 3.6.1) for the measured temperatures.

A notable feature of all maps is that the coincidences are concentrated along the antidiagonal stripe. This shape is a result of the JSI  $|\Psi(\lambda_+, \lambda_-)|^2$  of the twin-photon state we used and is generally a hallmark of spectral correlations between the signal and idler photons. For a comparison with simulated results assuming uncorrelated photon pairs, see sec. 3.6.4.

A cross-like shape at  $\lambda_0$  stems from a very rapid variation of the spectral phase near the resonance, beyond the spectrometer resolution. In such a case, fast fringes (visible in the simulated maps) are blurred due to the coincidences at each spectral point in this region being phase-averaged.

Notably, the phase sign flips around  $\lambda_0$ , as depicted in the right-most column of Fig. 3.6, and described by Eq. (3.17). For higher temperatures (and hence optical depths), the foot-print of the interaction is most pronounced. Its effects are visible several nm (order of a few THz) from the resonance line, even though the resonance itself is only ca.  $500 \, \mathrm{MHz}$  wide. Nevertheless, with lower temperatures the presence of  $^{87}\mathrm{Rb}$  is still distinctly visible, even with comparatively low optical depth and a peak-to-peak variation of the spectral phase of only  $20 \, \mathrm{rad}$ . Such a regime of parameters could be interesting in the non-destructive meteorological context for the task of binary hypothesis testing for the presence or absence of a

sample.

Let us note, that even though in fitting a model we assumed a prior knowledge of phase profile shape  $\varphi_s(\lambda)$ , in the absence of such assumptions the phase could still be reconstructed. The problem is analogous to the processing of classical interferograms and as such holographic reconstruction techniques [147, 148] can be adapted to its solving. We briefly investigate a very simple Fourier-domain-based reconstruction of  $\varphi_s(\lambda_+) - \varphi_s(\lambda_-)$  in section 3.6.5.

Finally, let us consider the experimental visibility of the two-photon interferometer. The visibility is not only a measure of the setup quality and a sign of the appropriate form of the two-photon state, but it can also carry valuable information if calculated locally  $\mathcal{V}(\lambda_+, \lambda_-)$ . Note that the 2-dimensional argument  $\varphi_s(\lambda_+) - \varphi_s(\lambda_-)$  of the cosine term in Eq. (3.13) is an abundant representation of a 1-dimensional  $\varphi_s(\lambda)$  and in its form ensures the cos function cannot stay constant over the wavelength range of  $\varphi_s(\lambda)$  except for a special case of  $P_c = 0$ . This way, if  $\mathcal{V}(\lambda_+, \lambda_-)$  is close to 0 over extended regions where coincidences are present  $P_c(\lambda_+, \lambda_-) \neq 0$ , it is a hallmark of fast phase oscillations in this regime which are below the spectrometer resolution and average the cos term to 0. With this observation, we can infer the *presence* of sub-resolution spectral features. The experimental measurement of the local visibility has been described in sec. 3.6.2.

# 3.6 METHODS AND DISCUSSION

## 3.6.1 RB OPTICAL DEPTH CALCULATION

The definition of optical depth may vary depending on the context. In this work we define OD as follows. Let us follow [149] and begin with  $^{87}$ Rb vapor pressure P given in Torrs

$$\log_{10} P(T) = 15.88253 - \frac{4529.635}{T} + 0.00058663T - 2.99138\log_{10} T. \quad (3.22)$$

The density of atoms reads

$$n = \frac{P(T)}{k_B T},\tag{3.23}$$

with  $k_B$  denoting the Boltzmann constant. The optical density is given by

$$\alpha(T) = n\sigma(T),\tag{3.24}$$

where

$$\sigma(T) = \frac{\omega_0 \tau(T) \mu^2}{2\epsilon_0 c\hbar},\tag{3.25}$$

with  $\mu=1.4646\times 10^{-29}~{\rm C}\cdot{\rm m}$  denoting the effective dipole moment of the D1 transition under the conditions of large detuning,  $\omega_0$  the angular frequency of this transition, and  $\tau(T)$  the Doppler-broadened lifetime of the excited state. The latter is given by [145]

$$\tau(T) = \frac{1}{\Delta(T)},\tag{3.26}$$

with

$$\Delta(T) = \frac{2\omega_0}{c} \sqrt{\frac{2k_B T}{m}},\tag{3.27}$$

where the  $^{87}{\rm Rb}$  mass is  $m=1.443\times 10^{-25}\,$  kg. In the relevant range of temperatures between  $86\,^{\circ}{\rm C}$  and  $188\,^{\circ}{\rm C}$  we have  $\tau(T)$  ranging from  $215\,{\rm ps}$  to  $240\,{\rm ps}$ .

With these quantities at hand, the optical depth is given as the optical density integrated along the interaction path i.e. the  $^{87}{\rm Rb}$  cell length  $L=5\,{\rm cm}$ . Assuming homogeneous optical density along the cell we have

$$OD = \frac{P(T)}{(k_B T)^{3/2}} \frac{\mu^2}{4\epsilon_0 \hbar} \sqrt{\frac{m}{2}} L.$$
 (3.28)

#### 3.6.2 VISIBILITY

We will estimate the local visibility directly from the coincidence maps  $C(\lambda_+, \lambda_-)$  collected in the main experiment. Let us demonstrate the process with the data for a cell temperature of  $T_1 = 188$  °C. Subsequent stages of the data analysis are depicted in Fig. 3.7. The initial map is filtered to mitigate outliers and parceled into squared regions of a chosen side length between 1 nm and 2.5 nm. Within each region, the local visibility is estimated as

$$\mathcal{V}_{i,j}(\mathcal{C}_{i,j}) = \frac{\max \mathcal{C}_{i,j} - \min \mathcal{C}_{i,j}}{\max \mathcal{C}_{i,j} + \min \mathcal{C}_{i,j}}.$$
(3.29)

Further, we calculate the average visibility over the regions i, j which satisfy  $0 \leq \mathcal{V}_{i,j} \leq$  1. This condition filters out regions where the JSI of the initial state is very low, hence no significant data can be collected.

For the analysis with regions of 1 nm side length we get  $\mathcal{V} \approx 0.69 \pm 0.16$ ,  $\mathcal{V} \approx 0.79 \pm 0.12$  and  $\mathcal{V} \approx 0.88 \pm 0.09$  for  $T_1 = 188$  °C,  $T_2 = 174$  °C and  $T_3 = 86$  °C, respectively. The uncertainties correspond to a standard deviation over the regions. For comparison, using classical light (pair of coherent states and averaging the results over the phase between the pair) the maximal attainable visibility of two-photon interference is 50% [150].

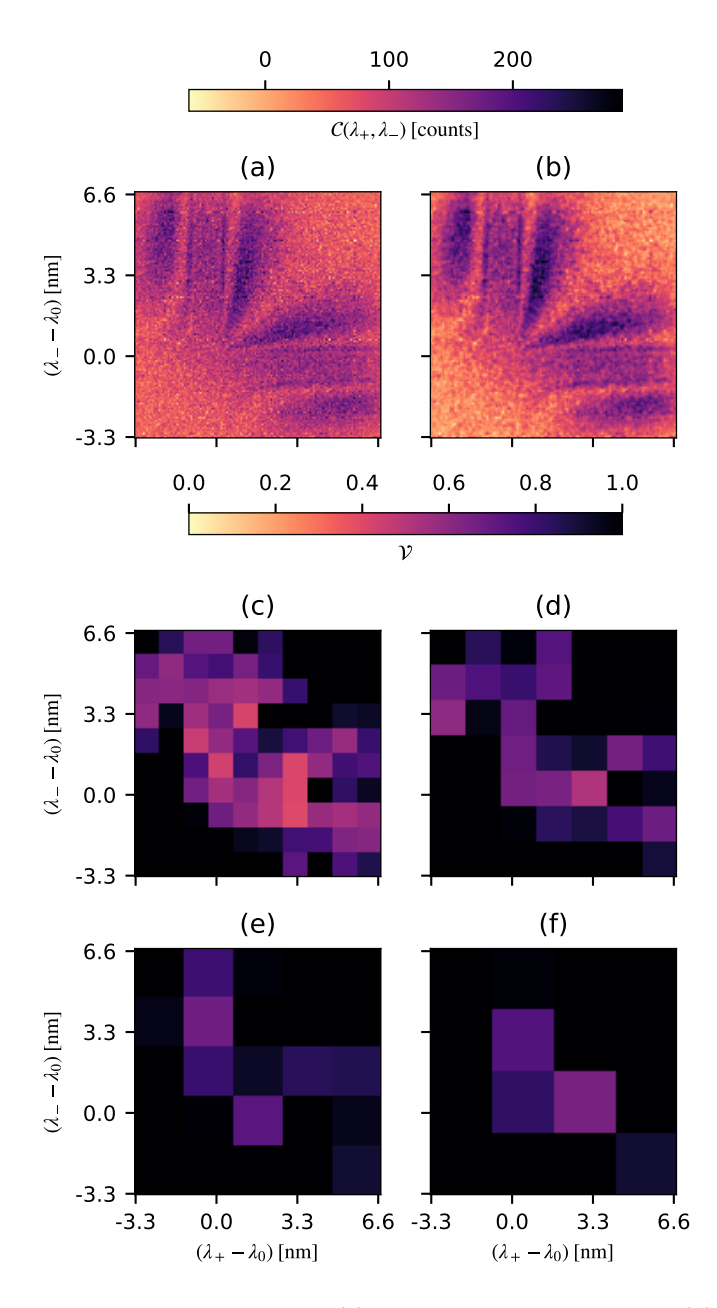


Figure 3.7: Stages of local visibility estimation. (a) The initial coincidence map. (b) The map after Gaussian filtering (Gaussian scale parameter  $\sigma=3.6\times10^{-2}~\mathrm{nm}$ ). (c)-(f) The filtered map is further analyzed in smaller square regions  $\mathcal{C}_{i,j}$  with a side of (c)  $1~\mathrm{nm}$ , (d)  $1.43~\mathrm{nm}$  (d), (e)  $2~\mathrm{nm}$ , (f)  $2.5~\mathrm{nm}$ . In each region, the local visibility is calculated using Eq. (3.29)

# 3.6.3 FIDELITY

For a quantitative comparison between the experimental results and the theoretical prediction, we employ fidelity  $0 \le \mathcal{F} \le 1$  calculated for a pair of maps: a normalized coincidence maps from the experiment  $c(\lambda_+, \lambda_-)$  and the best fit of the theoretical model  $p(\lambda_+, \lambda_-)$ .

Using [146]

$$\mathcal{F} = \sum_{\lambda_{+}, \lambda_{-}} \sqrt{c(\lambda_{+}, \lambda_{-})p(\lambda_{+}, \lambda_{-})}, \tag{3.30}$$

$$c(\lambda_{+}, \lambda_{-}) = \frac{\mathcal{C}(\lambda_{+}, \lambda_{-})}{\sum_{\lambda_{+}, \lambda_{-}} \mathcal{C}(\lambda_{+}, \lambda_{-})},$$
(3.31)

$$p(\lambda_+, \lambda_-) = \frac{P_c(\lambda_+, \lambda_-)}{\sum_{\lambda_+, \lambda_-} P_c(\lambda_+, \lambda_-)}.$$
 (3.32)

we have  $\mathcal{F}$  of 94%, 86% and 89% for  $T_1, T_2$  and  $T_3$ , respectively.

# 3.6.4 Join spectral intensity, uncorrelated and correlated photons

The probability of observing a coincidence  $P_c(\lambda_+, \lambda_-)$ , given by Eq. (3.10), consists of a product of two terms: the interference pattern  $\propto 1 - \cos(\varphi_s(\lambda_+) - \varphi_s(\lambda_-))$  and the join spectral intensity of the initial state  $|\Psi(\lambda_+, \lambda_-)|^2$ . The latter depends on the SPDC source. We will compare simulated coincidence maps with a JSI of our state, and with a JSI for spectrally uncorrelated photons. The two terms (JSI and interference pattern) for these two scenarios are depicted in Fig. 3.8.

For the uncorrelated case, the JSI has a product form

$$|\Psi(\lambda_s, \lambda_i)|^2 = |\Psi_s(\lambda_s)|^2 \times |\Psi_i(\lambda_i)|^2, \tag{3.33}$$

with *s* (*i*) index denoting the signal (idler) photon. For this example, we take a special case

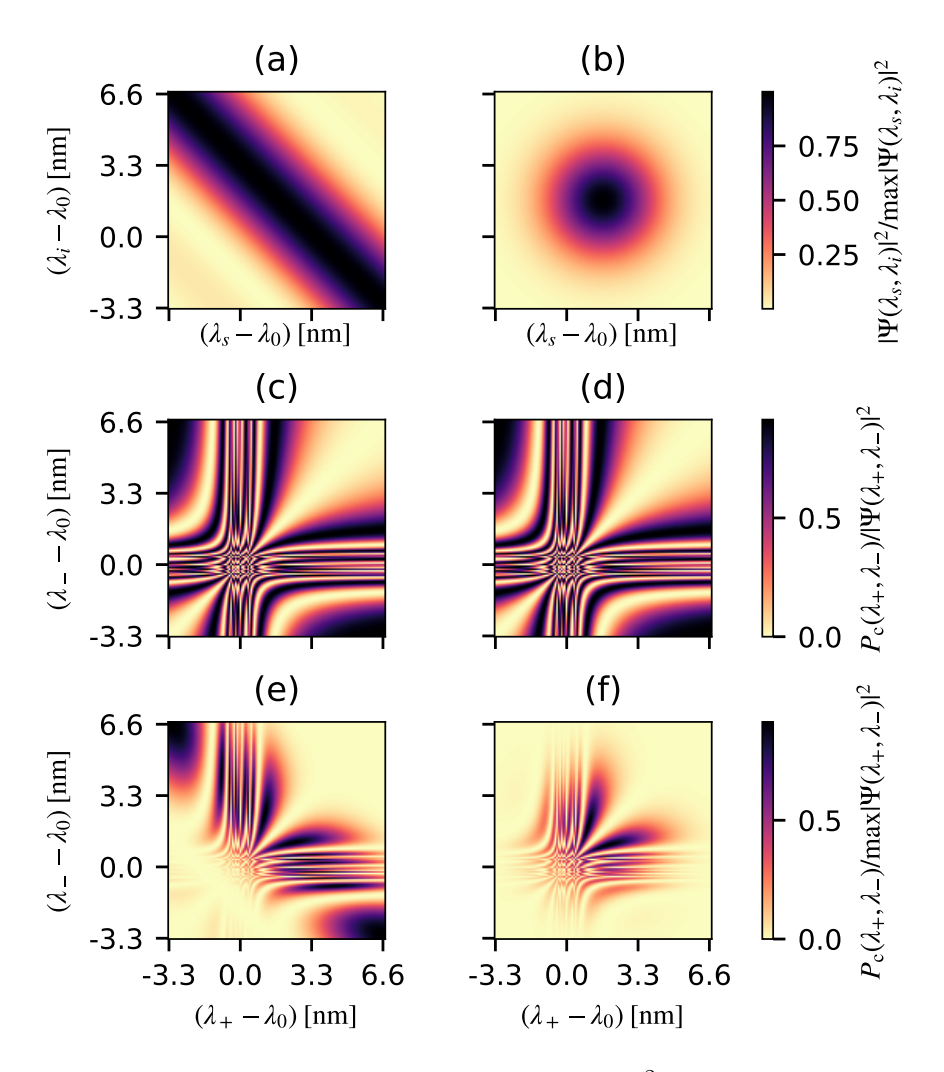


**Figure 3.8:** (a), (b) Simulated joint spectral intensity  $|\Psi(\lambda_+, \lambda_-)|^2$  normalized to a unit maximum, for (a) spectrally correlated photons (b) spectrally uncorrelated photons. (c), (d) The interference pattern which multiplies the JSI to produce final coincidence maps [(e), (f)].

of  $\Psi_s(\lambda)=\Psi_i(\lambda)$ , and assume an isotropic 2-dimensional Gaussian for  $\Psi_s(\lambda)$  with the center at 796.7 nm and the Gaussian scale parameter  $\sigma=1.2$  nm.

Let us note that experimentally the JSI can be measured in a similar setup to our spectrally-resolving two-photon interferometer, albeit without actually interfering the photons. In our polarization-based implementation, the alteration merely amounts to rotating the half-wave plate between the two polarizing beamsplitters of the setup, so that the photons leave

through different ports of the second PBS.

# 3.6.5 Phase reconstruction without prior knowledge

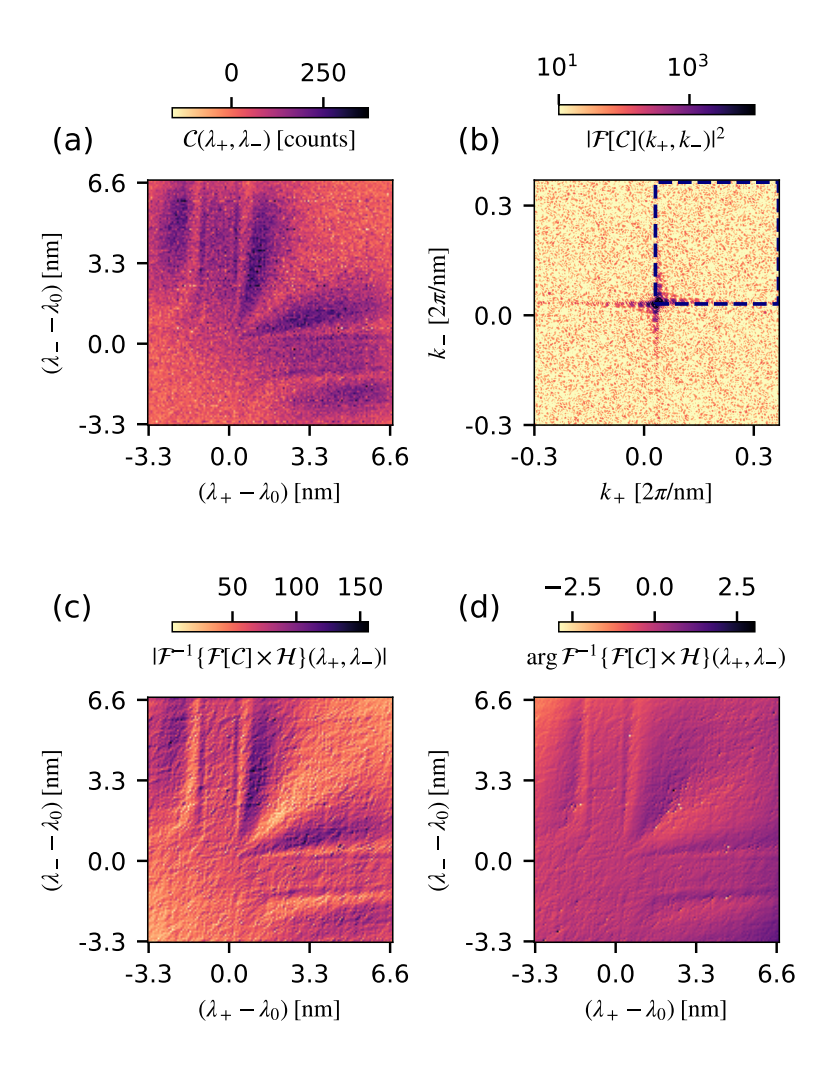


Figure 3.9: (a) Coincidence map collected in the experiment for  $T_1=188\,^\circ$ C. (b) Modulus squared of the map's Fourier Transform. A sharp filter  $\mathcal{H}(k_+,k_-)$  leaves only the part with positive frequencies (dashed rectangle). (c) Modulus and (d) retrieved phase modulo  $\pi$  of the inverse Fourier transform calculated after filtering. Selected units are omitted for clarity.

If no prior information on the structure of the spectral phase  $\varphi(\lambda)$  is assumed, a method to reconstruct this phase from a coincidence map  $\mathcal{C}(\lambda_+, \lambda_-)$  is necessary. In the expression

for the coincidence probability, the total 2-dimensional phase  $\Phi(\lambda_+,\lambda_-)=\varphi(\lambda_+)-\varphi(\lambda_-)$  appears in a cosine term in a form akin to encountered e.g. in holography. Hence, standard methods developed for similar problems can be modified for phase reconstruction. Having the 2-dimensional phase  $\Phi(\lambda_+,\lambda_-)$ , we can fix either of its arguments to get the spectral phase up to an offset e.g. fixing  $\lambda_-$  we get  $\varphi(\lambda_+)$  with an offset given by  $-\varphi(\lambda_-)$ . The offset can be accounted for by observing that for  $\lambda_-=\lambda_+$  the we must have  $\varphi(\lambda_+)=\varphi(\lambda_-)$ . Otherwise, we can also differentiate each of the rows and columns, average the result, and integrate back assuming that sufficiently far from resonance the phase should be 0.

A simple method to reconstruct  $\Phi(\lambda_+, \lambda_-)$  starts with a real-valued 2-dimensional signal  $\propto \cos[\Phi(\lambda_+, \lambda_-)]$  and converts it to its analytical form by taking a Fourier transform, leaving only the positive frequencies and inverting the transform. Hence, we get a complex signal  $\exp[i\Phi(\lambda_+, \lambda_-)]$  which argument corresponds to the reconstructed phase (modulo  $\pi$ )

$$\Phi(\lambda_+, \lambda_-) \mod \pi = \arg \exp[i\Phi(\lambda_+, \lambda_-)]. \tag{3.34}$$

The task of 2-dimensional phase unwrapping is not obvious; nevertheless, it is a commonly encountered problem and state-of-the-art unwrapping methods exist [148].

An alternative method to retrieve  $\Phi(\lambda_+,\lambda_-)$  is to add a known delay  $\delta t$  (on the order of  $10~{\rm ps}$  i.e. a few mm longer optical path) to one of the photons. This will produce equidistant fringes in the coincidence map, which in the Fourier domain shift the signal away from the origin enabling better filtering and more robust reconstruction. The linear spectral phase from the delay together with the unknown phase will produce a signal of the following form

$$\propto \cos[\Phi(\lambda_+, \lambda_-) + k(\lambda_+ - \lambda_-)] \tag{3.35}$$

for some  $k \propto \delta t$ . The linear phase (a shift in the Fourier domain) can be removed by shifting the filtered fragment back to its origin, or by first collecting a reference measurement without the source of  $\varphi(\lambda)$ . The Fourier-domain signal would then be divided by the reference.

A general limitation of the method with linear phase is its limited bandwidth equal at most to twice the Fourier-domain shift (since otherwise the filter would encompass also negative frequencies). Nevertheless, the approach is advantageous in terms of signal-to-noise ratio if the signal in the Fourier domain is fairly localized e.g. a slowly varying or dominantly periodic  $\varphi(\lambda)$ , and hence can be well filtered. In our particular case, the phase changes very rapidly near the resonance and very slowly far away, covering a very large area in the Fourier domain (relative to the scale set by the resolution of the spectrometer).

We performed an exemplary reconstruction of the 2-dimensional phase using the Fourier-filtering method without added delay. The coincidence map is taken from the  $T_1 = 188$  °C dataset. The process is depicted in Fig. 3.9. For filtering we choose a sharp filter  $\mathcal{H}(k_+, k_-) = \Theta(k_+)\Theta(k_-)$ , with  $\Theta(k)$  being the Heaviside Step Function.

# 3.6.6 Two or more photons per pixel

Since a single pixel of our single-photon camera is not photon number resolving, let us consider the possibility of an event when two or more photons should be detected at the same pixel (misclassification).

In the experiment we observe an average of  $\bar{n}\approx 0.2$  photons per frame i.e. per  $A=2\times 5\times 140\,$  px =  $1400\,$  px pixels. Each frame exposure corresponds to  $R=880\,$ laser pulses. On average there is  $\rho=\bar{n}/(RA)\approx 1.6\times 10^{-7}$  photons per px per pulse. The

probability that more than 1 photons in R repetitions will be observed in a single pixel is

$$\mathcal{P} = 1 - [R\rho(1-\rho)^{R-1} + (1-\rho)^R] \approx 10^{-8},\tag{3.36}$$

with the first term in square brackets being the probability of observing one photon and the second term the probability of observing no photons. The average number of misclassifications per frame is given by

$$\mathcal{P} \times A \approx 1.4 \times 10^{-5}.\tag{3.37}$$

Hence, the effect is not very significant.

#### 3.6.7 Comparison with homodyne tomography

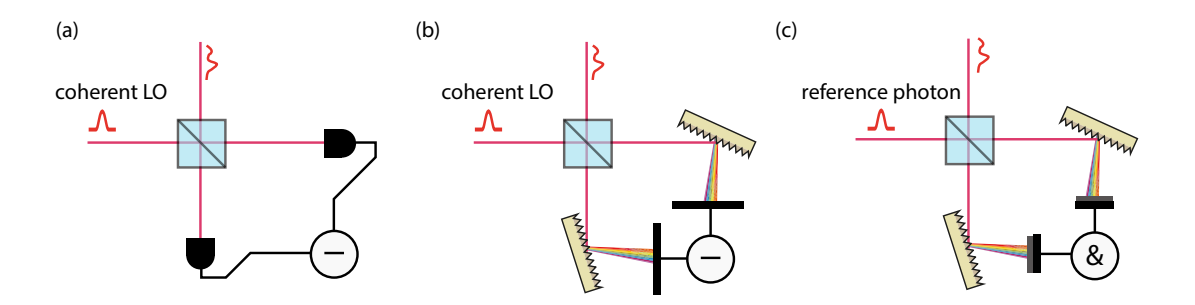


**Figure 3.10:** Schematic depiction of different tomographic techniques in the spectro-temporal domain. (a), (b) balanced homodyne detector with a shaped or swept strong local oscillator (LO) (a) with a bucket detector (b) with a spectrally-resolving multi-pixel detector. (c) Spectrally-resolved two-photon interference. A single reference photon is used. Detectors are photon counting.

We shall briefly compare spectrally-resolved two-photon interference with homodyne detection either with spectral resolution or without, for the task of spectral characterization of a single photon.

As depicted in Fig. 3.10 in all cases the investigated photon is interfered on a balanced

beamsplitter with some kind of a reference state of light.

Figure 3.10 (a) essentially presents a simplified version of the experiment of Costanzo et al. [137]. There the reference is in the form of a strong local oscillator (a coherent state). The detection is in the form of a balanced homodyne detector which consists of two quadratic-response detectors (e.g. photodiodes) observing the beamsplitter outputs, and an electronic subtraction of the signals. Such a homodyne detector measures a selected (with the LO phase relative to the measured optical signal) quadrature of the investigated field [151]. Since the detectors are not spectrally-resolving, the contribution from all spectral components are added to form the detector output i.e. the output signal depends on how closely the spectral mode of the LO matches that of the spectral wavefunction of the investigated photon. Conversely, we can optimize or sweep the shape of the LO to find a good matching and infer the photon's spectral wavefunction shape. Let us note for completeness that since a single photon has a uniform phase distribution, ultimately we measure the homodyne current variance.

Fig. 3.10 (b) extends the homodyne detection with spectrally-resolving detectors. Similarly, as with spectrally-resolved two-photon interference, the added spectral resolution enables localization of the differences between the LO spectral shape and the photon wavefunction. Nevertheless, since the homodyne detector in the best case is shot-noise-limited, it may be challenging to obtain a sufficiently high signal-to-noise ratio with the signal spread over many pixels.

Finally, for reference Fig. 3.10 (c) depicts the spectrally-resolved two-photon interference. We shall now consider homodyne detection and two-photon interference both without spectral resolution. We will consider the photon to be almost identical to the reference (photon or LO) and try to estimate the residual distinguishability. This is a vast simplification relative to the experimental setup; nevertheless, being analytically tractable it will allow

us to compare homodyning and two-photon interference on the grounds of asymptotic estimation theory.

#### Homodyne detection

Let us begin with a more quantitative description of the homodyne measurement. We define the indistinguishability  $\xi$  between the LO mode  $\psi_{LO}(\lambda)$  and the photon wavefunction  $\psi_s(\lambda)$ 

$$\xi = \left| \int d\lambda \, \psi_s(\lambda) \psi_{LO}(\lambda)^* \right|^2. \tag{3.38}$$

Assuming the mode functions have identical modules and only differ in a phase profile we have  $\varphi_s(\lambda)$  we get:

$$\xi = \left| \int d\lambda \, |\psi_s(\lambda)|^2 \exp(i\varphi_s(\lambda)) \right|^2. \tag{3.39}$$

Homodyning measures a selected quadrature. Since the photon has a uniform phase distribution, all quadratures are equiprobable. The probability of observing a given quadrature is given by [7]:

$$P_1(x) = \frac{1}{2\sqrt{\pi}} H_1(x)^2 \exp(-x^2), \tag{3.40}$$

with  $H_1(x)$  denoting the first Hermite polynomial and where we use dimensionless quantities. Let us simulate the distinguishability of the signal photon and the LO by inserting a beamsplitter in the path of the signal photon. The beamsplitter couples a vacuum component and introduces loss [152]. This way, the probability density of vacuum along any quadrature reads:

$$P_{vac}(x) = \frac{1}{\sqrt{\pi}} \exp(-x^2). \tag{3.41}$$

Finally, the measurement outcomes (homodyne current values) are distributed according to

$$P(x) = \xi P_1(x) + (1 - \xi) P_{vac}(x). \tag{3.42}$$

#### Two-photon interference without spectral resolution

For two-photon interference without spectral resolution let us define the indistinguishability V as

$$V = \iint d\lambda_+ d\lambda_- \psi_s(\lambda_+) \psi_r(\lambda_+)^* \psi_s(\lambda_-)^* \psi_r(\lambda_-), \qquad (3.43)$$

with  $\psi_s$ ,  $\psi_r$  denoting the spectral wavefunction of the signal and reference photons, respectively. Note that compared with the homodyne case we have  $\xi = V$ . With equal modules of the wavefunctions and merely a phase profile difference  $\varphi_s(\lambda)$ , we get

$$V = \iint d\lambda_{+} d\lambda_{-} |\psi_{s}(\lambda_{+})\psi_{s}(\lambda_{-})|^{2} \exp\left[i(\varphi_{s}(\lambda_{+}) - \varphi_{s}(\lambda_{-}))\right].$$
 (3.44)

The probability of detecting a coincidence between bucket single-photon detectors is then

$$P_c = \frac{1}{2}(1 - \mathcal{V}V),\tag{3.45}$$

with V denoting the intrinsic interference visibility (e.g. due to setup imperfections). If we assume perfect detectors (i.e. no losses, no dark counts), in a single repetition of the measurement we can observe at most a single coincidence, so there are two measurement outcomes: no coincidence with a probability  $P_0 = 1 - P_c$  or a coincidence with probability  $P_c$ .

Without dark counts, we can express the intrinsic interference visibility  ${\cal V}$  in terms of the

detections efficiency  $\eta$  and SPDC excitation probability  $\chi$  as [153]

$$\mathcal{V} = 2\left[ (\eta - 2)^2 \chi - 4 \right] \times \frac{\left[ (\eta - 1)^2 \chi - 1 \right] \left[ \frac{4 - 4\chi}{(\eta - 2)^2 \chi - 4} + \sqrt{\frac{\chi - 1}{(\eta - 1)^2 \chi - 1}} \right]}{\eta^2 \chi \left\{ \left[ (\eta - 6)\eta + 6 \right] \chi + 2 \right\}}.$$
 (3.46)

Assuming experimentally feasible values  $\eta = 90\%$ ,  $\chi = 1.5 \times 10^{-2}$ , we have  $\mathcal{V} \approx 99\%$ .

## Comparison on the grounds of estimation theory

With the measurements described, we can employ the asymptotic estimation theory to compare the bounds on the estimation precision of the indistinguishability for both schemes.

Intuitively, since the homodyne case will involve maximization of an inherently noisy homodyne current variance, while the two-photon interference will involve the minimization of the coincidence count, in the regime of small residual indistinguishability  $\alpha=1-\xi=1-V\ll 1 \text{ we expect better performance for the latter.}$ 

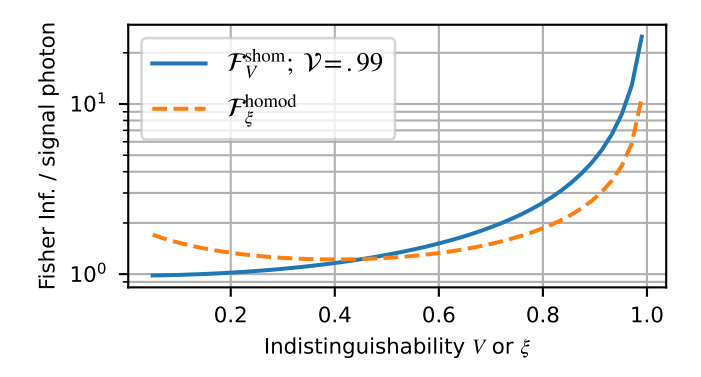


Figure 3.11: Fisher information per signal photon  $F_{\xi}$ ,  $F_V$  for the task of estimating the indistinguishability between the signal photon and a reference. (shom, V) For two-photon interference. (homod,  $\xi$ ) For homodyning. The intrinsic interference visibility for two-photon interference was taken as  $\mathcal{V}=99\%$ .

The variance of any locally unbiased estimator  $\hat{V}$  is limited by the Cramér–Rao bound:

$$\Delta^2 \hat{V} \ge F_V^{-1},\tag{3.47}$$

with  $F_V$  denoting the Fisher information per single signal photon given by [154]

$$F_V = (\partial_V \log P_c)^2 P_c + (\partial_V \log P_0)^2 P_0 = \frac{V^2}{1 - V^2 V^2}.$$
 (3.48)

In the homodyne case, the Fisher information per signal photon is given by

$$F_{\xi} = \int \mathrm{d}x \left[ \partial_{\xi} \log P(x) \right]^{2} P(x), \tag{3.49}$$

which can be expanded to

$$F_{\xi} = -\frac{\sqrt{2\pi}e^{\frac{1}{2}(\frac{1}{\xi}-1)}\sqrt{\frac{1}{\xi}-1}\text{erfc}\left(\frac{\sqrt{\frac{1}{\xi}-1}}{\sqrt{2}}\right) + 2\xi - 2}{2(\xi-1)\xi^2},$$
(3.50)

with  $\operatorname{erfc}(x) = 1 - \operatorname{erf}(x)$  and  $\operatorname{erf}(x)$  being the error function.

The comparison of Fisher information for these two measurement schemes has been depicted in Fig. 3.11 in the logarithmic scale. Note that for small residual distinguishability  $V=\xi\approx 1$  the two-photon interference outperforms the homodyning. The exact advantage depends on the intrinsic visibility level  $\mathcal V$ . In this regime, the formulae can be series expanded in  $\alpha=1-V=1-\xi\ll 1$  to observe the scaling. We have for homodyning

$$F_{\alpha} \sim \alpha^{-1/2} \tag{3.51}$$

while for the two-photon interference, the scaling is significantly improved

$$F_{\alpha} \sim \alpha^{-1}.\tag{3.52}$$

Anecdotally, these scalings are similar to the well-known standard quantum limit and the Heisenberg scaling.

Finally, let us note that in a general scenario of unknown V or  $\xi$  a hybrid adaptive method combining homodyning and two-photon interference could be beneficial.

## 3.7 Conclusion

In this Chapter, we have described an experimental method to probe a spectral phase of a single photon wavefunction. The method is based on a two-photon interferometer whose outputs are observed with a spectrally-resolving single-photon detector. The method compares the spectral wavefunction of the signal (interrogated) photon with a reference photon. If the signal is made to interact with a sample (in our case a hot  $^{87}$ Rb vapor) prior to entering the setup, the method can be regarded as a form of dispersive spectroscopy. The basic idea of spectrally-resolved two-photon interference is the extension of the Hong-Ou-Mandel effect with the ability to observe where the differences between the wavefunction are in the spectral degree of freedom i.e. resolving the coincidence rate in this DoF.

We have presented a proof-of-principle experiment together with a simple theoretical description. A good agreement with the theory was observed. Further, we analyzed the method's performance and metrics, discussed the role of the spectral correlations between the initial pair of photons, and proposed general phase reconstruction methods. Finally, in the framework of asymptotic estimation theory, we compared the simplified two-photon interference scheme with an equivalent homodyne measurement. The advantage of the for-

mer was demonstrated in the regime of small deviations of the signal spectral wavefunction shape from the reference.

This experiment can be regarded as demonstrating a unique combination of fundamental phenomena (single-photon zero-area pulses, Hong-Ou-Mandel effect, bandwidth-mismatched interaction) but also as a proof-of-principle demonstration of non-destructive spectroscopic sensing. Potentially, it may be also of interest for spectrally probing ultrafast transient phenomena, such as picosecond-scale chemical reactions, since the signal photon is in a very short temporal mode.

[This page intentionally left blank]

4

# Variable shearing interferometry

# 4.I FOREWORD

Hitherto our experiments were concerned with non-classical light. Here we turn to classical coherent states. Sometimes they will be highly attenuated so that the average number of photons per mode is relatively close to 1. In such scenarios, we should refer to the *single-photon level*.

Characterization of ultrafast pulses is a long-standing problem. The duration of a  $100\,\mathrm{fs}$ 

and even a  $10 \,\mathrm{ps}$  pulse is way too short to directly measure even the temporal intensity (although the research on fast photodetectors is very active, for instance in ref. [155] authors demonstrated  $265 \,\mathrm{GHz}$  bandwidth at telecom wavelengths). Ideally, we would like to know not only the intensity but also the phase profile, i.e. characterize the complex electric field envelope in time.

A plethora of methods have been developed to accomplish this task with probably the most widespread being Spectral Phase Interferometry for Direct Electric-field Reconstruction (SPIDER) [156], Frequency-Resolved Optical Gating (FROG) [157], and their variants [158, 159]. Both methods employ non-linear optical interactions. FROG is a spectrographic method, while SPIDER is based on interferometry. Another interferometric method – electro-optic shearing interferometry (EOIS) – is linear (in optical fields) and employs electro-optic modulation instead of optical non-linear processes. The advantage is higher sensitivity in the regime of single-photon level light, stemming mainly from the lack of optical noise introduced in the non-linear interactions and avoiding their low conversion efficiency. EOSI was first proposed by Wong and Walmsley [160] and around 20 years later demonstrated at the single-photon level [161–163].

Compared to FROG, SPIDER and EOSI scale better in terms of the measurement time. Roughly for N temporal points at which the pulse is probed, FROG requires  $\mathcal{O}(N^2)$  measurements and SPIDER or EOSI only  $\mathcal{O}(N)$ . The advantage is due to the 2-dimensional scan required in FROG and only a 1-dimensional for SPIDER and EOSI. Of course, as with any scaling, the constant factor may be more significant in a given scenario.

Focusing on the near-infrared wavelengths (e.g. 795 nm) and the single-photon level light, the most compatible method of the 3 is EOSI. However, in these circumstances, EOSI would require a single-photon-sensitive spectrometer working in near-infrared. It is certainly possible as demonstrated e.g. by our camera (albeit with low efficiency) or time-

of-flight spectrometers [164] which however require a custom-made chirped fiber Bragg grating (CFBG) prepared for a specific wavelength.

In this chapter, we explore an alternative approach with the potential of reducing the cost and complexity of the characterization setup. The method, which we call Variable Shearing Interferometry (VarSI) is, in essence, similar to EOSI, but employs a measurement of the second-order intensity correlation between both interferometer outputs instead of a spectrally-resolved measurement of a single output. Furthermore, as later described in detail, the spectral shift introduced by the electro-optic modulation needs to be scanned (hence a 2-dimensional scan is required).

The majority of the experimental work described in this chapter was carried out by Stanisław Kurzyna and Marcin Jastrzębski (at that time BSc students). We were supported on the theoretical side by Nicolas Fabre and on the experimental/technical side by Wojciech Wasilewski. Michał Parniak conceived the idea and supervised the project at a higher level. Finally, the author of this thesis supervised the works at a more operational level, built parts of the setup; wrote parts, and supported the development of the experiment control and measurement software and data analysis; and wrote substantial parts of the manuscript.

Let us note that in parallel another method of ultrashort pulse characterization based on spectral shift scanning was independently developed by Golestani *et al.* [165]. The authors call the method Fourier transform Chronometry and demonstrate the measurement of the ultrashort pulse width by scanning spectral shifts.

This chapter is based on ref. [166].

#### 4.2 Introduction

Although many methods of ultrashort pulse characterization have been described and demonstrated, the task remains challenging. This is especially true for the single-photon regime. Here we introduce a new method that directly measures the modulus of the short-time Fourier transform (STFT) of the pulse.

The method is based on a measurement of the second-order intensity correlation function between the two outputs of a Mach-Zehnder-type interferometer. The interrogated pulse enters the interferometer to be equally split into both arms. One arm contains a controlled delay (e.g. motorized free-space delay line) while the second arm, an equivalent operation in frequency i.e. spectral shift (implemented via time-dependent electro-optic phase modulation). Spectral shift is the most challenging part of the setup. It is implemented by imposing an optical phase that linearly changes in time (a direct result of time and frequency being Fourier-conjugate variables, sometimes referred to as the "Fourier Shift Theorem"). In practice, the linear modulation is implemented with a sinusoidal waveform driving the electro-optic modulator (EOM) and by synchronizing the optical pulse with the linear part of the sinusoid. Roughly a shift comparable to the spectral bandwidth of the pulse is necessary, which requires high modulation frequency and high amplitude (power).

For each setting of the delay and spectral shift, the second-order intensity correlation gives a single point of the STFT modulus squared. The complex electric field of the pulse can be then reconstructed using a modification of a standard algorithm (and with certain ambiguities).

Notably, since VarSI is based on the second-order intensity correlation measurement, it remains insensitive to the phase fluctuations between the interferometer arms. In the bright light regime, the measurement is equivalent to estimating the visibility of the fringes.

We experimentally demonstrate VarSI in the near-infrared (795 nm) including the electric field reconstruction for bright pulses and for weak single-photon level light.

# 4.3 THEORY

# 4.3.I IDEA OF VARSI

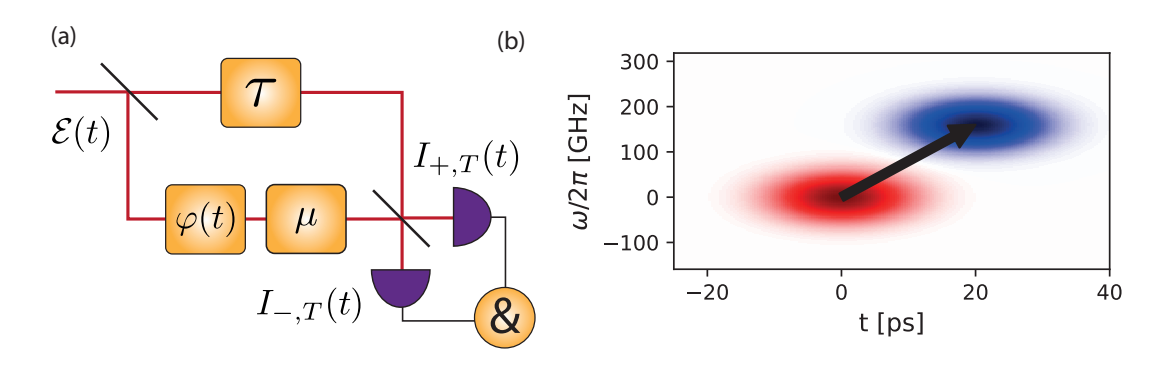


Figure 4.1: (a) Simplified schematic of a VarSI interferometer. The interrogated pulse with electric field  $\mathcal{E}(t)$  enters the interferometer and is split on a balanced beamsplitter (BS) into its two arms. One arm includes a controlled delay  $\tau$ , and the other a spectral shift  $\mu$ . Interferometric phase between the arms is accounted for by  $\varphi(t)$ . After temporal and spectral shifts the pulses are interfered on a second BS. Outputs of the interferometer are observed with quadratic photodetectors (photodiodes or single-photon-counting detectors). Assuming a quickly fluctuating phase  $\varphi(t)$ , the second-order intensity correlation function  $g^{(2)}(\mu,\tau)$  for a certain setting of  $(\mu,\tau)$  corresponds to the modulus squared of the self-gated short-time Fourier transform  $\left|\mathcal{S}_{\mathcal{E}(t)}(\mu,\tau)\right|^2$ . (b) Depiction of the temporal and spectral shift operations on the chronocyclic Wigner function of a coherent state (red - prior, blue - posterior).

A simplified setup for VarSI is depicted in Fig. 4.1. Alike other methods based on spectral shearing, the interrogated pulse with the electric field  $\mathcal{E}(t)$  is split into two parts. One is delay by  $\tau$ , yielding  $\mathcal{E}(t-\tau)$ . The other is shifted in frequency by  $\mu$  which gives  $\mathcal{E}(t)e^{i\mu t}$ . The pulses interfere on a balanced beamsplitter (BS) and exit the interferometer through the  $\pm$  ports. In EOSI one of the outputs would be observed with a spectrometer. However, in VarSI both outputs are only monitored with bucket detectors. Notably, the bandwidth

of the detectors can be very low. It is only necessary to resolve in time the interferometric phase  $\varphi(t)$  fluctuations. We will assume that the detectors are averaging the signal over a timescale T much longer than the pulse duration.

# 4.3.2 Classical case – analyzing fringe visibility

Let us start with the strong light regime. We will assume that the detectors (photodiodes) at  $\pm$  ports produce a signal proportional to the time-integrated optical intensity

$$I_{\pm} \equiv I_{\pm,T}(t) \propto \int_{t-T/2}^{t+T/2} \mathrm{d}t' \left| \mathcal{E}_{\pm}(t') \right|^2.$$
 (4.1)

Fixing the interferometric phase  $\varphi$  we can expand this equation

$$I_{\pm} \propto \int_{-\infty}^{+\infty} dt |\mathcal{E}(t)|^2 + \int_{-\infty}^{+\infty} dt |\mathcal{E}(t-\tau)|^2 \pm 2\mathcal{V} \operatorname{Re} \left( e^{i\varphi} \int_{-\infty}^{+\infty} dt \, \mathcal{E}(t) \mathcal{E}^*(t-\tau) e^{i\mu t} \right), \tag{4.2}$$

with  $0 \leq \mathcal{V} \leq 1$  denoting the intrinsic visibility of the interference. For clarity of the reasoning, we will assume  $\mathcal{V}=1$  and note that this assumption does not change the qualitative result.

In Eq. (4.2) all relevant information is contained in the last term (interference term). In particular, it can be directly expressed as the self-gated short-time Fourier transform

$$S_{\mathcal{E}(t)}(\mu,\tau) = \frac{1}{\sqrt{2\pi}} \int_{-\infty}^{+\infty} dt \mathcal{E}(t) \mathcal{E}^*(t-\tau) \exp(i\mu t). \tag{4.3}$$

In a more general scenario, let us consider incoherent states of light characterized by the

first-order coherence function

$$g^{(1)}(t,\tau) = \langle \mathcal{E}(t)\mathcal{E}^*(t-\tau)\rangle,\tag{4.4}$$

with  $\langle \cdots \rangle$  denoting an average over a statistical ensemble. We then have the following relation between the STFT and  $g^{(1)}$ .

$$\mathcal{S}_{\mathcal{E}(t)}(\mu,\tau) = \frac{1}{\sqrt{2\pi}} \int_{-\infty}^{+\infty} \mathrm{d}t \, g^{(1)}(t,\tau) e^{i\mu t}. \tag{4.5}$$

Hence, VarSI can be applied regardless of the coherence of light.

To measure a 2-dimensional map of the STFT modulus squared, we will scan the delay  $\tau \in \{\tau_j\}_{j=1...M}$  and the spectral shift  $\mu \in \{\mu_k\}_{k=1...N}$ . The interference term of Eq. (4.2) can be isolated by taking the difference between the intensities observed at the  $\pm$  ports  $I_+^{(j,k)} - I_-^{(j,k)}$ . Importantly, we will assume that  $\varphi$  fluctuates slowly relative to the averaging time of the detectors T and has a uniform probability distribution. We observe a time trace of the detector signal covering the whole range of  $\varphi$ . Calculating the standard deviation and averaging over the phase we essentially obtain the measured interference visibility (relative to the intrinsic visibility)

$$\sqrt{\langle [\operatorname{Re}(e^{i\varphi}\mathcal{S}_{\mathcal{E}(t)}(\mu_k, \tau_j))]^2 \rangle_{\varphi}} = |\mathcal{S}_{\mathcal{E}(t)}(\mu_k, \tau_j)|^2, \tag{4.6}$$

equivalent to the squared modulus of the STFT evaluated at  $(\tau_j, \mu_k)$ . The measurement is then repeated for  $M \times N$  points.

### 4.3.3 SINGLE-PHOTON-LEVEL PULSES

We shall now consider the scenario of dim light (single-photon level) where the interference fringes cannot be directly observed (in contrast to Eq. 4.2). In other words, not enough light can be collected for a reasonable signal-to-noise ratio within a time period when the phase  $\varphi(t)$  remains relatively stable. We note that from the experimental perspective, rapid scanning of the time delay (motorized delay line) introduces substantial phase instability, and complicates any potential stabilization.

In this case, we will consider the second-order intensity correlation function  $g^{(2)}(\mu, \tau)$  requiring only (again) that  $\varphi(t)$  remains stable for approximately the inverse of the photodetector bandwidth T. Henceforth dropping the (j,k) indices, for each pair of shift  $(\mu, \tau)$  we average the product of detector intensities  $\langle I_+(t)I_-(t)\rangle_{\varphi}$  to get

$$g^{(2)}(\mu,\tau) = \frac{\langle I_{+,T}(t;\mu,\tau)I_{-,T}(t;\mu,\tau)\rangle_{\varphi}}{\langle I_{+,T}(t;\mu,\tau)\rangle_{\varphi}\langle I_{-,T}(t;\mu,\tau)\rangle_{\varphi}} = 1 - \frac{1}{2}\mathcal{V}\frac{\left|\mathcal{S}_{\mathcal{E}(t)}(\mu,\tau)\right|^{2}}{\left(\int_{-\infty}^{+\infty} dt |\mathcal{E}(t)|^{2}\right)^{2}}, \tag{4.7}$$

where the average is again taken over the uniform distribution of  $\varphi$ . The factor of 1/2 appears from the phase averaging. It reflects a general behavior – the visibility in the second-order interferometry is limited to a maximum of 1/2 for coherent states. For the full derivation of Eq. (4.7) see section 4.6.1.

### 4.3.4 Exemplary simulated spectrograms

For a quantitative overview of how the collected spectrograms (modulus square of STFT) may look, we present an exemplary numerical calculation in Fig. 4.2. Gaussian shape of the temporal pulse envelope is assumed. Cases of a positive/negative chirp (second order spectral phase) and of third order spectral phase are depicted. We note that while the sign of the

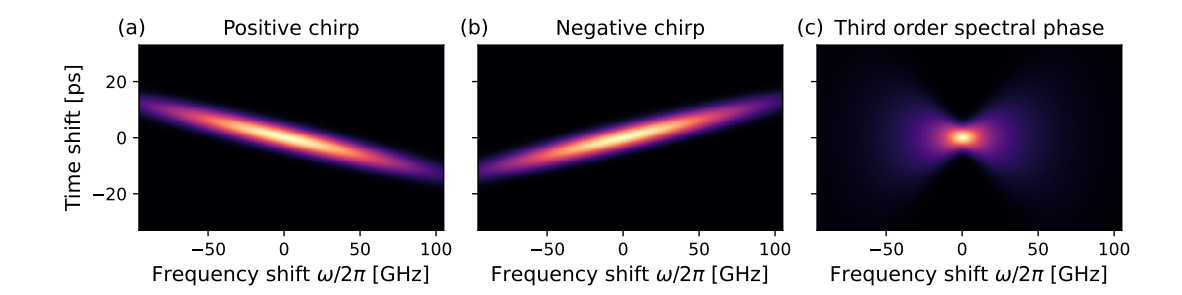


Figure 4.2: Exemplary simulated spectrograms (modulus squared STFT  $\left|\mathcal{S}_{\mathcal{E}(t)}(\mu,\tau)\right|^2$ ) calculated numerically for Gaussian pulses. (a) Positively chirped pulse. (b) Negativey chirped pulse. (c) Pulse with a third-order spectral phase.

second-order spectral phase can be directly inferred from the map, it remains ambiguous for the third-order phase.

### 4.3.5 RELATION TO CHRONOCYCLIC WIGNER FUNCTION

Self-gated STFT is one of the bilinear time-frequency distributions (also known as Cohen's class distributions) [167]. As such it is directly connected to the Chronocyclic Wigner Function (CWF) which is more widely recognized and used in optics. CWF has many intuitive properties and provides useful visualizations of the spectro-temporal mode structure and its transformations [168].

With the CWF defined as

$$W(\omega, t) = \frac{1}{2\pi} \int_{-\infty}^{+\infty} dt' \, \mathcal{E}\left(t + \frac{t'}{2}\right) \mathcal{E}^*\left(t - \frac{t'}{2}\right) e^{i\omega t'},\tag{4.8}$$

the relation between STFT and CWF is via a two-dimensional Fourier transform and multiplication by a phase term:

$$S_{\mathcal{E}(t)}(\mu,\tau) = \sqrt{2\pi} \mathcal{F}_{t \to \mu} [W(\omega,t)] e^{-\frac{i\mu\tau}{2}}.$$
 (4.9)

This way, the modulus squared reads

$$\left| \mathcal{S}_{\mathcal{E}(t)}(\mu, \tau) \right|^2 = 2\pi \mathcal{F}_{\substack{t \to \mu \\ \omega \to \tau}} [W(\omega, t)] \mathcal{F}_{\substack{t \to \mu \\ \omega \to \tau}}^* [W(\omega, t)], \tag{4.10}$$

which can be further simplified using the convolution theorem

$$\left| \mathcal{S}_{\mathcal{E}(t)}(\mu, \tau) \right|^2 = 2\pi \mathcal{F}_{\substack{t \to \mu \\ \omega \to \tau}} [W_{\mathcal{E}(t)}(\omega, t) * W_{\mathcal{E}(-t)}(\omega, t)]. \tag{4.11}$$

Hence, the STFT modulus squared is just the two-dimensional Fourier transform of a convolution between a CWF of the pulse and a CWF of a time-reversed pulse.

### 4.3.6 The reconstruction of the pulse complex electric field

The mapping of the pulse electric field to the spectrogram

$$\mathcal{M}: \mathcal{E}(t) \to \left| \mathcal{S}_{\mathcal{E}(t)}(\mu, \tau) \right|^2$$
 (4.12)

is not directly invertible. Nevertheless, the problem of finding  $\mathcal{E}(t)$  given  $\left|\mathcal{S}_{\mathcal{E}(t)}(\mu,\tau)\right|^2$  is mathematically equivalent to the standard inverse problem encountered in radar remote sensing. As this is an active area of research, a range of good algorithms exist and the reconstruction ambiguities are well-understood [169].

Assuming  $\mathcal{E}(t)$  described a time-limited pulse (i.e. with finite support) the ambiguities encompass only:

- 1. global phase,
- 2. reflection,
- 3. spectral or temporal shift,

with the last two equivalently corresponding to the sign of the cubic and linear spectral phase, respectively.

For the complex electric field reconstruction we modify the COPRA phase retrieval algorithm developed and described by Geib *et al.* [170]. The original algorithm was developed for non-linear interferometric schemes of pulse characterization. As such it required modifications to work with our form of the spectrogram. The details are described in section 4.6.2.

### 4.4 EXPERIMENTAL SETUP

The experimental setup for VarSI has been depicted in Fig. 4.3. The test pulse is prepared by spectrally filtering a 100 fs pulse from a Ti:Sapphire laser (SpectraPhysics MaiTai). The filtering is implemented by mapping the spectral components onto transverse dimension with a diffraction grating, far-field imaging the grating onto a slit with regulated width, and reversing the process. The temporal delay  $\tau$  is implemented via a motorized single-pass delay line (moving a collimator). The spectral shift  $\mu$  is obtained by modulating the temporal phase of the signal light with an EOM. The optical pulse needs to be aligned with the linear part of the EOM driving waveform. The driving waveform is formed by synchronizing a high-frequency (15 GHz) generator to the original optical pulses repetition (80 MHz). Interferometric phase averaging is ensured by placing a mirror on a piezo actuator inside the interferometer. For photon counting, we use superconducting detectors (idQuantique ID281). For bright-light measurements above 100  $\mu$ W we observe the root-mean-square of the fringes visibility over one period of the piezo oscillation, to obtain  $\left|\mathcal{S}_{\mathcal{E}(t)}\right|^2$ . The exemplary signals in this regime are depicted in Fig. 4.4

For measurement at the single-photon level neutral-density filters are introduced to at-

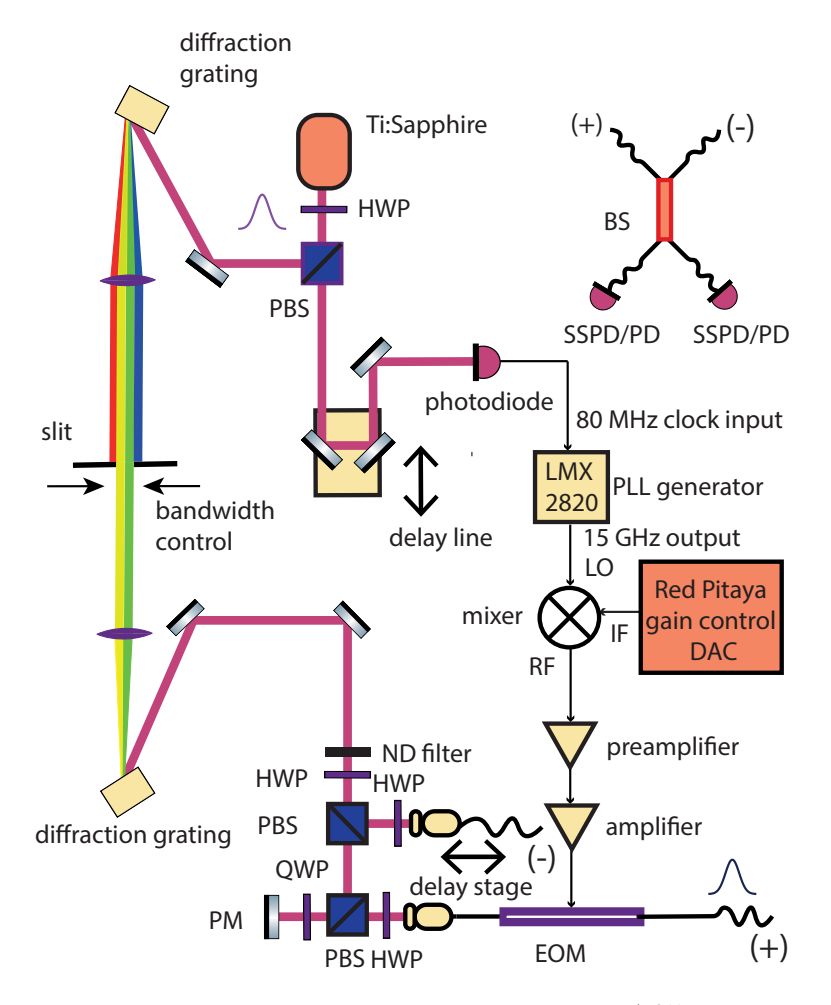
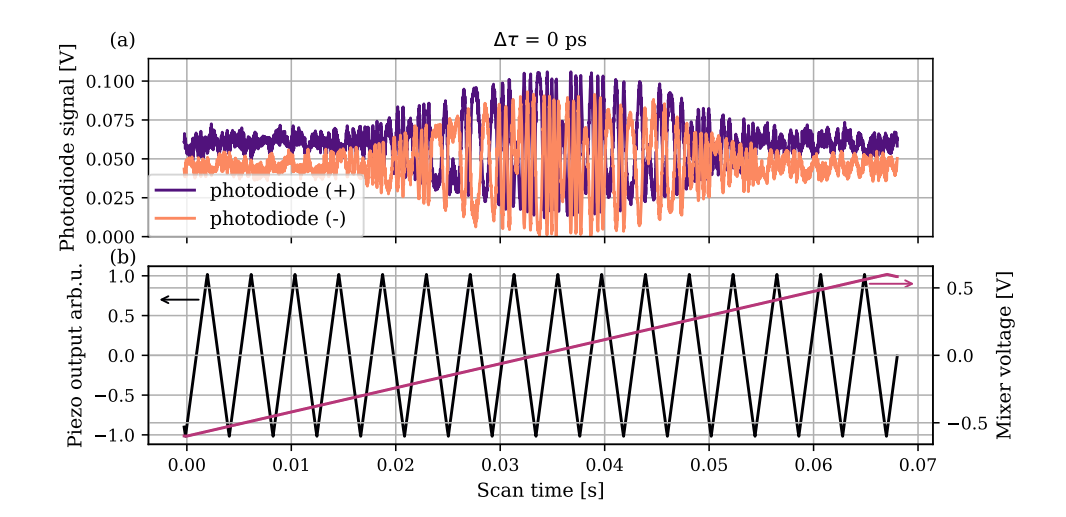


Figure 4.3: Schematic of the VarSI experimental setup. Near-infrared ( $795\,\mathrm{nm}$ ) pulses ( $100\,\mathrm{fs}$ ) from a Ti:Sapphire laser are spectrally filtered (in the range of  $48\,\mathrm{GHz}$  to  $96\,\mathrm{GHz}$ ) with a 4f setup consisting of a pair of diffraction gratings and a telescope with a slit of controlled width placed in the Fourier plane. The filtered pulse is attenuated to the single-photon level (ca.  $100\,\mu\mathrm{W}$ ) with neutral-density (ND) filters and enters the main VarSI interferometer implemented in a hybrid of free space and fiber. The delay line within the interferometer consists of moving a collimator along the propagation direction with a stepper-motor-driven stage. The spectral shift is implemented with an electro-optic phase modulator (EOM). Additionally, in one of the arms a mirror is mounted on a piezoelectric actuator (PM) which is continuously driven with a single tone to ensure proper averaging over  $\varphi$ . Polarizations are adjusted with half-wave plates (HWP) to match the axes of the EOM and the polarization-maintaining fibers. The final beamsplitter (BS) of the interferometer is implemented in fiber. For detection, we use either superconducting single-photon detectors (SSPDs) or photodiodes (PD). The radio frequency (RF) signal driving the EOM is obtained by optically driving a photodiode with a fraction of the original femtosecond light. The photodiode signal is amplified and clocks the high-frequency generator. The generator's output is variably attenuated with a mixer, amplified, and drives the EOM.



**Figure 4.4:** (a) Signal from phototiodes observing the  $\pm$  ports. Interference fringes are clearly visible. In this example, the temporal delay is set to  $\tau=0$ , while the spectral shift is scanned by altering the mixer voltage. (b) Piezoactuator driving signal (black) and mixer voltage (magenta) across the scan.

tenuate the signal to ca.  $\bar{n} = 0.013$  photons per pulse (at the detection stage).

We note that it is more convenient to scan over all frequency shifts (mixer voltage – an electronic signal change) for each setting of the delay (stage position – a mechanical change).

### 4.4.I EOM AND RF SETUP

The EOM driving signal is obtained from a high-frequency (15 GHz) sine generator synchronized with the laser repetition rate (80 MHz). The synchronization is achieved using a phase-locked loop (PLL). A small fraction of the original optical pulses (ca. 30 mW of average power) goes through a double-pass motorized delay and excites a fast photodiode (PD). The amplified signal from PD (ca. 2 V peak-to-peak) enters the clock input of a PLL generator (Texas Instruments LMX2820). A high stability of the phase lock is necessary to obtain a repeatable spectral shear. The output signal of the PLL is set to a frequency of

exactly  $184 \times 80 \, \mathrm{MHz} = 14\,720 \, \mathrm{MHz} \approx 15 \, \mathrm{GHz}$  and has a power of  $-2.3 \, \mathrm{dBm}$ . To implement variable attenuation the signal is sent to a mixer (Mini-Circuits ZX05-24MH-S+) and enters the LO input. A DC voltage on the IF input of the mixer controls the signal amplitude at the RF port output. Since the IF input must be DC-coupled by design, the control voltage must applied with care in order to avoid overvoltage which could damage diodes or transformers of the mixer. The output signal is further amplified (Mini-Circuits ZX60-06183LN+ and ZVE-3W-183+) and drives the EOM. The mean power of the driving waveform is  $28 \, \mathrm{dBm}$ . DC voltage control is provided by a Red Pitaya STEMlab 125-14 board with a 14-bit DAC output ( $\pm 1 \, \mathrm{V}$  range).

Since the optical pulse is chosen to be much shorter than the period of the driving waveform, we may approximate the modulation by a linear slope (after appropriate synchronization). The frequency shift due to the linear temporal phase is given by

$$\mu = 2\pi \times \frac{V_{\rm pp} f_{\rm RF}}{2V_{\pi}},\tag{4.13}$$

with  $V_{\rm pp}$  denoting the peak-to-peak driving voltage,  $f_{\rm RF}$  being the fundamental frequency of the driving waveform and  $V_{\pi}$  corresponding to the required voltage for the EOM to produce a  $\pi$  phase shift. In our system  $V_{\pi}=4/\pi~{\rm V/rad}$  and  $f_{\rm RF}\approx 15~{\rm GHz}$ . Hence, we have  $\mu/V_{\rm pp}=6~{\rm GHz/V}$ .

### 4.4.2 SPECTRAL SHEAR CALIBRATION

As a part of the setup calibration a the relation between the mixer voltage (variable attenuation of the EOM driving signal) and the amount of frequency shift needs to be established. The mixer voltage is scanned between  $\pm 1\,\mathrm{V}$  while at the same time observing the spectrum of a pulse after the EOM. Exemplary spectra and the obtained calibration curve are

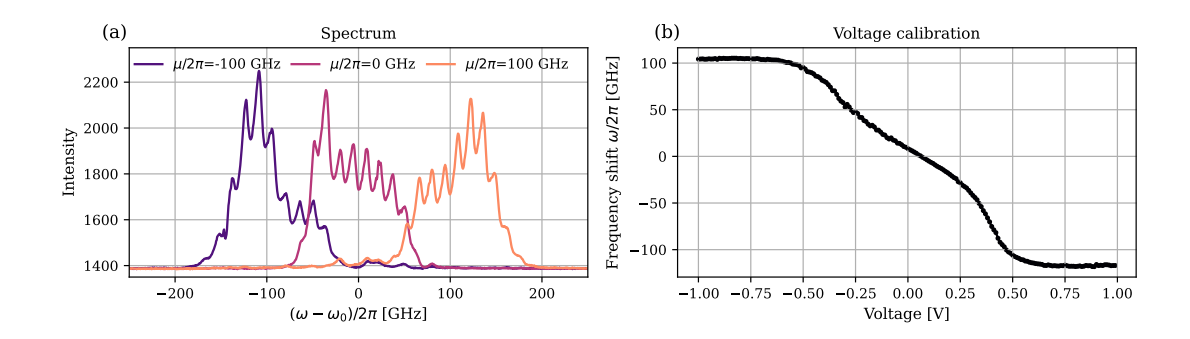


Figure 4.5: (a) Spectra of the pulses undergoing different levels of frequency shifts from  $-100\,\mathrm{GHz}$  to  $100\,\mathrm{GHz}$ . (b) Calibration curve obtained by varying the mixer voltage and observing the position of the spectrum centroid.

depicted in Fig. 4.5. The calibration curve is obtained via linear interpolation on the data points.

We use a custom-built spectrometer based on double-pass second-order diffraction on a diffraction grating (1200 ln/m, 750 nm blaze). For detection, the spectrometer employs a line camera (Toshiba TCD1304AP) controlled by an STM32f103c8t6 microcontroller. Camera images are averaged and a Gaussian fit provides the estimate of the centroid. The spectrometer was calibrated by observing a narrow line of a continous-wave (CW) external-cavity diode laser (ECDL) (Toptica DL100) with the spectrometer and a reference instrument – High FInesse WS/6 wavemeter. Calibration data was collected between 794.2 nm and 795.99 nm with 360 points. A polynomial fit to the data further serves as the calibration curve.

By observing the spectrum (its shift and shape distortion) we are able to best align the optical pulse with the driving waveform. Even at the best points, we observe a minute distortion due to the temporal tails of the pulse reaching beyond the regime where the driving waveform can be approximated as a linear slope.

### 4.5 RESULTS

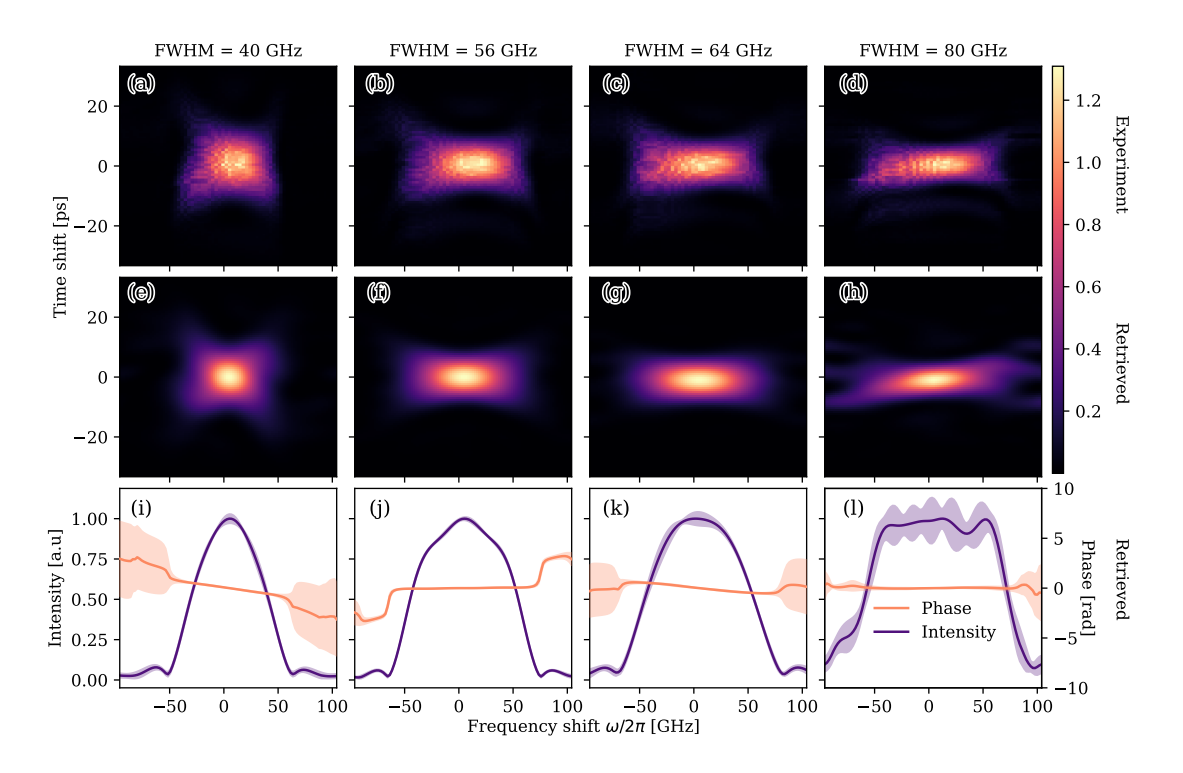


**Figure 4.6:** (a)-(d) Spectrograms measured for bright light with a range of pulse bandwidths. (i)-(l) Amplitude and phase of the reconstructed envelope of pulse's electric field in the spectral domain. (e)-(f) Calculated spectrograms corresponding to the reconstructed pulses.

Our demonstration of VarSI encompasses bright light and single-photon-level pulses in the near-infrared 795 nm for pulses with spectral bandwidths between 48 GHz and 96 GHz. A sharp spectral filter used to prepare the pulses ensures the presence of fine features in the spectrograms, providing a good test bench for VarSI. The results for bright pulses are depicted in Fig. 4.6 while for the single-photon-level light in Fig. 4.7. The spectrograms of reconstructed pulses closely match the experimental data. During reconstruction, we employ linear interpolation for the collected data. The last rows of Fig. 4.6 and Fig. 4.7 present the phase and amplitude of pulses electric field envelope, in the spectral domain. Reconstruction in the temporal domain is depicted in Fig. 4.8. As expected within

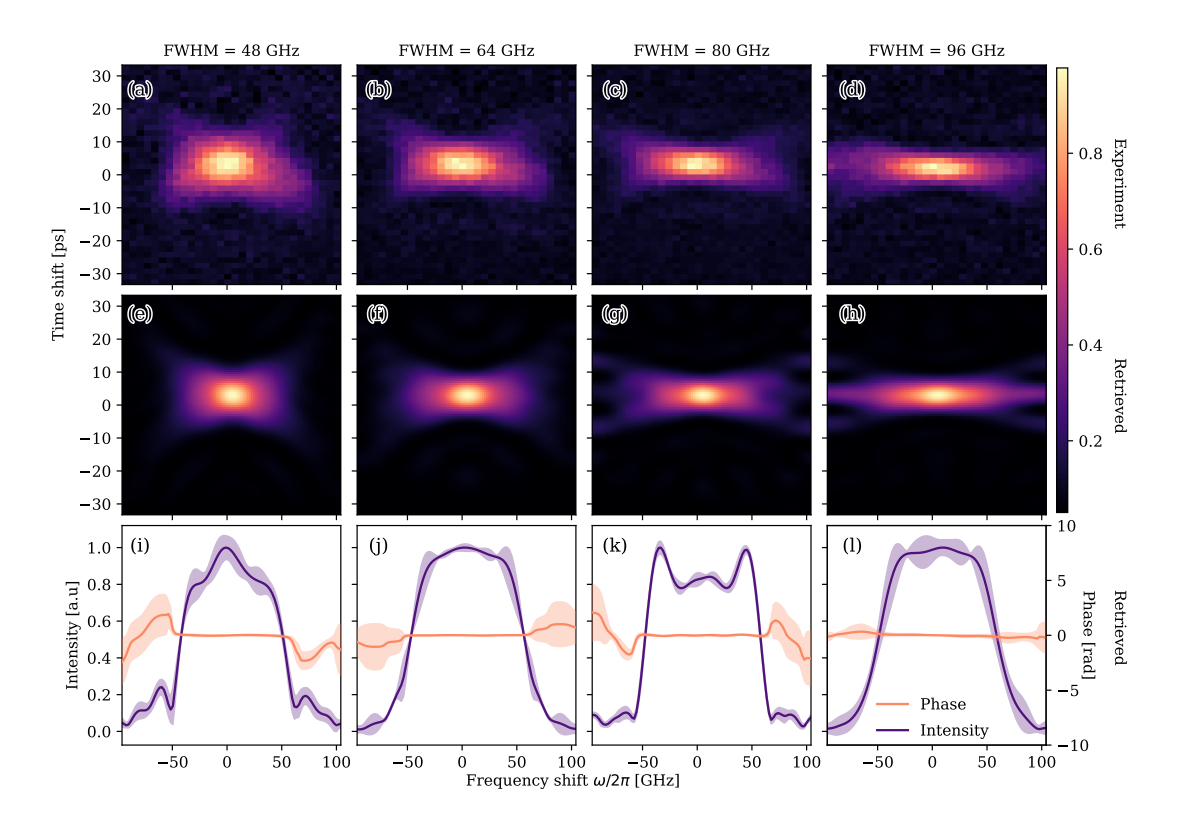


**Figure 4.7:** (a)-(d) Spectrograms measured for single-photon-level light with a range of pulse bandwidths. (i)-(l) Amplitude and phase of the reconstructed envelope of pulse's electric field in the spectral domain. (e)-(f) Calculated spectrograms corresponding to the reconstructed pulses.

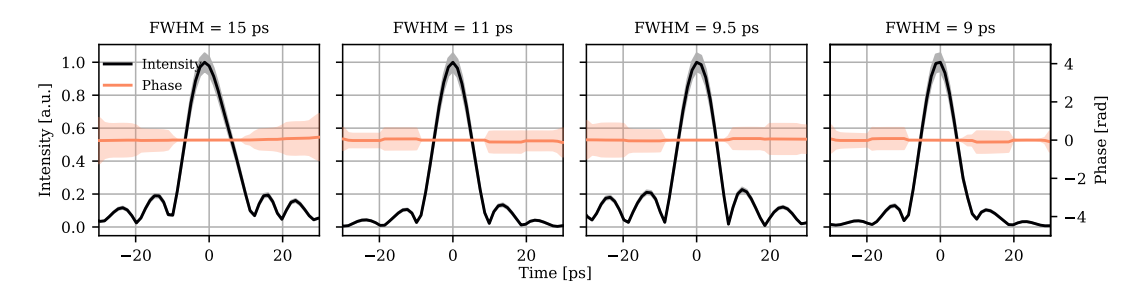


**Figure 4.8:** Reconstructed pulse's electric field envelope in temporal domain, for single-photon-level light.

the regions of non-vanishing amplitude, the reconstructed phase is flat.

To quantify the reconstruction quality, we calculate the fidelity between the recon-

structed and measured spectrograms.

$$F = \frac{\langle |S_{\text{exp}}||S_{\text{recon}}|\rangle}{\sqrt{\langle |S_{\text{exp}}|^2 \rangle \langle |S_{\text{recon}}|^2 \rangle}},$$
(4.14)

with the average  $\langle . \rangle$  calculated over the spectrogram extent. We note that the fidelity here is not a direct measure of the VarSI performance since no ground truth for the pulse electric field is known. Instead, it demonstrates the self-consistency of the reconstruction method. For bright light regime we get  $F_{\rm class}=94\%$  while at the single-photon level  $F_{\rm sp}=97\%$ . For practical reasons, the reconstruction algorithm was limited to a maximum of 300 iterations. Certainly, improvements in this area can be very beneficial to the overall quality of VarSI.

Let us discuss a basic limitation of VarSI. With smaller spectral bandwidths the pulses get longer in time. One limitation in this regard is the linear approximation region of the sinusoidal EOM driving waveform, which depends on the RF frequency. Conversely, if the spectral bandwidth of the pulse is increased, a larger frequency shift is required to map the whole extent of the spectrogram. This in turn necessitates higher RF driving frequencies and/or larger RF powers. Otherwise, the retrieved information on the pulse is limited, and the reconstruction may be deteriorated. Looking at Eq. (4.13), one way to improve the amplitude of modulation is by lowering  $V_{\pi}$ . Modulators with a  $V_{\pi}$  of 1.75 V [171] and 1.4 V [172] have been demonstrated. Development of thin-film modulators is particularly promising in this matter [173].

### 4.6 METHODS

### 4.6.1 Derivation of the $g^{(2)}$ function

Following ref. [174, 175] we will show how the  $g^{(2)}$  function can be measured in the VarSI setup. Let us begin with a linearly polarized pulse of light traveling along z axis with the electric field  $\mathcal{E}(t)$ . With a balanced beamsplitter, the pulse is split into two arms (denoted 1,2) of the interferometer  $\mathcal{E}_{1,2}(t)=\mathcal{E}(t)/\sqrt{2}$ . A delay and a frequency shift are introduced in the 1,2 arms, respectively

$$\mathcal{E}_1(t) \to \frac{\mathcal{E}(t-\tau)}{\sqrt{2}},$$
 (4.15)

$$\mathcal{E}_2(t) \to \frac{\mathcal{E}(t)e^{i\mu t}e^{i\varphi(t)}}{\sqrt{2}}.$$
 (4.16)

The fluctuation of the phase difference between the interferometer arms will be modeled by a random variable  $\varphi$  with a probability distribution P such that

$$\int d\varphi P(\varphi) \cos \varphi = 0. \tag{4.17}$$

Note that this is a less restrictive assumption than a uniform distribution. The interferometer arms 1,2 are intersected at a second balanced beamsplitter whose output ports will be denoted by  $\pm$ . For the fields after the second beamsplitter we can write

$$\mathcal{E}_{\pm}(t) = \frac{1}{2} \left( \mathcal{E}(t - \tau) \pm \mathcal{E}(t) e^{i\mu t} e^{i\varphi(t)} \right). \tag{4.18}$$

The intensity of the  $\pm$  fields is then measured with bucket detectors integrating over a time period T

$$\int_{-T/2}^{T/2} |\mathcal{E}_{\pm}(t)|^2 dt = \frac{1}{4} \left[ \int_{-T/2}^{T/2} dt \left( |\mathcal{E}(t-\tau)|^2 + |\mathcal{E}(t)|^2 \pm 2 \operatorname{Re} \left( \mathcal{E}(t) \mathcal{E}^*(t-\tau) e^{i\mu t} e^{i\varphi(t)} \right) \right) \right]. \tag{4.19}$$

Since T is much larger than the width of the pulse, we can extend the integral to infinity. Hence, the first two terms of the above equation are equal. The second-order intensity correlation function is given by

$$g^{(2)}(\tau,\mu) = \frac{\int d\varphi P(\varphi) \int_{-\infty}^{+\infty} dt |\mathcal{E}_{+}(t)|^{2} \int_{-\infty}^{+\infty} dt' |\mathcal{E}_{-}(t')|^{2}}{(\int d\varphi P(\varphi) \int_{-\infty}^{+\infty} dt |\mathcal{E}_{+}(t)|^{2})(\int d\varphi P(\varphi) \int_{-\infty}^{+\infty} dt |\mathcal{E}_{-}(t)|^{2})},$$
(4.20)

where we average over the phase distribution. The denominator of this equation can be evaluated to

$$\left(\int d\varphi P(\varphi) \int_{-\infty}^{+\infty} dt |\mathcal{E}_{+}(t)|^{2}\right) \left(\int d\varphi P(\varphi) \int_{-\infty}^{+\infty} dt |\mathcal{E}_{-}(t)|^{2}\right) = \frac{1}{4} \left(\int_{-\infty}^{+\infty} dt |\mathcal{E}(t)|^{2}\right)^{2}.$$
(4.21)

We can see that by first observing

$$\int d\phi P(\phi) \int_{-\infty}^{+\infty} dt \operatorname{Re}(\mathcal{E}(t)\mathcal{E}^*(t-\tau)e^{i\mu t}e^{i\varphi(t)}) = \int d\phi P(\phi) \int_{-\infty}^{+\infty} dt |\mathcal{E}(t)\mathcal{E}^*(t-\tau)| \times \cos(\phi_K(t,\tau,\mu) + \phi(t)) = 0, \quad (4.22)$$

where  $\phi_K(t,\tau,\mu)=\arg(\mathcal{E}(t)\mathcal{E}^*(t-\tau)e^{i\mu t})$  and we used Eq. (4.17). The numerator of  $g^{(2)}$  reads

$$\frac{1}{4} \left[ \left( \int_{-\infty}^{+\infty} dt |\mathcal{E}(t)|^2 \right)^2 - \int P(\varphi) d\varphi \left( \int_{-\infty}^{+\infty} dt \operatorname{Re} \left( \mathcal{E}(t) \mathcal{E}^*(t-\tau) e^{i\mu t} e^{i\varphi(t)} \right) \right)^2 \right], \tag{4.23}$$

where we again used Eq. (4.17) and the definition of the short-time Fourier transform of  $\mathcal E$  gated by  $\mathcal E^*$ , as given by Eq. (4.3). The phase  $\varphi$  is considered constant on timescale of E(t) and  $E^*(t-\tau)$  duration. This way we get the second term in the numerator

$$\int P(\varphi)d\varphi \left( \int_{-\infty}^{+\infty} d\text{Re} \left( \mathcal{E}(t)\mathcal{E}^*(t-\tau)e^{i\mu t}e^{i\varphi(t)} \right) \right)^2 = \int P(\varphi)d\varphi \left( \text{Re} \left( e^{i\varphi}\mathcal{S}_{\mathcal{E}(t)}(\tau,\mu) \right) \right)^2$$

$$= \int P(\varphi)d\varphi (\cos^2\varphi (\text{Re}(\mathcal{S}_{\mathcal{E}(t)}(\tau,\mu))^2 + \sin^2(\varphi) (\text{Im}(\mathcal{S}_{\mathcal{E}(t)}(\tau,\mu))^2$$

$$- 2\cos\varphi\sin\varphi \text{Re}(\mathcal{S}_{\mathcal{E}(t)}(\tau,\mu)) \text{Im}(\mathcal{S}_{\mathcal{E}(t)}(\tau,\mu)). \quad (4.24)$$

Again employing Eq. (4.17) and the property of  $\int d\varphi P(\varphi) \cos^2 \varphi = \int d\varphi P(\varphi) \sin^2 \varphi$  we have for the  $g^{(2)}$  function

$$g^{(2)}(\tau,\mu) = 1 - \frac{\left|\mathcal{S}_{\mathcal{E}(t)}(\tau,\mu)\right|^2}{\left(\int_0^\infty \left|\mathcal{E}(t)\right|^2 dt\right)^2} \int d\varphi \, P(\varphi) \cos^2 \varphi. \tag{4.25}$$

We can simplify the phase integral

$$\int d\varphi P(\varphi) \frac{1}{2} (1 + \cos(2\varphi)) = \frac{1}{2}, \tag{4.26}$$

to get the final result

$$g^{(2)}(\tau,\mu) = 1 - \frac{1}{2} \frac{\left| \mathcal{S}_{\mathcal{E}(t)}(\tau,\mu) \right|^2}{\left( \int_{-\infty}^{+\infty} \left| \mathcal{E}(t) \right|^2 dt \right)^2}.$$
 (4.27)

### 4.6.2 Derivation of the gradient function and numerical errors

We refer to the notation and detailed description of ref. [170] and here only briefly describe modifications introduced to the common pulse retrieval algorithm (COPRA). The electric field of the pulse is discretized. The temporal and spectral domains are related by the Fourier transform

$$\tilde{E}_n = \sum_{n} D_{nk} E_k = FT_{n \to k}(E_k)$$
(4.28)

$$E_k = \sum_{k} D_{kn}^{-1} \tilde{E}_n, (4.29)$$

with  $D_{nk}=\frac{\Delta t}{2\pi}e^{i\omega_nt_k}$  and  $D_{kn}^{-1}=\Delta\omega e^{-i\omega_nt_k}$ . Let us denote the shifted pulse by  $A_{mk}=FT_{n\to k}^{-1}(e^{i\tau_m\omega_n}\tilde{E}_n)$  and define the signal as  $S_{mk}=A_{mk}E_k^*$ .

The algorithm reconstructing the amplitude and phase of the pulse's electric field proceeds as follows.

- 1. begin with an initial guess of the electric field E,
- 2. calculate associated signal  $S_{mn}$ ,
- 3. make a projection of the measured intensity and define  $S'_{mn}$  for the measured spectrogram and guess signal (c.f. Eq. (14) in ref. [170]),
- 4. denote the distance  $Z_m$  between the discretized signal and its projection,

5. update the guess of the electric field as  $E_n'=E_n-\gamma_m\Delta_nZ_m$  and go to step 2.

The step size  $\gamma$  is related to the convergence of the local iteration. In our implementation, the algorithm is interrupted after 300 iterations.

The main modification for our setup is in the expression of the gradient  $Z_m$  which needs to be specific to a given form of the spectrogram (here modulus squared of the STFT). The gradient reads

$$\Delta_n Z_m = -2 \sum_k \Delta S_{mk}^* \frac{\partial S_{mk}}{\partial \tilde{E}_n^*} + \Delta S_{mk} \left[ \frac{\partial S_{mk}}{\partial \tilde{E}_n} \right]^*. \tag{4.30}$$

with the STFT derivative:

$$\frac{\partial S_{mk}}{\partial \tilde{E}_n} = D_{kn}^{-1} e^{i\tau_m \omega_n} E_k^* + D_{kn}^{*-1} A_{mk}.$$
 (4.31)

In our case there is no dependence on the field conjugate, hence:

$$\Delta_n Z_m = -2\sum_k \Delta S_{mk} [D_{kn}^{*-1} e^{-i\tau_m \omega_n} E_k + D_{kn}^{-1} A_{mk}^*].$$
 (4.32)

Finally, we get the following expression for  $Z_m$ 

$$\Delta_n Z_m = -\frac{4\pi\Delta\omega}{\Delta t} (FT_{n\to k}(\Delta S_{mk} E_k) + FT_{n\to k}^*(\Delta S_{mk}^* A_{mk})). \tag{4.33}$$

### 4.7 Conclusions

In this chapter, we have discussed a new ultrashort pulse characterization method dubbed Variable Shearing Interferometry. The technique modifies standard electro-optic shearing interferometry avoiding the need for a spectrally-resolved measurement while maintaining its single-photon-level compatibility. This is at the cost of a worse scaling of the measurement time with the number of resolved points in the pulse's electric field and a need for ambiguous algorithmic reconstruction of the electric field itself. Nevertheless, bucket detection with relatively slow photodetectors greatly reduces the cost and complexity of the setup, in particular for spectral regimes where a high-resolution single-photon-sensitive spectrometer is difficult to construct. Furthermore, being a variant of EOSI, VarSI avoids the optical noise and low conversion efficiency of non-linear methods such as FROG or SPIDER. This is important for single-photon-level light, which nevertheless is a niche application compared to the broad range of measurement or manufacturing techniques using ultrashort pulses of light, where standardized FROG, SPIDER, or their variants are a valid choice.

In VarSI both the delay and the frequency shift in the interferometer arms are scanned to form a 2-dimensional measurement map. The measured quantity is the second-order intensity correlation function between the interferometer outputs, which corresponds to the self-gated short-time Fourier transform modulus squared (a spectrogram) of the pulse's electric field. In the classical regime, this is equivalent to estimating the interference fringes visibility. Intensity interferometry has its innate advantages such as the robustness to phase fluctuation between the interferometer arms. VarSI could be also employed with incoherent or partially coherent light.

For the reconstruction of the pulse's complex electric field, we have modified a standard algorithm originally developed for non-linear ultrashort pulse characterization methods (that also require such reconstruction).

In the proof-of-principle experiment we characterized a series of pulses at  $795 \, \mathrm{nm}$  with bandwidths between  $48 \, \mathrm{GHz}$  and  $96 \, \mathrm{GHz}$  and with non-Gaussian profiles. We reconstructed the complex electric field of the pulses and compared the experimental and reconstructed

spectrograms achieving high fidelity.

An important extension of VarSI would be the addition of phase sensitivity allowing for a direct measurement of a complex STFT and mitigating the electric field reconstruction ambiguities. This could be achieved by incorporating a continuous-wave pilot beam into the interferometer which would track the interferometric phase between the arms  $\varphi(t)$ . Another direction would be to use the setup to perform a spectral tomography of a single photon (which would also require a known well-characterized reference photon) [176].

Time-frequency modes are a timely topic [177] and we believe that VarSI in this context well supplements the arsenal of existing characterization techniques and offers a valid basis for further extensions.

[This page intentionally left blank]

# 5

## Ultrafast Fractional Fourier Transform

### 5.1 Foreword

A natural progression from our experiments with ultrashort pulse characterization was in the direction of performing controlled operations coherently shaping the spectro-temporal mode of the pulse. While the ultimate goal and motivation for such operations was an implementation of a super-resolution imaging technique in the time-frequency degree of freedom (described in Chapter 6), the midway steps are of interest themselves.

In this chapter, we describe a single-photon-level-compatible electro-optic ultrafast implementation of the Fractional Fourier Transform (FRT). In the time-frequency (TF) space (e.g. Chronocyclic Wigner Function) of an ultrashort pulse, FRT corresponds to a rotation described by an angle  $\alpha$ . The special case of  $\alpha=\pi/2$  is just the ordinary Fourier transform. Within the framework of TF space, the ability to coherently rotate the state is a fundamental operation. Applications of FRT range from signal processing (e.g. filtering of time-correlated noise [178]) to serving as a fundamental block of complex TF protocols, also in the optical single-photon-level domain (as exemplified in Chapter 6).

In the optical domain FRT can be synthesized via spectral dispersion followed by a timelens and another spectral dispersion equal in magnitude to the first. Similarly, to a spectral shift discussed in Chapter 4, the time-lens (which is just a quadratic temporal phase modulation) may be implemented with an electro-optic modulator (EOM) or via a number of different non-linear optical interactions (such as wave-mixing, cross-phase modulation, or parametric processes) [179, 180]. The advantages of using electro-optic modulation are again mainly in terms of avoiding the optical noise of non-linear methods. EOM-based time lenses are not a new idea and have been demonstrated already in ref. [181]. Their main limitation is the magnitude of the phase modulation (i.e. limited focusing power of the lens). However, the technology of EOMs has undergone significant improvements since the first demonstration of an EOM-based time lens, and now is the technology of choice for single-photon-level applications [182, 183]. Another advantage of using an EOM is the electronic control of the driving waveform amplitude, which in the context of FRT changes the rotation angle  $\alpha$ .

This chapter is based on ref. [184].

### 5.2 Introduction

The fundamental role of the TF domain is reflected in extensive optical applications from the classical communication techquiues (e.g. wavelength-division-multiplexing) to quantum technologies [76, 185–191]. Complete TF frameworks have been proposed for the latter [78] and it also includes quantum-inspired or quantum-enhanced techniques such as super-resolution temporal imaging [87, 192], bandwidth shaping [182, 193], multi-mode quantum repeaters [76], mode sorting [194], spectroscopy [189], continuous-variables protocols [195, 196], waveform compressors [197] and optical oscilloscopes [198, 199]. The presence of ultrashort pulses-based techniques becomes more prevalent in biology, medicine, chemistry, and spectroscopy [200, 201], material science [202] or atomic and molecular physics [203]. In particular, quantum TF protocols often require well-controlled, low-noise, and coherent TF operations.

Optical FRT constitutes such an operation, corresponding to an arbitrary rotation of the state in the TF space. In the domain of signal processing the FRT operation is commonly employed for the filtration of time-correlated noise [178], and has been proposed for encryption protocols [204] or chirp-based encoding schemes [205]. Even with purely classical signals, optical FRT would enable signal processing directly in the optical domain avoiding often inefficient, noisy, and low-bandwidth conversion to the electronic domain. Optical FRT has also been proposed as an optical pulse-shaping method to reduce pulse distortion in optical communication [206], and for secure chaos-based communication [207]. In the single-photon-level regime, FRT enables for instance the TF implementation of super-resolution spectroscopy, discussed in chapter 6. This implementation can also be extended to mode sorting. In fact, a constellation of N parallel FRTs with their angles separated by  $2\pi/N$  and connected by a passive linear optical network implements mode sorting

into N modes [208]. Furthermore, FRT combined with a projective spectrally resolved measurement provides a cross-section of the TF space and when combined with spectral interferometry allows the retrieval of the third order spectral phase [209] which remained ambiguous for instance in our VarSI method (c.f. chapter 4).

FRT has been demonstrated in the optical domain in several implementations. A particularly simple one employs just a linearly chirped Bragg diffraction grating (LCFBG) which being a spectral disperser realizes the TF analog of Fresnel diffraction [210]. The drawbacks include unfeasible wavelength tuning (by replacing LCFBG) and limited resolution and bandwidth. In the regime of longer pulses (MHz bandwidth) a very promising solution has been presented in ref. [211]. The authors demonstrate a single-element FRT based on a feedback loop (which limits the bandwidth). Finally, with a fairly complicated cold-atomic quantum memory setup a high-quality FRT for sub-GHz pulses has been recently demonstrated by Niewelt *et al.* [212].

The FRT was introduced in the optical domain by Mendlovic and Ozaktas in 1993 [213] and a year after a general implementation compatible with ultrafast pulses was described by Lohmann and Mendlovic [214]. It is based on a chain of a dispersive element (pulse stretcher), quadratic temporal phase modulation (time-lens), and another dispersive element with an equal magnitude of dispersion to the first.

Here we present and discuss an electronically controlled low-noise implementation of FRT compatible with single-photon-level picosecond pulses. For the spectral dispersion, we employ a diffraction grating pulse stretcher, while the temporal quadratic phase modulation is implemented with an EOM. We note that an ordinary Fourier transform ( $\alpha=\pi/2$ ) has been previously demonstrated with diffraction grating-based pulse stretcher and an EOM-based time-lens [215]. However, it has not been extended (nor the extension discussed therein) to FRT. Electro-optic FRT promises good scalability if the pulse stretchers

are replaced with fiber Bragg gratings and the EOM with linear optical elements is implemented on-chip.

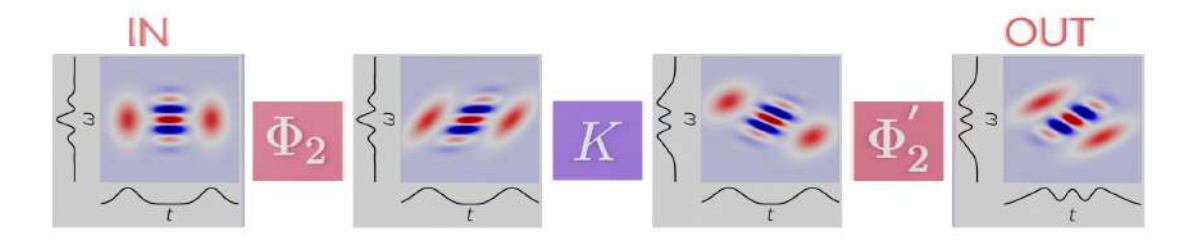


Figure 5.1: The Chronocyclic Wigner Function (CWF) of an optical state consisting of two coherent pulses separated in time. The CWF is presented before, after, and at intermediate stages of an optical FRT. The final operation corresponds to the rotation of the CWF.  $\Phi_2$ ,  $\Phi_2'$  – quadratic spectral phase (ideally  $\Phi_2' = \Phi_2$ ). K – quadratic temporal phase.

### 5.3 Fractional Fourier Transform

FRT naturally extends the Fourier transform which is fundamental in the fields of optics and signal processing [216–219]. Since the definition of FRT in the form of an integral transform (c.f. ref. [217]) does not provide much physical insight, instead of repeating it here, we will consider a more physics-oriented description. FRT can be defined as a propagator of the quantum harmonic oscillator, under the action of which the state's quasi-probability distribution rotates in its TF phase space. FRT can be characterized by a degree P corresponding to a rotation by an angle  $\alpha = P\pi/2$  [217]. Hence, P = 1 gives the ordinary Fourier transform. Let us define the Chronocyclic Wigner Function (CWF) defined for a pulse mode amplitude f(t) as [220]

$$W_f(\omega, t) = \int_{-\infty}^{+\infty} dt' f\left(t + \frac{t'}{2}\right) f^*\left(t - \frac{t'}{2}\right) e^{i\omega t'}.$$
 (5.1)

The rotation can be synthesized by alternating spectral and temporal quadratic phase

modulations. The are two possible orders: temporal-spectral-temporal or spectral-temporal-spectral [217]. We will focus on the latter since it is more experimentally feasible. Considering the light's electric field these operations can be written as the spectral phase modulation

$$\varphi_{\omega}(\omega) = \Phi_2(\omega - \omega_c)^2 / 2, \tag{5.2}$$

temporal phase modulation

$$\varphi_t(t) = Kt^2/2,\tag{5.3}$$

and another spectral ( $\Phi_2', \omega_c'$ ) which ideally has the same parameters as the first. In this description  $\omega_c$ ,  $\omega_c'$  are central frequencies of the transformation (e.g. in a grating pulse stretcher the frequency for which the optical path through the stretcher is the shortest), we have aligned the time t so that the pulse is centered at t=0,  $\Phi_2$  described the group delay dispersion (GDD) and K the time-lens chirp rate. The evolution of an exemplary CWF through the modulation stages has been depicted in Fig. 5.1. We have chosen a CWF of a pair of coherent pulses separated in time since such a state will be later used in the experiment. Notably, the series of quadratic modulations is analogous to the spatial domain. In the paraxial approximation a single transverse dimension propagating through free space, passing through a lens, and again propagating through space, will be described by the same transformation [17, 221, 222].

Following ref. [217] with our notation we have the following expression for the the FRT angle

$$\Phi_2 = \mathcal{G} \tan \frac{\alpha}{2},\tag{5.4a}$$

$$K = \mathcal{G}^{-1}\sin\alpha,\tag{5.4b}$$

with  $\mathcal G$  denoting a scale factor for the GDD. We can solve for  $\alpha$  to get

$$\alpha = \pm 2\arcsin\sqrt{\frac{\Phi_2 K}{2}},\tag{5.5}$$

where the + (-) sign is for  $0 \le \alpha < \pi$  ( $-\pi < \alpha \le 0$ ). We note that the Eqs. (5.4a) and (5.4b) are valid only when K and  $\Phi_2$  have equal signs. Experimentally, positive (negative) dispersion requires a positive (negative) time lens.

Employing the slowly varying envelope (SVE) approximation [223] we can write the electric field of the pulse as

$$\mathcal{E}(t) = \mathcal{A}(t) \exp(i\omega_0 t) = \frac{\exp(i\omega_0 t)}{\sqrt{2\pi}} \int d\tilde{\omega} \,\tilde{\mathcal{A}}(\tilde{\omega}) \exp\{(i\tilde{\omega}t)\},\tag{5.6}$$

with  $\tilde{\omega}=\omega-\omega_0$  and  $\omega_0$  denoting the central frequency. Let us further work with the SVE  $\mathcal{A}(t)$  alone while having Eq. (5.6) in mind.

The quadratic spectral phase modulation amounts to

$$\tilde{\mathcal{A}}(\tilde{\omega}) \to \tilde{\mathcal{A}}(\tilde{\omega}) \times \exp\left[i\varphi_{\omega}(\omega)\right].$$
 (5.7)

We note that potential misalignment  $\omega_c - \omega_0 \neq 0$  of the stretcher central frequency with respect to the pulse central frequency will manifest just as an additional linear spectral phase which in the time domain corresponds to a delay. Such a misalignment will be intrinsically corrected during the synchronization of the EOM radio-frequency (RF) driving waveform with the optical pulse.

$$\frac{\Phi_2}{2}(\omega - \omega_c)^2 = \frac{\Phi_2}{2} \left[ \tilde{\omega}^2 - 2\omega(\omega_c - \omega_0) \right] + \text{const.}$$
 (5.8)

Hence, the SVE after the pulses passes through the stretcher is given by

$$\mathcal{A}_1(t) = \frac{1}{\sqrt{2\pi}} \int d\tilde{\omega} \, \tilde{\mathcal{A}}(\tilde{\omega}) \exp\left\{ \left( i \frac{\Phi_2}{2} \tilde{\omega}^2 \right) \right\} \exp\{ (i \tilde{\omega} t) \}. \tag{5.9}$$

The EOM adds a temporal phase given by Eq. (5.3)

$$\mathcal{A}_2(t) = \mathcal{A}_1(t) \times \exp\{[i\varphi_t(t)]\}. \tag{5.10}$$

After the EOM the pulses will be interrogated with a spectrometer. Neglecting limited resolution, the measured quantity is

$$I_{\text{out}}(\omega) = |\tilde{\mathcal{A}}_2(\tilde{\omega})|^2, \tag{5.11a}$$

$$\tilde{\mathcal{A}}_{2}(\tilde{\omega}) = \frac{1}{\sqrt{2\pi}} \int dt \, \mathcal{A}_{1}(t) \exp\{[i\varphi_{t}(t)]\} \exp\{(-i\tilde{\omega}t)\}. \tag{5.11b}$$

Here we omitted the second pulse stretcher (c.f. Fig. 5.1) since ideally, it would only introduce a quadratic spectral phase which is not measurable with a spectrometer (spectral intensity measurement). In the regime of  $10 \, \mathrm{ps}$  pulses, phase-sensitive spectral characterization (or high-resolution temporal characterization) which would show the effect of the last stretcher is not easily accessible.

Let us note that our theoretical description is only valid up to the quadratic terms in the temporal and spectral phase. We shall further discuss the range of pulse bandwidths for which quadratic modulation is a good approximation (see sec. 5.5.7). Beyond this approximation, a general formalism is given in terms of integral transforms e.g. in ref. [224] or for a similar problem of time-frequency imaging in ref. [225].

### 5.3.1 Two pulses

From the perspective of experimental characterization, a special case of FRT applied to two coherent pulses separated in time is particularly informative. Such a state is an analog of the cat state encountered in quantum optics and will serve us as a good probe of the FRT setup parameters. The pulses are described by

$$\mathcal{A}(t) = \frac{1}{\sqrt{2}} \left[ a(t - \frac{\delta t}{2}) + e^{i\varphi} a(t + \frac{\delta t}{2}) \right],\tag{5.12}$$

with a(t) denoting the SVE of a single pulse,  $\varphi$  being the phase between pulses and  $\delta t$  describing their separation in time. The spectrum of such a state shows equidistant ( $\propto 1/\delta_t$ ) fringes

$$|\tilde{\mathcal{A}}(\tilde{\omega})|^2 = |\tilde{a}(\tilde{\omega})|^2 \left[1 + \cos\left(\tilde{\omega}\delta t + \varphi\right)\right]. \tag{5.13}$$

FRT rotates the state in the TF space. As the rotation angle  $\alpha$  is increased toward  $\pi/2$  the fringes are removed and the (initially identical) spectra of individual pulses are shifted into opposite directions.

For analytical traceability, we will assume Gaussian pulses described by the width  $\sigma$  in the frequency domain

$$a(t) = \left(\frac{\sigma^2}{\pi}\right)^{1/4} \exp\left\{\left(-\frac{1}{2}t^2\sigma^2\right)\right\}. \tag{5.14}$$

Using Eq. (5.11b), the following expression for spectral intensity is obtained

$$\frac{1}{\sqrt{\pi\xi\sigma^2}} \times \exp\left\{\left(-\frac{\tilde{\omega}^2}{\xi\sigma^2} - \frac{\delta t^2 K^2}{4\xi\sigma^2}\right)\right\} \times \left\{\cosh\left(\frac{\delta t\tilde{\omega}K}{\xi\sigma^2}\right) + \cos\left[\frac{\delta t\tilde{\omega}}{\xi}\left(1 - K\Phi_2\right) + \varphi\right]\right\},\tag{5.15}$$

with

$$\xi = \frac{K^2}{\sigma^4} + (K\Phi_2 - 1)^2. \tag{5.16}$$

As a sanity check let us substitute K=0 ( $\xi=1$ ). The initial spectrum (Eq. (5.13)) is correctly preserved. If we instead demand  $\alpha=\pi/2$ , the action of an ordinary Fourier transform ( $t\to\mathcal{G}\omega$ ) is recovered. Let us use Eq. (5.4b)) and Eq. (5.4a). In such a case  $K=\mathcal{G}^{-1}$ ,  $\Phi_2=\mathcal{G}$ ,  $\xi=1/(\sigma^4\mathcal{G}^2)$  and the spectrum after the transformation is given by

$$\frac{\mathcal{G}\sigma}{\sqrt{\pi}} \exp\left\{ \left( -\frac{\sigma^2 \delta t^2}{4} \right) \right\} \exp\left\{ \left( -\sigma^2 \tilde{\omega}^2 \mathcal{G}^2 \right) \right\} \times \left[ \cosh\left( \delta t \tilde{\omega} \mathcal{G} \sigma^2 \right) + \cos(\varphi) \right]. \tag{5.17}$$

After algebraic transformations, it can be shown to be a sum of two Gaussians separated in angular frequency by  $\delta t/\mathcal{G}$ . Since the cosine term lost any dependence on  $\omega$ , there are no interference fringes in the spectrum.

### 5.4 EXPERIMENT

The experimental setup is depicted in Fig. 5.2. Ca.  $100 \, \mathrm{fs}$  pulses are emitted from a Ti:Sapphire laser (SpectraPhysics MaiTai) with a  $80 \, \mathrm{MHz}$  repetition rate, at a central wavelength of  $800 \, \mathrm{nm}$ , and with an average power of ca.  $3 \, \mathrm{W}$ .

A custom pulse shaper (4f filter) carves ca. 74 GHz full width at half maximum (FWHM) pulses which are then coupled to a polarization-maintaining (PM) fiber. The pulse shaper consists of a diffraction grating (Newport 33067FL01-290R,  $1800 \frac{ln}{mm}$ ,  $26.7^{\circ}$  blaze angle) which maps the spectral degree of freedom (DoF) onto the angular (transverse wavevector) DoF in the horizontal plane. The grating is far-field imaged onto a rectangular slit with an adjustable width. A retro-reflecting mirror is placed in the near field of the slit, hence folding the far-field imaging setup to form a unit magnification telescope. By a slight deviation

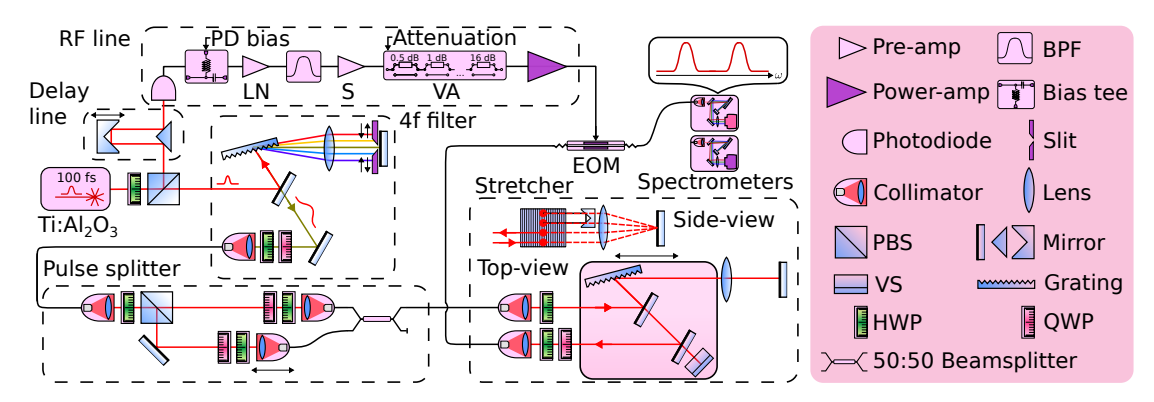


Figure 5.2: Schematic depiction of the experimental setup. The experiment begins with ca.  $100\,\mathrm{fs}$  pulses produced by a Ti:Sapphire laser. The pulses are filtered to ca.  $74\,\mathrm{GHz}$  via a diffraction grating followed by a folded telescope with a rectangular slit and a mirror in the Fourier plane (4f filter). A Mach-Zehnder-type interferometer with a controlled delay in one of the arms (Pulse splitter) splits the input pulse and produces a state of two coherent pulses separated in time. To implement the FRT a quadratic spectral phase modulation is imposed with a diffraction grating quadruple-pass stretcher. An electro-optic modulator (EOM) facilitates the quadratic temporal phase modulation. The radio frequency (RF) signal driving the EOM is obtained by exciting a fast photodiode with a small power fraction of the original femtosecond pulses (ca.  $1\,\mathrm{mW}$  of average power,  $80\,\mathrm{MHz}$  repetition rate). A series of amplifiers and filters, including a variable attenuator (VA), shapes the signal before it enters the EOM. The optical and RF pulses are aligned with delay lines so that the optical pulse is centered around the extremum of the RF waveform. The transformed signal is measured with either a single-photon-sensitive or a standard spectrometer. H(Q)WP – true-zero-order half- (quarter-) waveplate, PBS – polarizing beamsplitter, LN – low noise amplifier, S – standard amplifier, VS – vertical-shift retroreflector, BPF – band-pass filter, VA – variable attenuator.

of the mirror angle, the returning beam is vertically offset at the grating. This way it can be separated with a D-shaped mirror and exit the shaper.

The pulses are sent to a Mach-Zehnder-type interferometer partially implemented in free space and partially in fiber. The pulse power is equally split into the two arms of the interferometer. One arm contains an adjustable, motorized delay implemented by moving one of the collimators along the beam propagation. Each output of the interferometer contains two pulses separated in time. Each pulse is in the same spectro-temporal mode (up to the delay) as the input. One of the interferometer outputs is routed to the main FRT setup via fiber.

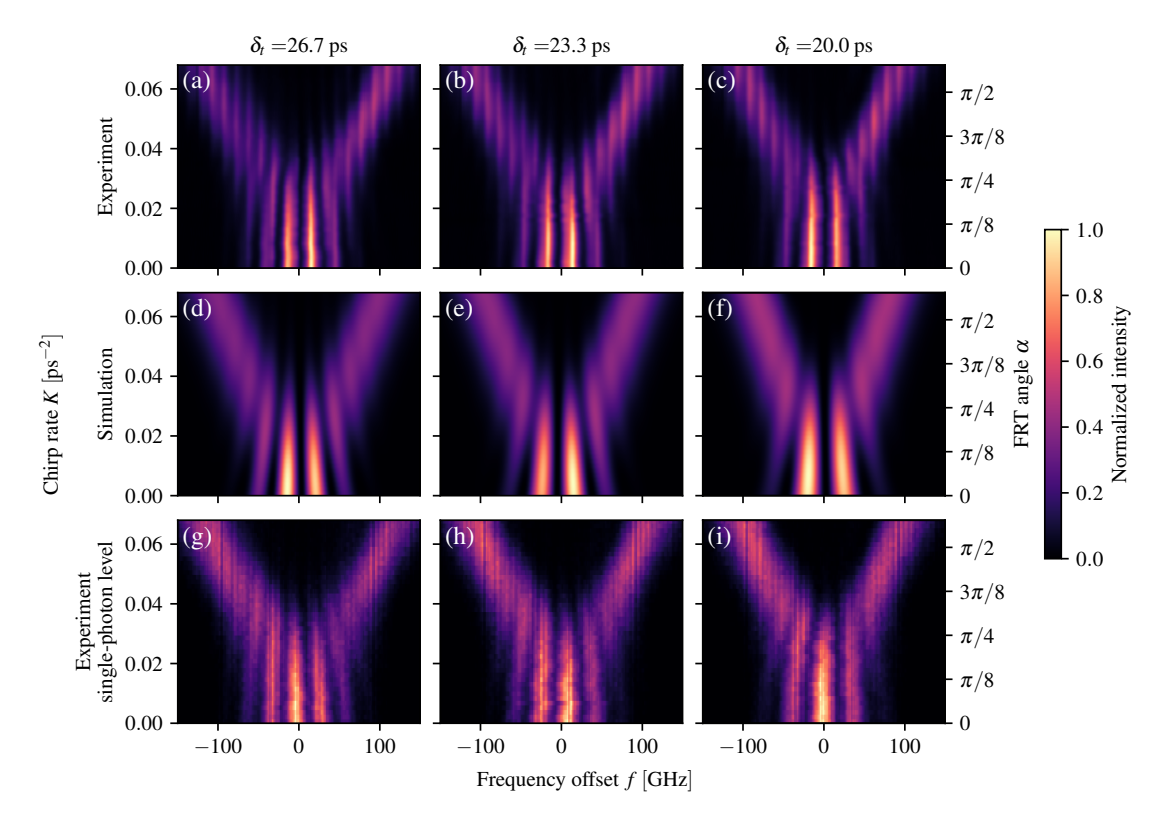


Figure 5.3: Experimental and simulated spectra for a pair of coherent pulses separated in time by  $\delta t$ , undergoing FRT. The GDD is fixed at  $\Phi_2=15.5~\mathrm{ps^2}$  while the chirp rate K is varied to produce different FRT angles  $\alpha$ . Each column corresponds to a distinct delay  $\delta t$ . (a)-(c) Experimental spectra in the bright-light regime. (d)-(f) Simulated spectra corresponding to the bright-light data. Parameters for the simulation (described in sec. 5.5.1) were  $f_m=15~\mathrm{GHz}, \Delta_t=11.6~\mathrm{ps}, \Phi_2=15.5~\mathrm{ps^2}$ . Fidelities between (a) and (d), (b) and (e), (c) and (f) were 96.28%, 96.27%, and 95.88%, respectively (c.f. sec. 5.5.2). (g)-(i) Single-photon-level spectra with the average photon number per frame  $\bar{n}=0.38$  amounting to  $2.4\times10^{-4}$  photons per pulse. A measurement for each K setting consisted of  $50\times10^3$  frames. Note that the phase between the pulses  $\varphi$  differs between the single-photon-level and the bright-light measurements.

The implemented FRT setup consists of a pulse stretcher and a fiber-based EOM modulator. The pulse stretcher is implemented in a single-grating quadruple-pass Martinez configuration (c.f. ref. [226]) described in more detail in sec. 5.5.4. For the details on the EOM and RF driving signal formation see sec. 5.5.6. The output of the FRT is observed with a spectrometer (c.f. sec. 5.5.8). Excluding the detection stage, our setup efficiency is ca. 1%.

For a full FRT transformation, the EOM should be in principle followed by another stretcher. Ultimately, the stretcher would only impose a quadratic spectral phase onto the state output from the EOM. Such a spectral phase cannot be measured with a spectrometer. Hence, since the second stretcher would further reduce already small setup efficiency, it is omitted for the main measurements. Nevertheless, we have implemented a second stretcher and experimentally verified that no observable difference was present in a small sample of measurement settings. See also sec. 5.5.3)

The experimental and simulated spectra for the regime of bright light have been depicted in Fig. 5.3 (a)-(c) and (d)-(f), respectively. The spectra were measured for different delays  $\delta t$  between the pulses and a range of FRT angles  $\alpha$  controlled by the chirp rate K. Corresponding measurements at the single-photon level are presented in Fig. 5.3 (g)-(i).

Notably, the experimental results show a very good agreement with the simulated model. Imperfections, as indicated by non-ideal fidelity, mostly originate from artificial low-contrast fringes present in all measurements with the standard (bright-light) spectrometer. Their origin is most likely a polarization-degree interference within the spectrometer setup. Such fringes are visibly absent from the single-photon-level measurements which utilize a different spectrometer.

While the GDD  $\Phi_2=15.5\,\mathrm{ps^2}$  of our stretcher is relatively low and could be still extended several times without significant modifications in the setup, the attainable range of FRT angles  $\alpha$  already reaches beyond the angle  $\alpha=\pi/2$  of the ordinary Fourier transform.

Finally, let us note that our state of two pulses, due to their relatively large separation in time, extends in time beyond the regime of quadratic temporal phase modulation, considered in sec. 5.3.1 (see also sec. 5.5.7). The theory outlined therein, still correctly predicts the qualitative behavior, nevertheless to capture all features of the experimental data higher-order terms in the temporal phase have to be accounted for. In fact, for the simulated maps

we numerically incorporate a full sinusoidal modulation. Theoretically, such an extended model is well described in ref. [224].

### 5.5 Methods

### 5.5.1 SIMULATION

To simulate the spectra we assume Gaussian, Fourier-limited pulses with the temporal FWHM of the pulse intensity  $\Delta_t=11.6~\mathrm{ps}$ , and a flat temporal phase. The pulses have their centroid at t=0 and are symmetrically moved to create the temporal separation  $\delta t$ . SVE of the pulses is calculated on a temporal grid. Care is taken to ensure that the initial grid (in time) for the numerical representation of the pulse amplitude is chosen with sufficient padding and granularity. Any artifacts can be quite easily detected by observing the intermediate steps of the simulation or verifying that the final result remains unaltered as the grid parameters are changed slightly.

The action of the stretcher is modeled as a purely quadratic spectral phase centered around the pulse central frequency.

The temporal phase of the EOM is modeled as a cosine with a frequency of  $f_m = 15 \, \mathrm{GHz}$  and an amplitude chosen as a function of K so that under the series expansions of the cosine around 0, the quadratic term matches Eq. 5.3. Additionally, the temporal phase modulation is slightly shifted in time to model imperfect synchronization between the RF waveform and the optical signal.

Between the subsequent transformations due to the stretcher and the EOM, the pulses undergo (an inverse) a Fast Fourier transform to match the domain of the next phase modulation.

Parameters of the simulation for comparison with the experimental data were mostly

fixed and taken as independently measured ( $\Phi_2$ , range of K,  $f_m$ ) with the exception of the relative phase between the pulses  $\varphi$ , pulse's FWHM  $\Delta_t$  and the time offset between the temporal phase modulation center and the pulses' centroid.

### 5.5.2 FIDELITY

The fidelity  $\mathscr{F}$  quantifies the level of similarity between the simulated  $\mathcal{I}^{(\mathrm{th})}(f,K)$  and experimental spectra  $\mathcal{I}^{(\mathrm{exp})}(f,K)$ . It is given by

$$\mathscr{F} = \frac{\sum_{f,K} \sqrt{\mathcal{I}^{(\exp)}(f,K)\mathcal{I}^{(\operatorname{th})}(f,K)}}{\sqrt{\sum_{f,K} \mathcal{I}^{(\exp)}(f,K)} \sqrt{\sum_{f,K} \mathcal{I}^{(\exp)}(f,K)}}},$$
(5.18)

with the summations taken over discrete points of the maps in the coordinates of the chirp rate K and the frequency f.

### 5.5.3 SECOND STRETCHER

In a complete FRT setup, after the EOM a second stretcher would be placed. It acts to correct the spectral phase so that a true rotation in the TF space is implemented (c.f. Fig. 5.1). With temporal intensity or spectral phase-sensitive characterization, the omission of the last stretcher would change the measurement outcome. However, with a spectral intensity measurement (a spectrometer), it does not alter the result beyond reducing the overall efficiency of the setup. We have also verified experimentally this theoretical prediction for a subset of measurement settings. To avoid the detrimental effect of further reduced setup efficiency, we omit the last stretcher in the final measurements. Finally, let us note that the simultaneous phase-sensitive characterization in the spectral and temporal domain is technically challenging in the  $100~\mathrm{GHz}$  pulses regime, especially with a sufficient resolution to interrogate the FRT operation.

### 5.5.4 Grating stretcher design

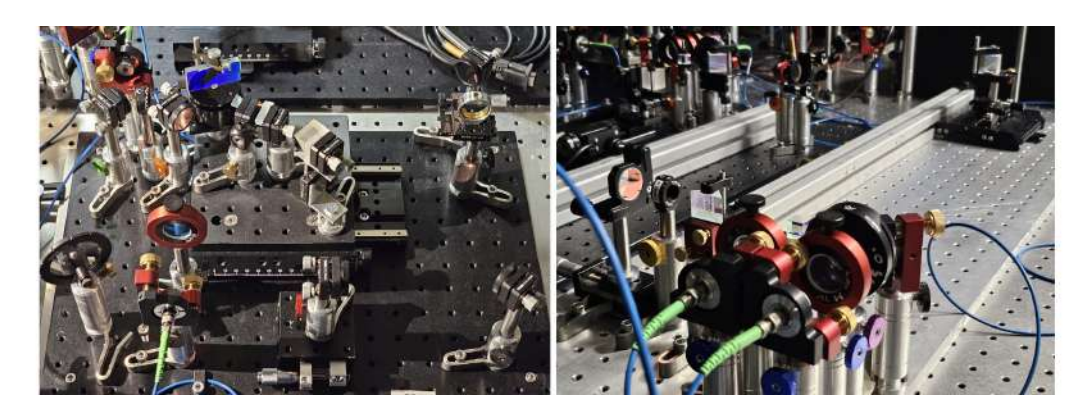


Figure 5.4: Photographs of (left) pulse stretcher and (right) quadruple-pass delay line.

The pulse stretcher design is similar to the one presented in ref. [227]. A single diffraction grating (Newport 33067FL01-290R,  $1800 \, \frac{\ln}{\mathrm{mm}}$ ,  $26.7^{\circ}$  blaze angle) is used. A translation stage with a  $10 \, \mathrm{cm} \times 10 \, \mathrm{cm}$  platform has its movement aligned with the input and output beams of the setup. On the platform, a complex of the diffraction grating, D-shaped input, and output routing mirrors, and a vertical-shift retro-reflecting prism is placed. The layout is illustrated in Fig. 5.2. Adjusting the input D-shape mirror and the grating angle the central frequency of the stretcher (i.e. the frequency of the shortest optical path)  $\omega_c$ , and the amount of GDD per distance L. The movement of the stage changes L while keeping the beams aligned and coupled to the output fiber (with large changes in L a slight correction of the collimator angle alone is required). A photograph of the stretcher is depicted in Fig. 5.4.

The first order of diffraction (horizontal plane) travels a distance  $L\approx71.5\,\mathrm{mm}$  (given for  $\omega_c$ ) before entering a folded telescope with a unit magnification. At the Fourier plane (far-field imaging lens with a focal length  $f=200\,\mathrm{mm}$ ) of the telescope, a retro-reflective mirror is placed. The lens in the telescope is vertically shifted so that the returning beam

is spatially separated from the input beam when reaching the grating. With the vertical-shift retro-reflector, the beam travels another round through the folded telescope and exits through a D-shaped mirror. This is facilitated by a careful choice of the vertical positions for each pass.

The GDD of such a stretcher reads [228]

$$\Phi_2 = \frac{m^2 \lambda^3 L}{2\pi c^2 d^2 \cos^2 \theta_d},\tag{5.19}$$

with m=1 denoting the order of diffraction, c the speed of light, d the period of the grating grooves, and finally  $\theta_d$  being the diffraction angle for the central frequency  $\omega_c$ .

Let us note that GDD is independent of f. Nevertheless, with a quadruple-pass design, the beams pass through the lens far from the optical axis. Their separation at the lens is approximately the same as at the grating and must allow for the coupling of the input and output beams through D-shaped mirrors. At the same time, the beams must be kept spatially large for a sufficient Rayleigh range (the total optical path through the stretcher is ca.  $2 \, \mathrm{m}$ ). Hence, the lens must be carefully chosen to avoid spherical aberration, which is particularly prevalent with short focal lengths. In an ideal scenario, an aspheric lens would be used.

Let us further note that in the regime of  $L\gg f$  the setup becomes very sensitive to the telescope calibration. With a simple ray optics calculation it can be shown that the axial displacement of the retro-reflective mirror from the Fourier plane  $\delta x$  needs to satisfy  $\delta x\ll f^2/L$ .

Fortunately, with relatively spectrally narrow  $\approx 100\,\mathrm{GHz}$  pulses, the chromatic aberrations are not very significant. Nevertheless, if shorter pulses are to be used, achromatic lenses should be considered. Furthermore, the grating's horizontal dimension and the cho-

sen diffraction angle must be compared with the horizontal spread of the returning beam.

Let us observe that the dispersion of the grating stretcher is fundamentally geometric [226]. With only a single transverse dimension acting as a proxy for the frequency DoF, the beam necessarily develops astigmatism while it passes through the stretcher. It is true even if the input beam is free of spatial-spectral correlations. If the GDD of the stretcher is chosen in the regime of  $\gg 100~{\rm ps^2}$  the output beam needs to be corrected for astigmatism to ensure reasonable fiber coupling efficiency. It can be achieved with a telescope acting in a single transverse dimension i.e. built with cylindrical lenses. A configuration that we have tested, yet not used in the final design due to a small GDD required in the experiment.

We have implemented two instances of the pulse stretcher. Their efficiencies were 8% (the one used in the final measurement) and 13%. It is consistent with the grating diffraction efficiency of ca. 70% ((70%)<sup>4</sup> = 24%) and output fiber coupling losses.

## 5.5.5 STRECHER GDD CALIBRATION

To calibrate how the GDD of the stretcher changes with the position of its translation stage we used a variant of the spectrally resolved interferometry – the stationary phase point (SPP) method [229]. A spectrally-wide (ca. 500 GHz FWHM) input pulse is split into two parts of equal power. The first is routed through the stretcher, while the second undergoes a delay  $\delta t$  (relative to the travel time through the stretcher for central frequency  $\omega_c$ ). The two paths are interfered on a balanced beamsplitter. One of the interferometer outputs is observed with a spectrometer. The quadratic spectral phase imprinted by the stretcher is given by Eq. (5.2), and the delay amounts to a linear spectral phase  $\delta t\omega$ . Hence, the fringe pattern corresponding to the spectral phase difference between the arms is given by

$$\propto \left(1 + \cos\left\{\frac{\Phi_2}{2}\left[\omega - \left(\omega_c + \frac{\delta t}{\Phi_2}\right)\right]^2\right\}\right),$$
 (5.20)

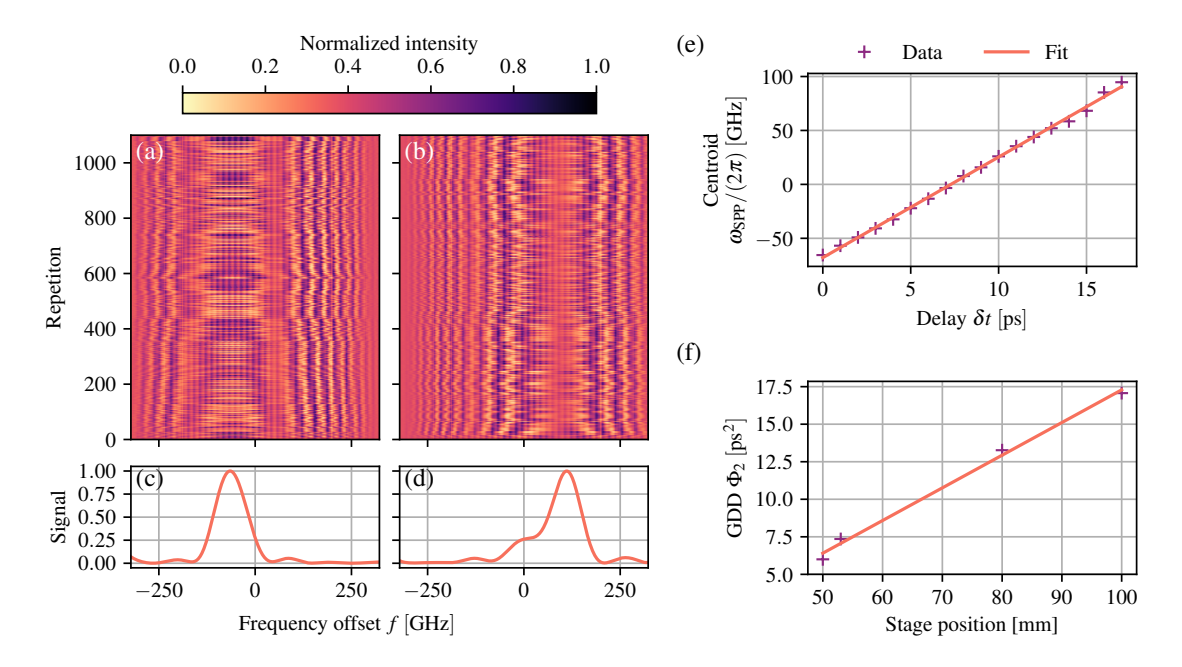


Figure 5.5: GDD measurement for the implemented pulse stretcher. The stationary phase point method is used. (a)-(e) Data collected for a single position of the stretcher translation stage  $(100\,\mathrm{mm})$  and a delay of (a),(c)  $\delta t=0\,\mathrm{ps}$  or (b),(d)  $\delta t=17\,\mathrm{ps}$ . (a),(b) Normalized interference spectra. Each row corresponds to a single sample (gathered at a rate of ca.  $100\,\mathrm{Hz}$ ). The interference phase is freely fluctuating. The zero point of the frequency offset is chosen arbitrarily. (c),(d) Normalized variance over repetitions of the interference spectra (which first undergo background subtraction and low-pass Fourier-domain filtering). The normalized variance shows maxima at the point of stationary phase point. (e) Centroids of Gaussians fitted to the normalized variance (estimated points of stationary phase) for varying delays. The GDD is estimated from the slope of the data after fitting a linear function. (f) The measurement is repeated for several positions of the pulse stretcher translation stage. Calculated error bars are below the size of the data points and typically correspond to a 1%-2% deviation.

where we assumed perfect visibility, omitted a constant (in  $\omega$ ) phase, and converted the quadratic (in  $\omega$ ) polynomial to the canonical form. The SPP corresponds to a spectral point where the frequency of the interference fringes is locally 0 i.e.

$$\omega_{\rm SPP} = \omega_c + \delta t / \Phi_2. \tag{5.21}$$

If we can measure  $\omega_{\rm SPP}(\delta t)$  for a range of delays  $\delta t$ , the inverse of GDD  $\Phi_2^{-1}$  can be estimated as the slope coefficient of a linear fit to the data.

To estimate  $\omega_{\text{SPP}}(\delta t)$  for a given, known delay  $\delta t$  we let the  $\omega$ -independent (but time-dependent) phase between the interferometer arms fluctuate and collect hundreds of spectra over a time of several seconds. The rough location of SPP is already very clearly visible in the raw maps of spectra versus time, as demonstrated in Fig. 5.5 (a),(b). To obtain a more precise estimate of SPP the maps undergo a 1-dimensional low-pass filtering along the frequency offset dimension (i.e. the maps are convolved with a Gaussian kernel row by row). The filter cutoff (kernel size) is adjusted empirically. We then calculate the variance over time of the filtered spectra. Notably, a low-pass filter will have the highest response where the frequency content is the lowest. Since SPP corresponds to the vanishing fringe frequency, the maximum of the variance well estimates the SPP.

We repeat the process for a series of delays, as depicted in Fig. 5.5 (e) and estimate the GDD with a linear fit. Finally, the measurement is done for different positions of the stretcher translation stage (which up to an offset corresponds to L), as depicted in Fig. 5.5 (f). This way, we can later set the GDD to a desired value by changing the stage position without the need to use the SPP method after every alteration.

The precision of GDD calculation, taken as the standard deviation of the fit slope, is on the order of 1%-2%. However, slight alterations in the filtering procedure (e.g. kernel size) produce already higher variations in GDD estimates. Based on such observations our estimate for the GDD error is around 5-10%. Notably, lower GDDs are more difficult to measure. With a limited bandwidth of the pulse, we can only observe interference fringes over ca. 500 GHz and a low GDD means that the quadratic phase will change slowly in this bandwidth resulting in few observed fringes. Extensions of the SPP using a 2-dimensional spectro-spatial measurement can provide better GDD estimates in this regime [230].

# 5.5.6 RF LINE AND EO MODULATION

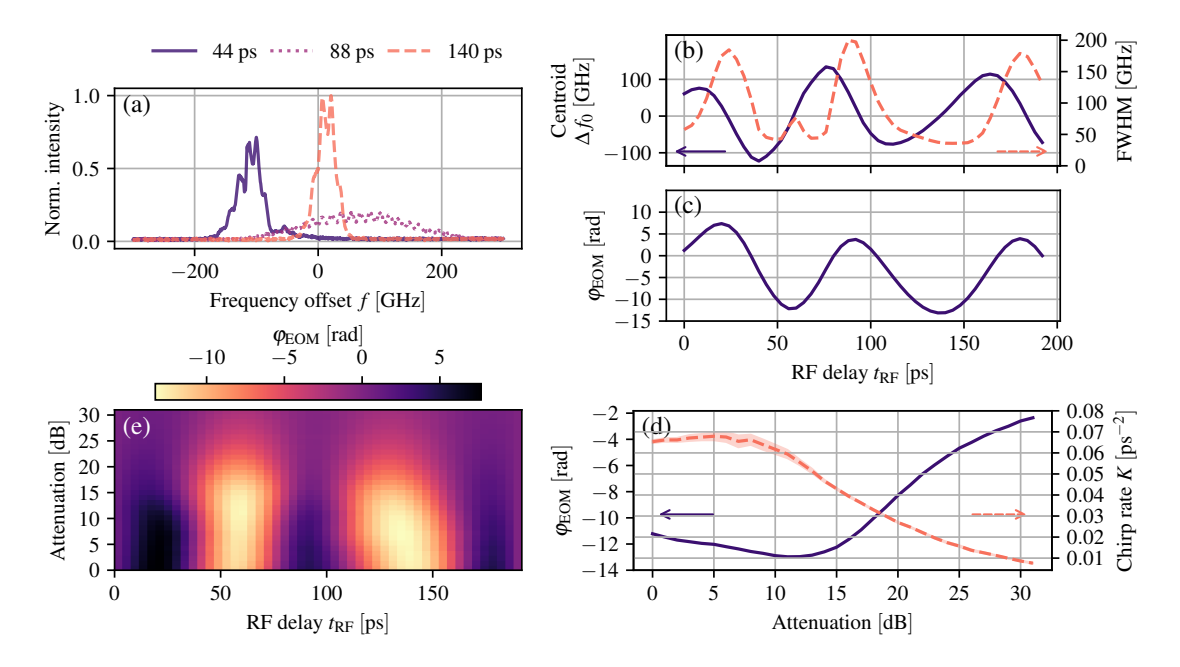


Figure 5.6: Characterization of the RF waveform driving the EOM. (a) Spectrum of an optical pulse passing in series through the pulse stretcher and the EOM with the RF attenuation set to  $5\,\mathrm{dB}$ . Data for a series of RF signal delays  $t_\mathrm{RF}$  is presented. (b) FWHM and centroid position of a Gaussian fit to the spectrum, as a function of the RF delay  $t_\mathrm{RF}$ . (c)-(e) Temporal phase imprinted by the EOM  $\varphi_\mathrm{EOM}$ , estimated by integrating the positions of the centroid over time. (c) Estimate of  $\varphi_\mathrm{EOM}$  for a single RF attenuation of  $5\,\mathrm{dB}$ . (d) (solid) Estimate of  $\varphi_\mathrm{EOM}$  for a single RF waveform delay of  $t_\mathrm{RF}=60\,\mathrm{ps}$ . (d) (dashed) Estimate of the chirp rate K as a function of the attenuation, obtained by fitting a quadratic function to a small region around a  $\varphi_\mathrm{EOM}$  maximum for each attenuation level.

To drive the EOM (iXblue NIR-MPX800-LN-20) we excite a fast photodiode (PD) (Hamamatsu Photonics G4176-03 with a bias tee Mini-circuits ZX85-12G-S+ providing a bias voltage of 10 V) with an unfiltered ca. 100 fs pulse. The average optical power is set to avoid saturation, by observing the RF waveform (after preamplification) on an oscilloscope. The signal from the PD is preamplified (low noise Mini-circuits ZX60-06183LN+ followed by Mini-circuits ZX60-183-S+), undergoes bandpass filtering (6 – 18GHz, Mini-circuits ZBSS-12G-S+) and passes through a programmable attenuator (6-bit, 0.5 dB LSB,

Analog Devices ADRF5720) to enter a power amplifier (3 W, Mini-circuits ZVE-3W-183+). The sequence of elements is depicted in Fig. 5.2.

To synchronize the optical pulse with the RF waveform extremum we use a motorized optical delay line for the pulse driving the PD. Additionally, we control the delay of the optical signal with a manual quadruple-pass delay line placed just at the output of the Pulse Splitter (the delay line is not explicitly shown in the figure).

To characterize and calibrate the EOM phase modulation we use an optical probe pulse. The pulse is sent through the stretcher and the EOM to be finally measured with a spectrometer. Notably, the frequency shift of the pulse centroid  $\Delta f_0$  is directly proportional to the slope of the EOM phase over the pulse extent

$$\partial_t \varphi_{\text{EOM}}(t) = 2\pi \Delta f_0.$$
 (5.22)

By integrating this equation, we can estimate  $\varphi_{\rm ROM}(t)$  from a measurement of  $\Delta f_0$  as a function of the RF waveform delay  $t_{\rm RF}$ . The EOM calibration has been depicted in Fig. 5.6.

Once  $\varphi_{\text{ROM}}(t)$  is obtained, the chirp rate of the time lens K can be retrieved by fitting a quadratic function in a small region around the waveform extremum.

Assuming the pulse is much shorter than the RF waveform period, we also theoretically predict the chirp rate in terms of the physical parameters of the EOM

$$K = 2\pi^3 \frac{V_{\rm pp}}{V_{\pi}} f_m^2, \tag{5.23}$$

with  $V_{\pi}$  [V] denoting the required voltage for  $\pi$  phase shift,  $V_{\rm pp}$  being the peak-to-peak RF amplitude, and where we have assumed a sinusoidal modulation at frequency  $f_m$  and

expanded the waveform around an extremum up to the quadratic terms. In the experiment we have  $V_{\pi}=4\,\mathrm{V}, V_{\mathrm{pp}}\approx19.5\,\mathrm{V}$ , and  $f_{m}\approx15\,\mathrm{GHz}$ . The attainable maximal  $V_{\mathrm{pp}}\approx34.6\,\mathrm{V}$  is limited by the amplifier power of ca.  $3\,\mathrm{W}$ , and further power dissipation in the EOM.

Repeatable and precise control of the RF waveform amplitude plays a crucial role in implementing arbitrary-angle FRT. In particular, avoiding a significant RF waveform phase shift with the changing amplitude poses a technical challenge. For our experiment, we have carefully chosen a programmable attenuator. It already has a relatively low nominal phase shift of ca.  $20^{\circ}$  at  $15~\rm GHz$  between  $0~\rm dB$  and the maximum of  $31.5~\rm dB$  of attenuation (scaling linearly in between). We operate at a reduced range of attenuations and empirically find a fragment of the RF driving waveform, where other imperfections mostly cancel the remaining phase shift. This is best illustrated in Fig.  $5.6~\rm (e)$  at  $t_{\rm RF}=60~\rm ps$ . The arg max  $\varphi_{\rm EOM}$  stays almost constant as the attenuation is changed. We reprogram the attenuator with a parallel digital interface directly from a Bluepill STM32F103C8T6 board (ARM processor). The attenuator has a 6-bit range and a least-significant-bit (LSB) step of  $0.5~\rm dB$ .

# 5.5.7 Pulse preparation and FRT bandwidth

Let us consider the range of the spectral widths of the optical pulses entering the FRT setup, for which the FRT operation contains at most a preset level of distortions. We will refer to this range as the optical bandwidth of the electro-optic FRT.

The most important bandwidth-limiting factor is the modulation frequency  $f_m$  of the EOM, which corresponds to a temporal aperture of the time lens. In our experiment  $f_m \approx 15\,\mathrm{GHz}$ . Since the EOM only modulates the phase and not the amplitude, a natural definition for the temporal aperture is not immediately obvious. We choose to compare an

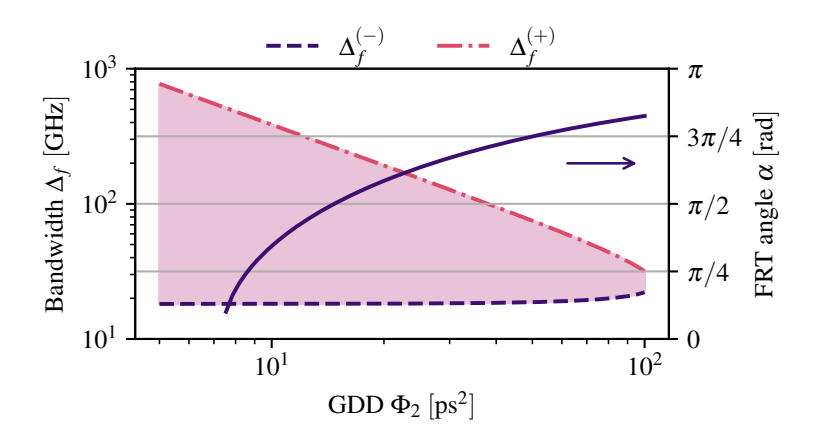


Figure 5.7: (left axis) The shaded region represents the range of initial optical pulse bandwidths compatible with the FRT implemented with a given GDD  $\Phi_2$  and assuming a temporal aperture at the EOM of  $D_t=24.3~\mathrm{ps}.$  (right axis) Corresponding FRT angle  $\alpha$  assuming a chirp rate of  $K=6.80\times10^{-2}~\mathrm{ps}^{-2}.$ 

ideal quadratic phase modulation with an equivalent cosine modulation, both centered at t=0. The argument t for which the cosine modulation deviates by 5% from the quadratic approximation is taken as half of the temporal aperture. In our case  $\mathcal{D}_t=0.34\times f_m^{-1}\approx 24.3\,\mathrm{ps}$ . Note that the limitation to the optical pulse duration due to the temporal aperture should be considered after the pulse passes through the stretcher and is elongated due to  $\Phi_2$ .

We will assume Fourier-limited Gaussian pulses with the intensity in time having  $\Delta_t$  FWHM. After the stretcher, this width will be transformed to [228]

$$\Delta_t^{\text{post}} = \Delta_t \sqrt{1 + \left(4\log(2)\frac{\Phi_2}{\Delta_t^2}\right)^2}.$$
 (5.24)

The constraint due to the temporal aperture reads  $\Delta_f^{\rm post} \leq \mathcal{D}_t$ . With the property of Fourier-limited pulses  $\Delta_t \Delta_\omega = 4 \log 2$ , we can write the bounds on the optical bandwidth

of initial pulses, in terms of the spectral intensity FWHM  $\Delta_f = \Delta_\omega/(2\pi)$ 

$$\Delta_f^{(-)} \le \Delta_f \le \Delta_f^{(+)},\tag{5.25a}$$

$$\Delta_f^{(\pm)} = \frac{\mathcal{D}_t}{2\pi\sqrt{2}\Phi_2} \sqrt{1 \pm \sqrt{1 - \left(\frac{8\Phi_2 \log 2}{\mathcal{D}_t^2}\right)^2}}.$$
 (5.25b)

Let us consider the limit of  $\Delta_f^{(-)}$  with small  $\Phi_2$ :

$$\lim_{\Phi_2 \to 0} \Delta_f^{(-)} = \frac{2 \log 2}{\pi \mathcal{D}_t}.$$
 (5.26)

It just expresses that the initial pulse, even without the stretcher, must fit within the temporal aperture. In this regime the FRT bandwidth is asymptotically

$$\Delta_f^{(+)} - \Delta_f^{(-)} \sim \frac{1}{2\pi} \frac{\mathcal{D}_t}{\Phi_2}.$$
 (5.27)

On the other hand, with large  $\Phi_2$  obeying  $\xi := 1 - (8\Phi_2 \log 2/\mathcal{D}_t^2)^2 \to 0$  we have

$$\Delta_f^{(+)} - \Delta_f^{(-)} \to \frac{2\sqrt{2}\log(2)}{\pi} \times \frac{\sqrt{\xi}}{d}.$$
 (5.28)

Figure 5.7 depicts the FRT bandwidth  $\Delta f$  alongside corresponding FRT angles  $\alpha$ , as a function of  $\Phi_2$ . A chirp rate of  $K=6.80\times 10^{-2}\,\mathrm{ps^{-2}}$  is assumed. With our experimental value of  $\Phi_2=15.5\,\mathrm{ps^2}$ , we get  $18.2\,\mathrm{GHz} \leq \Delta_f \leq 248.9\,\mathrm{GHz}$ .

Decreasing the GDD  $\Phi_2$  increases the FRT bandwidth; however, for a fixed angle  $\alpha$  would require a higher chirp rate K which with a given modulation frequency  $f_m$  would need higher RF power or a smaller  $V_{\pi}$  of the EOM.

Under the current capabilities of our experimental setup,  $\Phi_2$  could be increased several

times (even just by increasing L). Such an alteration would narrow the FRT bandwidth  $\Delta f$  yet increase the maximal FRT angle  $\alpha$ . For the experiment we selected  $\Delta_f \approx 74 \, \mathrm{GHz}$ .

Finally, let us note that a similar analysis of the optical bandwidth limits can be found in Refs. [231, 232].

# 5.5.8 Spectrometers



Figure 5.8: Photograph of the single-photon spectrometer.

We use two different spectrometers, albeit with a similar design, to measure the spectral intensity in the bright-light and in the single-photon-level regimes.

The bright-light spectrometer is the same device as used in our previous experiment and has been described in sec. 4.4.2 and in ref. [233].

The single-photon-level spectrometer employs a double pass through a diffraction grating (second-order diffraction,  $1200 \, \mathrm{ln} \, / \mathrm{mm}$ ). For the detection, we use our custom single-photon camera (c.f. chapter 1). The spectrometer input is fiber-based. A collimator produces a beam with ca.  $10 \, \mathrm{mm}$  diameter. The incidence angle onto the grating (in the horizontal plane)  $\theta_i$  is ca.  $67^\circ$  and the diffraction angle  $\theta_d$  is very close to  $90^\circ$ . The second pass is implemented with a retro-reflecting prism introducing a vertical shift of ca.  $10 \, \mathrm{mm}$  and routing the m=2 diffracted order back onto the grating. After the second pass the

diffracted beam returns alongside the input beam but at a different height and is picked by a D-shaped mirror. A lens (focal length  $f=400\,\mathrm{mm}$ ) far-field images the grating onto the camera. A photograph of the spectrometer is depicted in Fig. 5.8.

With the camera, we gather  $50 \times 400$  pixel frames at  $2 \times 10^4$  frames per second. The image intensifier gating time is  $20~\mu s$ . Each camera pixel corresponds to 1.67~GHz in frequency. This scaling has been calibrated with an interferometric measurement of the fringe density for a pair of coherent pulses with a known temporal separation.

The resolution of the spectrometer is limited by the diffraction grating and theoretically given by [234]:

$$\delta f = 2 \times \frac{c}{W|\sin\theta_i + \sin\theta_d|} \le \frac{c}{W},\tag{5.29}$$

with  $\theta_i$ ,  $\theta_d$  considered positive on the same side of a normal to the grating surface,  $W \approx 19.2 \, \mathrm{mm}$  denoting the diameter of the beam area on the grating surface (including elongation effects), c being the speed of light, and the 2 factor stemming from the double pass. In our setup  $\delta f \approx 8 \, \mathrm{GHz}$ .

The double-pass second-order diffraction configuration provides a high resolution, albeit at a cost of low efficiency which in our case is  $\approx 4 \times 10^{-5}$ .

## 5.6 CONCLUSION

In this chapter, we have described an ultrafast electro-optic implementation of a coherent time-frequency transformation – the Fractional Fourier Transform. Quadratic electro-optic phase modulation implements the time lens – a crucial component of an optical FRT, avoiding inherent noise present in implementations based on non-linear optical interactions, hence facilitating single-photon-level operation.

A careful design of the RF line shaping the EOM-driving signal ensures an all-electronic,

precise control of the FRT angle  $\alpha$  and avoids detrimental phase shifts of the RF signal when changing  $\alpha$ . Notably, the presented FRT implementation promises good scalability, being based on optical devices with on-chip or fiber-based equivalents available.

In our proof-of-principle experiment, we have demonstrated the FRT operation on an exemplary state of two coherent pulses (single-photon level or bright) separated in time.

After the FRT, the spectrum of this probe states provides a characterization of the transformation itself. An excellent agreement with a semi-independent model is observed.

The merits of the electro-optic FRT make it a good candidate for a building block of complex time-frequency domain quantum optical protocols. Possible applications include mode-sorting, super-resolution imaging (c.f. chapter 6), engineering of unitary transformations, quantum time-frequency processors [183, 235], or mode-division multiplexing protocols [236].

6

# Super-resolution of ultrafast pulses via spectral inversion

# 6.1 Foreword

In this chapter, we present a spectral-domain super-resolution method for ultrafast pulses, which we call Super-resolution of Ultrafast pulses via Spectral Inversion (SUSI). The experiment builds on the apparatus and expertise from Chapters 4 and 5 and concludes this

thesis. In particular, the ability to implement a Fractional Fourier Transform (c.f. Chapter 4) proves indispensable to the SUSI setup.

In a wider context, SUSI is a simple 2-mode implementation of a spectral mode sorter. As further outlined, it could be in principle expanded to multiple modes, and implemented with on-chip and fiber components only. These features combined with the single-photon-level compatibility (due to electro-optic time lenses, c.f. Chapter 4) make it a prominent platform for spectro-temporal quantum information processing. Frameworks that employ the time-frequency domain in this context have been recently proposed [78] and offer many advantages over spatial multiplexing such as compatibility with existing single-mode fiber architecture.

This chapter is based on ref. [237]

#### 6.2 Introduction

We shall consider the fundamental concept of resolution in measurement. While very intuitive and omnipresent, it is not straightforward to rigorously describe. In 1879 Lord Rayleigh formulated a practical limit, known as the Rayleigh limit, to the resolution in optical imaging [238]. The spectral domain has its analog of the Rayleigh limit, called the Fourier limit. Both descriptions are essentially similar and formulate the resolution in terms of a minimal image-plane separation between incoherent equally bright emitters. Since such formulations depend on the imaging system's point spread function (PSF), they are not very general or precise. Nevertheless, the Rayleigh or Fourier limits provide useful order-of-magnitude estimates.

A quantitative and more rigorous treatment of resolution was brought by the asymptotic parameter estimation theory [239]. On its grounds, the problem is formulated as a

task of estimating a separation (our parameter) between two emitters. In the simplest scenario, the emitters are incoherent, equally bright, and emit much less than 1 photon per coherence time. Compared to the formulations based on the PSF, the estimation theory brings a notion of resources. In this case, the resource may correspond to the number of collected photons or the allocated measurement time. This way, the resolution limit is no longer a sharp border between what can and cannot be resolved but rather expresses a resource cost associated with the required measurement precision. Well below the Rayleigh or Fourier limit, the resource cost becomes infeasible and in this sense the two formulations are equivalent. Notably, there are still limitations to such a treatment. Ultimately its results are accurate only in the asymptotic limit of many repetitions of an identical experiment. By no means, does it exhaust the experimental scenarios which may for instance include adaptive measurements. Some of these limitations are addressed in the framework of Bayesian estimation [154].

A clever combination of the estimation-theoretic treatment and a set of methods from quantum optics (without actually dealing with non-classical states) recently brought a groundbreaking realization of how the Rayleigh or Fourier limits may be beaten by carefully designing the measurement. Tsang  $et\ al.$  observed that the essential information contained in the phase of the complex-valued electromagnetic field E(f) is lost during imaging with quadratic-response photodetectors (direct imaging – DI) which measure the intensity  $\propto |E(f)|^2$ . However, the information can be efficiently extracted by a scenario-dependent change of measurement basis i.e. mode sorting before the intensity measurement [240]. This seminal quantum-inspired treatment has met with a great interest in the field and stimulated enormous efforts reflected in numerous theoretical extensions and experimental demonstrations [65, 241–260].

Super-resolution refers to the ability to surpass the classical Rayleigh or Fourier limits of

direct imaging. Most demonstrations are concerned with the problem of far-field imaging e.g. estimation of the angular separation between distant celestial objects. However, in the spectral domain, the experimental demonstrations are surprisingly scarce. Even if via the space-time analogy [222] the problem of spectral resolution is analogous to 1-dimensional imaging [261]. Notable implementations include an application of a quantum pulse gate as the mode demultiplexer [87, 262], heterodyne detection and mode-sorting in post-processing [263], and a quantum-memory-based protocol employing time-axis-reversal interferometry [30, 264]. The latter uses a very similar principle to the method we will describe. Nevertheless, these conceptually similar protocols, are very different in their implementation and target disparate spectral-bandwidth regimes (here on the order of 100 GHz, their on the order of tens of kHz).

Let us note that the term super-resolution often refers to a broader class of methods encompassing e.g. laser spectroscopy [265] and in the regime of quantum technologies to various methods employing engineered states of non-classical light for probing [52, 266, 267]. We shall focus on a scenario where the illumination cannot be controlled, and the light is incoherent and dim (on average below 1 photon per coherence time). It is for instance the case in fluorescence spectroscopy or stellar observations [268]. The former is predominantly a tool of organic chemistry, medicine, and biology [269].

SUSI is inspired by the image inversion interferometry – a method demonstrated to improve the resolution in spatial imaging [243, 244, 246, 270]. The spectral inversion in SUSI refers to the analog of image inversion in the real space. The input state of light is equally split into two arms of a Mach-Zehnder-type interferometer. In one of the arms the spectral mode of the state is inverted with respect to an *a priori* known centroid. This way, the output ports (labeled  $\pm$ ) of the interferometer contain the symmetric (+) and antisymmetric (–) parts of the spectral mode, respectively. The output states undergo photon counting.

Let us consider an incoherent mixture of two pulses that are of slightly different frequency (have a small separation between their spectra, relative to the spectrum width) and otherwise identical. Notably, if the setup is free of imperfections, and the separation is set to 0, the input state has only a symmetric component and the (—) output port remains dark. As soon as the separation is increased from 0 (i.e. one of the pulses shifts to lower frequencies while the other to the higher) each pulse contributes a small fraction of power to the antisymmetric mode. This way, the number of photons detected in the (—) port can be used to estimate the separation with high precision. Since we started from a completely dark (—) port, such a measurement has no background noise and provides a very efficient estimator. Of course in a realistic scenario, the interference visibility will be limited. Some of the main limiting factors are that the spectral mode of each pulse should be ideally symmetric to begin with and the interferometer has to remain stable throughout the measurement.

We can also imagine that instead of counting the photons in the  $\pm$  ports, the output modes are further processed, each in another SUSI interferometer. Such a setup would require many stable interferometers connected with linear optics, and as such would be most practical if implemented on-chip. We note that a very similar proposal has been recently described and analyzed in ref. [271]. There are also alternative approaches to ultrafast spectral mode sorting, based on a cascade of intertwined temporal phase modulations and spectral diffraction [272].

# 6.3 Theory

The spectroscopic equivalent of direct imaging would involve collecting a statistic of N photons with a spectrally-resolving detector. The observed photon counts would be binned according to their frequency and with an assumed statistical model an estimator would be

constructed (e.g. a maximum likelihood estimator) for the measured parameter (here the spectral separation between the pulses). Naturally, if N is increased (in most cases the measurement or averaging time) the estimator variance will be lower. Hence, there is no sharp border between the regime of parameters below and above the resolution. Even when the spectral features of width  $\sigma$  will be separated by  $\delta f$  obeying  $\varepsilon = \delta f/\sigma \ll 1$ , direct imaging remains an unfeasible but possible approach. We shall now quantify how the problem can be formulated in terms of the used resources (number of observed photons N) for a maximal acceptable variance  $\Delta^2 \hat{\varepsilon}$  of an estimator  $\hat{\varepsilon}$ .

In this context, the paradigm of frequentist inference brings a very convenient tool in the form of the Cramér–Rao bound and Fisher Information [154]. The former bounds the variance of any unbiased estimator

$$\Delta^2 \hat{\varepsilon} \ge \frac{1}{F(\varepsilon)},\tag{6.1}$$

with  $F(\varepsilon)$  denoting the Fisher information for  $\varepsilon$  corresponding to a measurement scheme described by possible outcomes  $\{i\}$  and probabilities of these outcomes  $\{P(i|\varepsilon)\}$  conditioned on the true value of  $\varepsilon$ . The Fisher information is given by

$$F(\varepsilon) = \sum_{i} \frac{\left(\partial_{\varepsilon} P(i|\varepsilon)\right)^{2}}{P(i|\varepsilon)}.$$
(6.2)

Under our assumptions of a low number of photons per coherence time (well discussed in ref. [240]), the probabilities  $\{P(i|\varepsilon)\}$  will follow a Poisson distribution with means  $\mu_i(\varepsilon) = Np(i|\varepsilon)$ , where  $p(i|\varepsilon)$  corresponds to a probability of a given measurement outcome for a single photon. With Poisson-distributed probabilities, the estimator variance exhibits shot-noise scaling  $\Delta^2 \hat{\varepsilon} \propto 1/N$  or  $F \propto N$  which can be readily seen by substi-

tuting the distribution into Eq. (6.2). Henceforth, we will consider Fisher information per photon  $\mathcal{F}=F/N$  which is equivalent to substituting  $P(i|\varepsilon)\to p(i|\varepsilon)$  in Eq. (6.2).

Let us limit our discussion to a pair of fully incoherent pulses with equal energy and an a priori known spectral centroid. Extensions beyond this simple scenario have been extensively studied in the spatial domain [273–277]. We note that in a practical scenario where the centroid is unknown a part of the allocated resources will be first used to estimate the centroid. Adaptive strategies are possible [278]. For clarity, we shall employ dimensionless quantities – the frequency  $\xi = f/\sigma$  and pulse separation  $\varepsilon = \delta f/\sigma$ . We will denote by  $\mathcal{A}(\xi)$  the slowly varying envelope of a single pulse's electric field in the spectral domain. It is assumed to be symmetric  $\mathcal{A}(\xi) = \mathcal{A}(-\xi)$  and normalized

$$\int d\xi |\mathcal{A}(\xi)|^2 \xi^2 = \int d\xi |\mathcal{A}(\xi)|^2 = 1.$$
(6.3)

Conveniently, with a fully incoherent mixture of two  $\pm \varepsilon/2$  pulses  $\mathcal{A}(\xi \pm \varepsilon/2)$ , we can calculate the result of our experiment for each pulse separately. Ultimately, photon counts for  $\pm \varepsilon/2$  cases will be added together.

# 6.3.1 SPECTRAL VERSUS SPATIAL DOMAINS

Let us briefly note the main difference between our problem in the spectral domain and its analog in 1-dimensional spatial imaging. Here the pulse spectral width is the scale parameter of the problem and at the same time an intrinsic property of the uncontrolled illumination. At the same time, we do not impose any restrictions on the resolving power of the instruments, even when considering the case of spectral direct imaging. This is in contrast to the far-field spatial imaging. There, the instrument's PSF determines the scale parameter and in the simplest case, the objects are point-like. This difference becomes substantial

when we compare SUSI with DI. If the spectral shape of the pulse contains rapidly changing components i.e. the pulse has a broad temporal shape, the DI will seemingly offer excellent performance. This is of course an artifact of our simplified analysis of the problem, since in any real scenario a spectrometer will have a PSF with a finite width. The temporal domain provides another view on this issue. If the pulse has a rapidly changing spectrum it must be temporally broad. The PSF of the spectrometer is equivalent to some temporal aperture (for instance corresponding to the exposure time of the detector). Notably, for SUSI a temporal aperture can also be identified and is associated with limitations of electrooptic modulation (c.f. sec. 5.5.7).

#### 6.3.2 Spectral inversion interferometry

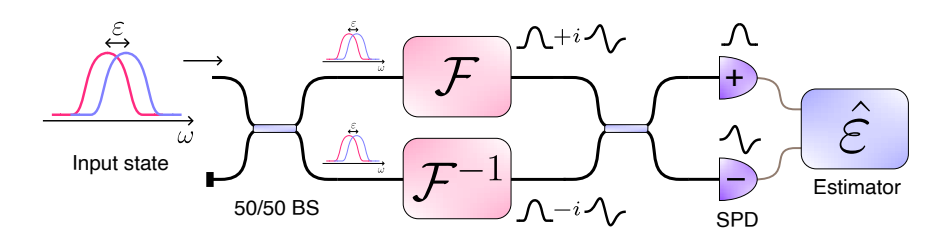


Figure 6.1: Schematic depiction of SUSI. Two incoherent pulses, with their spectra separated by  $\varepsilon$  and an *a priori* known centroid, are sent to a Mach-Zehnder-type interferometer. One of the interferometer arms contains a Fourier transform  $\mathscr{F}$  wile the other an inverse Fourier transform  $\mathscr{F}^{-1}$ . Their combined action will be equivalent to a spectral inversion in one of the arms only. The final beamsplitter of the interferometer separates the symmetric (+) and the antisymmetric (-) part of the input state spectral mode. The output ports undergo photon counting resulting in a better sensitivity in the estimation of  $\varepsilon$  than direct imaging (spectroscopy). 50/50 BS - balanced beam splitter, SPD - single photon detector.

The idea of SUSI has been depicted in Fig. 6.1. The main part of the setup consists of a Mach-Zehnder-type interferometer. In one arm of the interferometer, we place a device that performs a Fourier transform  $\mathscr{F}$  and in the other arm similarly an inverse Fourier transform  $\mathscr{F}^{-1}$ . Note that all elements are optically linear and the total energy of the

pulses does not change under the action of (inverse) Fourier transform (Parseval's theorem). Hence, the setup is equivalent to an interferometer with one arm empty and a series of two Fourier transforms in the other arm. Such a composition performs the spectral equivalent of image inversion  $\mathscr{F}\circ\mathscr{F}[g(x)]=g(-x)$ . With the operation split into two arms, the efficiency and the higher-order imperfections in both arms are similar.

We will now calculate the photon counts in a SUSI setup for a single pulse  $\mathcal{A}(\xi - \varepsilon/2)$  assuming the regime of  $\varepsilon \ll 1$ . Let us series expand the pulse envelope in  $\varepsilon$ 

$$\mathcal{A}(\xi - \frac{\varepsilon}{2}) = \mathcal{A}(\xi) - \frac{\varepsilon}{2} \partial_{\xi} \mathcal{A}(\xi) + \frac{\varepsilon^2}{8} \partial_{\xi}^2 \mathcal{A}(\xi) + \mathcal{O}(\xi^3). \tag{6.4}$$

Clearly, the information on  $\varepsilon$  is carried by antisymmetric part  $\partial_{\xi} \mathcal{A}(\xi)$ . Omitting higher-order terms and performing the (inverse) Fourier transform ( $\xi \to \tau$ ) we can write

$$\mathscr{F}\left[\mathcal{A}(\xi - \frac{\varepsilon}{2})\right] = \tilde{\mathcal{A}}(\tau) \left[1 + i\tau \frac{\varepsilon}{2} - \frac{\varepsilon^2 \tau^2}{8}\right],\tag{6.5}$$

$$\mathscr{F}^{-1}\left[\mathcal{A}(\xi - \frac{\varepsilon}{2})\right] = \tilde{\mathcal{A}}(\tau)\left[1 - i\tau\frac{\varepsilon}{2} - \frac{\varepsilon^2\tau^2}{8}\right],\tag{6.6}$$

with  $\tilde{\mathcal{A}} = \mathscr{F}[\mathcal{A}]$ . We shall include the limited interference visibility  $0 \leq \mathcal{V} < 1$  and look at the spectral intensity  $I_{\pm}$  in the output ( $\pm$ ) ports

$$I_{\pm} = \frac{1}{4} \left( \left| \mathscr{F} \left[ \mathcal{A}(\xi - \frac{\varepsilon}{2}) \right] \right|^2 + \left| \mathscr{F}^{-1} \left[ \mathcal{A}(\xi - \frac{\varepsilon}{2}) \right] \right|^2 \right)$$

$$\pm \frac{\mathcal{V}}{2} \operatorname{Re} \left\{ \mathscr{F} \left[ \mathcal{A}(\xi - \frac{\varepsilon}{2}) \right] \mathscr{F}^{-1} \left[ \mathcal{A}(\xi - \frac{\varepsilon}{2}) \right]^* \right\}. \quad (6.7)$$

Using Eqs. (6.5) and (6.6) we have

$$I_{\pm}(\tau) = \left| \tilde{\mathcal{A}}(\tau) \right|^2 \left[ \frac{1 \pm \mathcal{V}}{2} \mp \frac{\mathcal{V}}{4} \tau^2 \varepsilon^2 \right] + \mathcal{O}(\varepsilon^3). \tag{6.8}$$

We will assume bucket single-photon detectors i.e. no resolution in frequency or time (at least not on the timescale of the pulses). This way, we may integrate over  $\tau$ . Using the Parseval's theorem,  $\mathcal{A}(\xi)$  normalization and omitting higher-order  $\varepsilon$  terms we get

$$n_{\pm} = \int d\tau \, I_{\pm}(\tau) = \frac{1 \pm \mathcal{V}}{2} \mp \frac{\mathcal{V}}{4} \varepsilon^2 \Delta, \tag{6.9}$$

$$\Delta = \int d\tau \left| \tilde{\mathcal{A}}(\tau) \right|^2 \tau^2, \tag{6.10}$$

where the variance  $\Delta$  is determined by the shape of a single pulse's spectrum. For reference, Gaussian pulses give  $\Delta_{Gauss} = 1/4$  in the dimensionless units.

We can now add together the photon count  $n_{\pm}$  for the  $\pm \varepsilon/2$  pulses. Employing Eq. (6.2) with  $P(i|\varepsilon) \to p(i|\varepsilon)$  and taking

$$p(\pm|\varepsilon) = n_{\pm}/(n_{+} + n_{-}), \tag{6.11}$$

the Fisher information per photon  $\mathcal{F}(\varepsilon) = F(\varepsilon)/N$  is given by

$$\mathcal{F}(\varepsilon) = \frac{\mathcal{V}^2}{1 - \mathcal{V}^2} \frac{\varepsilon^2 \Delta^2}{\left(1 - \frac{\varepsilon^2 \Delta}{2}\right)^2} = \frac{\mathcal{V}^2 \Delta^2}{1 - \mathcal{V}^2} \varepsilon^2 + \mathcal{O}(\varepsilon^3). \tag{6.12}$$

# 6.3.3 Super-resolution parameter

The Quantum Fisher Information (QFI) upper-bounds the Fisher Information over the set of all measurement schemes. In a perfect scenario of perfect visibility  $\mathcal{V}=1$  and an equally bright, incoherent pair of pulses, the QFI remains constant regardless of  $\varepsilon$  [240]. Nevertheless, any imperfection deteriorates the QFI to a  $\propto \varepsilon^2$  scaling [279, 280]. Since a quadratic scaling is expected, the comparison of the scaling factors constitutes a meaningful way to compare super-resolution protocols. We follow ref. [264] and define the super-resolution

parameter as

$$\mathbf{s} = \lim_{\varepsilon \to 0} \frac{\mathcal{F}_{\text{SUSI}}(\varepsilon)}{\mathcal{F}_{\text{DI}}(\varepsilon)}.$$
 (6.13)

The super-resolution factor of s can be understood as a reduction by s (compared to DI) in the number of required resources for a given precision. For instance, let use analyze the case of Gaussian pulses. We have  $\mathcal{F}_{SUSI}^{(Gauss)} = \varepsilon^2/16 \times \mathcal{V}^2/(1-\mathcal{V}^2)$  and  $\mathcal{F}_{DI}^{(Gauss)} = \varepsilon^2/8$ , so  $s^{(Gauss)} = 1/2 \times \mathcal{V}^2/(1-\mathcal{V}^2)$ . In the case of Gaussian pulses, SUSI would require visibility of more than ca. 81.7%. to outperform DI.

We shall also note that as  $\varepsilon$  approaches 0 (limit of  $\varepsilon \to 0$ ), a large part (fraction of  $(1 + \mathcal{V})/2$ ) of Fisher information  $\mathcal{F}_{SUSI}$  corresponds to the dark port (–) measurement alone. E.g. with our experimental  $\mathcal{V}=93\%$ , this fraction is 96.5%.

# 6.4 EXPERIMENT

## 6.4.I SETUP

Figure 6.2 depicts the experimental setup for SUSI. The main part is a Mach-Zehnder-type interferometer with electro-optic (inverse) Fourier transformers in its arms. Each (inverse) Fourier transformer comprises a pulse stretcher with the group delay dispersion (GDD)  $\Phi_2$ , an electro-optic time lens with a chirp rate of  $K=1/\Phi_2$ , and the second pulse stretcher with a GDD of  $\Phi_2$ . Direct Fourier transform requires K>0, while the inverse K<0. The frequency with the shortest optical path in the pulse stretcher determines the central (0) frequency of the transform. The transformers are just the Fractional Fourier Transform setups, described in detail in chapter 5, set to  $\alpha=90^\circ$  and extended to include the final pulse stretcher.

Since the interferometer comprises a spatially large setup with meters of fiber and free space lines, it has to be actively stabilized. This is achieved with an intermittent continuous-

wave (CW) laser reference bean. For details see sec. 6.4.5.

Our input state is prepared with a custom pulse shaper. It consists of diffraction grating followed by a folded telescope with unit magnification. In the Fourier plane of the telescope, a slit with regulated width and lateral position is placed. The retro-reflecting mirror which folds the telescope is placed in the near-field of the slit. As in other experiments, we start with  $100 \, \mathrm{fs}$  pulses from a Ti:Sapphire laser (SpectraPhysics MaiTai). The spectral width after filtering is  $85 \, \mathrm{GHz}$  full width at half maximum. The motorized lateral movement of the slit shifts the central frequency and effectively alters  $\varepsilon$ . Details are given in sec. 6.4.5.

## 6.4.2 RESULTS

Figure 6.3 depicts the experimental results. First, we place a spectrometer at the output of the SUSI interferometer and observe how shifting the central frequency of a single input pulse changes the spectrum. The results are depicted in Fig. 6.3 (a). Then the spectrometer is replaced with a pair of single-photon bucket detectors at the  $\pm$  output ports of the interferometer. Photon counts undergo time-tagging and temporal histograms are constructed, as depicted in Fig. 6.3 (b). For clarity of presentation, the regime of large  $\varepsilon$  is compared with  $\varepsilon=0$ . During the main SUSI measurement, similar histograms  $h_{\pm}(t,\varepsilon)$  are collected and further integrated over the measurement period  $n_{\pm}(\varepsilon)=\int {\rm d}t \ h_{\pm}(t,\varepsilon)$ . Such results are accumulated and added together over the course of many experiment repetitions. Finally, we estimate the conditional probability of observing a photo count in the dark port  $p(-|\varepsilon)$  as the fraction photon counts in this port. We then fit a parabolic model, given by Eqs. (6.9) and (6.11) to  $p(-|\varepsilon)$ . This allows us to calculate the corresponding Fisher information using Eq. (6.12). Experimental  $p(-|\varepsilon)$  together with a parabolic fit and the result of SUSI simulation is depicted in Fig. 6.4.2 (c). Ultimately, the Fisher information per pho-

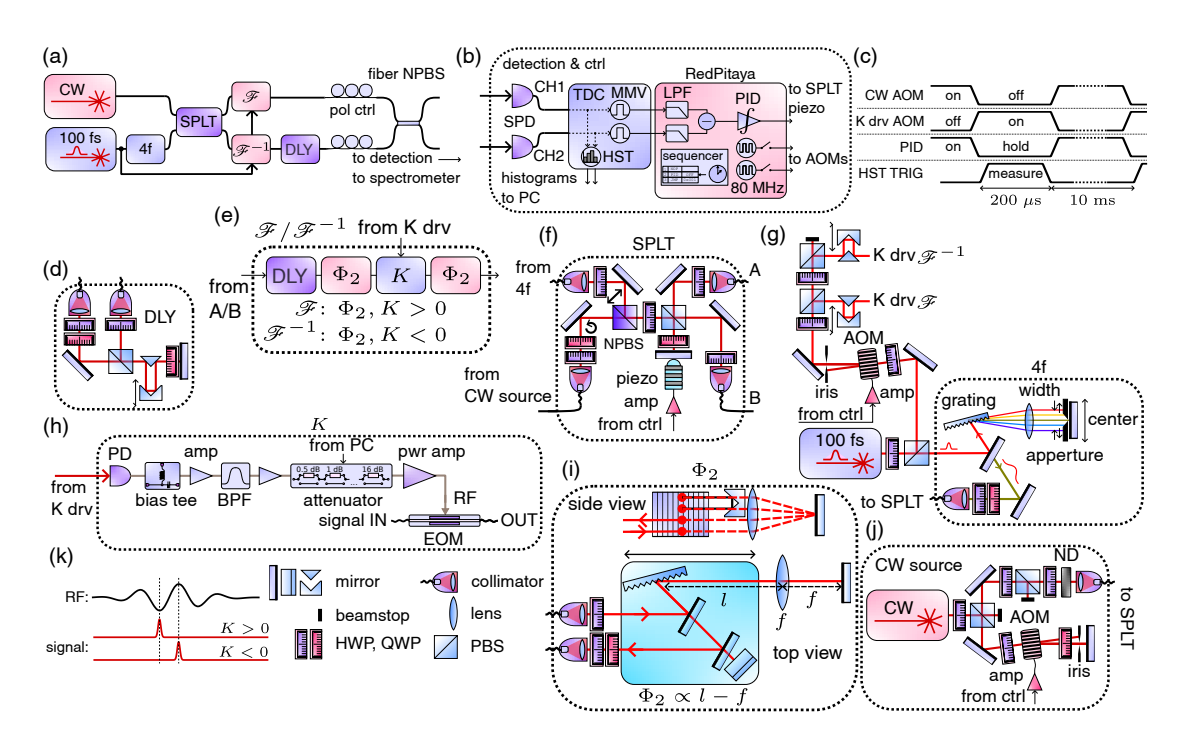


Figure 6.2: (a)-(j) SUSI setup and the experimental sequence. (a) High-level schematic depicting the Mach-Zehnder-type actively phase-stabilized interferometer with electro-optic (inverse) Fourier transformations in the arms. (b) Photon-counting detection followed by the time-to-digital converter (time-tagger), histogramming module, and digital-domain signal processing implemented in an FPGA (RedPitaya). During the phase-stabilization period, photon counts are processed via the FPGA-based feedback loop. (c) Experimental cycle controlled from the FPGA-based sequencer. (d) Free space delay line with a quadruple pass. (e) Schematic of the (inverse) Fourier transformer  $\mathscr{F}(\mathscr{F}^{-1})$ . (f) Part of the setup splitting the signal pulses and injecting the CW reference beam. (g) Splitting of the initial  $100\,\mathrm{fs}$  pulses. A small power fraction drives the time lenses and the rest is filtered to produce the signal pulses. (h) Schematic of the electro-topic time lens. The RF setup is slightly improved since the experiment of Chapter 5. (i) Schematic of the pulse stretcher. (j) CW reference beam switching facilitated with a double-pass acousto-optical modulator (AOM). (k) RF driving signal and the optical pulse have to be properly synchronized to produce a quadratic phase modulation for the time lens with the desired sign of the chirp rate K. HWP (QWP) – half-(quarter-)waveplate, (N)PBS - (non) polarizing beamsplitter, piezo - piezoelectric actuator, amp - amplifier, EOM - electro-optical modulator, BPF - bandpass filter, pol ctrl - fiber polarization controller, SPD - single-photon detector, PID - proportional-integral controller, HST - histogramming module, TDC - time-digital converter, MMV - monostable multivibrator, LPF - low-pass filter, ND - neutraldensity filter.

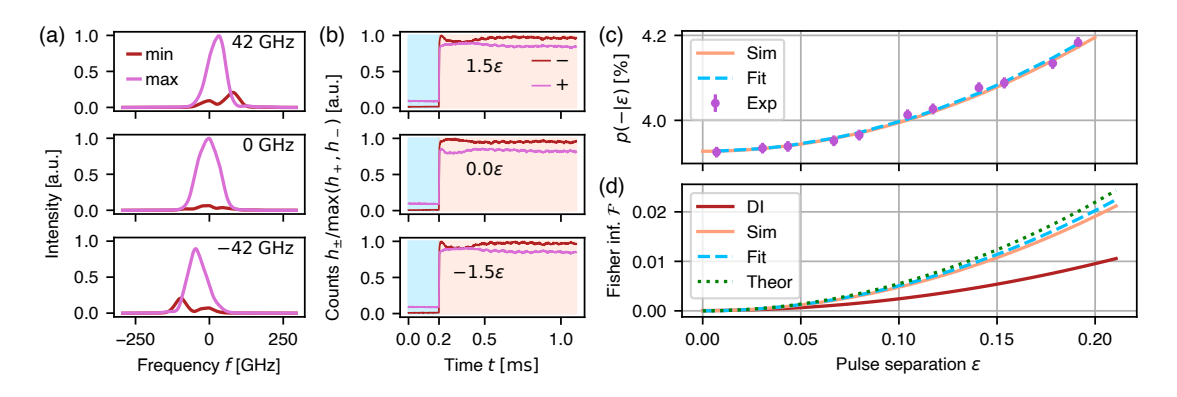


Figure 6.3: (a) Spectra collected at the output of the SUSI interferometer for a single input pulse with the frequency shifted by 0 or  $\pm 42\,\mathrm{GHz}$  from the central frequency of the Fourier transformers. The interferometer phase is freely fluctuating. The presented spectra correspond to constructive (max) and destructive (min) interference. (b) Normalized histograms of single-photon counts observed at the  $\pm$  SUSI interferometer outputs. The measurement period ( $0 \le t \le 200~\mu\mathrm{s}$ ) and a part of the phase-stabilization period ( $t > 200~\mu\mathrm{s}$ ) has been depicted. Subsequent rows correspond to different shifts  $\varepsilon/2$  of the input pulse. (c) Fraction of the photo counts present in the (–) port  $p(-|\varepsilon)$  among all counts observed during the measurement period. Depicted data (Exp) corresponds to an incoherent mix of pulses separated in frequency by  $\varepsilon$ . The experimental result closely matches a parabolic fit (Fit) and a simulation (Sim) described in sec. 6.4.3. (d) Fisher information for  $\varepsilon$  estimation, per an observed photon  $\mathscr{F}$ . A model fitted to experimental data (Fit) is compared with the analytical model (Theor) and SUSI simulation (Sim) and bench-marked against the DI simulation detailed in sec. 6.4.4.

ton  $\mathcal{F}(\varepsilon)$  corresponding to either the parabolic fit, SUSI simulation, or DI simulation is depicted in Fig. 6.4.2 (d). For both simulations, an experimentally measured spectral intensity of the pulse (and a flat spectral phase) is assumed. Additionally, for the SUSI simulation, we take an independently measured interferometric visibility of 93%. The analytical model is based on the variance  $\Delta \approx 0.293$  calculated from the numerical Fourier transform of the experimental spectrum of the pulse.

Comparing the the parabolic fit to the data with the simulation of perfect DI we get a super-resolution parameter of s=2.13. A summary of results and used parameters is presented in Tab. 6.1.

A good agreement between the experimental results and both the analytical model and

simulation is observed. Via a measurement model fitted to the experimental data, we are able to demonstrate a super-resolution behavior with respect to the DI. It is quantified in terms of a higher Fisher information per photon regardless of the separation  $\varepsilon$ . While, our comparison is limited to the regime of small separations  $\varepsilon \ll 1$ , outside of this regime DI performs very well and is a standard method of choice. Higher Fisher information can be interpreted via the Cramér-Rao bound as a proportional reduction in the required number of observed photons for a given estimation precision.

## 6.4.3 SUSI SIMULATION

The SUSI setup has been simulated with the experimental imperfections accounted for in a single parameter – interferometric visibility  $\mathcal{V}=93\%$ . The input state was taken as a fully incoherent mixture of two identical pulses. Each pulse starts with a flat spectral phase and the spectral intensity as measured experimentally. Central frequencies of the pulses are chosen so that their separation is  $\varepsilon$ . Here we outline the simulation procedure:

1. We first collect an average experimental spectrum of a single pulse. The background of the spectrum is removed by fitting a mixture of linear and Gaussian functions and subtracting the best fit of the former.

**Table 6.1:** Results and parameters. Visibility of  $\mathcal{V}=93\%$  is assumed. DI – direct spectral imaging, Theor – analytical prediction, Sim – simulated result, Fit – fit to experimental data, Gauss – the case of Gaussian pulses.

	$\Delta$	$\partial_{\varepsilon}^2 \mathcal{F}(0)/2$	$\mathbf{s}$
DI	0.293	0.24	1
Theor		0.55	2.29
Sim		0.48	2.01
Fit		0.51	2.13
DI Gauss	1/4	1/8	1
Theor Gauss		0.40	1.60

- 2. The spectral envelope of the pulse is taken as the square root of such spectrum. If the values are negative (which happens rarely and far from the center of the pulse), they are replaced with zeros. The envelope is interpolated to a chosen numerical grid.
- 3. We shift the envelope by  $\varepsilon/2$ .
- 4. Such obtained signal is padded with zeros. We calculate both the fast Fourier transform (FFT) of the signal and its inverse (iFFT).
- 5. A beamsplitter transformation is calculated between the FFT part (*a*) and the iFFT part (*b*). Limited visibility is accounted for.

$$\tilde{c}_{\pm}(\varepsilon) = \frac{1}{2} \left[ \mathcal{V} | a \pm b |^2 + (1 - \mathcal{V}) \left( |a|^2 + |b|^2 \right) \right].$$
 (6.14)

6. We repeat the process for an opposite sign of  $\varepsilon/2$  and average the results.

$$c_{\pm}(\varepsilon) = \frac{1}{2}(\tilde{c}_{\pm}(\varepsilon) + \tilde{c}_{\pm}(-\varepsilon)), \tag{6.15}$$

7. Finally, the dark port fraction is calculated.

$$p_{\text{sim}}(-|\varepsilon) = \frac{c_{-}(\varepsilon)}{c_{+}(\varepsilon) + c_{-}(\varepsilon)}.$$
(6.16)

From the dark port fraction, we can calculate the Fisher information by fitting a parabolic model (exactly like with the experimental data).

## 6.4.4 Direct imaging

If Gaussian spectrum of the pulses is assumed, the Fisher information for DI can be calculated analytically  $\mathcal{F}_{DI} = \varepsilon^2/8$ . Nevertheless, our experimental spectrum cannot be well-enough approximated with a Gaussian since very small changes in the spectrum shape vastly affect  $\mathcal{F}_{DI}$ . It is a consequence of perfect DI (unlimited resolution) assumed for our discussion. Hence, to make the comparison with SUSI fair, we will use the experimentally measured spectrum and calculate the Fisher information for DI numerically. Here we outline the procedure:

- We prepare the spectrum in the same way as described in sec. 6.4.3.
- We add together two copies of the spectrum (not the spectral envelope) shifted by  $\pm \varepsilon/2$ , respectively.
- Such obtained signal is normalized to have a unit integral. We denote the result as  $\rho(f|\varepsilon)$ .

In each frequency bin (spectrometer pixel), whose center is denoted as f, the photo counts are distributed according to a Poisson distribution with a mean of  $N\rho(f|\varepsilon)$ . Here N is the total number of photons and we have  $\int \mathrm{d}f \, \rho(f|\varepsilon) = 1$ . Hence, the Fisher information reads

$$\mathcal{F}_{\mathrm{DI}} = \int \mathrm{d}f \, \mathcal{R}_{\mathrm{DI}}(f), \tag{6.17}$$

with the Fisher information density being

$$\mathcal{R}_{\mathrm{DI}}(f) = \frac{\left(\partial_{\varepsilon} \rho(f|\varepsilon)\right)^{2}}{\rho(f|\varepsilon)}.$$
(6.18)

This expression is evaluated numerically and integrated to  $\mathcal{F}_{DI}$ . Figure 6.4 depicts the Fisher information density for DI. A parabolic fit gives  $\mathcal{F}_{DI}=0.24\times\varepsilon^2$ .

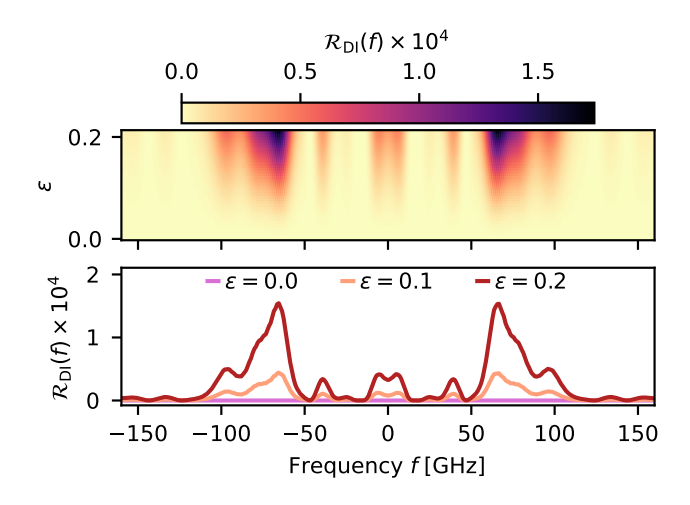


Figure 6.4: Numerical calculation of the Fisher information density in the frequency domain for the estimation of  $\varepsilon$  with DI. See main text for details.

# 6.4.5 SETUP DETAILS AND CALIBRATION

# Pulse preparation



Figure 6.5: Photographs of (left) the 4f spectral filter and (right) the electro-optic time lens.

Similarly to previous experiments, the pulse preparation begins with  $100~\rm fs$  of  $798~\rm nm$  central wavelength at a  $80~\rm MHz$  repetition rate from a Ti:Sapphire laser (Spectra-Physics

Mai Tai) with an average power of ca. 4 W. The pulses are spectrally filtered with a 4f filter depicted in Fig. 6.2 (g). It comprises a diffraction grating (1800 lines/mm) which is far-field imaged onto a rectangular slit with adjustable width and lateral position. The manually controlled width adjusts the bandwidth of the pulses (for the main experiment set to 85 GHz), while the motorized (stepper motor) lateral position changes the central frequency of the pulses. A retro-reflecting mirror is placed in the near-field of the slit. The reflected beam returns at a slightly different height which facilitates its outcoupling through a D-shaped mirror. The output pulses are fiber coupled to a polarization-maintaining single-mode fiber and travel to the SUSI interferometer. A photograph of the 4f filter is depicted in Fig. 6.5.

# Interferometer stabilization



**Figure 6.6:** Photograph of the double-pass AOM setup which switches on the CW reference beam during the stabilization period.

The experimental cycle, depicted in Fig. 6.2 (c), consists of a measurement period ( $200 \,\mu s$ ) and the interferometer stabilization period ( $10 \, m s$ ). During the latter, the optical signal driving the time lenses (K drv) is switched off with a (single-pass) acousto-optical modulator (AOM). Additionally, the programmable attenuator which is a part of each electro-

optic time lens is set to the maximal attenuation. The CW laser probe is switched on via a (double-pass) AOM setup, a photograph of which is depicted in Fig. 6.6

Figure 6.2 (a), (f), and (j) depicts how the CW reference beam and the signal light are spatially overlapped and enter the interferometer together. The CW external cavity diode laser (Toptica DL pro 780) is tuned to match the central frequency of the pulse stretchers and signal pulses (for  $\varepsilon=0$ ). To combine the reference and signal beams we employ a non-polarizing balanced beamsplitter (NPBS). The reference beam has a circular polarization while the signal has a diagonal polarization. This way, there is a 90° phase delay between the electric field of the signal and the reference and the beamsplitter outputs. Only one of the output ports is used, hence approximately half of the power is lost. Let us set the interferometric phase such that the reference beam exits with equal power through the ( $\pm$ ) output ports of the SUSI setup. Due to the 90° phase delay between the signal and reference, in such a setting, the signal will only exit through one of the ports (+) while leaving the other dark (-). This way, during the stabilization period we can treat the difference between the number of photons in the  $\pm$  ports as an unambiguous and sensitive error signal. It would not be possible without additional intensity modulation of the reference beam if we kept the reference and signal in phase.

The reference beam is highly attenuated so that we can still use the same superconducting single-photon detectors (ID Quantique) as for signal light. The average number of photons during the stabilization phase is around  $5\times10^6$  counts per second in each port.

Figure 6.2 (b) depicts the processing of the photon counts. Raw signal from the detectors is discriminated and timestamped by a time-to-digital converter (ID Quantique ID900) which also implements a triggered generator (monostable multivibrator). For each photon count the generator outputs a normalized single pulse of 50 ns width. The pulses are sent to analog-digital converters of an FPGA board (RedPitaya + our custom system).

The FPGA implements lows-pass filtering, subtraction of the signals, and a proportional-integral controller (PID) in the digital domain. The pulses from both ports are filtered and their difference is used as the PID error signal. The output of the PID is fed to an on-board digital-analog converter and further to an external amplifier which drives a piezo-electric actuator placed within one of SUSI interferometer arms [c.f. Fig. 6.2 (f)].

Small experimental imperfections such as unequal efficiency of the interferometer arms, deviations from the 90° phase delay between the signal and reference, and imbalanced splitting of the NPBS can be corrected by fine-tuning the PID set-point.

For the measurement period, we stop the PID and hold the last value of its output. If the integral part of the PID overflows, it is reset to 0 instead of saturating. This is required since the interferometric phase is a periodic quantity.

Due to fast switching between the measurement and stabilization periods (limited by AOMs, on the order of at most a few  $\mu s$ ) we can employ short measurement windows (200  $\mu s$ ) avoiding phase drift during measurement. Since the interferometer is large and employs meters of fiber and free space lines, the unstabilized phase fluctuates rapidly and such a short window is required.

To control the experimental cycle we use a sequencer implemented within the FPGA with the ability to program the sequence from the PC.

#### FOURIER TRANSFORMER CALIBRATION

As detailed in Chapter 5, to configure the electro-optic Fractional Fourier transform setup as an ordinary Fourier transform ( $\alpha=90^\circ$ ) the two pulse stretchers of the setup should have the same GDD  $\Phi_2$ . Furthermore, to implement the inverse Fourier transform the same absolute value of the GDD with the opposite sign is required for the second pair of stretchers. To cross-calibrate the 4 stretchers we put each positive-dispersion one in se-

ries with a negative-dispersion one. Such a pair is then placed in a single arm of a Mach-Zehnder-type interferometer. The second arm consists of a regulated delay. We input a test pulse with ca. 500 GHz bandwidth (maximal for the our pulse shaper) into the interferometer. Its output is observed with a spectrometer. Observing the interference fringes, we set the delay to cancel the linear component of the spectral phase difference between the arms. The remaining fringes correspond to the difference between the quadratic phases of the two opposite-sign stretchers. This way we adjust the GDD of one of the stretchers (moving its platform with the grating, c.f. sec. 5.5.4). When the GDDs of both stretchers cancel each other, the fringes disappear. During the measurement, a piezo-actuator within the interferometer is slowly driven with a sine waveform so that we observe consistent fluctuations in the fringes.

The second requirement to achieve a Fourier transform concerns the chirp rate of the time lens  $K=1/\Phi_2$ . We perform a calibration measurement equivalent to the main experiment of Chapter 5. Two coherent temporally separated pulses are sent via the calibrated Fourier transform setup and observed with a spectrometer. We adjust the chirp rate K to observe a spectral separation between the pulses matching our theoretical prediction for the case of  $K=1/\Phi_2$ , where the value of  $\Phi_2$  is independently measured with the stationary phase point method (c.f. sec. 5.5.5).

#### SINGLE-PHOTON HISTOGRAMS

The temporal photon count histograms are collected within the TDC module. Histogramming is triggered by the FPGA sequencer. In each experimental cycle around  $3.5\,\mathrm{ms}$  histogram with 1  $\mu\mathrm{s}$  wide bins is gathered. The cycle is repeated at ca.  $100\,\mathrm{Hz}$ . PC controls the collection and storage of the histograms, settings of the sequencer, and position of the stepper motor ( $\varepsilon$ ). The stepper motor is driven with an ARM controller (stm32f103c8t6)

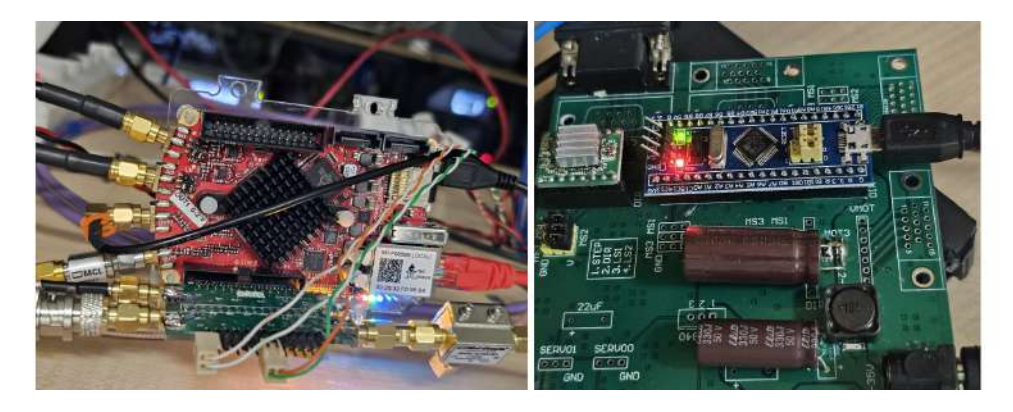


**Figure 6.7:** Photographs of (left) the FPGA (RedPitaya) board and (right) the stepper motor driver board with an ARM microcontroller.

and an integrated motor driver.

Photographs of the FPGA board and the stepper motor driver are depicted in Fig. 6.7.

## 6.5 Mode sorting

SUSI being a method based on the spatial-domain image inversion interferometry, fundamentally performs demultiplexing of the symmetric and antisymmetric part of the spectral mode of the input state. In the regime of small separations,  $\varepsilon \ll 1$  the spectral mode of the state can be decomposed into two orthogonal modes which correspond to these parts [240]. Hence, in this regime, SUSI implements a simple mode sorting of two modes. A further extension to more modes is possible and has been theoretically proposed [271]. In this case the setup consists of a network of SUSI interferometers connected with linear optics. Spectral mode sorting is particularly important for the rapidly developing field of time-frequency quantum information processing [78].

Another approach to spectral mode sorting has been proposed by Shah *et al.* [192]. The authors use a cascade of electro-optic phase modulations intertwined with spectral dispersers. While their method does not require a stabilized interferometer, the phase modu-

lation needs to be arbitrary (and not only parabolic) and is optimized on a scenario-specific basis. Hence, it would require much higher bandwidths of the phase modulation, making the solution unfeasible for tens-of-GHz bandwidth light. Furthermore, with the increasing number of sorted modes the setup grows in the number of elements in series leading to a rapid decrease in overall efficiency. In contrast, the depth of a network of SUSI interferometers would grow logarithmically.

## 6.6 Conclusion

In this final chapter, we have presented a frequency-domain super-resolution method that builds on the spatial-domain ideas of image inversion interferometry. SUSI is aimed at ultrafast pulses in the bandwidth regime of tens of GHz. We have studied a paradigmatic case of two incoherent closely separated spectral features under the conditions of dim ( $\ll 1$  photon per coherence time) and uncontrolled illumination. Compared with ideal direct spectral imaging, we demonstrated a two-fold reduction in the required number of photons (or the measurement time) for a given precision of estimating the separation between the features. SUSI is an optically-linear method applicable to single-photon-level light, in a wide range of wavelengths. Compatibility of the employed components with the on-chip integration and possible extensions to a network of SUSI interferometers promise further applications in spectroscopy and mode sorting.

## Conclusion

In this thesis, we have discussed a series of experiments in quantum optics with spectrally broadband light. Most of the studies employed a custom fast single-photon camera presented in chapter 1 and benefited from its high frame acquisition rates. In chapter 2 we have presented a measurement of hybrid 4-dimensional correlations between the spectral and transverse degrees of freedom for a pair of photons (a twin photon state). Chapter 3 outlines a dispersive spectroscopy method based on two-photon interference with spectrally resolved photon counting. From chapter 4 we turned more towards characterization

and transformation of single-photon-level ultrafast pulses (on the order of 10 ps). First, we presented an extension of the electro-optic shearing interferometry, based on the measurement of the second-order intensity correlation and not requiring a spectrometer. In chapter 5 we discussed an electro-optic implementation of the Fractional Fourier transform, a practical and fundamentally interesting time-frequency domain coherent transformation which generalizes the ordinary Fourier Transform. Finally, in chapter 6 we extended the setup to implement a frequency-domain super-resolution technique able to estimate the separation between two incoherent spectral features with a 2-fold improvement over the direct spectroscopic imaging.

The time-frequency domain of nonclassical and single-photon level light holds a vast potential for technological applications and fundamental studies. The variety of discussed quantum optical experiments – from studies of hybrid entanglement and quantum-enhanced spectroscopy to super-resolution methods – speaks to the versatility and universality of broadband light. Furthermore, considering the compatibility of spectrally multimode states with current fiber architectures and on-chip integrated photonic processing, the TF domain represents a prominent and practical development direction for near-term quantum-enhanced or quantum-inspired technologies.



Custom camera mechanical design

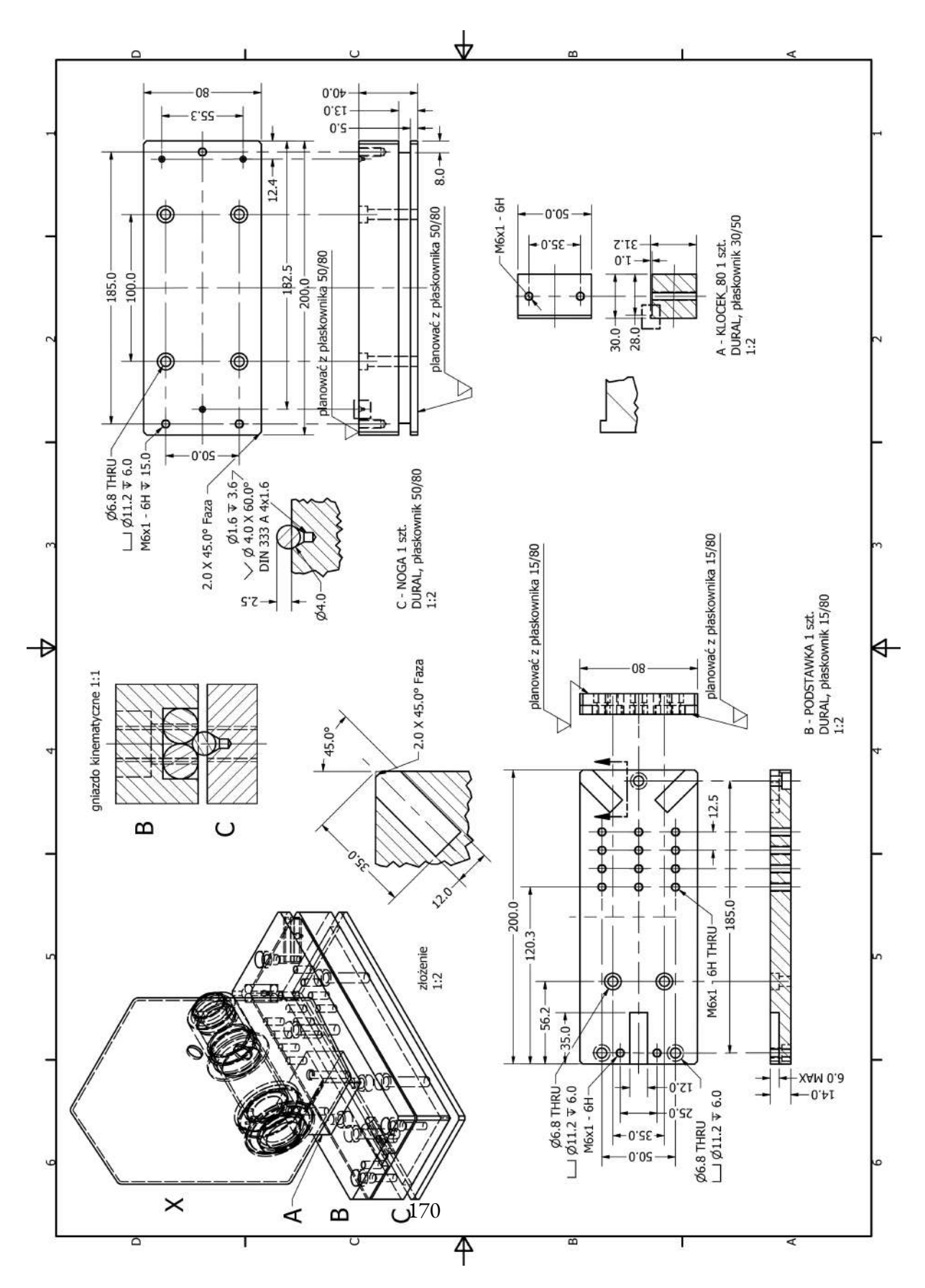


**Figure A.1:** Mechanical drawing of the custom camera housing, including enclosure and shielding of the image intensifier and the relay lens. The drawing is included only for illustrative purposes. The scale has not been preserved and the annotations have not been translated. Page 1.

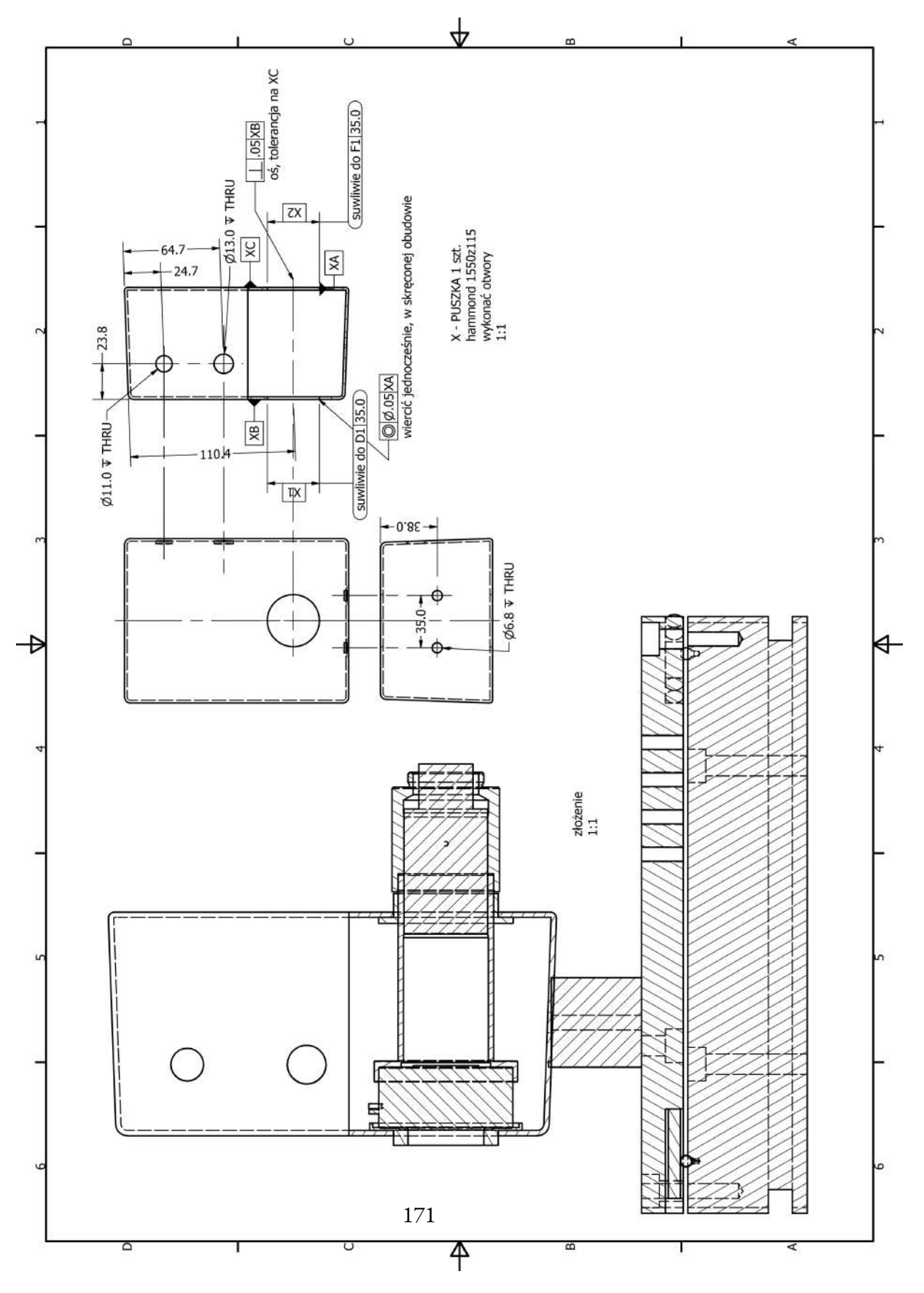


**Figure A.2:** Mechanical drawing of the custom camera housing, including enclosure and shielding of the image intensifier and the relay lens. The drawing is included only for illustrative purposes. The scale has not been preserved and the annotations have not been translated. Page 2.

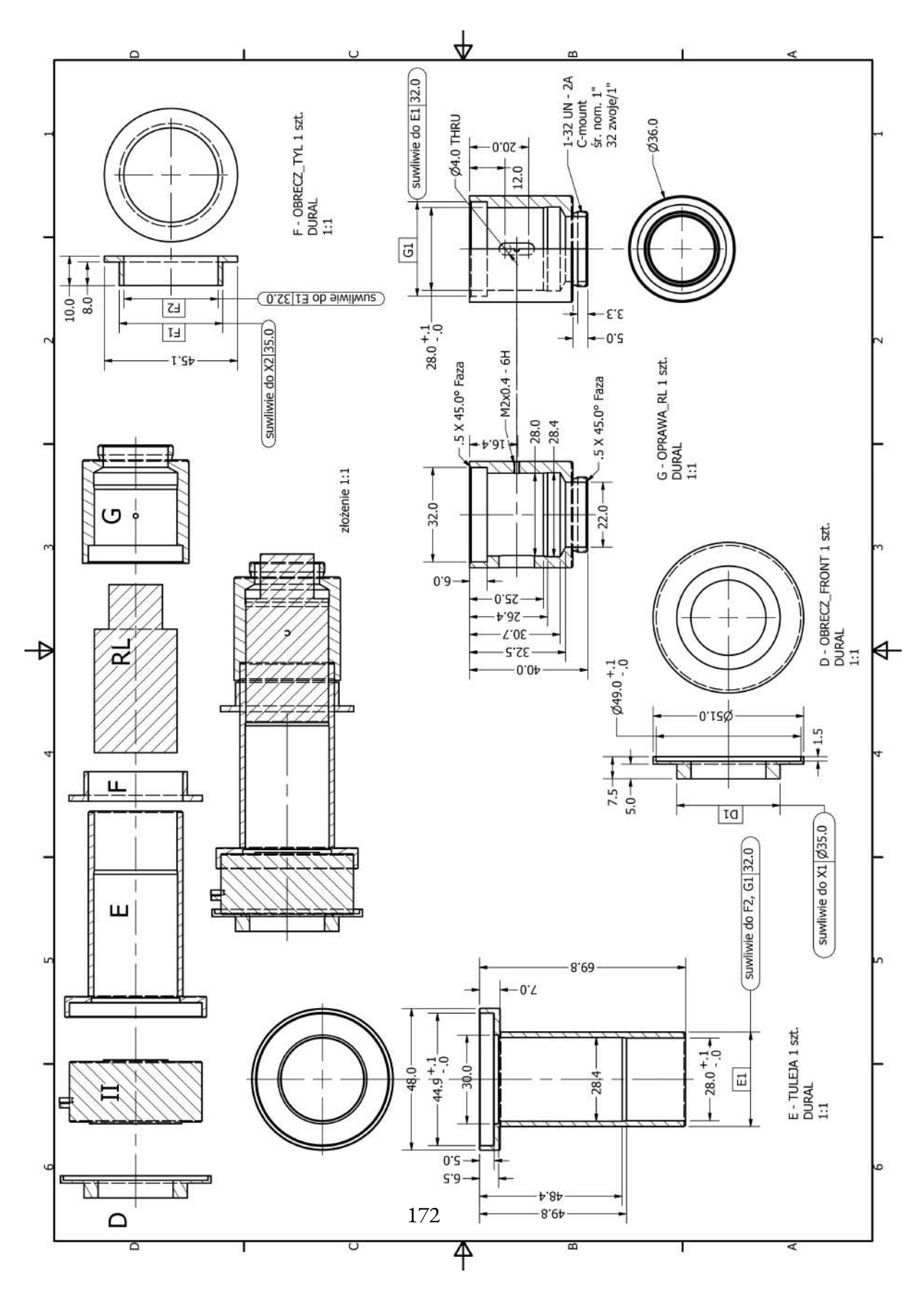


**Figure A.3:** Mechanical drawing of the custom camera housing, including enclosure and shielding of the image intensifier and the relay lens. The drawing is included only for illustrative purposes. The scale has not been preserved and the annotations have not been translated. Page 3.

## B

Schematics of the image intensifier gating driver

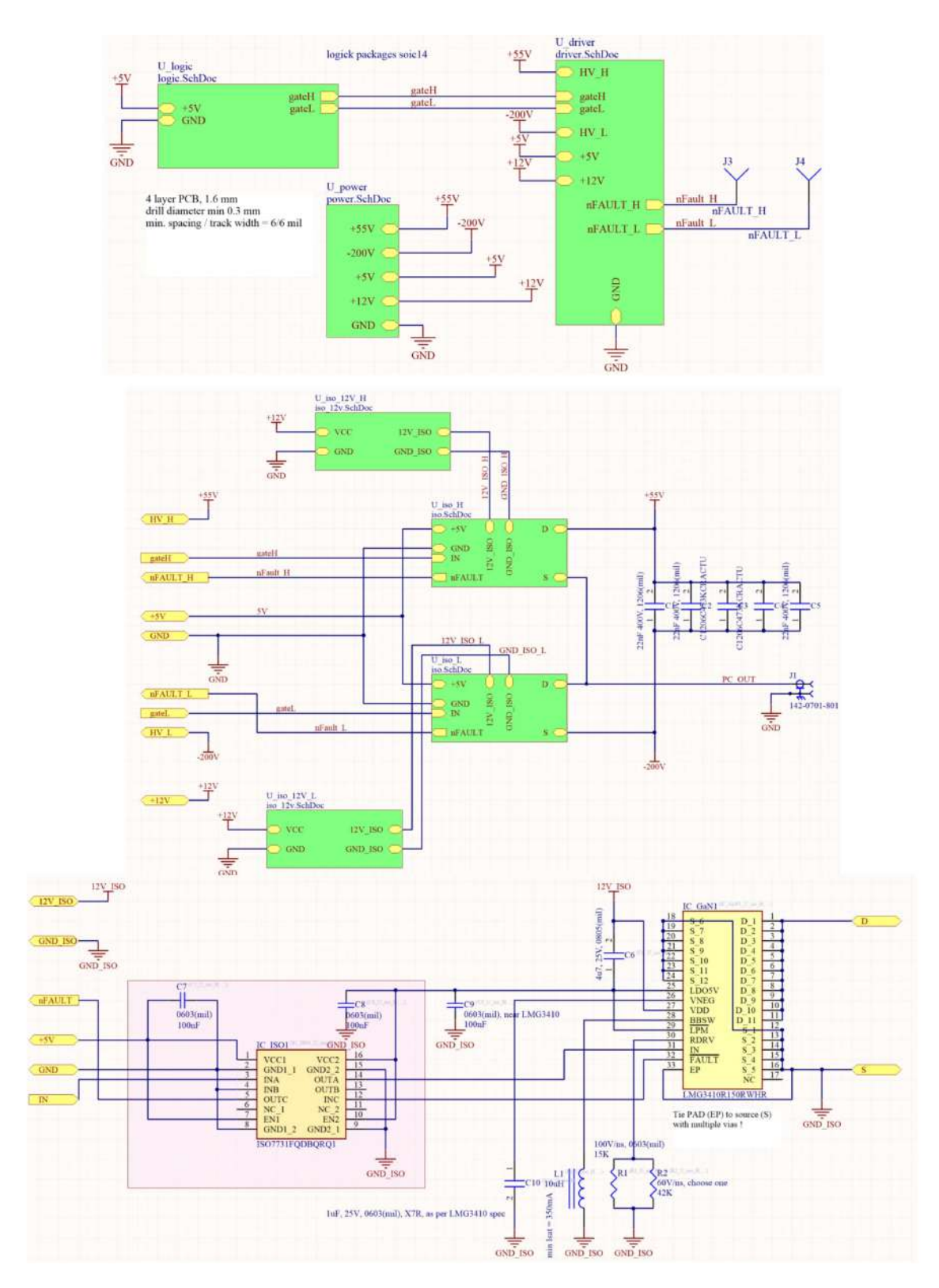
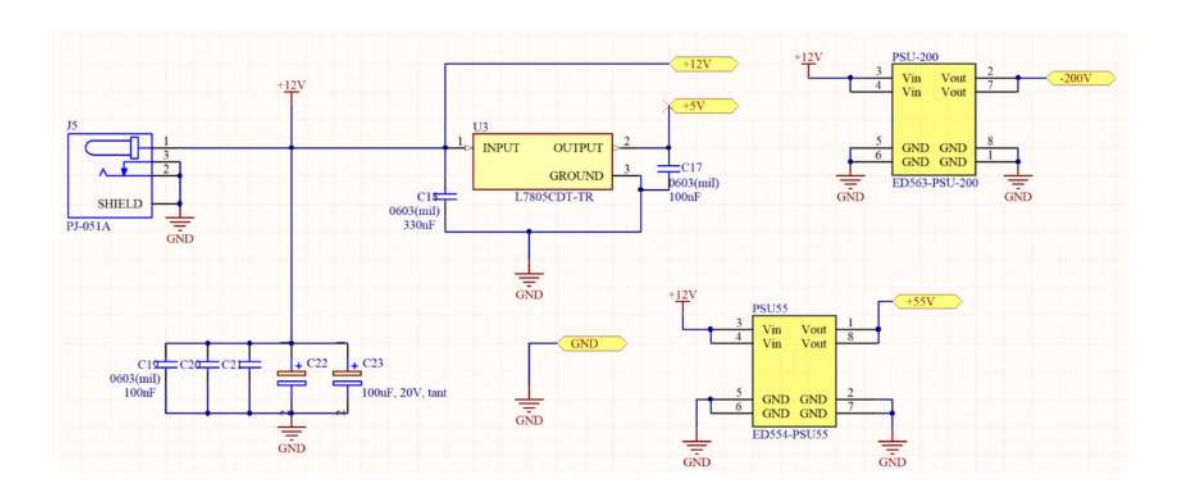
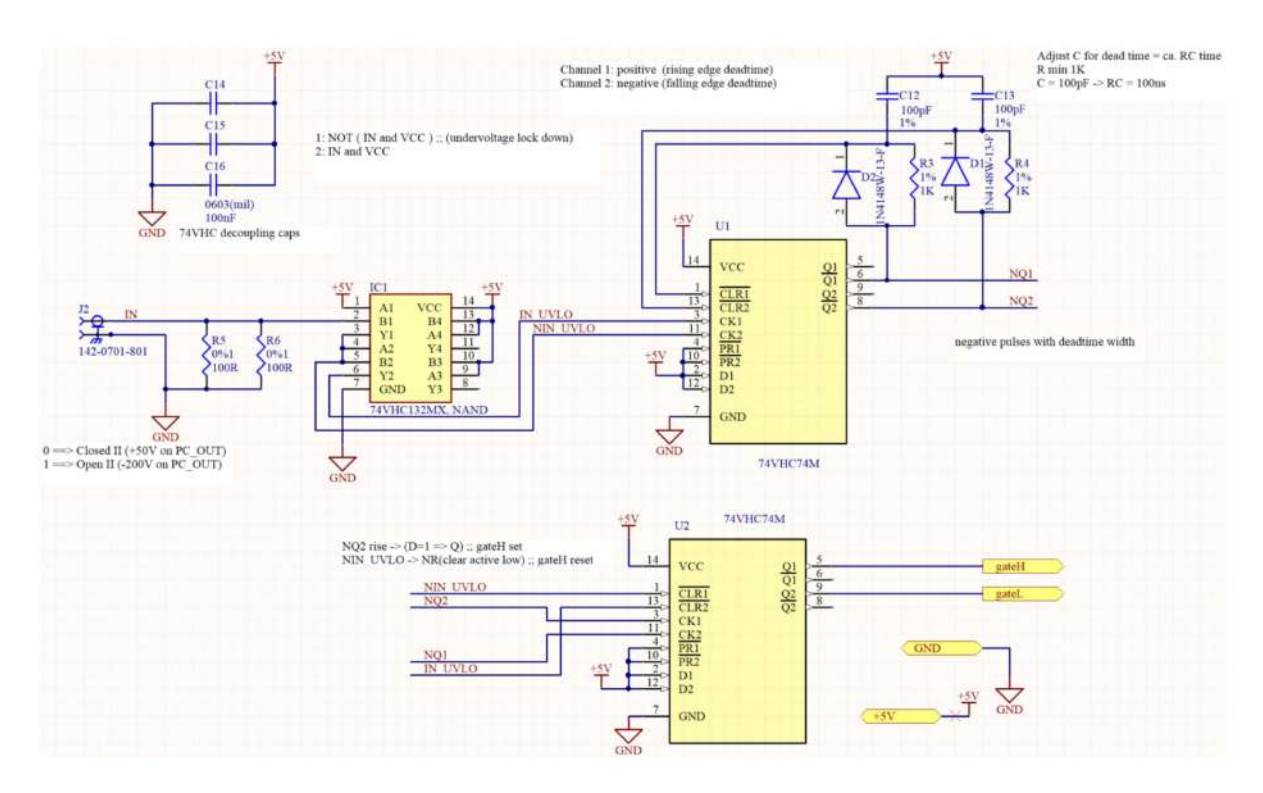
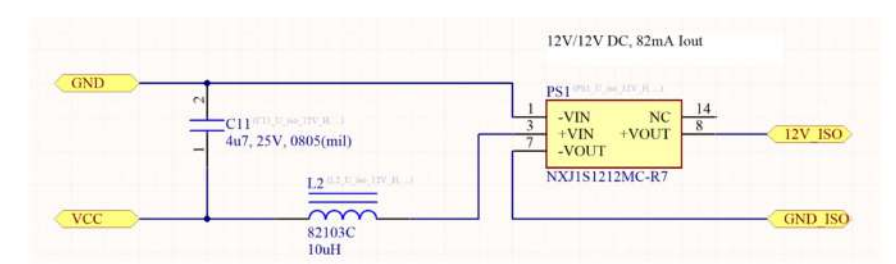


Figure B.1: Schematics of a custom image intensifier high-voltage gate driver. The drawing is included only for illustrative purposes. Page 1. 174







**Figure B.2:** Schematics of a custom image intensifier high-voltage gate driver. The drawing is included only for illustrative purposes. Page 2. 175

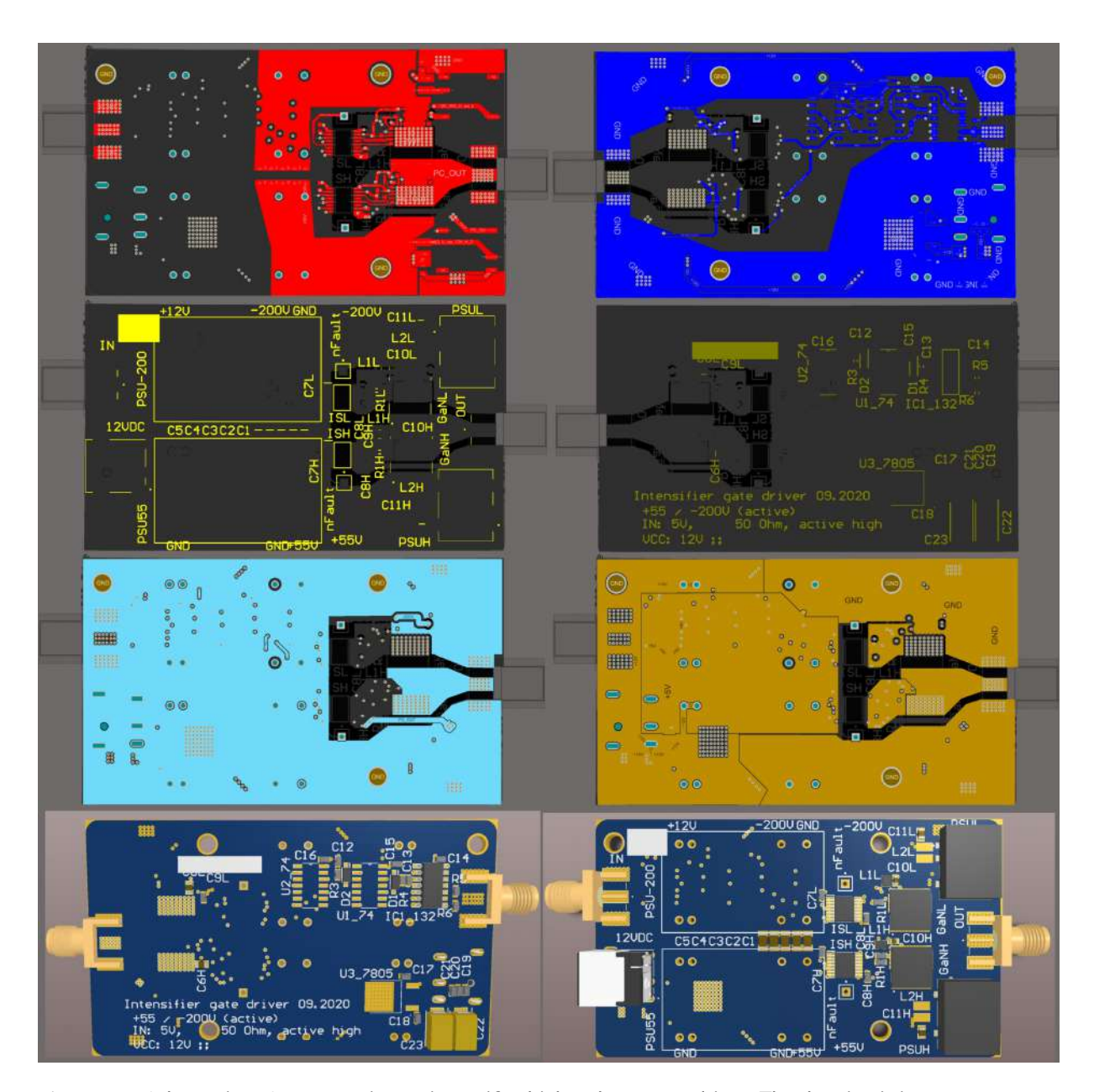


**Figure B.3:** Schematics of a custom image intensifier high-voltage gate driver. The drawing is included only for illustrative purposes. Page 3.

## Bibliography

- <sup>1</sup>A. Einstein, "On a heuristic point of view concerning the production and transformation of light", Ann. Phys-new. York. **322**, 132–148 (1905).
- <sup>2</sup>M. Planck, "Ueber das Gesetz der Energieverteilung im Normalspectrum", Ann. Phys. **309**, 553–563 (1901).
- <sup>3</sup>P. A. M. Dirac and N. H. D. Bohr, "The quantum theory of the emission and absorption of radiation", Proc. R. Soc. London A. **114**, 243–265 (1927).
- <sup>4</sup>E. Fermi, "Quantum Theory of Radiation", Rev. Mod. Phys. 4, 87–132 (1932).
- <sup>5</sup>J. P. Gordon, H. J. Zeiger, and C. H. Townes, "The Maser—New Type of Microwave Amplifier, Frequency Standard, and Spectrometer", Phys. Rev. **99**, 1264–1274 (1955).
- <sup>6</sup>T. H. Maiman, "Stimulated Optical Radiation in Ruby", Nature 187, 493–494 (1960).
- <sup>7</sup>W. P. Schleich, Quantum Optics in Phase Space (Wiley-VCH, 2001).
- <sup>8</sup>H. J. Kimble, M. Dagenais, and L. Mandel, "Photon Antibunching in Resonance Fluorescence", Phys. Rev. Lett. **39**, 691–695 (1977).
- <sup>9</sup>V. Giovannetti, S. Lloyd, and L. Maccone, "Quantum-Enhanced Measurements: Beating the Standard Quantum Limit", Science **306**, 1330 (2004).
- <sup>10</sup>C. H. Bennett and G. Brassard, "Quantum cryptography: Public key distribution and coin tossing", Theor. Comput. Sci. **560**, Theoretical Aspects of Quantum Cryptography celebrating 30 years of BB84, 7–11 (2014).
- <sup>11</sup>L. M. Duan, M. D. Lukin, J. I. Cirac, and P. Zoller, "Long-distance quantum communication with atomic ensembles and linear optics.", Nature **414**, 413–8 (2001).
- <sup>12</sup>S. E. Dwyer, G. L. Mansell, and L. McCuller, "Squeezing in Gravitational Wave Detectors", Galaxies **10** (2022).
- <sup>13</sup>C. Gerry and P. Knight, *Introductory Quantum Optics* (Cambridge University Press, 2005).
- <sup>14</sup>J. Garrison and R. Chiao, *Quantum Optics*, Oxford Graduate Texts (OUP Oxford, 2008).

- <sup>15</sup>M. Scully and M. Zubairy, *Quantum Optics*, Quantum Optics (Cambridge University Press, 1997).
- <sup>16</sup>J. S. Lundeen, B. Sutherland, A. Patel, C. Stewart, and C. Bamber, "Direct measurement of the quantum wavefunction", Nature 474, 188–191 (2011).
- <sup>17</sup>B. Kolner, "Space-time duality and the theory of temporal imaging", IEEE J. Quantum Electron. **30**, 1951–1963 (1994).
- <sup>18</sup>O. Keller, "On the theory of spatial localization of photons", Phys. Rep. **411**, 1–232 (2005).
- <sup>19</sup>I. Białynicki-Birula, "Photon Wave Function", in, Vol. 36, edited by E. Wolf, Progress in Optics (Elsevier, 1996), pp. 245–294.
- <sup>20</sup>I. Białynicki-Birula, "Exponential Localization of Photons", Phys. Rev. Lett. **80**, 5247–5250 (1998).
- <sup>21</sup>I. Białynicki-Birula and Z. Białynicka-Birula, "Uncertainty Relation for Photons", Phys. Rev. Lett. **108**, 140401 (2012).
- <sup>22</sup>I. Białynicki-Birula and Z. Białynicka-Birula, "The role of the Riemann–Silberstein vector in classical and quantum theories of electromagnetism", J. Phys. A: Math. Theor. **46**, 053001 (2013).
- <sup>23</sup>J. W. Goodman, *Statistical Optics* (John Wiley & Sons, 1985).
- <sup>24</sup>L. Cohen, "Generalized Phase-Space Distribution Functions", J. Math. Phys. 7, 781–786 (1966).
- <sup>25</sup>H. Schneckenburger, "Laser Application in Life Sciences", Int. J. Mol. Sci. 24 (2023).
- <sup>26</sup>W. T. Silfvast, *Laser Fundamentals*, 2nd ed. (Cambridge University Press, Cambridge, 2004).
- <sup>27</sup>M. Giustina et al., "Significant-Loophole-Free Test of Bell's Theorem with Entangled Photons", Phys. Rev. Lett. **115**, 250401 (2015).
- <sup>28</sup>B. Hensen et al., "Loophole-free Bell inequality violation using electron spins separated by 1.3 kilometres", Nature **526**, 682–686 (2015).
- <sup>29</sup>M. Parniak, "Multimode Quantum Optics with Spin Waves and Photons", PhD thesis (Faculty of Physics, University of Warsaw, 2019).
- <sup>30</sup>M. Mazelanik, "Atomowy generator i procesor kwantowych stanów światła", PhD thesis (Faculty of Physics, University of Warsaw, 2022).
- <sup>31</sup>A. Leszczyński, "Przestrzenna modulacja fazy jako nastawny mechanizm transferu informacji między światłem, a pamięcią kwantową", PhD thesis (Faculty of Physics, University of Warsaw, 2021).

- <sup>32</sup>M. Parniak, M. Dabrowski, M. Mazelanik, A. Leszczyński, M. Lipka, and W. Wasilewski, "Wavevector multiplexed atomic quantum memory via spatially-resolved single-photon detection", Nat. Commun. 8, 2140 (2017).
- <sup>33</sup>M. Parniak, M. Mazelanik, A. Leszczyński, M. Lipka, M. Dąbrowski, and W. Wasilewski, "Quantum optics of spin waves through ac Stark modulation", Phys. Rev. Lett. **122**, 063604 (2019).
- <sup>34</sup>M. Dąbrowski, M. Mazelanik, M. Parniak, A. Leszczyński, M. Lipka, and W. Wasilewski, "Certification of high-dimensional entanglement and Einstein-Podolsky-Rosen steering with cold atomic quantum memory", Phys. Rev. A 98, 042126 (2018).
- <sup>35</sup>M. Mazelanik, M. Parniak, A. Leszczyński, M. Lipka, and W. Wasilewski, "Coherent spin-wave processor of stored optical pulses", npj Quantum Inf. 5, 22 (2019).
- <sup>36</sup>M. Lipka, A. Leszczyński, M. Mazelanik, M. Parniak, and W. Wasilewski, "Spatial spin-wave modulator for quantum-memory-assisted adaptive measurements", Phys. Rev. Applied 11, 034049 (2019).
- <sup>37</sup>M. Lipka, M. Mazelanik, A. Leszczyński, W. Wasilewski, and M. Parniak, "Massively-multiplexed generation of Bell-type entanglement using a quantum memory", Commun. Phys. 4, 46 (2021).
- <sup>38</sup>M. Mazelanik, A. Leszczyński, M. Lipka, M. Parniak, and W. Wasilewski, "Temporal imaging for ultra-narrowband few-photon states of light", Optica 7, 203–208 (2020).
- <sup>39</sup>M. Mazelanik, M. Dąbrowski, and W. Wasilewski, "Correlation steering in the angularly multimode Raman atomic memory", Opt. Express 24, 21995–22003 (2016).
- <sup>40</sup>M. Lipka, M. Mazelanik, and M. Parniak, "Entanglement distribution with wavevector-multiplexed quantum memory", New J. Phys. **23**, 053012 (2021).
- <sup>41</sup>R. Chrapkiewicz, "Generation and characterization of spatially structured few-photon states of light", PhD thesis (Faculty of Physics, University of Warsaw, 2015).
- <sup>42</sup>F. Kaneda, B. G. Christensen, J. J. Wong, H. S. Park, K. T. McCusker, and P. G. Kwiat, "Time-multiplexed heralded single-photon source", Optica 2, 1010–1013 (2015).
- <sup>43</sup>F. Kaneda, F. Xu, J. Chapman, and P. G. Kwiat, "Quantum-memory-assisted multiphoton generation for efficient quantum information processing", Optica 4, 1034–1037 (2017).
- <sup>44</sup>C. Joshi, A. Farsi, S. Clemmen, S. Ramelow, and A. L. Gaeta, "Frequency multiplexing for quasi-deterministic heralded single-photon sources", Nat. Commun. 9, 847 (2018).
- <sup>45</sup>F. Kaneda and P. G. Kwiat, "High-efficiency single-photon generation via large-scale active time multiplexing", Sci. Adv. **5**, eaaw8586 (2019).
- <sup>46</sup>M. Jachura, M. Lipka, M. Jarzyna, and K. Banaszek, "Quantum fingerprinting using two-photon interference", Opt. Express **25**, 27475–27487 (2017).

- <sup>47</sup>T. B. H. Tentrup, T. Hummel, T. A. W. Wolterink, R. Uppu, A. P. Mosk, and P. W. H. Pinkse, "Transmitting more than 10 bit with a single photon", Opt. Express **25**, 2826–2833 (2017).
- <sup>48</sup>C. Simon, "Towards a global quantum network", Nat. Photonics 11, 678–680 (2017).
- <sup>49</sup>H. J. Kimble, "The quantum internet", Nature **453**, 1023–1030 (2008).
- <sup>50</sup>H. Krovi, S. Guha, Z. Dutton, J. A. Slater, C. Simon, and W. Tittel, "Practical quantum repeaters with parametric down-conversion sources", Appl. Phys. B Lasers Opt. **122**, 1–8 (2016).
- <sup>51</sup>I. R. Berchera and I. P. Degiovanni, "Quantum imaging with sub-Poissonian light: challenges and perspectives in optical metrology", Metrologia **56**, 024001 (2019).
- <sup>52</sup>S. Mukamel et al., "Roadmap on quantum light spectroscopy", J. Phys. B: At. Mol. Opt. Phys. **53**, 072002 (2020).
- <sup>53</sup>K. E. Dorfman, F. Schlawin, and S. Mukamel, "Nonlinear optical signals and spectroscopy with quantum light", Rev. Mod. Phys. 88, 045008 (2016).
- <sup>54</sup>I. Afek, O. Ambar, and Y. Silberberg, "High-NOON States by Mixing Quantum and Classical Light", Science **328**, 879 (2010).
- <sup>55</sup>R. B. Jin, R. Shimizu, T. Ono, M. Fujiwara, G. W. Deng, Q. Zhou, M. Sasaki, and M. Takeoka, "Spectrally resolved NOON state interference", arXiv preprint arXiv:2104.01062 (2021).
- <sup>56</sup>F. Wolfgramm, C. Vitelli, F. A. Beduini, N. Godbout, and M. W. Mitchell, "Entanglement-enhanced probing of a delicate material system", Nat. Photonics 7, 28–32 (2013).
- <sup>57</sup>L.-K. Chen et al., "Observation of ten-photon entanglement using thin BiB3O6 crystals", Optica 4, 77–83 (2017).
- <sup>58</sup>Q. Pian, R. Yao, N. Sinsuebphon, and X. Intes, "Compressive hyperspectral time-resolved wide-field fluorescence lifetime imaging", Nat. Photonics **11**, 411–414 (2017).
- <sup>59</sup>Y. Y. Hui, L. J. Su, O. Y. Chen, Y. T. Chen, T. M. Liu, and H. C. Chang, "Wide-field imaging and flow cytometric analysis of cancer cells in blood by fluorescent nanodiamond labeling and time gating", Sci. Rep. 4, 5574 (2014).
- <sup>60</sup>F. Rezaei, A. Nikiforov, R. Morent, and N. De Geyter, "Plasma Modification of Poly Lactic Acid Solutions to Generate High Quality Electrospun PLA Nanofibers", Sci. Rep. 8, 2241 (2018).
- <sup>61</sup>C. J. Picken, R. Legaie, and J. D. Pritchard, "Single atom imaging with an sCMOS camera", Appl. Phys. Lett. **111**, 164102 (2017).
- <sup>62</sup>D. S. Tasca, R. M. Gomes, F. Toscano, P. H. Souto Ribeiro, and S. P. Walborn, "Continuous-variable quantum computation with spatial degrees of freedom of photons", Phys. Rev. A 83, 052325 (2011).

- <sup>63</sup>Z.-Y. Zhou, Y. Li, D.-S. Ding, W. Zhang, S. Shi, B.-S. Shi, and G.-C. Guo, "Orbital angular momentum photonic quantum interface", Light: Sci. Appl. **5**, e16019 (2016).
- <sup>64</sup>T. B. H. Tentrup, T. Hummel, T. A. W. Wolterink, R. Uppu, A. P. Mosk, and P. W. H. Pinkse, "Transmitting more than 10 bit with a single photon", Opt. Express **25**, 2826–2833 (2017).
- <sup>65</sup>M. Parniak, S. Borówka, K. Boroszko, W. Wasilewski, K. Banaszek, and R. Demkowicz-Dobrzański, "Beating the Rayleigh Limit Using Two-Photon Interference", Phys. Rev. Lett. 121, 250503 (2018).
- <sup>66</sup>O. Schwartz, J. M. Levitt, R. Tenne, S. Itzhakov, Z. Deutsch, and D. Oron, "Superresolution microscopy with quantum emitters", Nano Lett. **13**, 5832–5836 (2013).
- <sup>67</sup>Y. Israel, R. Tenne, D. Oron, and Y. Silberberg, "Quantum correlation enhanced superresolution localization microscopy enabled by a fibre bundle camera", Nat. Commun. **8**, 14786 (2017).
- <sup>68</sup>O. Haderka, J. Peřina, M. Hamar, and J. Peřina, "Direct measurement and reconstruction of nonclassical features of twin beams generated in spontaneous parametric downconversion", Phys. Rev. A **71**, 033815 (2005).
- <sup>69</sup>M. Reichert, X. Sun, and J. W. Fleischer, "Quality of spatial entanglement propagation", Phys. Rev. A **95**, 063836 (2017).
- <sup>70</sup>L. Feng, F. Shi, L. Yin, Z. Miao, H.-c. Cheng, L. Wang, S. Niu, and X.-h. Zhang, "Influence of Ageing Processing on GaAs Photocathode of 3rd Generation Low-Light-Level Image Intensifier", in 7th International Symposium on Advanced Optical Manufacturing and Testing Technologies: Optoelectronics Materials and Devices for Sensing and Imaging, Vol. 9284 (SPIE, 2014), pp. 214–218.
- <sup>71</sup>M. A. Popecki et al., "Microchannel plate fabrication using glass capillary arrays with Atomic Layer Deposition films for resistance and gain", J. Geophys. Res.: Space Phys. **121**, 7449–7460 (2016).
- <sup>72</sup>A. D. Payne, A. A. Dorrington, M. J. Cree, and D. A. Carnegie, "Characterizing an Image Intensifier in a Full-Field Range Imaging System", IEEE Sens. J. 8, 1763–1770 (2008).
- <sup>73</sup>M. Lipka, M. Parniak, and W. Wasilewski, "Microchannel plate cross-talk mitigation for spatial autocorrelation measurements", Appl. Phys. Lett. **112** (2018).
- <sup>74</sup>N. Gisin and R. Thew, "Quantum communication", Nat. Photonics 1, 165–171 (2007).
- <sup>75</sup>M. Lipka and M. Parniak, "Fast imaging of multimode transverse–spectral correlations for twin photons", Opt. Lett. **46**, 3009–3012 (2021).
- <sup>76</sup>T.-S. Yang et al., "Multiplexed storage and real-time manipulation based on a multiple degree-of-freedom quantum memory", Nat. Commun. 9, 3407 (2018).

- <sup>77</sup>F. Graffitti, V. D'Ambrosio, M. Proietti, J. Ho, B. Piccirillo, C. de Lisio, L. Marrucci, and A. Fedrizzi, "Hyperentanglement in structured quantum light", Phys. Rev. Res. 2, 043350 (2020).
- <sup>78</sup>B. Brecht, D. V. Reddy, C. Silberhorn, and M. G. Raymer, "Photon Temporal Modes: A Complete Framework for Quantum Information Science", Phys. Rev. X 5, 041017 (2015).
- <sup>79</sup>J. T. Barreiro, N. K. Langford, N. A. Peters, and P. G. Kwiat, "Generation of Hyperentangled Photon Pairs", Phys. Rev. Lett. **95**, 260501 (2005).
- <sup>80</sup>X.-L. Wang, X.-D. Cai, Z.-E. Su, M.-C. Chen, D. Wu, L. Li, N.-L. Liu, C.-Y. Lu, and J.-W. Pan, "Quantum teleportation of multiple degrees of freedom of a single photon", Nature 518, 516–519 (2015).
- <sup>81</sup>J. T. Barreiro, T.-C. Wei, and P. G. Kwiat, "Beating the channel capacity limit for linear photonic superdense coding", Nat. Phys. 4, 282 (2008).
- <sup>82</sup>S. P. Walborn, S. Pádua, and C. H. Monken, "Hyperentanglement-assisted Bell-state analysis", Phys. Rev. A 68, 042313 (2003).
- <sup>83</sup>M. Caloz, M. Perrenoud, C. Autebert, B. Korzh, M. Weiss, C. Schönenberger, R. J. Warburton, H. Zbinden, and F. Bussières, "High-detection efficiency and low-timing jitter with amorphous superconducting nanowire single-photon detectors", Appl. Phys. Lett. 112, 061103 (2018).
- <sup>84</sup>A. O. C. Davis, P. M. Saulnier, M. Karpiński, and B. J. Smith, "Pulsed single-photon spectrometer by frequency-to-time mapping using chirped fiber Bragg gratings", Opt. Express 25, 12804–12811 (2017).
- <sup>85</sup>R. Cheng, C.-L. Zou, X. Guo, S. Wang, X. Han, and H. X. Tang, "Broadband on-chip single-photon spectrometer", Nat. Commun. **10**, 4104 (2019).
- <sup>86</sup>T. Zhong et al., "Photon-efficient quantum key distribution using time–energy entanglement with high-dimensional encoding", New J. Phys. **17**, 022002 (2015).
- <sup>87</sup>J. M. Donohue, V. Ansari, J. Řeháček, Z. Hradil, B. Stoklasa, M. Paúr, L. L. Sánchez-Soto, and C. Silberhorn, "Quantum-Limited Time-Frequency Estimation through Mode-Selective Photon Measurement", Phys. Rev. Lett. 121, 090501 (2018).
- <sup>88</sup>R.-B. Jin et al., "Spectrally resolved Hong-Ou-Mandel interference between independent photon sources", Opt. Express 23, 28836–28848 (2015).
- <sup>89</sup>M. Jachura, M. Jarzyna, M. Lipka, W. Wasilewski, and K. Banaszek, "Visibility-Based Hypothesis Testing Using Higher-Order Optical Interference", Phys. Rev. Lett. 120, 110502 (2018).
- <sup>90</sup>M. Jachura, M. Lipka, M. Jarzyna, and K. Banaszek, "Quantum fingerprinting using two-photon interference", Opt. Express **25**, 27475–27487 (2017).

- <sup>91</sup>M. Lipka, M. Jarzyna, and K. Banaszek, "Quantum Fingerprinting Over AWGN Channels With Power-Limited Optical Signals", IEEE J. Sel. Areas Commun. 38, 496–505 (2020).
- <sup>92</sup>R. Tenne, U. Rossman, B. Rephael, Y. Israel, A. Krupinski-Ptaszek, R. Lapkiewicz, Y. Silberberg, and D. Oron, "Super-resolution enhancement by quantum image scanning microscopy", Nat. Photonics 13, 116–122 (2019).
- <sup>93</sup>P.-A. Moreau, E. Toninelli, T. Gregory, and M. J. Padgett, "Imaging with quantum states of light", Nat. Rev. Phys. **1**, 367–380 (2019).
- <sup>94</sup>A. B. Mikhalychev, B. Bessire, I. L. Karuseichyk, A. A. Sakovich, M. Unternährer, D. A. Lyakhov, D. L. Michels, A. Stefanov, and D. Mogilevtsev, "Efficiently reconstructing compound objects by quantum imaging with higher-order correlation functions", Commun. Phys. 2, 134 (2019).
- <sup>95</sup>O. Schwartz, J. M. Levitt, R. Tenne, S. Itzhakov, Z. Deutsch, and D. Oron, "Superresolution microscopy with quantum emitters", Nano Lett. **13**, 5832–5836 (2013).
- <sup>96</sup>M. Jachura, R. Chrapkiewicz, R. Demkowicz-Dobrzański, W. Wasilewski, and K. Banaszek, "Mode engineering for realistic quantum-enhanced interferometry", Nat. Commun. 7, 11411 (2016).
- <sup>97</sup>H. Defienne and S. Gigan, "Spatially entangled photon-pair generation using a partial spatially coherent pump beam", Phys. Rev. A **99**, 053831 (2019).
- <sup>98</sup>M. Reichert, H. Defienne, and J. W. Fleischer, "Massively Parallel Coincidence Counting of High-Dimensional Entangled States", Sci. Rep. **8**, 7925 (2018).
- <sup>99</sup>F. Devaux, A. Mosset, P.-A. Moreau, and E. Lantz, "Imaging Spatiotemporal Hong-Ou-Mandel Interference of Biphoton States of Extremely High Schmidt Number", Phys. Rev. X 10, 031031 (2020).
- <sup>100</sup>K. Sun et al., "Mapping and measuring large-scale photonic correlation with single-photon imaging", Optica **6**, 244–249 (2019).
- <sup>101</sup>J. W. Goodman, *Introduction to Fourier optics* (Roberts and Company publishers, 2005).
- <sup>102</sup>N. Montaut, O. S. Magaña-Loaiza, T. J. Bartley, V. B. Verma, S. W. Nam, R. P. Mirin, C. Silberhorn, and T. Gerrits, "Compressive characterization of telecom photon pairs in the spatial and spectral degrees of freedom", Optica 5, 1418–1423 (2018).
- <sup>103</sup>J. Bavaresco, N. Herrera Valencia, C. Klöckl, M. Pivoluska, P. Erker, N. Friis, M. Malik, and M. Huber, "Measurements in two bases are sufficient for certifying high-dimensional entanglement", Nat. Phys. 14, 1032–1037 (2018).
- <sup>104</sup>S. P. Neumann, D. Ribezzo, M. Bohmann, and R. Ursin, "Experimentally optimizing QKD rates via nonlocal dispersion compensation", Quantum Sci. Technol. 6, 025017 (2021).

- <sup>105</sup>P. Kolenderski, W. Wasilewski, and K. Banaszek, "Modeling and optimization of photon pair sources based on spontaneous parametric down-conversion", Phys. Rev. A **80**, 013811 (2009).
- <sup>106</sup>J. W. Goodman, *Statistical Optics*, 2nd (John Wiley & Sons, 2000).
- <sup>107</sup>D. Klyshko, "Use of two-photon light for absolute calibration of photoelectric detectors", Sov. J. Quantum Electron. **10**, 1112 (1980).
- <sup>108</sup>L. Qi, F. Just, G. Leuchs, and M. V. Chekhova, "Autonomous absolute calibration of an ICCD camera in single-photon detection regime", Opt. Express 24, 26444–26453 (2016).
- <sup>109</sup>C. Chen, B. Wu, A. Jiang, and G. You, "A new-type ultraviolet SHG crystal-beta-BaB2O4", Scientia Sinica Series B-Chemical Biological Agricultural Medical & Earth Sciences 28, 235–243 (1985).
- <sup>110</sup>D. Nikogosyan, "Beta barium borate (BBO) a review of its properties and applications", Appl. Phys. A **52**, 359–368 (1991).
- <sup>111</sup>D. Eimerl, L. Davis, S. Velsko, E. Graham, and A. Zalkin, "Optical, mechanical, and thermal properties of barium borate", J. Appl. Phys. **62**, 1968–1983 (1987).
- <sup>112</sup>K. Zielnicki, K. Garay-Palmett, D. Cruz-Delgado, H. Cruz-Ramirez, M. F. O'Boyle, B. Fang, V. O. Lorenz, A. B. U'Ren, and P. G. Kwiat, "Joint spectral characterization of photon-pair sources", J. Mod. Optic. 65, 1141–1160 (2018).
- <sup>113</sup>R. Chrapkiewicz, M. Jachura, K. Banaszek, and W. Wasilewski, "Hologram of a single photon", Nat. Photonics **10**, 576 (2016).
- <sup>114</sup>M. Lipka and M. Parniak, "Single-Photon Hologram of a Zero-Area Pulse", Phys. Rev. Lett. **127**, 163601 (2021).
- <sup>115</sup>J. Leach et al., "Quantum Correlations in Optical Angle-Orbital Angular Momentum Variables", Science **329**, 662 (2010).
- <sup>116</sup>R. Fickler, R. Łapkiewicz, W. N. Plick, M. Krenn, C. Schaeff, S. Ramelow, and A. Zeilinger, "Quantum Entanglement of High Angular Momenta", Science **338**, 640 (2012).
- <sup>117</sup>N. Uribe-Patarroyo, A. Fraine, D. S. Simon, O. Minaeva, and A. V. Sergienko, "Object Identification Using Correlated Orbital Angular Momentum States", Phys. Rev. Lett. 110, 043601 (2013).
- <sup>118</sup>M. Kues et al., "On-chip generation of high-dimensional entangled quantum states and their coherent control", Nature **546**, 622–626 (2017).
- <sup>119</sup>M. Karpiński, M. Jachura, L. J. Wright, and B. J. Smith, "Bandwidth manipulation of quantum light by an electro-optic time lens", Nat. Photonics **11**, 53–57 (2017).

- <sup>120</sup>T. Nitsche, S. De, S. Barkhofen, E. Meyer-Scott, J. Tiedau, J. Sperling, A. Gábris, I. Jex, and C. Silberhorn, "Local Versus Global Two-Photon Interference in Quantum Networks", Phys. Rev. Lett. 125, 213604 (2020).
- <sup>121</sup>C. K. Hong, Z. Y. Ou, and L. Mandel, "Measurement of subpicosecond time intervals between two photons by interference", Phys. Rev. Lett. **59**, 2044–2046 (1987).
- <sup>122</sup>M. Jachura, M. Jarzyna, M. Lipka, W. Wasilewski, and K. Banaszek, "Visibility-based hypothesis testing using higher-order optical interference", Phys. Rev. Lett. 120, 110502 (2018).
- <sup>123</sup>M. Lipka, M. Jarzyna, and K. Banaszek, "Quantum Fingerprinting Over AWGN Channels With Power-Limited Optical Signals", IEEE J. Sel. Areas Commun. 38, 496–505 (2020).
- <sup>124</sup>V. Thiel, A. O. C. Davis, K. Sun, P. D'Ornellas, X.-M. Jin, and B. J. Smith, "Single-photon characterization by two-photon spectral interferometry", Opt. Express 28, 19315–19324 (2020).
- <sup>125</sup>R.-B. Jin et al., "Spectrally resolved Hong-Ou-Mandel interference between independent photon sources", Opt. Express 23, 28836–28848 (2015).
- <sup>126</sup>V. Prakash, A. Sierant, and M. W. Mitchell, "Autoheterodyne Characterization of Narrow-Band Photon Pairs", Phys. Rev. Lett. **127**, 043601 (2021).
- <sup>127</sup>T. Gerrits, F. Marsili, V. B. Verma, L. K. Shalm, M. Shaw, R. P. Mirin, and S. W. Nam, "Spectral correlation measurements at the Hong-Ou-Mandel interference dip", Phys. Rev. A 91, 013830 (2015).
- <sup>128</sup>V. V. Orre, E. A. Goldschmidt, A. Deshpande, A. V. Gorshkov, V. Tamma, M. Hafezi, and S. Mittal, "Interference of Temporally Distinguishable Photons Using Frequency-Resolved Detection", Phys. Rev. Lett. 123, 123603 (2019).
- <sup>129</sup>A. M. Kaufman, B. J. Lester, C. M. Reynolds, M. L. Wall, M. Foss-Feig, K. R. A. Hazzard, A. M. Rey, and C. A. Regal, "Two-particle quantum interference in tunnel-coupled optical tweezers", Science **345**, 306 (2014).
- <sup>130</sup>R. Lopes, A. Imanaliev, A. Aspect, M. Cheneau, D. Boiron, and C. I. Westbrook, "Atomic Hong-Ou-Mandel experiment", Nature **520**, 66–68 (2015).
- <sup>131</sup>J. Li, M.-T. Zhou, B. Jing, X.-J. Wang, S.-J. Yang, X. Jiang, K. Mølmer, X.-H. Bao, and J.-W. Pan, "Hong-Ou-Mandel Interference between Two Deterministic Collective Excitations in an Atomic Ensemble", Phys. Rev. Lett. 117, 180501 (2016).
- <sup>132</sup>M. Parniak, M. Mazelanik, A. Leszczyński, M. Lipka, M. Dąbrowski, and W. Wasilewski, "Quantum Optics of Spin Waves through ac Stark Modulation", Phys. Rev. Lett. 122, 063604 (2019).
- <sup>133</sup>K. Toyoda, R. Hiji, A. Noguchi, and S. Urabe, "Hong-Ou-Mandel interference of two phonons in trapped ions", Nature **527**, 74–77 (2015).

- <sup>134</sup>S. L. McCall and E. L. Hahn, "Self-Induced Transparency by Pulsed Coherent Light", Phys. Rev. Lett. **18**, 908–911 (1967).
- <sup>135</sup>M. D. Crisp, "Propagation of Small-Area Pulses of Coherent Light through a Resonant Medium", Phys. Rev. A 1, 1604–1611 (1970).
- <sup>136</sup>J. Eberly, "Area theorem rederived", Opt. Express 2, 173–176 (1998).
- <sup>137</sup>L. S. Costanzo, A. S. Coelho, D. Pellegrino, M. S. Mendes, L. Acioli, K. N. Cassemiro, D. Felinto, A. Zavatta, and M. Bellini, "Zero-Area Single-Photon Pulses", Phys. Rev. Lett. 116, 023602 (2016).
- <sup>138</sup>W. Grice and I. A. Walmsley, "Homodyne detection in a photon counting application", J. Mod. Optic. 43, 795–805 (1996).
- <sup>139</sup>A. Dragan, "Efficient fiber coupling of down-conversion photon pairs", Phys. Rev. A 70, 053814 (2004).
- <sup>140</sup>W. P. Grice and I. A. Walmsley, "Spectral information and distinguishability in type-II down-conversion with a broadband pump", Phys. Rev. A **56**, 1627–1634 (1997).
- <sup>141</sup>K. Wang, "Quantum theory of two-photon wavepacket interference in a beamsplitter", J. Phys. B: At. Mol. Opt. Phys. 39, R293 (2006).
- <sup>142</sup>D. J. Richardson, J. M. Fini, and L. E. Nelson, "Space-division multiplexing in optical fibres", Nat. Photonics 7, 354–362 (2013).
- <sup>143</sup>Y. Ding, D. Bacco, K. Dalgaard, X. Cai, X. Zhou, K. Rottwitt, and L. K. Oxenløwe, "High-dimensional quantum key distribution based on multicore fiber using silicon photonic integrated circuits", npj Quantum Inf. 3, 25 (2017).
- <sup>144</sup>H. Buhrman, R. Cleve, J. Watrous, and R. de Wolf, "Quantum Fingerprinting", Phys. Rev. Lett. **87**, 167902 (2001).
- <sup>145</sup>U. Kallmann, S. Brattke, and W. Hartmann, "Propagation of resonant  $0\pi$  pulses in rubidium", Phys. Rev. A **59**, 814–818 (1999).
- <sup>146</sup>R. Jozsa, "Fidelity for Mixed Quantum States", J. Mod. Opt **41**, 2315–2323 (1994).
- <sup>147</sup>D. J. Bone, H.-A. Bachor, and R. J. Sandeman, "Fringe-pattern analysis using a 2-D Fourier transform", Appl. Opt. **25**, 1653–1660 (1986).
- <sup>148</sup>S. A. Karout, M. A. Gdeisat, D. R. Burton, and M. J. Lalor, "Two-dimensional phase unwrapping using a hybrid genetic algorithm", Appl. Opt. **46**, 730–743 (2007).
- <sup>149</sup>A. Nesmeyanov and R. Gary, *Vapor pressure of the chemical elements* (Elsevier, 1963).
- <sup>150</sup>P. Hong, L. Xu, Z. Zhai, and G. Zhang, "High visibility two-photon interference with classical light", Opt. Express **21**, 14056–14065 (2013).
- <sup>151</sup>U. Leonhardt, *Measuring the quantum state of light*, Vol. 22 (Cambridge university press, 1997).

- <sup>152</sup>J. C. Garrison and R. Y. Chiao, *Quantum Optics* (Oxford University Press Inc., 2008).
- <sup>153</sup>P. Sekatski, N. Sangouard, F. Bussières, C. Clausen, N. Gisin, and H. Zbinden, "Detector imperfections in photon-pair source characterization", J. Phys. B: At. Mol. Opt. Phys. 45, 124016 (2012).
- <sup>154</sup>S. M. Kay, Fundamentals of Statistical Signal Processing: Estimation Theory (PTR Prentice Hall, 1993).
- <sup>155</sup>S. Lischke et al., "Ultra-fast germanium photodiode with 3-dB bandwidth of 265 GHz", Nat. Photonics **15**, 925–931 (2021).
- <sup>156</sup>C. Iaconis and I. A. Walmsley, "Self-referencing spectral interferometry for measuring ultrashort optical pulses", IEEE J. Quantum Electron. **35**, 501–509 (1999).
- <sup>157</sup>D. J. Kane and R. Trebino, "Characterization of arbitrary femtosecond pulses using frequency-resolved optical gating", IEEE J. Quantum Electron. **29**, 571–579 (1993).
- <sup>158</sup>M. Lelek, F. Louradour, A. Barthélémy, C. Froehly, T. Mansourian, L. Mouradian, J.-P. Chambaret, G. Chériaux, and B. Mercier, "Two-dimensional spectral shearing interferometry resolved in time for ultrashort optical pulse characterization", J. Opt. Soc. Am. B 25, A17–A24 (2008).
- <sup>159</sup>J. R. Birge, H. M. Crespo, and F. X. Kärtner, "Theory and design of two-dimensional spectral shearing interferometry for few-cycle pulse measurement", J. Opt. Soc. Am. B 27, 1165–1173 (2010).
- <sup>160</sup>V. Wong and I. A. Walmsley, "Analysis of ultrashort pulse-shape measurement using linear interferometers", Opt. Lett. **19**, 287–289 (1994).
- <sup>161</sup>A. O. C. Davis, V. Thiel, M. Karpiński, and B. J. Smith, "Measuring the Single-Photon Temporal-Spectral Wave Function", Phys. Rev. Lett. 121, 083602 (2018).
- <sup>162</sup>A. O. C. Davis, V. Thiel, M. Karpiński, and B. J. Smith, "Experimental single-photon pulse characterization by electro-optic shearing interferometry", Phys. Rev. A 98, 023840 (2018).
- <sup>163</sup>A. O. C. Davis, V. Thiel, and B. J. Smith, "Measuring the quantum state of a photon pair entangled in frequency and time", Optica 7, 1317 (2020).
- <sup>164</sup>A. O. Davis, P. M. Saulnier, M. Karpiński, and B. J. Smith, "Pulsed single-photon spectrometer by frequency-to-time mapping using chirped fiber bragg gratings", Opt. Express 25, 12804–12811 (2017).
- <sup>165</sup>A. Golestani, A. O. C. Davis, F. So śnicki, M. Mikołajczyk, N. Treps, and M. Karpiński, "Electro-Optic Fourier Transform Chronometry of Pulsed Quantum Light", Phys. Rev. Lett. 129, 123605 (2022).
- <sup>166</sup>S. Kurzyna, M. Jastrzębski, N. Fabre, W. Wasilewski, M. Lipka, and M. Parniak, "Variable electro-optic shearing interferometry for ultrafast single-photon-level pulse characterization", Opt. Express 30, 39826–39839 (2022).

- <sup>167</sup>L. Cohen, *Time-frequency Analysis*, Electrical engineering signal processing (Prentice Hall PTR, 1995).
- <sup>168</sup>M. A. Alonso, "Wigner functions in optics: describing beams as ray bundles and pulses as particle ensembles", Adv. Opt. Photonics 3, 272–365 (2011).
- <sup>169</sup>S. Pinilla, K. V. Mishra, B. M. Sadler, and H. Arguello, "Phase Retrieval for Radar Waveform Design", arXiv preprint arXiv:2201.11384 (2022).
- <sup>170</sup>N. C. Geib, M. Zilk, T. Pertsch, and F. Eilenberger, "Common pulse retrieval algorithm: a fast and universal method to retrieve ultrashort pulses", Optica **6**, 495 (2019).
- $^{171}$ Y. Liu, H. Li, J. Liu, S. Tan, Q. Lu, and W. Guo, "Low  $V_{\pi}$  thin-film lithium niobate modulator fabricated with photolithography", Opt. Express **29**, 6320–6329 (2021).
- Winzer, and M. Lončar, "Integrated lithium niobate electro-optic modulators operating at CMOS-compatible voltages", Nature 562, 101–104 (2018).
- <sup>173</sup>D. Zhu et al., "Spectral control of nonclassical light using an integrated thin-film lithium niobate modulator", arXiv preprint arXiv:2112.09961 (2021).
- <sup>174</sup>S. Sadana, D. Ghosh, K. Joarder, A. N. Lakshmi, B. C. Sanders, and U. Sinha, "Near-100 % two-photon-like coincidence-visibility dip with classical light and the role of complementarity", Phys. Rev. A 100, 013839 (2019).
- <sup>175</sup>T. Legero, T. Wilk, A. Kuhn, and G. Rempe, "Characterization of Single Photons Using Two-Photon Interference", Advances In Atomic, Molecular, and Optical Physics **53**, 253–289 (2006).
- <sup>176</sup>N. Fabre, "Spectral single photons characterization using generalized Hong–Ou–Mandel interferometry", J. Mod. Optic. **69**, 653–664 (2022).
- <sup>177</sup>B. Brecht, D. V. Reddy, C. Silberhorn, and M. G. Raymer, "Photon Temporal Modes: A Complete Framework for Quantum Information Science", Phys. Rev. X 5, 041017 (2015).
- <sup>178</sup>A. Kutay, H. Ozaktas, O. Ankan, and L. Onural, "Optimal filtering in fractional Fourier domains", IEEE Trans. Signal Process. **45**, 1129–1143 (1997).
- <sup>179</sup>R. Salem, M. A. Foster, A. C. Turner, D. F. Geraghty, M. Lipson, and A. L. Gaeta, "Optical time lens based on four-wave mixing on a silicon chip", Opt. Lett. **33**, 1047–1049 (2008).
- <sup>180</sup>J. Zhou, C. Guo, and R. Wang, "Fractional Fourier transform based on a temporal gradient-index lens", Opt. Continuum 1, 1418–1424 (2022).
- <sup>181</sup>B. H. Kolner, "Active pulse compression using an integrated electro-optic phase modulator", Appl. Phys. Lett. **52**, 1122–1124 (1988).

- <sup>182</sup>M. Karpiński, M. Jachura, L. J. Wright, and B. J. Smith, "Bandwidth manipulation of quantum light by an electro-optic time lens", Nat. Photonics **11**, 53–57 (2017).
- <sup>183</sup>H.-H. Lu, J. M. Lukens, N. A. Peters, O. D. Odele, D. E. Leaird, A. M. Weiner, and P. Lougovski, "Electro-Optic Frequency Beam Splitters and Tritters for High-Fidelity Photonic Quantum Information Processing", Phys. Rev. Lett. 120, 030502 (2018).
- <sup>184</sup>M. Lipka and M. Parniak, "Ultrafast electro-optic time-frequency fractional Fourier imaging at the single-photon level", Opt. Express **32**, 9573–9588 (2024).
- <sup>185</sup>B. Li, B. Yuan, C. Chen, X. Xiang, R. Quan, R. Dong, S. Zhang, and R.-B. Jin, "Spectrally resolved two-photon interference in a modified Hong–Ou–Mandel interferometer", Opt. Laser Technol. 159, 109039 (2023).
- <sup>186</sup>Y. Zhang, D. England, A. Nomerotski, and B. Sussman, "High speed imaging of spectral-temporal correlations in Hong-Ou-Mandel interference", Opt. Express 29, 28217–28227 (2021).
- <sup>187</sup>F. Albarelli, E. Bisketzi, A. Khan, and A. Datta, "Fundamental limits of pulsed quantum light spectroscopy: Dipole moment estimation", Phys. Rev. A **107**, 062601 (2023).
- <sup>188</sup>Y. He, Z. Liu, C. Ott, A. N. Pfeiffer, S. Sun, M. B. Gaarde, T. Pfeifer, and B. Hu, "Resonant Perfect Absorption Yielded by Zero-Area Pulses", Phys. Rev. Lett. 129, 273201 (2022).
- <sup>189</sup>M. Lipka and M. Parniak, "Single-Photon Hologram of a Zero-Area Pulse", Phys. Rev. Lett. **127**, 163601 (2021).
- <sup>190</sup>M. Lipka and M. Parniak, "Fast imaging of multimode transverse–spectral correlations for twin photons", Opt. Lett. **46**, 3009–3012 (2021).
- <sup>191</sup>H.-H. Lu, N. B. Lingaraju, D. E. Leaird, A. M. Weiner, and J. M. Lukens, "High-dimensional discrete Fourier transform gates with a quantum frequency processor", Opt. Express 30, 10126–10134 (2022).
- <sup>192</sup>M. Shah and L. Fan, "Frequency Superresolution with Spectrotemporal Shaping of Photons", Phys. Rev. Applied **15**, 034071 (2021).
- <sup>193</sup>F. Sośnicki, M. Mikołajczyk, A. Golestani, and M. Karpiński, "Interface between picosecond and nanosecond quantum light pulses", Nat. Photonics **17**, 761–766 (2023).
- <sup>194</sup>C. Joshi, B. M. Sparkes, A. Farsi, T. Gerrits, V. Verma, S. Ramelow, S. W. Nam, and A. L. Gaeta, "Picosecond-resolution single-photon time lens for temporal mode quantum processing", Optica 9, 364–373 (2022).
- <sup>195</sup>N. Fabre et al., "Generation of a time-frequency grid state with integrated biphoton frequency combs", Phys. Rev. A **102**, 012607 (2020).
- <sup>196</sup>N. Fabre, A. Keller, and P. Milman, "Time and frequency as quantum continuous variables", Phys. Rev. A **105**, 052429 (2022).

- <sup>197</sup>M. A. Foster, R. Salem, Y. Okawachi, A. C. Turner-Foster, M. Lipson, and A. L. Gaeta, "Ultrafast waveform compression using a time-domain telescope", Nat. Photonics 3, 581–585 (2009).
- <sup>198</sup>M. A. Foster, R. Salem, D. F. Geraghty, A. C. Turner-Foster, M. Lipson, and A. L. Gaeta, "Silicon-chip-based ultrafast optical oscilloscope", Nature **456**, 81–84 (2008).
- <sup>199</sup>V. J. Hernandez, C. V. Bennett, B. D. Moran, A. D. Drobshoff, D. Chang, C. Langrock, M. M. Fejer, and M. Ibsen, "104 MHz rate single-shot recording with subpicosecond resolution using temporal imaging", Opt. Express 21, 196–203 (2013).
- <sup>200</sup>P. Kukura, D. W. McCamant, and R. A. Mathies, "Femtosecond Stimulated Raman Spectroscopy", Annu. Rev. Phys. Chem. **58**, 461–488 (2007).
- <sup>201</sup>M. E. Fermann, A. Galvanauskas, and G. Sucha, *Ultrafast lasers: technology and applications*, Vol. 80 (CRC Press, 2002).
- <sup>202</sup>K. Sugioka and Y. Cheng, "Ultrafast lasers—reliable tools for advanced materials processing", Light Sci. Appl. 3, e149 (2014).
- <sup>203</sup>R. de Vivie-Riedle and U. Troppmann, "Femtosecond Lasers for Quantum Information Technology", Chem. Rev. **107**, 5082–5100 (2007).
- <sup>204</sup>B. Hennelly and J. T. Sheridan, "Optical image encryption by random shifting in fractional Fourier domains", Opt. Lett. **28**, 269–271 (2003).
- <sup>205</sup>X. Ouyang and J. Zhao, "Orthogonal Chirp Division Multiplexing", IEEE Trans. Commun. **64**, 3946–3957 (2016).
- <sup>206</sup>Q. Han, W. Li, and M. Yang, "An optical waveform pre-distortion method based on time domain fractional Fourier transformation", Opt. Commun. **284**, 660–664 (2011).
- <sup>207</sup>M. Cheng, L. Deng, H. Li, and D. Liu, "Enhanced secure strategy for electro-optic chaotic systems with delayed dynamics by using fractional Fourier transformation", Opt. Express **22**, 5241–5251 (2014).
- <sup>208</sup>Y. Zhou, M. Mirhosseini, D. Fu, J. Zhao, S. M. Hashemi Rafsanjani, A. E. Willner, and R. W. Boyd, "Sorting Photons by Radial Quantum Number", Phys. Rev. Lett. 119, 263602 (2017).
- <sup>209</sup>M. Brunel, S. Coetmellec, M. Lelek, and F. Louradour, "Fractional-order Fourier analysis for ultrashort pulse characterization", J. Opt. Soc. Am. A **24**, 1641–1646 (2007).
- <sup>210</sup>C. Cuadrado-Laborde, A. Carrascosa, A. Díez, J. L. Cruz, and M. V. Andres, "Photonic fractional Fourier transformer with a single dispersive device", Opt. Express 21, 8558–8563 (2013).
- <sup>211</sup>C. Schnébelin and H. G. de Chatellus, "Agile photonic fractional Fourier transformation of optical and RF signals", Optica 4, 907–910 (2017).

- <sup>212</sup>B. Niewelt, M. Jastrzębski, S. Kurzyna, J. Nowosielski, W. Wasilewski, M. Mazelanik, and M. Parniak, "Experimental Implementation of the Optical Fractional Fourier Transform in the Time-Frequency Domain", Phys. Rev. Lett. **130**, 240801 (2023).
- <sup>213</sup>D. Mendlovic and H. M. Ozaktas, "Fractional Fourier transforms and their optical implementation: I", J. Opt. Soc. Am. A **10**, 1875–1881 (1993).
- <sup>214</sup>A. W. Lohmann and D. Mendlovic, "Fractional fourier transform: photonic implementation", Appl. Opt. **33**, 7661–7664 (1994).
- <sup>215</sup>M. T. Kauffman, W. C. Banyai, A. A. Godil, and D. M. Bloom, "Time-to-frequency converter for measuring picosecond optical pulses", Appl. Phys. Lett. **64**, 270–272 (1994).
- <sup>216</sup>V. Namias, "The Fractional Order Fourier Transform and its Application to Quantum Mechanics", IMA J. Appl. Math. **25**, 241–265 (1980).
- <sup>217</sup>A. W. Lohmann, "Image rotation, Wigner rotation, and the fractional Fourier transform", J. Opt. Soc. Am. A **10**, 2181–2186 (1993).
- <sup>218</sup>H. M. Ozaktas and D. Mendlovic, "Fractional Fourier optics", J. Opt. Soc. Am. A **12**, 743–751 (1995).
- <sup>219</sup>E. Sejdić, I. Djurović, and L. Stanković, "Fractional Fourier transform as a signal processing tool: An overview of recent developments", Signal Process. **91**, Fourier Related Transforms for Non-Stationary Signals, 1351–1369 (2011).
- <sup>220</sup>J. Paye, "The chronocyclic representation of ultrashort light pulses", IEEE J. Quantum Electron. **28**, 2262–2273 (1992).
- <sup>221</sup>R. Salem, M. A. Foster, and A. L. Gaeta, "Application of space-time duality to ultrahigh-speed optical signal processing", Adv. Opt. Photon. **5**, 274–317 (2013).
- <sup>222</sup>V. Torres-Company, J. Lancis, and P. Andrés, "Chapter 1 Space-Time Analogies in Optics", in, Vol. 56, edited by E. Wolf, Progress in Optics (Elsevier, 2011), pp. 1–80.
- <sup>223</sup>G. Agrawal, "Chapter 2 Pulse Propagation in Fibers", in *Nonlinear fiber optics*, 5th (Academic Press, Boston, 2013), pp. 27–56.
- <sup>224</sup>G. Patera, D. B. Horoshko, and M. I. Kolobov, "Space-time duality and quantum temporal imaging", Phys. Rev. A **98**, 053815 (2018).
- <sup>225</sup>C. Bennett and B. Kolner, "Aberrations in temporal imaging", IEEE J. Quantum Electron. **37**, 20–32 (2001).
- <sup>226</sup>O. Martinez, J. Gordon, and R. Fork, "Negative group-velocity dispersion using refraction", J. Opt. Soc. Am. A 1, 1003–1006 (1984).
- <sup>227</sup>M. Lai, S. T. Lai, and C. Swinger, "Single-grating laser pulse stretcher and compressor", Appl. Opt. **33**, 6985–6987 (1994).

- <sup>228</sup>A. M. Weiner, "Dispersion and Dispersion Compensation", in *Ultrafast optics* (John Wiley & Sons, Ltd, 2009) Chap. 4, pp. 147–197.
- <sup>229</sup>C. Sainz, P. Jourdian, R. Escalona, and J. Calatroni, "Real time interferometric measurements of dispersion curves", Opt. Commun. **110**, 381–390 (1994).
- <sup>230</sup>A. Kovács, K. Osvay, G. Kurdi, M. Görbe, J. Klebniczki, and Z. Bor, "Dispersion control of a pulse stretcher–compressor system with two-dimensional spectral interferometry", Appl. Phys. B 80, 165–170 (2005).
- <sup>231</sup>S. Srivastava, D. B. Horoshko, and M. I. Kolobov, "Making entangled photons indistinguishable by a time lens", Phys. Rev. A **107**, 033705 (2023).
- <sup>232</sup>S. Srivastava, D. B. Horoshko, and M. I. Kolobov, "Erecting time telescope for photonic quantum networks", Opt. Express **31**, 38560–38577 (2023).
- <sup>233</sup>S. Kurzyna, M. Jastrzębski, N. Fabre, W. Wasilewski, M. Lipka, and M. Parniak, "Variable electro-optic shearing interferometry for ultrafast single-photon-level pulse characterization", Opt. Express **30**, 39826–39839 (2022).
- <sup>234</sup>E. G. Loewen and E. Popov, *Diffraction gratings and applications* (Marcel Dekker, Inc., New York, 1997).
- <sup>235</sup>A. J. Pizzimenti, J. M. Lukens, H.-H. Lu, N. A. Peters, S. Guha, and C. N. Gagatsos, "Non-Gaussian photonic state engineering with the quantum frequency processor", Phys. Rev. A **104**, 062437 (2021).
- <sup>236</sup>J. Schröder, M. A. F. Roelens, L. B. Du, A. J. Lowery, S. Frisken, and B. J. Eggleton, "An optical FPGA: Reconfigurable simultaneous multi-output spectral pulse-shaping for linear optical processing", Opt. Express 21, 690–697 (2013).
- <sup>237</sup>M. Lipka and M. Parniak, "Super-resolution of ultrafast pulses via spectral inversion", arXiv preprint arXiv:2403.12746 (2024).
- <sup>238</sup>Rayleigh, "XXXI. Investigations in optics, with special reference to the spectroscope", The London, Edinburgh, and Dublin Philosophical Magazine and Journal of Science 8, 261–274 (1879).
- <sup>239</sup>E. Bettens, D. Van Dyck, A. den Dekker, J. Sijbers, and A. van den Bos, "Model-based two-object resolution from observations having counting statistics", Ultramicroscopy 77, 37–48 (1999).
- <sup>240</sup>M. Tsang, R. Nair, and X.-M. Lu, "Quantum Theory of Superresolution for Two Incoherent Optical Point Sources", Phys. Rev. X 6, 031033 (2016).
- <sup>241</sup>M. Paúr, B. Stoklasa, Z. Hradil, L. L. Sánchez-Soto, and J. Rehacek, "Achieving the ultimate optical resolution", Optica **3**, 1144–1147 (2016).
- <sup>242</sup>S. J. Yang, X. J. Wang, X. H. Bao, and J. W. Pan, "An efficient quantum light-matter interface with sub-second lifetime", Nat. Photonics **10**, 381–384 (2016).

- <sup>243</sup>R. Nair and M. Tsang, "Far-Field Superresolution of Thermal Electromagnetic Sources at the Quantum Limit", Phys. Rev. Lett. **117**, 190801 (2016).
- <sup>244</sup>Z. S. Tang, K. Durak, and A. Ling, "Fault-tolerant and finite-error localization for point emitters within the diffraction limit", Opt. Express 24, 22004–22012 (2016).
- <sup>245</sup>W.-K. Tham, H. Ferretti, and A. M. Steinberg, "Beating Rayleigh's Curse by Imaging Using Phase Information", Phys. Rev. Lett. **118**, 070801 (2017).
- <sup>246</sup>W. Larson, N. V. Tabiryan, and B. E. Saleh, "A common-path polarization-based image-inversion interferometer", Opt. Express 27, 5685–5695 (2019).
- <sup>247</sup>C. Datta, M. Jarzyna, Y. L. Len, K. Łukanowski, J. Kołodyński, and K. Banaszek, "Sub-Rayleigh resolution of two incoherent sources by array homodyning", Phys. Rev. A 102, 063526 (2020).
- <sup>248</sup>J. Frank, A. Duplinskiy, K. Bearne, and A. I. Lvovsky, "Passive superresolution imaging of incoherent objects", Optica **10**, 1147–1152 (2023).
- <sup>249</sup>A. N. Jordan and J. C. Howell, "Fundamental Limits on Subwavelength Range Resolution", Phys. Rev. Appl. **20**, 064046 (2023).
- <sup>250</sup>D. Triggiani, G. Psaroudis, and V. Tamma, "Ultimate Quantum Sensitivity in the Estimation of the Delay between two Interfering Photons through Frequency-Resolving Sampling", Phys. Rev. Appl. **19**, 044068 (2023).
- <sup>251</sup>M. Paúr, B. Stoklasa, J. Grover, A. Krzic, L. L. Sánchez-Soto, Z. Hradil, and J. Řeháček, "Tempering Rayleigh's curse with PSF shaping", Optica **5**, 1177–1180 (2018).
- <sup>252</sup>J. Řehá ček, M. Paúr, B. Stoklasa, D. Koutný, Z. Hradil, and L. L. Sánchez-Soto, "Intensity-Based Axial Localization at the Quantum Limit", Phys. Rev. Lett. **123**, 193601 (2019).
- <sup>253</sup>P. Boucher, C. Fabre, G. Labroille, and N. Treps, "Spatial optical mode demultiplexing as a practical tool for optimal transverse distance estimation", Optica 7, 1621–1626 (2020).
- <sup>254</sup>S. De, J. Gil-Lopez, B. Brecht, C. Silberhorn, L. L. Sánchez-Soto, Z. ě. Hradil, and J. Řehá ček, "Effects of coherence on temporal resolution", Phys. Rev. Res. 3, 033082 (2021).
- <sup>255</sup>U. Zanforlin, C. Lupo, P. W. R. Connolly, P. Kok, G. S. Buller, and Z. Huang, "Optical quantum super-resolution imaging and hypothesis testing", Nat. Commun. **13**, 5373 (2022).
- <sup>256</sup>J. Frank, A. Duplinskiy, K. Bearne, and A. I. Lvovsky, "Passive superresolution imaging of incoherent objects", Optica **10**, 1147–1152 (2023).
- <sup>257</sup>S. A. Wadood, K. R. Sethuraj, K. Liang, M. R. Grace, G. L. Rue, S. Guha, and A. N. Vamivakas, "Experimental demonstration of quantum-inspired optical symmetric hypothesis testing", Opt. Lett. 49, 750–753 (2024).

- <sup>258</sup>A. Sajjad, M. R. Grace, Q. Zhuang, and S. Guha, "Attaining quantum limited precision of localizing an object in passive imaging", Phys. Rev. A **104**, 022410 (2021).
- <sup>259</sup>G. Sorelli, M. Gessner, M. Walschaers, and N. Treps, "Optimal Observables and Estimators for Practical Superresolution Imaging", Phys. Rev. Lett. **127**, 123604 (2021).
- <sup>260</sup>Y. Wang and V. O. Lorenz, "Fundamental limit of bandwidth-extrapolation-based superresolution", Phys. Rev. A **108**, 012602 (2023).
- <sup>261</sup>Ł. Rudnicki and T. Linowski, "Spectral and temporal metrology with bandlimited functions and finite-time measurements", arXiv preprint arXiv:2402.12995 (2024).
- <sup>262</sup>V. Ansari, B. Brecht, J. Gil-Lopez, J. M. Donohue, J. Řeháček, Z. Hradil, L. L. Sánchez-Soto, and C. Silberhorn, "Achieving the Ultimate Quantum Timing Resolution", PRX Quantum 2, 010301 (2021).
- <sup>263</sup>W. Krokosz, M. Mazelanik, M. Lipka, M. Jarzyna, W. Wasilewski, K. Banaszek, and M. Parniak, "Beating the spectroscopic Rayleigh limit via post-processed heterodyne detection", Opt. Lett. 49, 1001–1004 (2024).
- <sup>264</sup>M. Mazelanik, A. Leszczyński, and M. Parniak, "Optical-domain spectral super-resolution via a quantum-memory-based time-frequency processor", Nat. Commun. **13**, 691 (2022).
- <sup>265</sup>A. Boschetti, A. Taschin, P. Bartolini, A. K. Tiwari, L. Pattelli, R. Torre, and D. S. Wiersma, "Spectral super-resolution spectroscopy using a random laser", Nat. Photonics 14, 177–182 (2020).
- <sup>266</sup>K. Hashimoto, D. B. Horoshko, M. I. Kolobov, Y. Michael, Z. Gefen, and M. V. Chekhova, "Fourier-transform infrared spectroscopy with undetected photons from high-gain spontaneous parametric down-conversion", arXiv preprint arXiv:2403.05423 (2024).
- <sup>267</sup>F. Grenapin, D. Paneru, A. D'Errico, V. Grillo, G. Leuchs, and E. Karimi, "Superresolution Enhancement in Biphoton Spatial-Mode Demultiplexing", Phys. Rev. Appl. 20, 024077 (2023).
- <sup>268</sup>Z. Huang, C. Schwab, and C. Lupo, "Ultimate limits of exoplanet spectroscopy: A quantum approach", Phys. Rev. A **107**, 022409 (2023).
- <sup>269</sup>A. Bose, I. Thomas, and E. Abraham, "Fluorescence spectroscopy and its applications: A Review", Int. J. Adv. Pharm. Res **8**, 1–8 (2018).
- <sup>270</sup>K. Wicker, S. Sindbert, and R. Heintzmann, "Characterisation of a resolution enhancing image inversion interferometer", Opt. Express 17, 15491–15501 (2009).
- <sup>271</sup>D. B. Horoshko and M. I. Kolobov, "Interferometric sorting of temporal Hermite-Gauss modes via temporal Gouy phase", arXiv preprint arXiv:2310.11918 (2023).
- <sup>272</sup>L. Serino, J. Gil-Lopez, M. Stefszky, R. Ricken, C. Eigner, B. Brecht, and C. Silberhorn, "Realization of a multi-output quantum pulse gate for decoding high-dimensional temporal modes of single-photon states", PRX quantum 4, 020306 (2023).

- <sup>273</sup>M. Tsang, "Resolving starlight: a quantum perspective", Contemp. Phys. **60**, 279–298 (2019).
- <sup>274</sup>L. S. Amato, F. Sgobba, and C. Lupo, "Single-photon sub-Rayleigh precision measurements of a pair of incoherent sources of unequal intensity", arXiv preprint arXiv:2309.02295 (2023).
- <sup>275</sup>L. Santamaria, D. Pallotti, M. S. de Cumis, D. Dequal, and C. Lupo, "Spatial-mode demultiplexing for enhanced intensity and distance measurement", Opt. Express 31, 33930–33944 (2023).
- <sup>276</sup>A. B. Greenwood, R. Oulton, and H. Gersen, "On the impact of realistic point sources in spatial mode demultiplexing super resolution imaging", Quantum Sci. Technol. **8**, 015024 (2023).
- <sup>277</sup>C. Hu, L. Xu, B. Wang, Z. Li, Y. Zhang, Y. Zhang, and L. Zhang, "Experimental 3D super-localization with Laguerre–Gaussian modes", Quantum Frontiers 2, 20 (2023).
- <sup>278</sup>M. R. Grace, Z. Dutton, A. Ashok, and S. Guha, "Approaching quantum-limited imaging resolution without prior knowledge of the object location", J. Opt. Soc. Am. A 37, 1288–1299 (2020).
- <sup>279</sup>C. Oh, S. Zhou, Y. Wong, and L. Jiang, "Quantum limits of superresolution in a noisy environment", Phys. Rev. Lett. **126**, 120502 (2021).
- <sup>280</sup>K. Schlichtholz, T. Linowski, M. Walschaers, N. Treps, Ł. Rudnicki, and G. Sorelli, "Practical tests for sub-Rayleigh source discriminations with imperfect demultiplexers", Optica Quantum 2, 29–34 (2024).